Measurement of the Dipion Mass Spectrum in the Decay $X(3872) \rightarrow J/\psi\,\pi^+\pi^-$ at the CDF II Experiment

by

Alexander Rakitin

Submitted to the Department of Physics
in partial fulfillment of the requirements for the degree of

Doctor of Philosophy

at the

MASSACHUSETTS INSTITUTE OF TECHNOLOGY

June 2005

Author . . . .
Department of Physics
June 27, 2005

Certified by . . . .
Christoph M. E. Paus
Associate Professor
Thesis Supervisor

Accepted by . . . .
George W. Koster
Chairman, Department Committee on Graduate Students

Measurement of the Dipion Mass Spectrum in the Decay $\boldsymbol{X(3872) \to J/\psi\, \pi^+\pi^-}$ at the CDF II Experiment

by

Alexander Rakitin

Submitted to the Department of Physics
on June 27, 2005, in partial fulfillment of the
requirements for the degree of
Doctor of Philosophy

Abstract

We present a measurement of the dipion mass spectrum in the decay $X(3872) \to J/\psi\, \pi^+\pi^-$ using a 360 pb^{-1} sample of $p\bar{p}$ collisions at $\sqrt{s} = 1.96$ TeV collected with the CDF II detector at the Fermilab Tevatron Collider. As a benchmark, we also extract the dipion mass distribution for $\psi(2S) \to J/\psi\, \pi^+\pi^-$ decay. The $X(3872)$ dipion mass spectrum is compared to QCD multipole expansion predictions for various charmonium states, as well as to the hypothesis $X(3872) \to J/\psi \rho^0$. We find that the measured spectrum is compatible with $^3S_1$ charmonium decaying to $J/\psi\, \pi^+\pi^-$ and with the $X(3872) \to J/\psi \rho^0$ hypothesis. There is, however, no $^3S_1$ charmonium state available for assignment to the $X(3872)$. The multipole expansion calculations for $^1P_1$ and ^3D_J states are in clear disagreement with the $X(3872)$ data. For the $\psi(2S)$ the data agrees well with previously published results and to multipole expansion calculations for $^3S_1$ charmonium. Other, non-charmonium, models for the $X(3872)$ are described too.

We conclude that since the dipion mass spectrum for $X(3872)$ is compatible with $J/\psi \rho^0$ hypothesis, the $X(3872)$ should be C-positive. This conclusion is supported by recent results from Belle Collaboration which observed $X(3872) \to J/\psi\, \gamma$ decay. We argue that if $X(3872)$ is a charmonium, then it should be either $1^1D_{2^{-+}}$ or $2^3P_{1^{++}}$ state, decaying into $J/\psi\, \pi^+\pi^-$ in violation of isospin conservation. A non-charmonium assignment, such as $D\overline{D}^*$ molecule, is also quite possible.

Thesis Supervisor: Christoph M. E. Paus
Title: Associate Professor

To the memory of my mother

Acknowledgments

I want to thank everybody who was around me for the last few years for a constant support and help. I want to thank Gerry Bauer for his guidance, extreme patience and readiness to give advice and help even in the most complicated situations. Without his tremendous influence this work would not be done. I want to thank my advisor, Christoph Paus for his permanent encouragement to "work hard" and for wonderful example of a strong, persistent and motivated leader. I want to thank my friend and office-mate Ilya Kravchenko for his wise input and willingness to help – in science, in programming and in life. I want to specifically thank Konstantin Anikeev and Andreas Korn for their succor. Their theses contributed significantly into mine. I thank Petar Maksimović, with whom I worked on B_d-mixing in the first few years in Fermilab. I thank Jeff Tseng for his useful advices in the search of $B_s \to D_s^+ D_s^-$, and for his wonderful peaceful personality.

I want to thank all the members of my family in Russia, America, Lithuania and Israel, who were eagerly waiting for the completion of this thesis.

I also want to thank my fellow graduate students and postdocs from MIT: Alberto Belloni, Guillelmo Ceballos, Nuno Leonardo, Jeff Miles, Ivan Furić, Michael Mulhearn, Arkadii Bolshov, Boris Iyutin, Stephan Gromoll, Tushar Shah, Paul Ngan and the people from other Institutions: Rodion Tikhoplav, Jonatan Piedra, Andrew Kovalev. I want to thank them both for their scientific help and for the personal inputs in my life. I thank all the members of the CDF Collaboration who built and operated the detector and collected the data, which allowed me to perform this analysis.

I thank the staff of the International Student Office at MIT, especially Danielle Guichard-Ashbrook, and all those who helped me to resolve the problems with obtaining the US visa. Also, I am thankful to Lauren Saragosa, Sandy Fowler and Roger Gaul for their administrative help.

I want to thank all my friends in the Geneva ward and in the Naperville 5th YSA branch of the Church of Jesus Christ of Latter-day Saints. I want to especially thank Corey Nielsen for being a wonderful friend and a constant spiritual support for me throughout all these years.

Also, I want to thank my friends both in America and Russia, who were praying for my successful graduation.

And most of all I am grateful to my wife, Katya Smirnova, who supported me in all possible ways, implemented corrections to the text of this thesis, invested tremendous effort and time into it, spent sleepless nights over it and kept inspiring me to work further when I was tired.

Contents

Chapter 1

Introduction: What is the $X(3872)$?

One of the interesting problems in contemporary Heavy Quark physics is to determine the properties of newly discovered particles. It becomes especially captivating when such a particle does not fit into the existing scheme, and many new hypotheses are created to interpret this fact.

The discovery of the state $X(3872)$ with unexpected properties reported by the Belle Collaboration [1], and confirmed by CDF [2], D0 [3] and BaBar [4], gave rise to many hypotheses trying to explain the nature of this new state. The original, and most natural, interpretation of the $X(3872)$ was a new $c\bar{c}$ state, but the $X(3872)$ does not seem to fit into the conventional $c\bar{c}$ framework. So, many other theories came forth — molecular models, more general 4-quark interpretations including a diquark-antidiquark model, hybrid models *etc* — to explain the nature of the $X(3872)$. We will review these ideas, including the simple $c\bar{c}$ options, in the subsequent sections.

One of the ways to gain insight into the nature of the $X(3872)$ is to investigate its decays. Originally the $X(3872)$ was found through its decay into $J/\psi\,\pi^+\pi^-$, but other decay modes were also investigated. No evidence was found for $X(3872)$ decaying into $\chi_{c1}\gamma$ [1], $\chi_{c2}\gamma$ [5], $J/\psi\eta$ [6], D^+D^- [7], or $D^0\overline{D}^0$ [7]. Also, there are no traces of the $X(3872)$ found in e^+e^- collisions [8], nor in $\gamma\gamma$ fusion [9]. Charged partners $X^\pm$ are also not observed [10]. The Belle Collaboration has reported an ostensible signal in the $X(3872) \rightarrow J/\psi\,\pi^+\pi^-\pi^0$ decay mode, interpreted as $J/\psi\omega$ [11]. More information about these searches will be given in Section 1.1.

Another way to investigate the $X(3872)$ is to look at the distributions of different parameters of its decay. This approach has the merit of directly studying a property *of the* $X(3872)$ rather than making inferences based on what one *does not see*, as is the case for null searches of decay modes. As was pointed out in the literature [1, 12, 13] the shape of the distribution of the invariant mass, $m_{\pi\pi}$, of the two pions coming out of the decay $X(3872) \rightarrow J/\psi\,\pi^+\pi^-$ may shed light on the properties of the $X(3872)$. For example, if these two pions are consistent with coming from a virtual ρ^0, then the C-parity of the $X(3872)$ should correspond to it decaying into $J/\psi\rho^0$.

Figure 1-1 shows a $\pi^+\pi^-$ invariant mass distribution obtained by Belle. It is fitted with two theoretical curves, corresponding to two different quantum states of the dipion. Based on the results of such fits one could distinguish between these states and, therefore, help extract information about the $X(3872)$ properties. We will discuss this in more detail in Chapter 6. Due to the small data sample, the points on the plot have large errors that make it hard to determine the true shape of the $m_{\pi\pi}$ distribution. Only the general inclination for high dipion masses is observed. The $m_{\pi\pi}$ spectrum reported by BaBar [16] is shown in the top plot in Figure 1-2. It has the same drawbacks — a small data sample and, therefore, large error bars. Because of this, it is hard to draw any definite conclusions about the dipion mass shape from this plot. One can not even judge if the dipion system favors high or low masses.

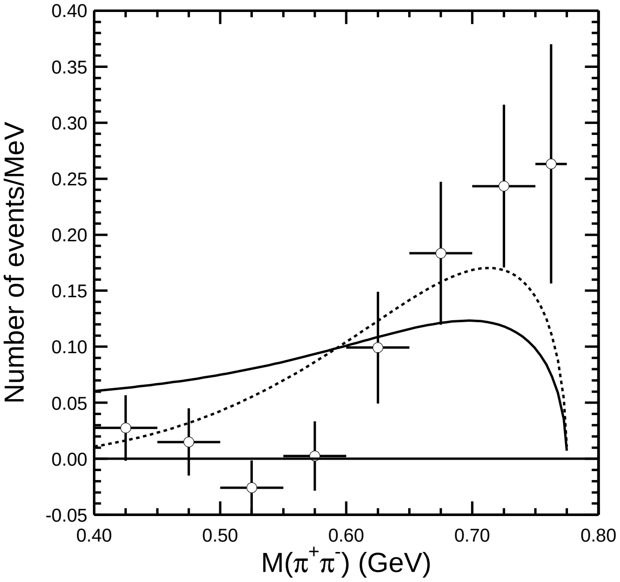

Figure 1-1: A modified version (sideband-subtracted and rebinned) of Belle's dipion invariant mass spectrum for the $X(3872)$ [14]. The solid line is a multipole expansion prediction [15] for a D-wave charmonium state decaying into $J/\psi\,\pi^+\pi^-$, and the dashed-dotted line is for an S-wave state.

This thesis is a measurement of the dipion invariant mass distribution in $X(3872) \to J/\psi\pi^+\pi^-$ decays at CDF. We use the large $X(3872)$ sample available at CDF to obtain the $X(3872)$ $m_{\pi\pi}$ distribution with greater precision, *i.e.* a better constrained shape. The thesis is organized as follows: in this chapter a general overview of different $X(3872)$ models is given. The second and third chapters are devoted to the description of the CDF detector and the data sample selection. The actual measurement of the dipion invariant mass spectrum $m_{\pi\pi}$ is described in Chapter 4. Chapter 5 discusses the systematic uncertainties. After that, in Chapter 6, the $m_{\pi\pi}$ spectrum is compared to different theoretical models. The conclusions come last, in Chapter 7.

1.1 Established Facts About the $X(3872)$

The $X(3872)$ was first announced by the Belle Collaboration in August 2003. It was found in an exclusive decay $B^+ \to K^+X(3872) \to K^+J/\psi\,\pi^+\pi^-$ [1]. Figure 1-3 shows the mass distribution of $J/\psi\,\pi^+\pi^-$ from Belle's report. One can see a quite sharp peak in the middle of the plot, to the right of the larger peak, corresponding to the $\psi(2S)$. The smaller peak corresponds to the $X(3872)$. As we will see later, the small width of this peak may help to identify the $X(3872)$ or, at least, provide grounds for excluding some hypotheses about its nature. Belle observed a signal of 34.4 ± 6.5 events and measured mass:

$$m(X(3872)) = 3872.0 \pm 0.6(\text{stat.}) \pm 0.5\ \text{MeV}/c^2(\text{syst.}), \tag{1.1}$$

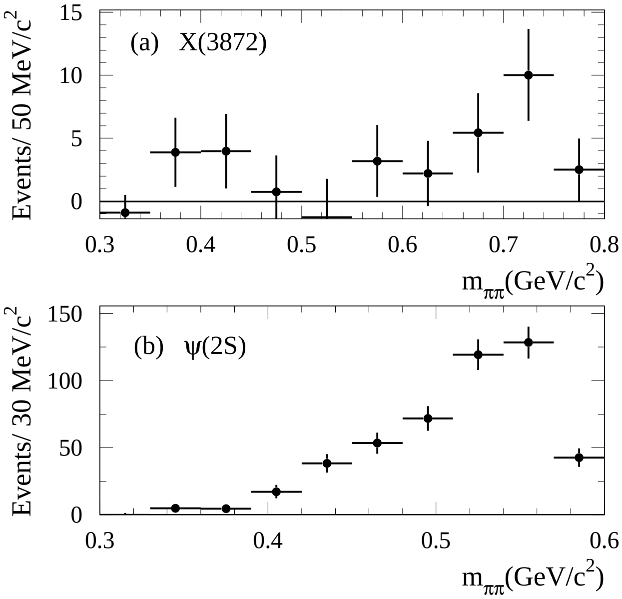

Figure 1-2: The $m_{\pi\pi}$ spectrum from BaBar [16]: a) for the $X(3872)$ and b) for the $\psi(2S)$.

and set a quite tight limit on its decay width:

$$\Gamma(X(3872)) < 2.3 \text{ MeV (at confidence level (CL) } 90\%). \tag{1.2}$$

Also, the relative branching ratio is given:

$$\frac{\text{Br}(B^+ \to X(3872)K^+) \times \text{Br}(X(3872) \to J/\psi\,\pi^+\pi^-)}{\text{Br}(B^+ \to \psi(2S)K^+) \times \text{Br}(X(3872) \to J/\psi\,\pi^+\pi^-)} = 0.063 \pm 0.012(\text{stat.}) \pm 0.007(\text{syst.}).$$

The CDF [2] and the D0 [3] Collaborations later confirmed this discovery in proton-antiproton collisions and measured the $X(3872)$ mass. The BaBar Collaboration [4] also found the $X(3872)$ in B-meson decays and obtained its mass. All the four mass measurements are summarized in Figure 1-4.

Belle has performed a few more searches for different $X(3872)$ decay modes, mostly with null results. One of the searches, for the $X(3872) \to J/\psi\,\pi^+\pi^-\pi^0$ [11], showed an enhancement in the yield which was interpreted as $J/\psi\,\omega$. The ω signal obtained by Belle is depicted in Figure 1-5 [11]. The left plot displays the distribution of the "beam-constrained" mass M_{bc}, which is calculated as a difference between the energy of the beam and the 3-momentum of the reconstructed B-meson in quadrature. The center plot shows the distribution of ΔE, *i.e.* the difference between the energy of the beam and the energy of the reconstructed B-meson. The right plot gives the tripion mass from the M_{bc}-ΔE signal region. The tripion mass peaks at the upper kinematic limit, as one would expect for the $J/\psi\,\omega$ hypothesis.

The relative $X(3872)$ width for this decay is found to be:

$$\frac{\Gamma(X \to J/\psi\,\omega)}{\Gamma(X \to J/\psi\,\pi^+\pi^-)} = 0.8 \pm 0.3(\text{stat.}) \pm 0.1(\text{syst.}). \tag{1.3}$$

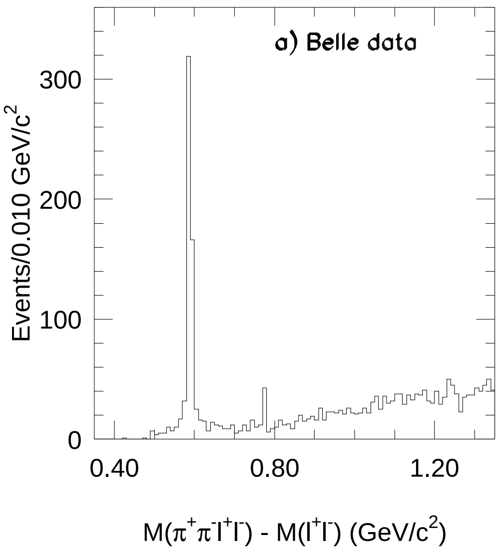

Figure 1-3: The $J/\psi\,\pi^+\pi^-$ mass distribution from Belle [1].

The Belle result looks encouraging, but it has quite low statistics, and we will still reserve final judgment at this point.

The other $X(3872)$ decay modes searched for by Belle fall into two categories:

1. *Radiative* decays: *i.e.* decays with emission of a photon [1, 11]:

$$\frac{\Gamma(X(3872) \to \chi_{c1}\gamma)}{\Gamma(X(3872) \to J/\psi\,\pi^+\pi^-)} < 0.89 \text{ (at 90\% CL) [1]} \tag{1.4}$$

$$\frac{\Gamma(X(3872) \to \chi_{c2}\gamma)}{\Gamma(X(3872) \to J/\psi\,\pi^+\pi^-)} < 1.1 \text{ (at 90\% CL) [11]} \tag{1.5}$$

$$\frac{\Gamma(X(3872) \to J/\psi\,\gamma)}{\Gamma(X(3872) \to J/\psi\,\pi^+\pi^-)} < 0.40 \text{ (at 90\% CL) [11].} \tag{1.6}$$

2. *Double-charm* decays, *i.e.* decays into two D-mesons [7]:

$$\mathrm{Br}(B^+ \to X(3872)K^+) \times \mathrm{Br}(X(3872) \to D^+D^-) < 4 \times 10^{-5} \text{ (at 90\% CL),} \tag{1.7}$$

$$\mathrm{Br}(B^+ \to X(3872)K^+) \times \mathrm{Br}(X(3872) \to D^0\overline{D^0}) < 6 \times 10^{-5} \text{ (at 90\% CL),} \tag{1.8}$$

$$\mathrm{Br}(B^+ \to X(3872)K^+) \times \mathrm{Br}(X(3872) \to D^0\overline{D}^0\pi^0) < 6 \times 10^{-5} \text{ (at 90\% CL).} \tag{1.9}$$

All of these results are negative. This means that the $X(3872)$ decays to these final states with quite low branching ratios, if at all[1].

---

[1] After this work was completed, Belle announced a new result indicating that the $X(3872)$ decays into

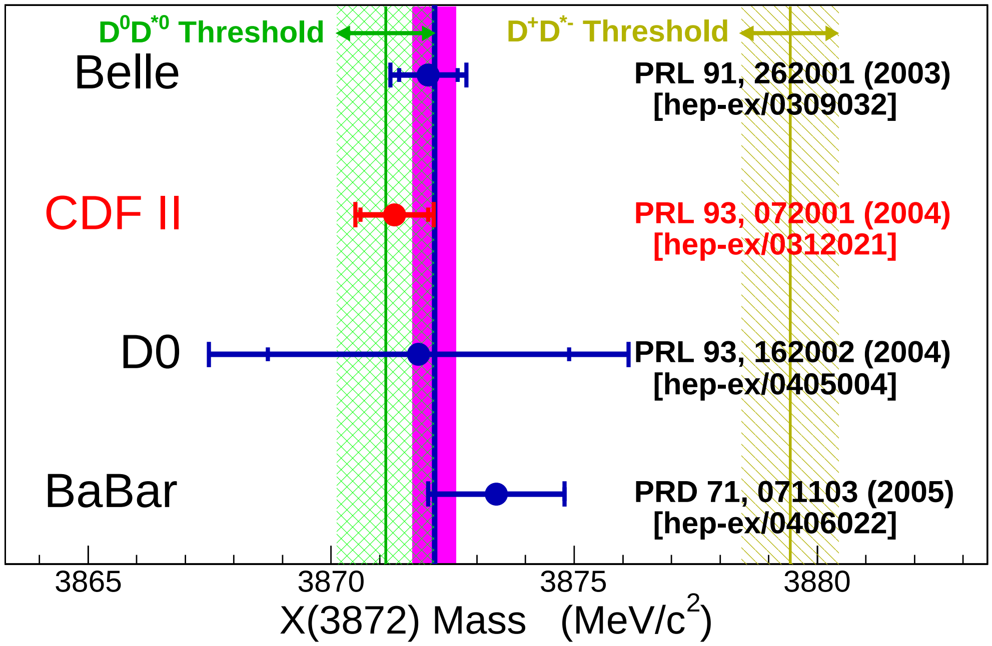

Figure 1-4: The $X(3872)$ mass measurements from References [1, 2, 3, 4]. The D^0-$\overline{D}^{*0}$ and D^+-D^{*-} thresholds are shown. The uncertainty bands around the mass values are given too.

The BaBar Collaboration performed a search for $X(3872) \to J/\psi\,\eta$ decay, which yielded [6]:

$$\mathrm{Br}(B^+ \to X(3872)K^+) \times \mathrm{Br}(X(3872) \to J/\psi\,\eta) < 7.7 \times 10^{-6} \text{ at } 90\% \text{ CL.} \tag{1.10}$$

As mentioned earlier, BaBar also looked for charged companions of the $X(3872)$ with negative results [10]:

$$\mathrm{Br}(\overline{B^0}/B^0 \to X^\pm K^\mp, X^\pm \to J/\psi\,\pi^\pm\pi^0) < 5.8 \times 10^{-6} \text{ at } 90\% \text{ CL,} \tag{1.11}$$

$$\mathrm{Br}(B^\pm \to X^\pm K^0_S, X^\pm \to J/\psi\,\pi^\pm\pi^0) < 11 \times 10^{-6} \text{ at } 90\% \text{ CL.} \tag{1.12}$$

The BES Collaboration contributed to this list by setting a strong limit on the relative width of $X(3872) \to e^+e^-$ decay [8]:

$$\Gamma(X(3872) \to e^+e^-) \times \mathrm{Br}(X(3872) \to J/\psi\,\pi^+\pi^-) < 10 \text{ eV at } 90\% \text{ CL.} \tag{1.13}$$

CLEO III confirmed that this branching ratio is very small [9]:

$$\Gamma(X(3872) \to e^+e^-) \times \mathrm{Br}(X(3872) \to J/\psi\,\pi^+\pi^-) < 8.3 \text{ eV at } 90\% \text{ CL.} \tag{1.14}$$

$J/\psi\,\gamma$ [17]:

$$\frac{\Gamma(X(3872) \to J/\psi\,\gamma)}{\Gamma(X(3872) \to J/\psi\,\pi^+\pi^-)} = 0.14 \pm 0.05.$$

Also they now claim to see $X(3872) \to D^0\overline{D^0}\pi^0$. The discussion of the possible implications of these results has been added to Chapter 7.

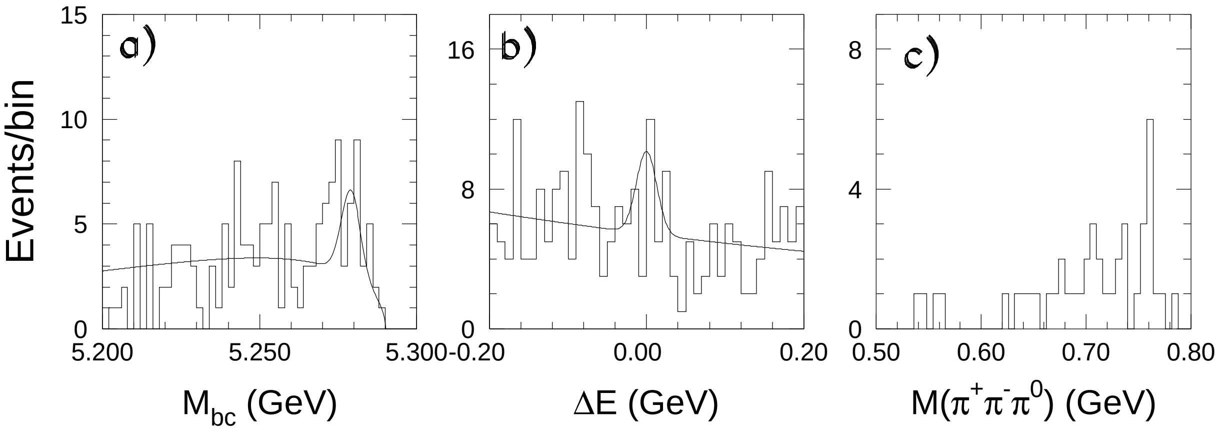

Figure 1-5: The $X(3872) \to J/\psi\,\pi^+\pi^-\pi^0$ signal from Belle. The tripion invariant mass (right plot) peaks near the upper kinematic limit [11].

They also looked for the production of a C-positive $X(3872)$ via two-photon fusion and set the limit [9]:

$$(2J+1)\Gamma(X \to \gamma\gamma) \times \mathrm{Br}(X(3872) \to J/\psi\,\pi^+\pi^-) < 12.9 \text{ eV (at 90\% CL)}, \tag{1.15}$$

where J stands for the (unknown) spin of the $X(3872)$.

We can see that the final states searched for by Belle, BaBar, BES and CLEO III are not among the preferred $X(3872)$ decay channels. Based on all the listed facts we will make a few conclusions about the properties of the $X(3872)$ in the subsequent sections, but first we review some basic features of quantum numbers of particle states.

1.2 Review of C- and P-parity, and Isospin

Before proceeding further, we remind the reader about the concepts of C- and P-parity and isospin. An important characteristic of any quark state is the behavior of its wave-function under certain transformations. One very important transformation is the replacement of all particles with their anti-particles, so-called C-conjugation. Another one, called P-transformation, is the switching the signs of all coordinates. Many, but not all, quark states are eigenstates of these transformations. This means that for such states the wave-function Φ' after the transformation is proportional to the wave-function Φ before the transformation: $\Phi' = C\Phi = \lambda_C \cdot \Phi$, and $\Phi' = P\Phi = \lambda_P \cdot \Phi$. These numbers, λ_C and λ_P, are called the *C-parity* and *P-parity* of the particular quark state and are usually referred to simply as C and P. Both these transformations have a special property: being applied twice to the wave-function Φ they return it into the original condition. From mathematical point of view this means that $C^2\Phi = \Phi$ and $P^2\Phi = \Phi$. It immediately follows that $C^2 = P^2 = 1$, *i.e.* that the particular quark state may have C or P-parity either "+1" or "−1". For example, the P-parity of π-meson family is known to be −1: $P\pi^0 = -\pi^0$, $P\pi^+ = -\pi^+$, $P\pi^- = -\pi^-$. The symbol π here stands for the wave-function of the π-meson. As for the C-parity, it is "+1" for π^0, $C\pi^+ = +\pi^0$; but π^+ and π^- do not have definite

C-parity. Under the C-transformation they turn into each other, $C\pi^+ = \pi^-$, $C\pi^- = \pi^+$, but not into themselves.

The C- and P-parity of a system of a quark and an antiquark with half-integer spins (fermions) depend on its orbital angular momentum L and spin S as follows:

$$P = (-1)^{L+1}, \quad C = (-1)^{L+S}. \tag{1.16}$$

For particles with an integer spin (bosons) these formulae look differently. For example, for a system of π^+ and π^- mesons:

$$P = C = (-1)^L. \tag{1.17}$$

It is common practice to talk about the J^{PC} combination for a particular system, denoting it as, for example, 0^{++}, 1^{--} *etc.* This combination is referred to as a *spin-parity* of a particle.

An important property of C and P parities is that they are conserved in strong and electromagnetic interactions [18]. This means that C and P parities of a particle may be determined via the C and P parities of its decay products, if the decay occurs via strong or electromagnetic interactions. We will use this property when discussing possible C and P assignments for the $X(3872)$. Though we do not know the nature of the $X(3872)$ and, therefore, the exact mechanism of its decay, we may assume that it decays via strong or electromagnetic interaction. Had the $X(3872)$ been decaying via the weak interaction into a final state containing c and $\bar{c}$ quarks, it should have contained at least one b quark and, therefore, have a mass much larger than what is observed. We, therefore, assume that the $X(3872)$ does not decay weakly and that both C and P parities are conserved in its decays.

Another important characteristic of any quark-antiquark state is its *isospin*, I. This is a quantum number which is "almost" conserved in strong interactions and which obeys the same algebraic rules as the regular spin S. It is convenient to characterize a quantum state by the combination of the isospin itself and its third projection, I_3, in complete analogy with regular spin states $|S, S_z\rangle$. The sets of states having equal or close masses, and equal isospin, but differing by the values of I_3 or, equivalently, by the electric charges[2], are called *isospin multiplets.* The I_3-component is strictly conserved in both strong and electromagnetic interactions. The isospin itself is not conserved in the electromagnetic interactions, as demonstrated in the following decay:

$$\Sigma^0 |I = 1, I_3 = 0\rangle \to \Lambda\,\gamma |I = 0, I_3 = 0\rangle.$$

Neither isospin nor its third component is conserved by the weak interaction, as exhibited in the decay:

$$\Lambda|0,0\rangle \to p\,\pi^-|1,-1\rangle \Big|\frac{1}{2}, -\frac{1}{2}\Big\rangle = \sqrt{\frac{1}{3}}\Big|\frac{3}{2}, \frac{1}{2}\Big\rangle - \sqrt{\frac{2}{3}}\Big|\frac{1}{2}, -\frac{1}{2}\Big\rangle.$$

We said that the isospin is "almost" conserved in strong interactions meaning that its conservation is actually an approximate law. This law holds with the same precision with which the mass difference between u and d quarks is negligible compared to the energy scale in the experiment E: $m_u - m_d << E$, so that $m_u \approx m_d << E$. This equality of the quark masses is often referred to as "isospin symmetry". The higher the masses and energies we are dealing with, the more exact this symmetry becomes. In the realm of low energies, of order of m_u or m_d, the isospin is not conserved. The isospin symmetry is said to be "broken". The isospin of u and

---

[2] The electric charge is related to I_3 so that the members of the isospin multiplet with different I_3 have different electric charges.

d quarks is equal to $\frac{1}{2}$, with u-quark having positive isospin projection $I_3 = +\frac{1}{2}$, and d-quark a negative one, $I_3 = -\frac{1}{2}$. The isospins of all the other quarks are zero. In particular, the isospin of any charmonium state is zero. We will often refer to isospin considerations when discussing possible assignments for the $X(3872)$.

In the following we derive the relationship between C-parity and isospin I of $\pi^+\pi^-$ system. This relationship will be important in our analysis. Let us factorize the total dipion wave-function into spatial, spin and isospin components. The spin component is irrelevant, because pions have zero spin. If we swap the pions, the spatial component of the total wave-function acquires a factor of $(-1)^L$. As for the isospin component, it behaves just like the normal spin and is symmetric under swapping of the pions if I is even and antisymmetric if I is odd. This is easy to see, for example, from the Clebsch-Gordan coefficients for addition of two states with spin one [19]. Thus it obtains a factor of $(-1)^I$. Since the total wave-function of two pions (bosons) must be symmetric under their swapping, the total obtained factor must be +1, *i.e.* $(-1)^{L+I} = +1$. This means that even I must correspond to even L, odd I to odd L. From Equation 1.17 it follows that the C- and P-parity of the $\pi^+\pi^-$ system are equal to

$$P = C = (-1)^I. \tag{1.18}$$

Using this knowledge let us consider the C-parity and isospin of the $X(3872)$.

1.3 Experimental Evidence for the *C*-parity and Isospin for the *X*(3872)

We do not know *a priori* the C- and P-parity of the $X(3872)$, but there is some evidence of its decay into $J/\psi\,\pi^+\pi^-\pi^0$, interpreted as a decay into $J/\psi\,\omega$ [11], leading to the implication that $X(3872)$ should have positive C-parity, because of negative C-parities of both J/ψ and ω. If the decay $X(3872) \to J/\psi\,\omega$ is confirmed, the positive C-parity of the $X(3872)$ will be established. The same implication does not hold for P-parity, because J/ψ and ω after the decay may have an orbital angular momentum L with respect to each other and then P-parity of the $X(3872)$ is determined as $P_{J/\psi} \cdot\ P_\omega \cdot (-1)^L$.

The observation of the decay $X(3872) \to J/\psi\,\pi^0\pi^0$ would also help resolve the question about its isospin and C-parity. For the $\pi^0\pi^0$ system the C-parity is always positive, since the pions in this system are identical and the total wave-function does not acquire a $(-1)^L$ factor under their swapping. So that the decay $X(3872) \to J/\psi\,\pi^0\pi^0$ is only possible for C-negative $X(3872)$. The dipion $\pi^0\pi^0$ (*i.e.* the sum of two $|I = 1, I_3 = 0\rangle$ states) contains only the $|I = 0, I_3 = 0\rangle$ and $|I = 2, I_3 = 0\rangle$ components and has zero contribution from the $|I = 1, I_3 = 0\rangle$ component [19]. Neglecting the $I = 2$ possibility for the $X(3872)$, we see that the observation of the decay $X(3872) \to J/\psi\,\pi^0\pi^0$ is only possible if the $X(3872)$ has isospin $I = 0$ and $I_3 = 0$. This state $|I = 0, I_3 = 0\rangle$ is decomposed into the sum of the three states

$$|I = 1, I_3 = +1\rangle\, |I = 1, I_3 = -1\rangle (\pi^+\pi^-),$$

$$|I = 1, I_3 = 0\rangle\, |I = 1, I_3 = 0\rangle (\pi^0\pi^0),$$

$$|I = 1, I_3 = -1\rangle\, |I = 1, I_3 = +1\rangle (\pi^-\pi^+)$$

in such a way that the partial width $\Gamma(X(3872) \to J/\psi\,\pi^0\pi^0)$ is two times smaller than the partial width $\Gamma(X(3872) \to J/\psi\,\pi^+\pi^-)$ [19]. So, the observation of the $X(3872) \to J/\psi\,\pi^0\pi^0$ decays in

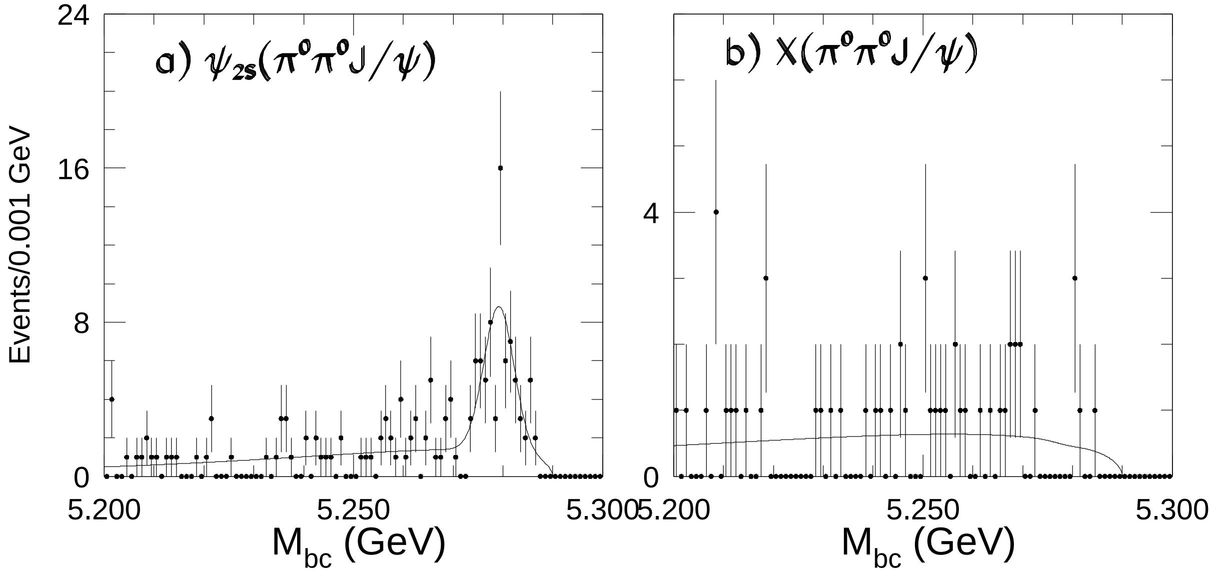

Figure 1-6: Belle's search for: a) $\psi(2S) \to J/\psi\,\pi^0\pi^0$; b) $X(3872) \to J/\psi\,\pi^0\pi^0$ [11].

the comparative rate of 50% to the $X(3872) \to J/\psi\,\pi^+\pi^-$ decays would select negative C-parity for the $X(3872)$. If the $X(3872) \to J/\psi\,\pi^0\pi^0$ decay rate is negligible with respect to $X(3872) \to J/\psi\,\pi^+\pi^-$, it would select positive C-parity [20]. Belle searched for $X(3872) \to J/\psi\,\pi^0\pi^0$ and measured the ratio of the widths of $X(3872) \to J/\psi\,\pi^0\pi^0$ and $X(3872) \to J/\psi\,\pi^+\pi^-$. Figure 1-6 [11] displays the main distributions for this search. The M_{bc} in this plot stands for beam-constrained mass which is described in Section 1.1. The result

$$\frac{\Gamma(X(3872) \to J/\psi\,\pi^0\pi^0)}{\Gamma(X(3872) \to J/\psi\,\pi^+\pi^-)} < 1.3\frac{\Gamma(\psi(2S) \to J/\psi\,\pi^0\pi^0)}{\Gamma(\psi(2S) \to J/\psi\,\pi^+\pi^-)} \text{ (at 90\% CL)}$$

is not sufficiently stringent to distinguish between the $I = 0$ and the $I = 1$ hypotheses.

The C-parity of the $X(3872)$ can also be determined from the C-parity of the $\pi^+\pi^-$ system in the decay $X(3872) \to J/\psi\,\pi^+\pi^-$. Equation 1.17 gives the possible values for the J^{PC} for the dipion: 0^{++}, 1^{--}, 2^{++} *etc.* The corresponding C-parity of the $X(3872)$ is opposite to the C-parity of the dipion because of the negative C-parity of the J/ψ ($J^{PC} = 1^{--}$ [21]). The determination of the C-parity of the dipion system will also help to obtain its isospin, since these quantities are related as $C = (-1)^I$ (Equation 1.18). Thus, C-positive dipion ($J^{PC} = 0^{++}, 2^{++}$ *etc*) would imply isospin $I = 0$, while C-negative one ($J^{PC} = 1^{--}$ *etc*) isospin $I = 1$. One should mention an important fact here: dipions in the mass range of interest with $J^{PC} = 1^{--}$ and isospin $I = 1$ couple to a (virtual) ρ^0-meson, because the ρ^0 has the same J^{PC} and I. Even though the $X(3872)$ is nominally too light to decay via $J/\psi\,\rho^0$, the broad width of the ρ^0 easily extends down into the allowed range. This feature would cause the dipion system to favor high masses. This preference is seen in Belle's Figure 1-1, which may actually mean that the $X(3872)$ really decays via $J/\psi\,\rho^0$ and has positive C-parity. In Chapter 6 we will apply this $J/\psi\,\rho^0$ hypothesis to our dipion mass spectrum.

1.4 Charmonium Hypotheses

The fact that the $X(3872)$ decays to $J/\psi\,\pi^+\pi^-$ suggests that it contains c and $\bar{c}$ quarks, and the most obvious and natural choice would be to try to interpret the $X(3872)$ as a so-far unseen charmonium state.

The $c\bar{c}$ system is very similar to a regular hydrogen atom, or better yet to positronium[3]. Thus, to characterize the charmonium quantum state, one can use the same quantum numbers as for the hydrogen atom: the radial quantum number n, the orbital angular momentum L, the total spin S and the total angular momentum J. The quantum states are classified using the spectroscopic notation $n^{2S+1}L_J$. The states with different orbital quantum number L are usually denoted with letters: S, P, D, $F\ldots$ for $L = 0, 1, 2, 3\ldots$ For example, the state with $L = 0$ is called *S-state* or *S-wave*. Sometimes it is convenient to combine the $n^{2S+1}L_J$ notation with the spin-parity J^{PC} to give a fully explicit characterization of a quantum state: $n^{2S+1}L_{J^{PC}}$.

The lightest charmonium state is called η_c. This is the S-state in which the spins of the c and $\bar{c}$ quarks are antiparallel, so that the total spin $S = 0$ and the total angular momentum $J = 0$. The radial quantum number of the η_c is $n = 1$, so that the spectroscopic notation for this state is 1^1S_0 and the J^{PC} is 0^{-+}. The next, a bit heavier, state is the J/ψ. It differs from the η_c by the fact that the spins of both c and $\bar{c}$ quarks are parallel to each other, so that the total spin $S = 1$, the total angular momentum $J = 1$ and the spectroscopic notation is 1^3S_1. The J^{PC} for the J/ψ is 1^{--}. The next $c\bar{c}$ state is called the χ_{c0}. It is a P-wave, more exactly 1^3P_0, with J^{PC} being 0^{++}. This is a part of a triplet — three particles with the same L and S, but different J. The other two particles in the triplet are called $\chi_{c1}(1^3P_{1^{++}})$ and $\chi_{c2}(1^3P_{2^{++}})$. Another particle with the same $L = 1$, but different $S = 0$ is called h_c, and has the spectroscopic notation 1^1P_1 and $J^{PC} = 1^{+-}$. These states, as well as a few of their higher radial and orbital excitations, are shown in Figure 1-7. The lowest line in this figure gives the spectroscopic notations of the states, and the lines above it display L, S and J^{PC} for them. The arrows schematically show the directions of the spins of individual quarks and the orbital momentum of their relative motion. The states themselves are represented by horizontal bars. The long thin arrows between them indicate possible strong (denoted as *hadrons*) or electromagnetic (via real γ, *radiative*, or via virtual γ^*) decays of the charmonium states into lighter states. We discuss the upper part of this picture later.

Most of the low-lying states, such as $\eta_c(1S)$, $J/\psi(1S)$, $\chi_{c0}(1P)$, $\chi_{c1}(1P)$, $\chi_{c2}(1P)$ and $\psi(2S)$, have been discovered and their properties are well established. Some others, like $\eta(2S)$ or $h_c(1P)$, were seen, but were confirmed only very recently. The $\eta(2S)$ was first reported by the Crystal Ball Collaboration over 20 years ago [23], but just a few years ago it was re-discovered at a different mass by the Belle Collaboration [24], and was so confirmed by the BaBar Collaboration [25]. The $h_c(1^1P_1)$ state is less well investigated. Even though some observations of this state have been made [26], none of them were very convincing. Only recently the Fermilab experiment E835 observed a few $\eta_c\,\gamma$ candidates [27], and another recent observation of h_c was made by CLEO Collaboration [28].

Only a few of the charmonia states with masses above the $D\overline{D}$ threshold are identified. In Figure 1-7 the higher states are plotted by "spread" rectangles which symbolize their substantial widths. The expected (*i.e.* not forbidden by spin-parity conservation) decays of these states into $D\overline{D}$ are shown too. The rapid decays via this channel (so-called *open-charm* or *double-charm* channel) should make these charmonia states very broad and difficult to find, *e.g.* the

---

[3] Positronium is a bound state of electron and positron e^+e^-, discovered by Martin Deutsch of MIT in 1951 [22].

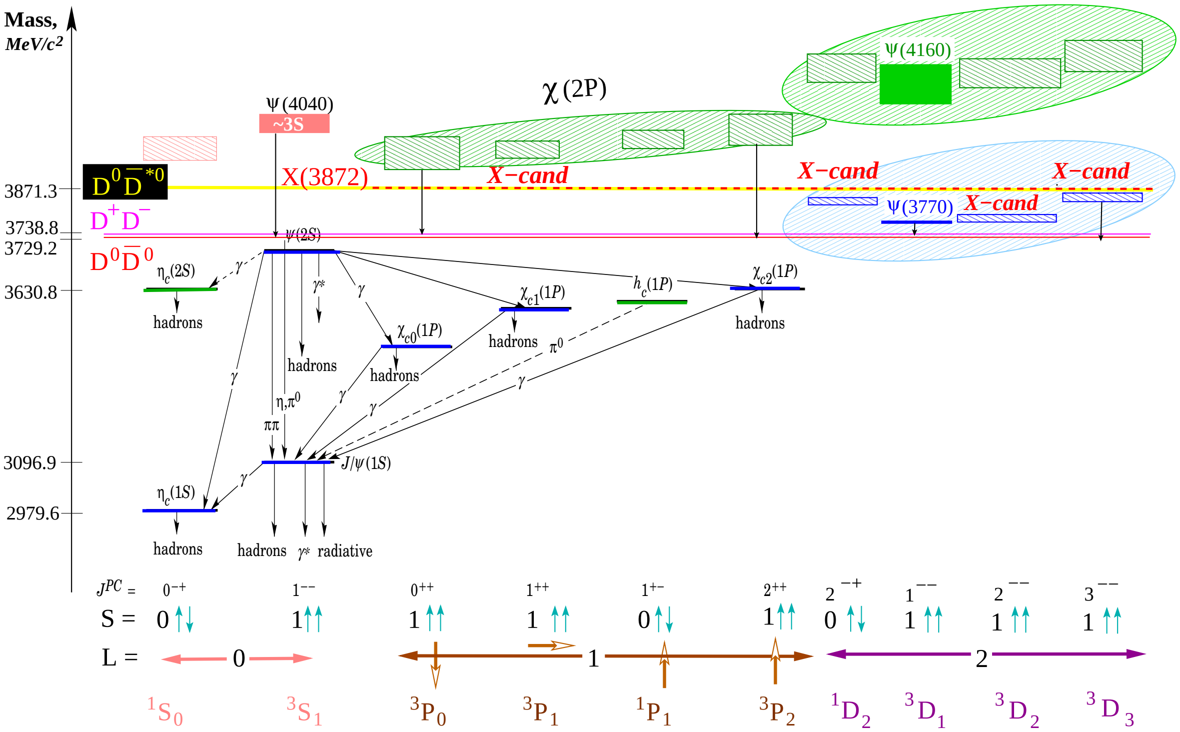

Figure 1-7: The lower mass part of the charmonium spectrum. The known states with masses below the $D\overline{D}$ threshold are shown with horizontal lines. The arrows denote the hadronic and electromagnetic transitions between the states. The most of the states above the $D\overline{D}$ threshold are not observed. Four of them can be candidates for the $X(3872)$ — see text for a detailed discussion.

$\psi(3770)$ ($^3D_1$) lies just above $D\overline{D}$, and yet it has width of about 20 MeV. The heavier charmonia states should have a width of the same order or even larger. There are a few interesting exceptions, *e.g.* $^1D_2$ and $^3D_2$ states. The decay of these states into $D\overline{D}$ is forbidden because of their spin-parity $J^{PC} = 2^{-\pm}$. Indeed, both D and $\overline{D}$ have zero spin and the spin-parity of the $D\overline{D}$ system is determined by Equation 1.17, the same way as for two pions: $J^{PC} = J^{(-1)^L(-1)^L} = J^{(-1)^J(-1)^J}$. Therefore, the even total angular momentum J of $D\overline{D}$ system constrains the C- and P-parities to be positive. Since J, C and P must be conserved in the decay, the states $^1D_2$ and $^3D_2$ cannot decay into $D\overline{D}$ and are, therefore, expected to have small widths.

The E705 Collaboration offered evidence for 1^3D_2 at 3836 MeV/c^2 [29] but this claim has been disputed by the higher statistics result of the E672/E706 Collaborations [30], and by the BES Collaboration [31].

As mentioned earlier, initially the $X(3872)$ was expected to be one of the so far unknown higher-mass charmonium states. However, interpreting the $X(3872)$ as such a conventional state is problematic. Let us go through all the $c\bar{c}$ states which are not yet identified and evaluate their suitability for the $X(3872)$.

The list of all the $c\bar{c}$ states considered is given in the form $n^{2S+1}L_{J^{PC}}$ in the first column of

Table 1.1. The second column of this table contains the name of this $c\bar{c}$ state, if the particle has been observed. The mass of this particle, or its predicted value for yet unobserved particles, are shown in the third column. The fourth column gives the width for the known particles. The next two columns are related to the possibility for a given particle to decay into $J/\psi\,\pi^+\pi^-$. The fifth column represents the J^{PC} of the dipion system in this decay. We ignore the possibility of D-wave dipions. Last comes the main objections against interpreting $X(3872)$ as this particular state.

We need not consider $1S$, $1P$ and $2S$ states, because they are unambiguously identified already. The states $2D$, $3P$, $3D$ and higher are expected to be too heavy to be associated with the $X(3872)$. The same statement is true for the states with $L > 2$ [32]. Ten states remain. Two of them are known: $1^3D_{1^{--}}$ is $\psi(3770)$ and $3^3S_{1^{--}}$ is $\psi(4040)$, so we will not consider them as serious candidates for the $X(3872)$. Furthermore, had the $X(3872)$ been one of these states, it would have $J^{PC} = 1^{--}$, would decay electromagnetically to e^+e^- via a virtual photon, which has the same $J^{PC} = 1^{--}$, and would therefore have likely been discovered in e^+e^- collisions already.

Now we discuss the eight remaining states.

$1^1D_{2^{-+}}$ State

As was mentioned earlier, the state $1^1D_{2^{-+}}$ cannot decay to the open-charm channel $D\overline{D}$, so that it must decay through the weaker short-distance $c\bar{c}$ annihilation processes, radiative decays and closed-flavor hadronic transitions. All these decays lead to a predicted total width of about 1 MeV [13], which makes this state a plausible candidate for the $X(3872)$. The closeness of the predicted [32] mass to the observed one is also favorable to this hypothesis.

The positive C-parity of this state and negative C-parity of the J/ψ ($J^{PC} = 1^{--}$) forces the pions in the decay $1^1D_{2^{-+}} \to J/\psi\,\pi^+\pi^-$ to have a negative C-parity, *i.e.* odd L. As we saw in Section 1.2, this leads to a necessity of having isospin $I = 1$ in the final state. The charmonium in the initial state, though, has isospin $I = 0$. So that, the decay of $1^1D_{2^{-+}}$, or any other charmonium state, into a 1^{--} dipion state breaks the conservation of isospin. As was mentioned earlier, the isospin conservation is an approximate law of nature. This means that such decay is possible, but should normally be highly suppressed. A quantitative example of an isospin-violation suppression comes from $\psi(2S) \to J/\psi\,\pi^0$ decay. Its width is 0.3 keV, which is 200 times smaller than the width of a similar isospin conserving decay $\psi(2S) \to J/\psi\,\pi^0\pi^0$ [21]. Therefore, the $1^1D_{2^{-+}}$ should have a very small partial width to $J/\psi\,\pi^+\pi^-$. The isospin-conserving decay to $\eta_c\,\pi^+\pi^-$ should have a much larger partial width [13, 32], but it has not yet been observed, though Belle is searching for this mode. This fact makes the interpretation of the $X(3872)$ as $1^1D_{2^{-+}}$ state questionable[4].

On the other hand, a large isospin violation could be explained by the fact of the proximity of the $X(3872)$ mass to the mass of D^0D^{*0} system, making the virtual coupling between the $X(3872)$ and D^0D^{*0} possible. The D^0D^{*0} system is not an isospin eigenstate, so that the $X(3872)$, even being a conventional charmonium, may "bypass" the isospin conservation law and decay into 1^{--} dipions via the virtual coupling to this system.

The $1^1D_{2^{-+}}$ state can be produced in the $\gamma\gamma$ fusion. The $X(3872)$ was not seen in this channel by CLEO III [9], but they did not have enough sensitivity to exclude the $X(3872)$. The predicted [33] partial width to $\gamma\gamma$ for this state is nearly six times smaller than the limit from

---

[4] The same reasoning applies to all C-positive charmonium states because all of them must decay into a 1^{--} dipion. We will discuss this again in Section 6.7.1.

1	2	3	4	5	
$n\,^{2s+1}\ell_{JPC}$	Known States	Mass, MeV/c^2	Width, MeV	$\pi^+\pi^-$ J^{PC}	Main objections for the $X(3872)$ assignment
$1\,^1S_{0-+}$	$\eta_c(1S)$	2980 [21]	17 [21]	—	
$1\,^3S_{1--}$	J/ψ	3097 [21]	0.1 [21]	—	
$1\,^1P_{1+-}$	$h_c(1P)$	3526 [21]		0^{++}	
$1\,^3P_{0++}$	$\chi_{c0}(1P)$	3415 [21]	10 [21]	1^{--}	
$1\,^3P_{1++}$	$\chi_{c1}(1P)$	3511 [21]	1 [21]	1^{--}	
$1\,^3P_{2++}$	$\chi_{c2}(1P)$	3556 [21]	2 [21]	1^{--}	
$1\,^1D_{2-+}$		**$\sim$ 3838** [32]		**1^{--}**	**expect $\eta_c\,\pi\pi \gg J/\psi\,\pi\pi$ [32]**
$1\,^3D_{1--}$	$\psi(3770)$	3770 [21]	25 [21]	0^{++}	
$1\,^3D_{2--}$		**$\sim$ 3830** [32]		**0^{++}**	**not seen decay to $\chi_{c1}\,\gamma$ [1]**
$1\,^3D_{3--}$		**$\sim$ 3868** [32]		**0^{++}**	**not seen decay to $\chi_{c2}\,\gamma$ [5]**
$2\,^1S_{0-+}$	$\eta_c(2S)$	3654 [21]	17 [25]	1^{--}	
$2\,^3S_{1--}$	$\psi(2S)$	3686 [21]	0.3 [21]	0^{++}	
$2\,^1P_{1+-}$		**$\sim$ 3968** [32]		**0^{++}**	**wrong $\cos\theta_{J/\psi}$ distribution [5]**
$2\,^3P_{0++}$		**$\sim$ 3932** [32]		**1^{--}**	**$D\overline{D}$ not suppressed → broad [13]** **not seen in $\gamma\gamma$ fusion [9]**
$2\,^3P_{1++}$		**$\sim$ 4008** [32]		**1^{--}**	**too large expected width to $J/\psi\,\gamma$ [5]**
$2\,^3P_{2++}$		**$\sim$ 3966** [32]		**1^{--}**	**$D\overline{D}$ not suppressed → broad [13]** **not seen in $\gamma\gamma$ fusion [9]**
$3\,^1S_{0-+}$				**1^{--}**	**mass expected to be close to $^3S_1$**
$3\,^3S_{1--}$	$\psi(4040)$	4040 [21]	52 [21]	0^{++}	

Table 1.1: Summary of conventional charmonium states and the main objections for assigning them to the $X(3872)$.

Equation 1.15.

The evidence of the decay $X(3872) \to J/\psi\,\omega$ (Equation 1.3) implies positive C-parity of $X(3872)$, and, therefore, is consistent with 1^1D_{2-+} assignment.

Overall we conclude that 1^1D_{2-+} is a possible, though a bit problematic, charmonium interpretation of the $X(3872)$.

1^3D_{2--} State

Similar to 1^1D_{2-+}, this state is expected to have a narrow width about 1 MeV [13] due to absence of an open-charm decay mode. One of the objections for the interpretation of the $X(3872)$ as this state is that it should have a substantial radiative width to $J/\psi\,\gamma$, much larger than Belle's limit from Equation 1.4. Though, this prediction may suffer from inaccurate estimation of the $X(3872) \to J/\psi\,\pi^+\pi^-$ decay rate [13].

The evidence of the decay $X(3872) \to J/\psi\,\omega$ (Equation 1.3) also plays against the 1^3D_{2--} interpretation of the $X(3872)$ because of the negative C-parity of this state. But overall we consider 1^3D_{2--} state as a plausible assignment for the $X(3872)$.

1^3D_{3--} State

The state 1^3D_{3--} does have an open-charm decay mode ($D\overline{D}$), but due to the large (L=3) centrifugal barrier[5] it should have a small width, maybe a few MeV [13]. Reference [32] argues that the open-charm decay should be a dominant one for this state, and that its partial width at mass 3872 MeV/c^2 should be even less than 1 MeV. The predicted [32] mass of this state is close to 3872 MeV/c^2.

The problem with this assignment, is that the 1^3D_{3--} partial width to $\chi_{c2}\,\gamma$ is expected to be of the same order or larger than to $J/\psi\,\pi^+\pi^-$, opposing Belle's results from Equation 1.5 [32]. The evidence for $X(3872) \to J/\psi\,\omega$ decay does not support the C-negative 1^3D_{3--} assigment for the $X(3872)$ either. But overall we will still consider this state as a possible $X(3872)$ candidate.

2^1P_{1+-} State

Assigning the observed mass of the $X(3872)$ to the 2^1P_{1+-} state would result in a total predicted width of this state to be about 1-2 MeV [13]. This is consistent with the observed width for the $X(3872)$. But the predicted mass of this state is about 80 MeV/c^2 higher than the $X(3872)$'s observed mass [12, 13, 34, 35]. This state should prefer to decay into $\eta_c\,\gamma$ and $\eta_c(2S)\,\gamma$, and the partial width to $2^1P_{1+-} \to J/\psi\,\pi^+\pi^-$ is predicted to be small [13], which does not support the $X(3872)$ assignment.

The main obstacle for interpreting the $X(3872)$ as this state can be inferred from Belle's Figure 1-8 [36]. This plot shows the angular distribution of the J/ψ in the decays $B^+ \to K^+X(3872)$. If we denote $\theta_{J/\psi}$ the angle between the momentum of J/ψ and the negative momentum of K^+

---

[5] In systems with central symmetry the energy conservation law can be written as: $\frac{m}{2}\left(\frac{dr}{dt}\right)^2 + \frac{L^2}{2mr^2} + V(r) =$ const, where L^2 is the square of the orbital angular momentum. The term $L^2/(2mr^2)$ is called *centrifugal barrier*. In quantum mechanics it remains almost the same, only the operator of the square of total angular momentum $\hat{\boldsymbol{L}}^{\mathbf{2}}$ gets replaced with its eigenvalue $L(L+1)$. The $D\overline{D}$ system coming from the 1^3D_{3--} charmonium state must have orbital angular momentum $L = 3$ (because the intrinsic spins of both D and $\overline{D}$ are equal to zero). Thus the centrifugal barrier for this system is large. For the decay of, for example, 1^3D_{1--} charmonium state the $D\overline{D}$ orbital momentum equals $L = 1$, the centrifugal barrier is small, the decay is not suppressed and, therefore, this state has a large width into $D\overline{D}$.

in the $X(3872)$ rest frame then the measured distribution of $|\cos\theta_{J/\psi}|$ is in clear disagreement with the expectation for the $2^1P_{1^{+-}}$ state. The χ^2 per degree of freedom for the comparison of the measured and the expected distribution is 75/9 [36].

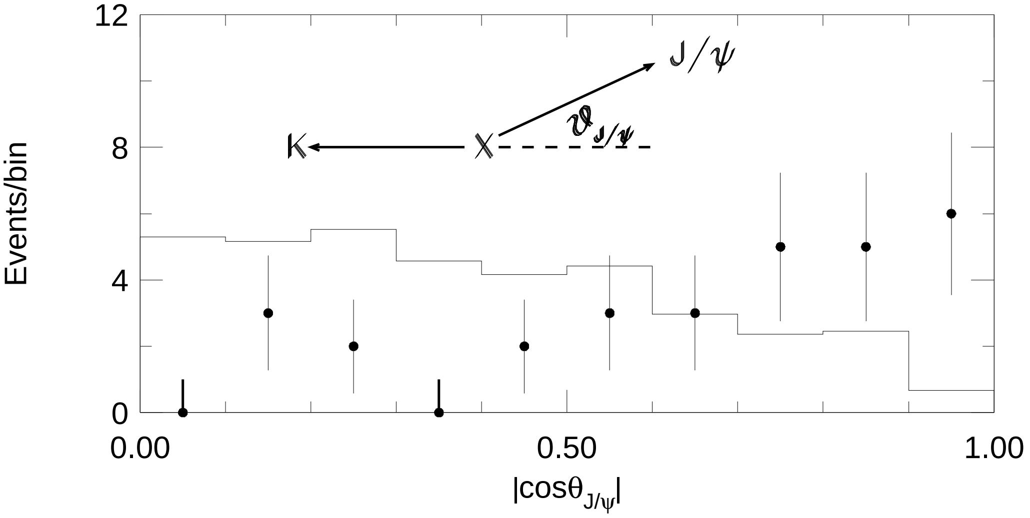

Figure 1-8: The $|\cos\theta_{J/\psi}|$ distribution for $X(3872) \to J/\psi\,\pi^+\pi^-$ events from Belle [36]. The histogram shows the expectations for a 1^{+-} hypothesis.

The evidence for the $X(3872) \to J/\psi\,\omega$ decay also does not support assigning $2^1P_{1^{+-}}$ state to the $X(3872)$ because of C-parity.

$2^3P_{0^{++}}$ State

The $2^3P_{0^{++}}$ state is allowed to decay into open charm channels and has a predicted total width an order of magnitude larger than 2.3 MeV [13], which makes the $X(3872)$ interpretation as $2^3P_{0^{++}}$ unlikely.

Another point against such interpretation is that the $X(3872)$ was not seen in $\gamma\gamma$ fusion by CLEO III [9]. The partial width into $\gamma\gamma$ of the lighter companion of $2^3P_{0^{++}}$ state, the $\chi_{c0}(1^3P_{0^{++}})$ state, is almost 4 times greater than the limit in Equation 1.15. Assuming that the partial widths of $2^3P_{0^{++}}$ and $1^3P_{0^{++}}$ states into $\gamma\gamma$ are of the same order we can dismiss hypothesis of the $X(3872)$ being $2^3P_{0^{++}}$ state.

$2^3P_{1^{++}}$ State

According to Reference [13] the $2^3P_{1^{++}}$ state, similar to the $2^1P_{1^{+-}}$ state, should have a narrow width of about 1-2 MeV, if its mass is set to be equal to the observed mass of the $X(3872)$. This is consistent with the observed narrow width for the $X(3872)$. The predicted value of the $2^3P_{1^{++}}$ state's mass, though, is about 80 MeV/c^2 higher than the observed mass of the $X(3872)$ [12, 13, 34, 35].

Other shortcomings of $2^3P_{1^{++}}$ assignment include a small partial width to $J/\psi\,\pi^+\pi^-$ and dominant decays to $J/\psi\,\gamma$ and $\psi(2S)\,\gamma$, in contradiction with Belle's result (Equation 1.6). But despite all these difficulties we consider the $2^3P_{1^{++}}$ state as a possible $c\bar{c}$ candidate for $X(3872)$.

The lack of $X(3872)$ being seen in $\gamma\gamma$ fusion is not a problem for this assignment. Two photons with $J = 1$ can produce a state with $J = 0$ or $J = 2$ but not with $J = 1$ because the production cross-section in $\gamma\gamma$ fusion is normally proportional to the partial width of the decay into $\gamma\gamma$, and the latter must vanish for mesons with $J = 1$ according to Yang's theorem [37].

$2^3P_{2^{++}}$ State

The state $2^3P_{2^{++}}$, just like the state $2^3P_{0^{++}}$, is allowed to decay into open charm and should have a large width. Reference [13] predicts its total width to be an order of magnitude larger than 2.3 MeV. These predictions make this state a poor candidate for the $X(3872)$.

Another point against the $X(3872)$ assignment is that CLEO III did not see the $X(3872)$ in $\gamma\gamma$ fusion [9]. This reasoning is similar to that for the $2^3P_{0^{++}}$ state. The lighter companion of $2^3P_{2^{++}}$ state, the $\chi_{c2}(1^3P_{2^{++}})$ state, has the partial width into $\gamma\gamma$ almost 4 times greater than the limit in Equation 1.15. Assuming that the partial widths of $2^3P_{2^{++}}$ and $1^3P_{2^{++}}$ states into $\gamma\gamma$ are of the same order, we can dismiss the $2^3P_{2^{++}}$ hypothesis for the $X(3872)$.

$3^1S_{0^{-+}}$ State

The state $3^1S_{0^{-+}}$ is a part of $3S_J$ doublet. Its mass is pegged by $\psi(4040)$, which is interpreted as the $3^3S_{1^{--}}$-state. From the $1S$ and $2S$ states we know that the mass splitting between ${}^1S_{0^{-+}}$ and ${}^3S_{1^{--}}$ is about 120 MeV/c^2 and about 50 MeV/c^2 respectively, *i.e.* it is relatively small and gets smaller as one goes further up the potential well — a pattern also seen in the Υ family. This makes it difficult to imagine how the normal ${}^1S_0$-${}^3S_1$ splitting could be so badly corrupted as to bring the 3^1S_0 anywhere near the X-mass.

Also, the $X(3872)$ as the $3^1S_{0^{-+}}$ would require a severe violation of the pattern observed for η_c widths: $\Gamma \sim 17$ MeV for both the $\eta_c(1^1S_{0^{-+}})$ [21] and $\eta_c(2^1S_{0^{-+}})$ [25], which is much larger than the observed $X(3872)$ width.

Summary

In conclusion, we found four more or less reasonable $c\bar{c}$ candidates for the $X(3872)$: ${}^1D_{2^{-+}}$, ${}^3D_{2^{--}}$, ${}^3D_{3^{--}}$ and ${}^3P_{1^{++}}$. The C-positive ones, ${}^1D_{2^{-+}}$ and ${}^3P_{1^{++}}$, decay into $J/\psi\,\pi^+\pi^-$ with the $\pi^+\pi^-$ system having $J^{PC} = 1^{--}$. The other two decay into 0^{++} dipion. We will consider the theoretical models for the shapes of the dipion mass distribution for both types of the dipion system in Chapter 6.

1.5 Weakly Bound D-D^* State and Other 4-Quark States

Conventional charmonium is not the only possible interpretation of the $X(3872)$. The most popular non-charmonium hypothesis is that of a weakly bound deuteron-like "molecule" made of D^0 and D^{*0} mesons. The weighted-average mass of the $X(3872)$ from References [1, 2, 3, 4]

$$m(X) = 3871.9 \pm 0.5\ \text{MeV}/c^2$$

is equal, given the uncertainties, to the sum of the masses of D^0 and D^{*0} mesons

$$m(D^0\overline{D}^{*0}) = 3871.2 \pm 1.0\ \text{MeV}/c^2\quad \text{(Ref. [21])},$$

as shown in Figure 1-4. This fact suggests that the $X(3872)$ may be some kind of D^0-$\overline{D}^{*0}$ compound.

The general possibility of meson-meson molecules within QCD is quite old. It started in the late-sixties with the attempt to explain a low mass $I = 1$ enhancement in $p\bar{p} \to K\bar{K}\pi$ [38] by a K-$\bar{K}$ bound state. Later, in the mid-seventies, the light scalar mesons $a(980)$ and $f(980)$ were considered as candidates for K-$\bar{K}$ molecules [39]. At the same time the concept of "molecular charmonium" was proposed [40]. This hypothesis was applied, for example, to the $\psi(4040)$ state [41] to explain the anomalously high decay rate of $D\overline{D}^*$ compared to $D\overline{D}$. Later this phenomenon was explained without molecular hypothesis, and the conventional charmonium interpretation of $\psi(4040)$ prevailed.

The binding forces in the $D\overline{D}^*$ and $B\overline{B}^*$ systems, described by the pion-exchange interaction, are investigated in References [42, 43]. There is no attractive forces in the $D\overline{D}$ and $B\overline{B}$ systems. It can be shown that the $D\overline{D}^*$ molecule can only be loosely bound, if at all, while the $B\overline{B}^*$ can be bound more tightly [42].

A very important feature of the molecular model is that the D^0-D^{*0} system is not a pure isospin eigenstate and the isospin conservation does not forbid it to decay into 1^{--} dipion states. This decay proceeds via an intermediate ρ^0-meson (which also has $J^{PC} = 1^{--}$), just like for the charmonium case. Of course, the decays of such molecules into dipions with other J^{PC} are also possible.

If the molecular interpretation of the $X(3872)$ is correct, one could as well expect there to be charged analogs of the $X(3872)$. The search for them performed by the BaBar Collaboration gave negative results. This could be explained by the fact that the binding by pion exchange forces is expected to be three times stronger for isoscalar ($I = 0$) molecules, than for the molecules coming in isospin triplets ($I = 1$). Reference [42] argues that in the limit of complete isospin symmetry only isoscalar molecules can be bound. Reference [44] adds that this conclusion should hold even in the case of broken isospin symmetry. The symmetry must be broken because the binding energy of the $D\overline{D}^*$ molecule (about 8 MeV) is of the same order as the isospin mass splitting between D^0 and D^+ mesons (about 5 MeV). This symmetry breaking results in more tightly bound $D^0\overline{D}^{*0}$ and less tightly bound $D^+\overline{D}^{*0}$ and D^+D^{*-} molecules. This gives us a reason as to why the charged $D\overline{D}^*$ molecules need not exist.

It is hard to bind charm mesons with high orbital momentum, therefore the D and $\overline{D}^*$ in the weakly-bound molecule are most likely to be in S-wave. The total angular momentum of $D\overline{D}^*$ molecule is $J = 1$ and the P-parity is $P = P_D \cdot P_{\overline{D}^*} \cdot \ (-1)^L = (-1) \cdot (-1) \cdot (+1) = +1$. Either C-parity is possible [13]. Reference [20] points out that C-positive $D^0\overline{D}^{*0}$ molecules should preferentially decay into $D^0\overline{D}^0\pi^0$, while C-negative ones – into $D^0\overline{D}^0\gamma$. Many other authors predict the ratio of the width for the decays into $D^0\overline{D}^0\pi^0$ and $D^0\overline{D}^0\gamma$ to be approximately 3:2, and their sum to be about 60-100 keV [13, 42, 44, 45]. This is consistent with the small observed total $X(3872)$ width < 2.3 MeV [1].

Reference [42], considering pion-exchange interactions, suggests that not only S-wave, but also P-wave molecules can be bound. It considers models with 0^{-+} and 1^{++}. The positive C-parity forbids the decay into J/ψ plus S-wave dipion with $J^{PC} = 0^{++}$ and $I = 0$ (see Section 1.4), so, Reference [42] concludes, such molecule should decay via a 1^{--} dipion with $I = 1$, *i.e.* via $J/\psi\rho$. The preferred decay mode for this model, though, is $D^0\overline{D}^0\pi^0$. The total width of such molecule is estimated to be $\sim$50 keV, which is also consistent with the upper limit on the observed $X(3872)$ width [1].

An interesting molecular model is proposed in Reference [46]. It assumes that the mesons in the molecule are bound not only with pion-exchange forces, but also with quark-gluon forces.

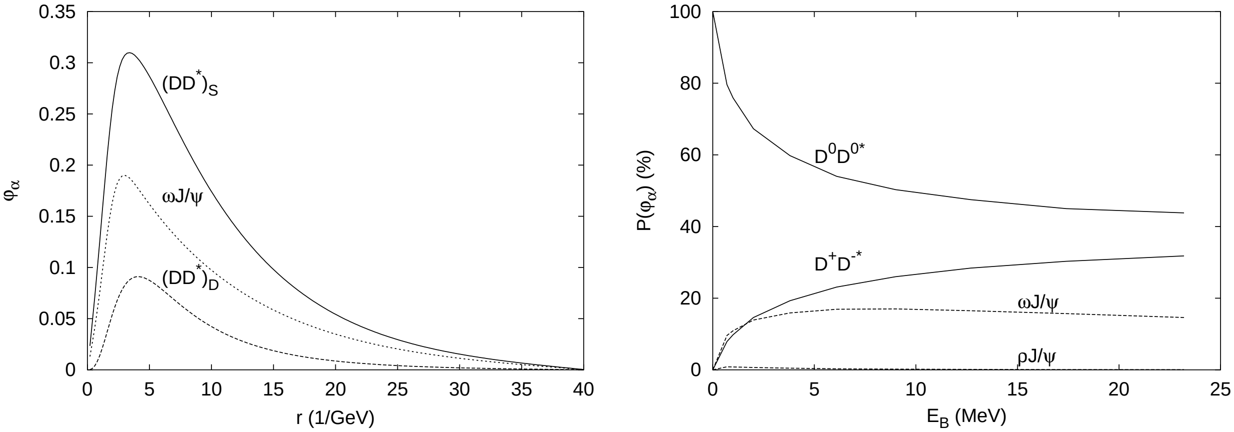

Figure 1-9: LEFT: The various components of the "molecular" wavefunction from the model of Reference [46]. RIGHT: The relative contributions of each component versus the molecular binding energy.

Actually, in this model the $X(3872)$ is not a simple $D^0\overline{D}^{*0}$ molecule, but a 1^{++} state composed of $D^0\overline{D}^{*0}$ with a little mix of $J/\psi\,\omega$, $J/\psi\rho$, and D^+D^{*-}. The wavefunction of this mixture is shown in the left part of Figure 1-9 [46]. The relative contributions of different components versus the binding energy are shown in the right part in this figure. The molecule in this model decays into both $J/\psi\rho$ and $J/\psi\,\omega$ due to internal rescattering of molecular components. The model makes the prediction that the $X(3872)$ branching ratio to $J/\psi\rho$ and $J/\psi\,\omega$ are of the same order, and that the branching ratios to $D\overline{D}$ and $D\overline{D}\pi^0$ are small. The branching ratio into $J/\psi\,\gamma$ is expected to be smaller than into $J/\psi\,\pi^+\pi^-$, which is consistent with Equation 1.6. The total width is predicted to be ≈ 2 MeV$/c^2$, which is close to the $X(3872)$ width reported by Belle [1]. Though the ω meson is kinematically above threshold, it may manifest itself through its width, similar to the ρ^0. The tripion invariant mass should peak near the upper kinematic boundary [47]. The prediction of a significant $J/\psi\,\omega$ decay rate in this model prompted Belle to search for this mode, and indeed, they found the evidence for the $X(3872) \to J/\psi\,\pi^+\pi^-\pi^0$ decay with a large rate [11].

Reference [12] considers mixtures between molecules and $c\bar{c}$. For such mixing to occur both the molecule and the charmonium should have the same spin-parity. The most favored candidates for this model are 2^{--} and 1^{+-}. Both of them have negative C-parity and may decay into a scalar 0^{++} or a tensor 2^{++} dipion. Unfortunately, Reference [12] does not provide predictions for the shape of the dipion mass spectrum.

Diquark-Antidiquark Model

All the exotic models considered so far worked with a "molecular" $[c\bar{q}][\bar{c}q]$ state. This is a particular case of a more general scenario, where all four quarks interact with each other equally, without being paired. Reference [48] considers a different "extreme" of a 4-quark system, the so-called diquark-antidiquark $[cq][\bar{c}\bar{q}']$ state with $q, q' = u, d$. Different quarks make different X particles, which can be put in the same isospin multiplet with components:

$$X_u = [cu][\bar{c}\bar{u}], \qquad X_d = [cd][\bar{c}\bar{d}]. \tag{1.19}$$

This model gives a rich X spectrum (Figure 1-10) and accommodates the states $X(3940)$ seen

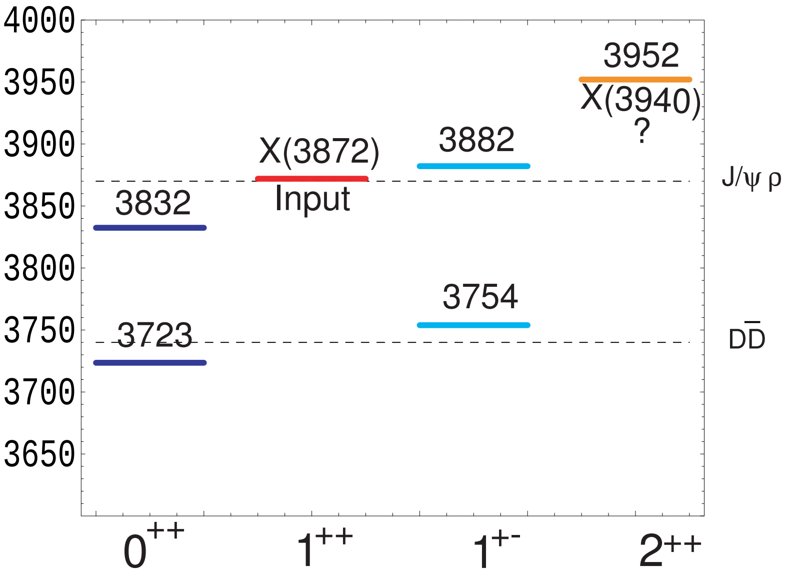

Figure 1-10: The full spectrum of "X" particles predicted by the diquark model of Reference [48].

by Belle [49] and $D^*_{sJ}(2632)$ claimed by the SELEX Collaboration [50]. The model predicts two 0^{++} states, two 1^{+-}, one 1^{++} and one 2^{++}. The 1^{++} state is proposed for the $X(3872)$, because it explains many of its properties. In particular, the 1^{++} state is predicted to be narrow, just like all the other low-lying diquark-antidiquark states. Its decay to $D\overline{D}$ is forbidden by parity conservation. The decay into $\eta_c + \texttt{mesons}$ is also forbidden. The decays into both $J/\psi\rho$ and $J/\psi\,\omega$ are allowed. All these features are consistent with the observations of the $X(3872)$.

The states in Equation 1.19 can mix with some angle θ forming the mass eigenstates:

$$X_{low} = X_u \cos\theta + X_d \sin\theta,$$

$$X_{high} = -X_u \sin\theta + X_d \cos\theta.$$

The mass difference between them is predicted to be

$$M(X_{high}) - M(X_{low}) = (7 \pm 2)/\cos(2\theta)\ \mathrm{MeV}/c^2. \tag{1.20}$$

This model considers the decays of both B^+ and B^0 into $X_{u,d}$. From the limit on the $X(3872)$ width [1] the authors infer that one of these states, X_u or X_d, should dominate in B^+ decays and another one in B^0 decays. The mass difference in Equation 1.20 can be observed by separately reconstructing $B^+ \to X(3872)\ K^+$ and $B^0 \to X(3872)\ K_S$ decays. In CDF's inclusive sample both X_u and X_d would be produced equally. Our inclusive $J/\psi\,\pi^+\pi^-$ mass histogram in Figure 3-1 shows no "double-hump" structure in the $X(3872)$ peak, unless we see an unresolved mixture of both X_u and X_d.

Also, this model possesses charged members of an X multiplet, in addition to Equation 1.19:

$$X^+ = [cu][\bar{c}\bar{d}], \qquad X^- = [cd][\bar{c}\bar{u}].$$

The limits on the production of these states in B decays from BaBar [10] are not in contradiction with this model.

1.6 Hybrid Hypothesis

There are a number of other exotic models considered for the $X(3872)$ — neither simple $c\bar{c}$, nor $D\overline{D}^*$ molecules, even including general 4-quark states. One of these models is a "hybrid meson". It interprets the $X(3872)$ as a $c\bar{c}g$ system, *i.e.* charmonium with a valence gluon [13, 44, 51]. Such states were proposed back in 1978 [52]. The question about the existence of these gluonic excitations is one of the most important in the contemporary hadron physics. The *bona fide* discovery of such a state would open an entirely new domain of QCD to explore [53]. The main drawbacks for the hybrid interpretation of the $X(3872)$ is that the expected masses for the hybrids are higher than 3872 MeV/c^2. The so-called flux tube model predicts eight low-lying hybrid states in the mass region between 4 and 4.2 GeV/c^2 [54, 55, 56, 57] with $J^{PC} = 0^{\pm\mp}, 1^{\pm\mp}, 2^{\pm\mp}$, and $1^{\pm\pm}$. Three of these states have non-$q\bar{q}$ quantum numbers, incompatible with Equation 1.16: 0^{+-}, 1^{-+} and 2^{+-}. The mesons with non-$q\bar{q}$ spin-parity J^{PC}, also known as *unnatural* spin-parity, are important because they must have an exotic, non-$q\bar{q}$, content. Reference [55] predicts the masses of these states to be 4.7 GeV/c^2, 4.3 GeV/c^2, 4.9 GeV/c^2, respectively. Other lattice QCD predictions [56, 57] for the mass of the lightest 1^{-+} state are between 4.04 GeV/c^2 and 4.4 GeV/c^2. These results put the 1^{-+} state close to DD^{**} threshold of 4.287 GeV/c^2 [53]. There is a possibility though, that this state could lie close to the observed mass of the $X(3872)$, *i.e.* below DD^{**} and therefore have a relatively small width [53]. This would then make it a possible candidate for the $X(3872)$. The observed $X(3872)$ properties are consistent with 2^{+-} and 0^{+-} hybrids, but the mass discrepancy makes these assignments unlikely.

The width for the hadronic transitions `hybrid` → $c\bar{c}$+`light mesons` can be obtained with the aid of the multipole expansion model. conventional quarkonia may in some cases be viewed as a transition via an intermediate hybrid state [58]. Thus, the matrix elements for the conventional quarkonia interactions and for hybrid–conventional conversions are related. This facilitates the prediction of the hybrid widths to conventional final states. These widths turn out to be of the order of 10-100 keV for transitions like $1^{-+} \to \eta_c + (\pi\pi, \eta, \eta')$ and $(0^{+-}, 2^{+-}) \to J/\psi + (\pi\pi, \eta, \eta')$. BaBar found no evidence of $X(3872) \to J/\psi\,\eta$ decay (Equation 1.10), which puts restrictions on the hybrid hypothesis for the $X(3872)$.

There are no direct calculations for the radiative widths of charmonium hybrids, but similar calculations for hybrids with light quarks [59, 60] suggest that the partial widths for $1^{-+} \to \gamma + (J/\psi, h_c)$ and $(0^{+-}, 2^{+-}) \to \gamma + (\eta_c, \chi_{cJ})$ are of the same order of magnitude as for the conventional charmonium: 1-100 keV. This is consistent with the observed narrow width of the $X(3872)$.

Reference [51] predicts that a hybrid $X(3872)$ should be seen in the photon fusion: $\gamma\gamma \to X(3872) + \pi^+\pi^-$, though CLEO's search gave negative results (Equation 1.15).

1.7 Glueball–Charmonium Mixture

Reference [61] suggests an interesting idea that the $X(3872)$ could be a *glueball* — a bound state containing no quarks, but only gluons — with a small (about 3%) admixture of $c\bar{c}$. A lattice QCD calculation [62] predicts a 3-gluon vector glueball with mass $3850 \pm 50 \pm 190$ MeV/c^2 and

$J^{PC} = 1^{--}$. The pure glueball does not couple to e^+e^-, which explains why the $X(3872)$ was not found in e^+e^- collisions long time ago despite the suitable spin-parity.

This model supposes that the $c\bar{c}$ admixture is the $\psi(2S)$ state and that it is responsible for the observed decay $X(3872) \to J/\psi\,\pi^+\pi^-$. The model predicts decays $X(3872) \to J/\psi\,\eta$ and $X(3872) \to J/\psi\,\pi^0\pi^0$, but it is unable to say anything about $X(3872) \to D^0\overline{D}^0$ or $X(3872) \to D^+D^-$. The decays of $X(3872)$ to $J/\psi\,\gamma$, $J/\psi\,\rho$ and to $J/\psi\,\omega$ are forbidden because of negative C-parity of the $X(3872)$ in this model.

1.8 Dynamic "Cusp" Hypothesis

In the dynamic "cusp" model [63, 64] the $X(3872)$ arises as a dynamical effect of the $\overline{D}$ and D^* interaction. Cusps can appear in the cross-section for any process at the threshold where coupled channels are open and where there is an effective attraction between the particles [65]. The rescattering cross-section is proportional to $1/k$, where k is the momentum of the components in their center-of-mass reference frame. It competes with the available phase-space and produces a peak in the rescattering amplitude, but not a true resonance.

Reference [63] claims that this model can explain the threshold $p\bar{p}$ peak observed by the BES Collaboration in $J/\psi \to \gamma\,p\bar{p}$ [66], the low mass $p\bar{p}$ peaks in $B^+ \to K^+p\bar{p}$ [67] and $\overline{B}^0 \to D^0\,p\bar{p}$ [68], reported by Belle, the peaks in $p\bar{p} \to \Lambda\bar{\Lambda}$, reported by the PS185 Collaboration [69], ΣN threshold in $K^-d \to \pi^-(\Lambda p)$ [70] and other similar observations, including the $X(3872)$.

The proximity of the $X(3872)$ mass to the $D\overline{D}^*$ threshold is an implied feature of this model, while in some other models (charmonium, hybrid, glueball) this is just an effect to be accommodated. A large isospin violation is an inherent part of the model, which allows the decays into $J/\psi\rho$. The favorite decay, though, is to $D^0\overline{D}^{*0}$. The author suggests that the observation of D-wave decays for $X(3872)$ with $J^{PC} = 1^{++}$ would be a sign that this is a bound state and their absence would indicate a cusp.

1.9 Summary

As we saw in this chapter, the nature of the $X(3872)$ is an open question. It could be a conventional charmonium (with ${}^1D_{2^{-+}}$, ${}^3D_{2^{--}}$, ${}^3D_{3^{--}}$ and ${}^3P_{1^{++}}$ being the most viable options), a $D\overline{D}^*$ molecule, a hybrid meson or some other exotic object. These hypotheses do not exclude each other. The $X(3872)$ can be some mixture of any of them [12, 14, 71]. This would be the most complicated scenario, and, probably, even more difficult to identify.

Our goal is to measure the distribution of the dipion invariant mass $m_{\pi\pi}$ in the decay $X(3872) \to J/\psi\,\pi^+\pi^-$ and compare it to various theoretical hypotheses, with the intention of shedding light on the $X(3872)$ puzzle.

Chapter 2

The Experimental Apparatus

2.1 Tevatron Overview

> A particle Z, a particle Y,
> Travel fast in concrete tube
> Underground, ride mile after mile...
>
> Particle Song, “Army of Lovers”.

The Tevatron [72] is a large (2 km in diameter) particle collider, located at Fermilab. It is devised to accelerate protons and collide them with antiprotons at the center-of-mass energy $\sqrt{s} = 1.96$ TeV$/c^2$. This is the highest particle collision energy available in the contemporary world. This fact makes Tevatron a unique research instrument at the frontier of the modern high energy physics.

The Tevatron complex is shown in Figure 2-1. The protons are produced from gaseous negatively ionized hydrogen in a Cockcroft-Walton electrostatic generator, where it is accelerated to a kinetic energy of 750 keV. Then, the H^- ions are fed into a linear accelerator, the Linac [73], where they are accelerated up to an energy of 400 MeV. The Linac consists of two parts: the *drift tube Linac*, accelerating the ions to 116 MeV, and the *side-coupled cavity Linac*, which pushes their kinetic energy up to 400 MeV. The bunches of protons in the Linac output are usually about 40 ms long. This means that it takes 40 ms for the whole bunch to go past a specific point. After the Linac, the H^- ions pass through a carbon foil, which strips the electrons, and the remaining protons are injected into a synchrotron accelerator called Booster. There their energy is pushed up further until 8 GeV. The Booster’s radius is 74.47 m [74] and the revolution time is about 2.78 ms. It takes 13 turns in the Booster to fill the main injector [75], in which the protons enter after leaving the Booster. The main injector is a new part of the accelerator, completed in 1999 for Run II. It has four different functions:

1. It increases the energy of the protons from 8 GeV to 150 GeV.
2. It produces 120 GeV protons, which are used for the antiproton production in the antiproton source.
3. It receives antiprotons from the antiproton source and accelerates them to 150 GeV.
4. It injects protons and antiprotons into the Tevatron itself.

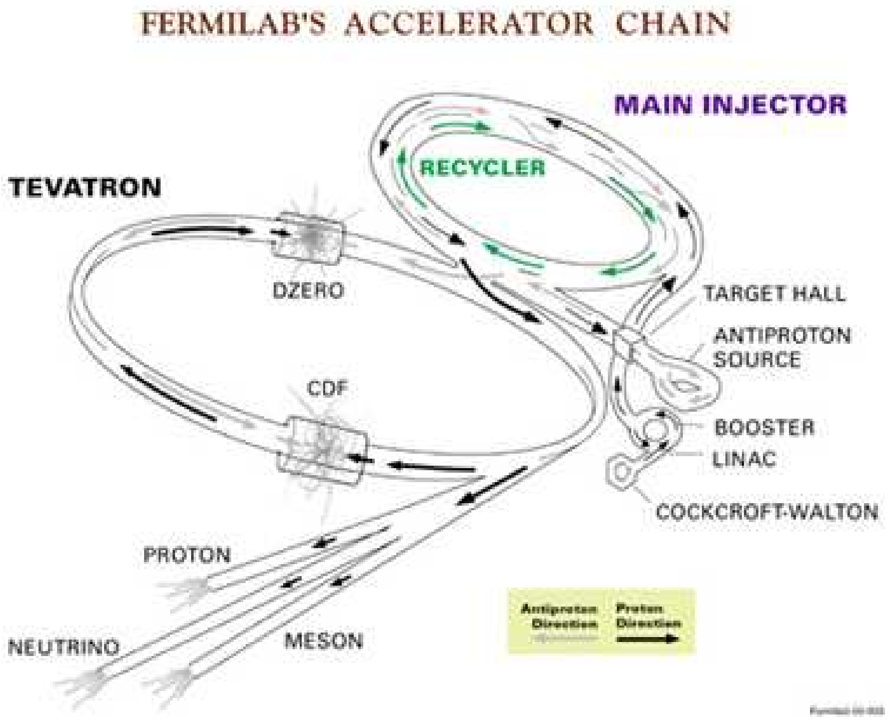

Figure 2-1: The Fermilab's accelerator chain.

To produce antiprotons, the main injector sends 120 GeV protons to the antiproton source, where they hit a nickel target. These collisions produce a lot of secondary particles including many antiprotons. The antiprotons are focused, collected and then stored in the accumulator ring. To focus them a Lithium lens (a high-current magnet) is used. Another magnet separates the antiprotons from the other particles using the mass-spectrometer principle. The antiproton source produces about 20 antiprotons for each million protons on target. When a sufficient number of antiprotons has been collected, they are sent to the main injector for acceleration and injection into the Tevatron.

Another important part of the facilities in the Tevatron complex is an antiproton recycler. Initially it was designed to store the antiprotons returning from a store in the Tevatron and to re-inject them after cooling, hence the name. But currently the recycler only receives the antiprotons from the accumulator, focuses them even better, and stores them. It serves as an additional storage ring.

The Tevatron receives 150 GeV protons and antiprotons from the main injector and accelerates them to the energy 980 GeV. The protons and antiprotons circle the Tevatron in opposite directions. During Run I there were 6 proton bunches and 6 antiproton bunches in the Tevatron ring during normal operation. For Run II this number is 36 bunches of each kind. The bunches cross each other every 396 ns. During the bunch crossing, a few actual collisions between the protons and antiprotons may occur.

The bunches cross each other in two points in the ring. The point of proton-antiproton interaction is called *primary vertex.* They are surrounded by the detectors – CDF and D0 (see Figure 2-1). The detectors are arranged in such a way that the primary vertices are located near the geometrical centers of the detectors.

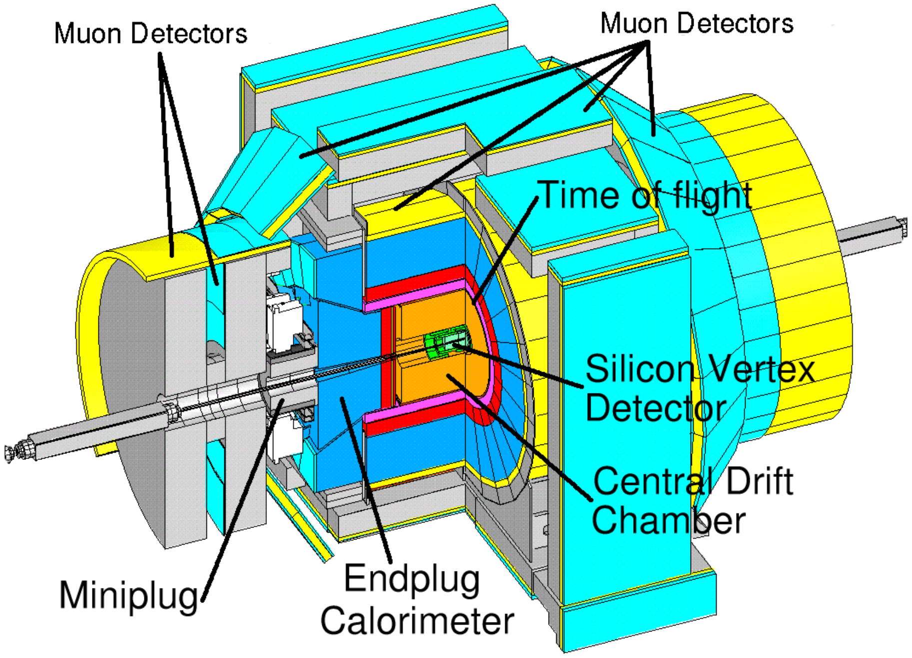

Figure 2-2: Cutaway view of the CDF detector.

The next section will be devoted to the description of the CDF detector. Similar description could be found in References [76, 77].

2.2 CDF Detector

2.2.1 General Overview

The CDF detector is a multi-purpose solenoidal detector, which includes a precision tracking system and fine-grained muon detection. These are the parts which are the most important for this analysis. The other parts of the detector include electromagnetic and hadronic calorimeters, a Time-of-Flight system and a Cherenkov Luminosity Counter. They will be described in further sections.

The detector's cutaway view is shown in Figure 2-2 and its elevation view in Figure 2-3. They depict the main parts of the detector – the innermost silicon system, surrounded by the central drift chamber, the Time-of-Flight system, the magnetic solenoid, calorimeters and outermost muon detectors.

The niobium-titanium magnetic solenoid has a radius of 1.5 m and a length of 4.8 m. It generates a 1.4 T magnetic field, parallel to the beam axis. The current in the solenoid is 4605 A, which is regulated by a feedback loop monitoring an NMR probe. The magnetic field curves the particles' tracks, and the measured curvature allows us to obtain the tracks' momenta. It is important to know the magnetic field precisely, because the accuracy of the track parameters depends on it.

It is convenient to use Cartesian (x, y, z), cylindrical (r, ϕ, z) or polar (r, ϕ, θ) coordinates to describe the detector. The origin of the CDF coordinate system lies in the center of the Central

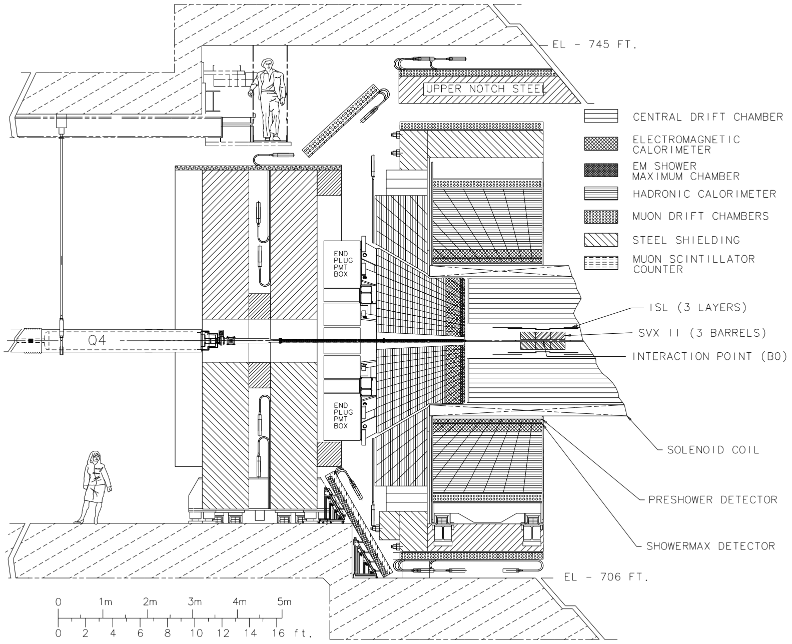

Figure 2-3: Elevation view of the CDF detector.

Outer Tracker. The z axis is directed horizontally along the beamline, the positive direction is to the east. The protons move in the positive direction, the antiprotons in the negative one. The x axis is also directed horizontally, pointing towards the outside of the main ring, and the y axis is upwards. The ϕ angle is calculated from the x axis in the x-y plane. It ranges from 0 to 2π. The azimuthal angle θ measured with respect to the positive direction of the z axis.

The protons and antiprotons in the detector travel along the z axis of the detector's reference frame. It is often convenient to describe their motion in their own reference frame. To do so one should perform a Lorentz boost of the particles momenta and energy along the z axis. The θ coordinate is not invariant under these boosts what makes it somewhat inconvenient to use. The quantity

$$y = \frac{1}{2}\log\frac{E+P_z}{E-P_z},$$

called *rapidity*, is invariant under such boosts. Here E is the energy of a particle and P_z is its momentum along the z axis. In the ultrarelativistic (massless) limit the energy E can be replaced with the momentum P of the particle, and the rapidity turns into the *pseudorapidity*

$$\eta = \frac{1}{2}\log\frac{P+P_z}{P-P_z} = -\log\tan\frac{\theta}{2}.$$

This purely geometrical quantity is used instead of y. The coordinates (r, ϕ, η) are usually chosen to describe the detector. The components of the detector are usually partitioned in ϕ and η. In the following sections we will use these coordinates.

With this coordinate system it is often more convenient to express the distance between two different directions (*e.g.* two different tracks) not in terms of an opening angle between them, but in terms of a quantity $\Delta R = \sqrt{\Delta\phi^2 + \Delta\eta^2}$. Though, the shape of a surface described by an equation $\Delta R = \texttt{const}$ around some direction is not really a cylindrical cone, it is still referred to as a cone.

2.2.2 Tracking Systems

When charged particles pass through matter, they ionize the atoms and molecules of the medium nearby their trajectories. By detecting this ionization the tracks of the particles reconstructed. This process is called *tracking*.

The tracking systems in the CDF detector are located inside the homogeneous solenoidal magnetic field parallel to the z axis. The charged particles inside such a field move along helices with axes parallel to the magnetic field. For this reason the tracks at CDF are described by five parameters: *curvature* C, the angle $\cot\theta$ in the r-z plane, the coordinates of the point of the closest approach of the track to the primary vertex ϕ_0 and z_0, and the distance from this point to the primary vertex d_0, called *impact parameter*.

The curvature and the impact parameter can be positive or negative. They are defined by the relations:

$$C = \frac{q}{2R}, \quad d_0 = q(\sqrt{x_c^2 + y_c^2} - R),$$

where q is the charge of the particle, (x_c, y_c) is the center of the projection of the helix onto the r-ϕ plane, and R is the radius of the helix.

The momentum components of the track are expressed in terms of the five track parameters as follows:

$$\begin{aligned} p_t &= \text{const} \cdot \frac{B}{2|C|} \\ p_x &= p_t \cdot \sin\phi_0 \\ p_y &= p_t \cdot \cos\phi_0 \\ p_z &= p_t \cdot \cot\theta \end{aligned}$$

The particle's production point cannot be determined from only these 5 parameters, because the defined helix extends to infinity in both directions. We only can say that the particle was created somewhere on the helix. To determine the place of the particle production more precisely we need to find another particle which, presumably, originated from the same space point. Generally more than two particles come from the same place. The point of intersection in space of the particles' tracks gives us the *vertex* for all of them. The process of finding this point is called *vertexing*. The determination of the vertex coordinates with good precision is very important for this analysis.

The tracking system in CDF detector consists of two main parts: the Silicon VerteX detector (SVX) and Central Outer Tracker (COT). There are two additional parts: the Intermediate Silicon Layer (ISL) and Layer 00 (L00). Figure 2-4 gives the schematic view of the CDF tracking volume. The calorimeters are also shown in this picture.

Below is a short description of all of the tracking systems.

Silicon Vertex Detector

The Silicon VerteX detector (SVX) is the innermost part of the CDF detector serving for a precise determination of the position of the secondary vertices. SVX consists of 720 silicon microstrip detectors, also called *wafers*. The microstrip detectors are assembled in so-called *ladders*, 4 wafers

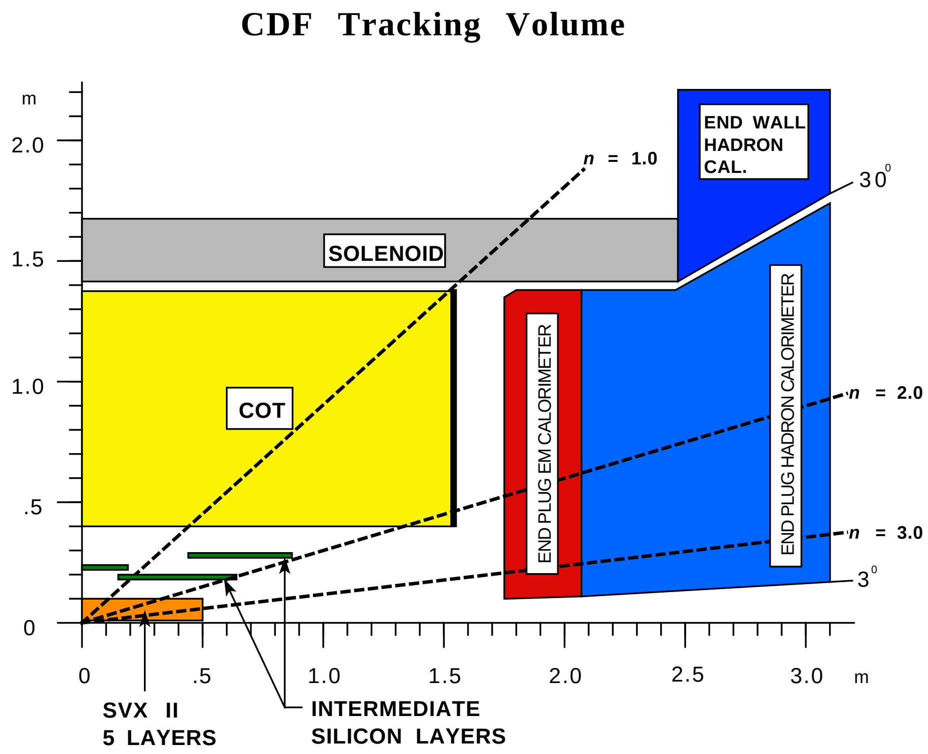

Figure 2-4: The schematic view of the CDF tracking system.

in each ladder. Twelve ladders in ϕ comprise a layer. Five layers of radii from 2.5 cm to an outer radius of 10.7 cm make a *barrel*. SVX consists of 3 such barrels, each is 29 cm long, oriented coaxially. The ladders in the barrels are mounted on beryllium bulkheads, together with the water channels necessary to cool the readout electronics. The side view of a bulkhead is shown in Figure 2-5, and the description of different parts of the picture is given in Table 2.1.

The silicon microstrip detector consists of strips of strongly p-doped silicon (p^+) which are implanted on a lightly n-doped silicon (n^-) substrate of about 300 μm thick. The opposite side of the substrate is covered with the strips of strongly n-doped silicon (n^+). The n^+ strips are oriented at some angle with respect to the p^+ strips. A positive voltage, applied to the n^+ side, takes away the free electrons from the n^- volume and creates an electric field in it. A charged particle traversing the n^- volume creates the electron-hole pairs along its track. The holes drift toward the p^+ strips and produce a signal. The electrons drift toward the n^+, also producing a signal. The position of the hit on p^+ side gives us an r-ϕ coordinate of the hit, while the n^- side is used to measure the stereo coordinate.

Usually, the signal is found on several strips rather than just one. In this case the exact position of the hit is calculated as an average position of all the hit strips, weighted by the amount of charge on them. The precision achieved in CDF with this method is 12 μm.

The SVX layers are numbered from 0 (innermost) to 4. In the layers 0, 1 and 3 the n^+ stripes are oriented at 90° angle with respect to the axis of the detector (stereo angle), and in the layers 2 and 4 the stripes are oriented at the stereo angle 1.2° (Table 2.2). Perspective views of ϕ-side and z-side of a Layer 0 ladders are shown in Figure 2-6.

The SVX barrels are placed as coaxially, as possible. The remaining alignment shifts are taken into account when we assemble hits into a track. It is more important that the axis of

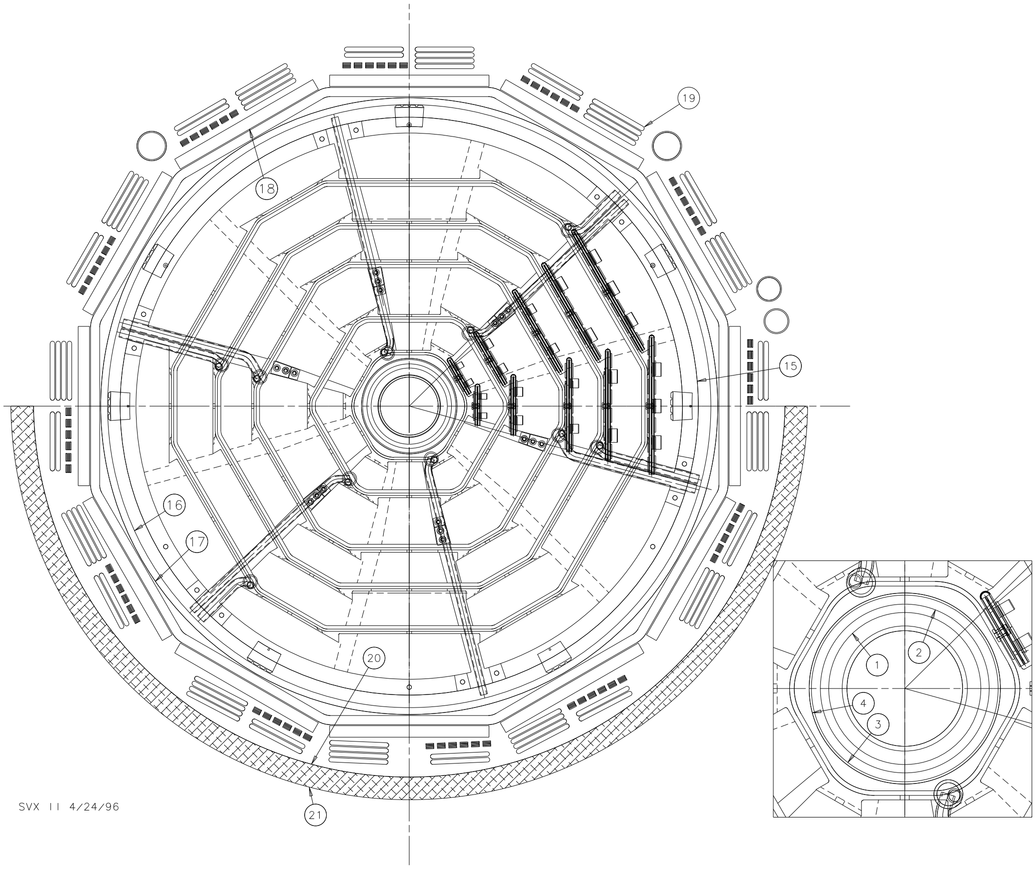

Figure 2-5: The side view of the SVX system.

#	Description	Radius, cm
1	Beam pipe outer radius	1.6700
2	Beam pipe flange outer radius	1.8542
3	Inner screen inner radius	2.0500
4	Bulkhead inner radius	2.1000
15	Bulkhead outer radius	12.9000
16	Outer screen inner radius	12.9000
17	Outer screen outer radius	13.2500
18	Port card inner radius	14.1000
19	Cables	16.1000
20	Half cylinder inner radius	16.3000
21	Half cylinder outer radius	17.3000

Table 2.1: The description of different parts of Figure 2-5.

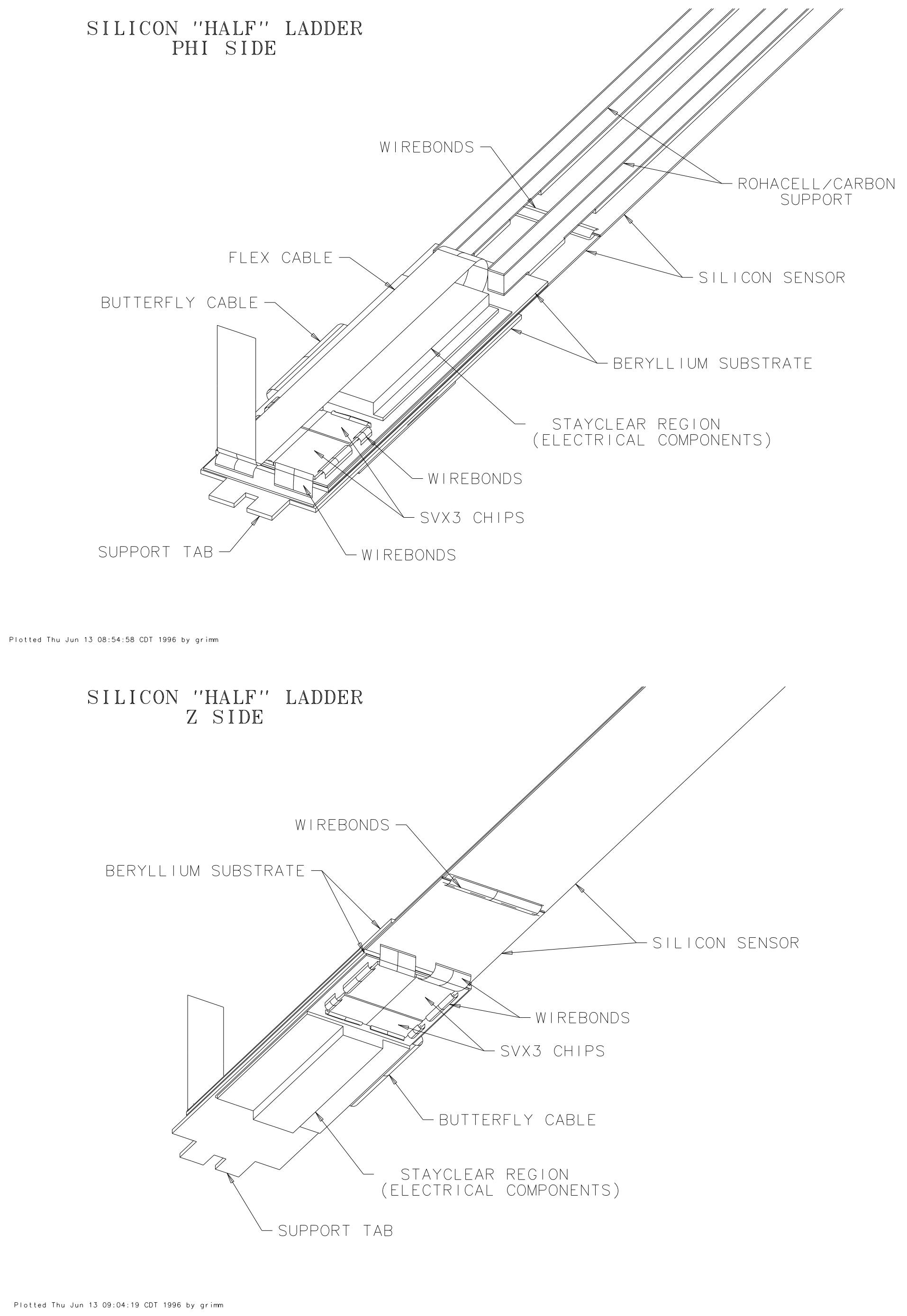

Figure 2-6: Side perspective views of r-ϕ side (top) and r-z side (bottom) of Layer 0 ladder in the SVX system.

Layer	Radius, cm		# of strips		Stereo	Ladder active, mm		Strip Pitch, μm	
	stereo	r-ϕ	stereo	r-ϕ	angle	width	length	stereo	r-ϕ
0	2.55	3.00	256	256	90°	15.30	4×72.43	60	141
1	4.12	4.57	576	384	90°	23.75	4×72.43	62	125.5
2	6.52	7.02	640	640	+1.2°	38.34	4×72.38	60	60
3	8.22	8.72	512	768	90°	46.02	4×72.43	60	141
4	10.10	10.65	896	896	−1.2°	58.18	4×72.38	65	65

Table 2.2: The summary of SVX mechanical parameters

.

the SVX would coincide with the beam axis, rather than with the axis of the detector. The SVT trigger relies on the impact parameter of the track, d_0, measured by SVX, and it must be measured with respect to the beamline. It turns out to be more convenient to store the locations of the primary vertices throughout the run, then fit all these locations with a straight line and use this fitted beamline rather than the primary vertices in the physics analyses. Actually, due to misalignment the beamline in the CDF detector is a few millimeters away from the geometrical central line of the detector. This shift is taken into account in the SVT trigger and in the track reconstruction.

Intermediate Silicon Layer and Layer 00

The Intermediate Silicon Layer (ISL) and Layer 00 (L00) were introduced in Run II. Together with the SVX they comprise the CDF silicon tracking system, shown in Figure 2-7 [77]. The ISL and L00 were integrated into the detector system relatively late and the latter did not become fully operational for the data in this thesis.

The **L00** is a silicon detector inside the SVX. It consists of 6 narrow and 6 wide groups of the microstrip detectors, called “wedges”. Six of them are placed at radius 1.35 cm and the other six at the radius 1.62 cm. There are 6 modules in z of a total length of 95 cm. The sensors in L00 are single-sided and made of more light-weight and radiation-hard silicon than the SVX. They are mounted on a carbon-fiber support structure, which also provides cooling. L00 helps to overcome the multiple scattering effects for tracks passing through the high-density SVX material. This results in the d_0 resolution being as small as 25 μm.

The **ISL** consists of three layers of silicon placed outside of SVX. The region $0 < |\eta| < 1$ is covered by a single layer of radius of 22 cm, and the region $1 < |\eta| < 2$ is covered by two layers, at the radii 20 and 28 cm. The layers consist of the double-sided silicon microstrip detectors, similar to that of SVX, with 55 μm strip pitch on the axial side and 73 μm strip pitch on the stereo side with a 1.2° stereo angle. Only every other strip is readout, which makes the single hit resolution about 16 μm on the axial side and 23 μm on the stereo side. ISL improves the tracking in the central region and allows (together with SVX) for the silicon standalone tracking in the region $1 < |\eta| < 2$. The schematic view of the ISL system is represented in Figure 2-8.

Central Outer Tracker

The Central Outer Tracker (COT) is a cylindrical drift chamber with inner radius of 40.6 cm, and outer radius of 137.99 cm, and length of 310 cm. It is filled with a 50:50 mixture of Argon

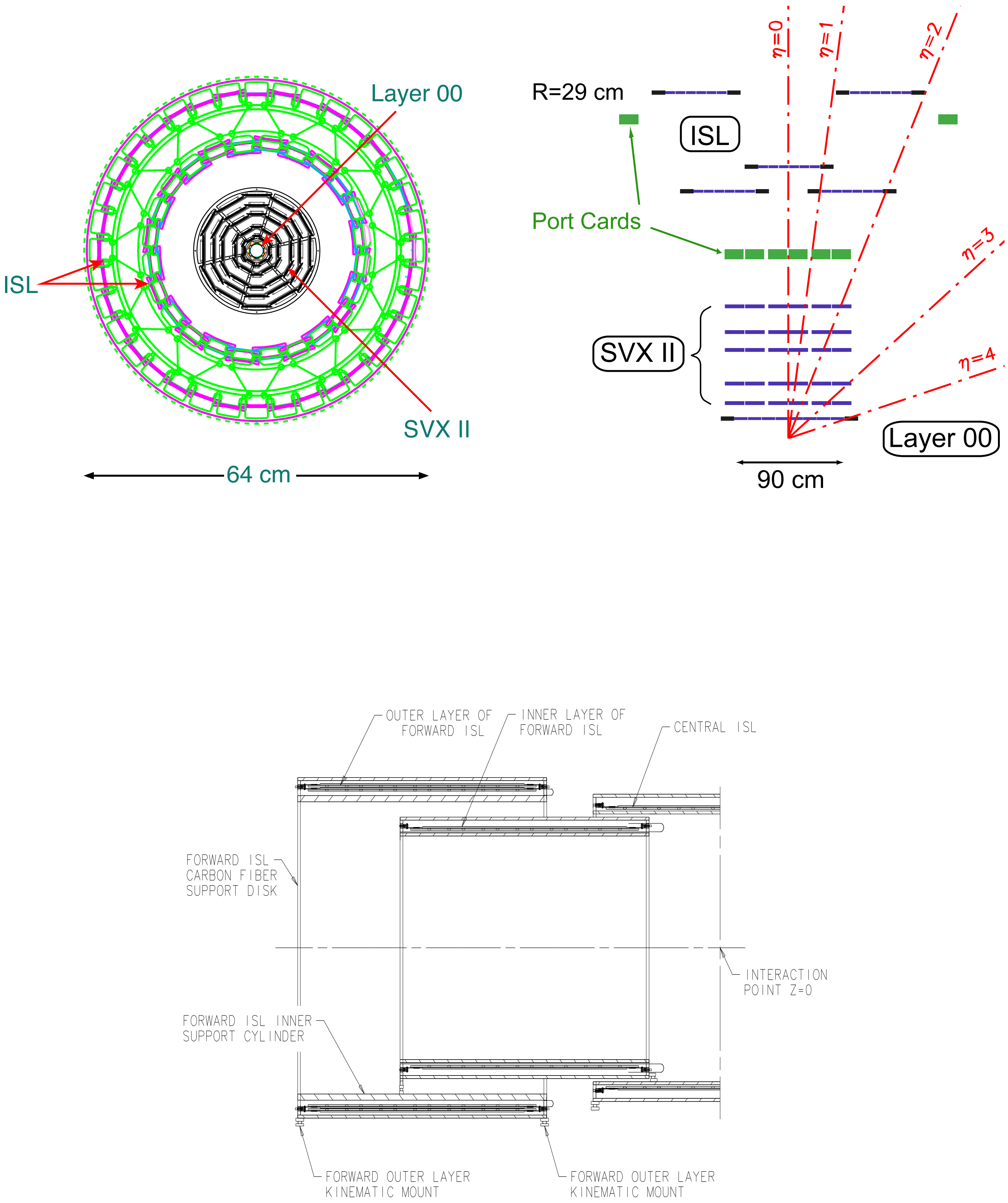

Figure 2-8: The schematic view of the ISL system.

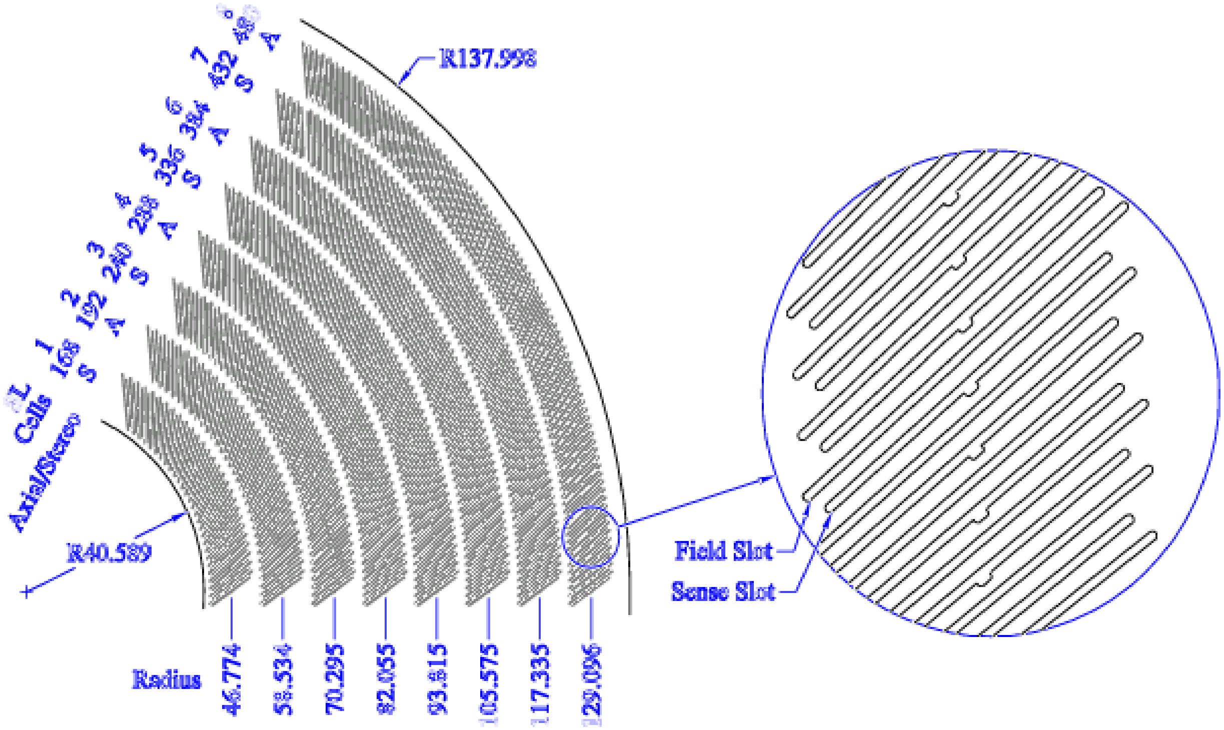

Figure 2-9: A quarter of the COT sense wires.

and Ethane plus trace amounts of alcohol. The information about the particle tracks is obtained from the wires. The wires are subdivided into two classes: sense wires, which are actually used to collect the information about the particle tracks, and the potential wires, configuring the electric field in the COT. When a particle passes through the gas, it excites and ionizes gas molecules. Under the influence of the electric field the released electrons start drifting towards the sense wires. In close vicinity of the wire the $1/r$ electric field accelerates the electrons, causing them to produce more electrons when hitting the gas molecules. These secondary electrons form an "avalanche", which is registered by the sense wire. The time difference between the original $p\bar{p}$ collision and the occurrence of the hit gives us r-ϕ position of the track with respect to the sense wire.

The electrons in the COT do not drift along the electric field direction because of the presence of the magnetic field. In such crossed fields, a charged particle, initially at rest, moves at an angle α with respect to the electric field lines. At COT this angle is $\alpha = 35°$ [78].

The sense wires are subdivided into 96 layers, which are organized into 8 *superlayers*, containing 12 wire layers each. The view of a quarter of the COT is shown in Figure 2-9. One can see the 8 superlayers and the end slots for the potential (field) wires and for the sense wires. Four superlayers have the wires parallel to the axis of the detector. They are called *axial* superlayers and give us the information about r-ϕ position of the track. The hits in them are called *axial hits*. The other four superlayers are tilted with respect to the axis of the detector and are called *stereo* superlayers and they provide *stereo hits*. The tilt angle of the stereo wires, 35°, is chosen so that the drift of the ions would be in the direction perpendicular to the wire, which ensures the best resolution. The sense wire planes are separated by gold-plated Mylar cathode field sheets.

Two such sheets together with a sense wire plane in the middle are called a drift cell. The cell layout for superlayer 2 is shown in Figure 2-10. Other superlayers have similar layout.

The relative precision with which the COT determines the transverse momenta of the tracks, *i.e.* the raw momentum resolution, is given by:

$$\frac{\sigma(p_t)}{p_t} = 0.7 \oplus 0.1\frac{p_t}{\mathrm{GeV}/c}\%$$

Track reconstruction

Two different algorithms are used to reconstruct the tracks from the hits in the COT – segment linking and histogram linking. The first one looks for 3-hit seeds in each axial superlayer. The hits are fit with a straight line and all the other hits within a given distance from this line are added to the segment. The segments are linked to each other by a simple circle fit. After the r-ϕ projection of the track is found, the stereo information is added, and then the final helix fit is performed.

The histogram linking algorithm also uses the 3-hit seeds. For each new hit we determining the radius of a potential track from the positions of the 3-hit seed, the new hit itself, and the beamline. All these radii for all the hits are histogrammed and the position of the highest bin in the histogram is taken as the radius of the track helix.

The hits from the SVX are added to the tracks, found in COT by using the so-called “Outside-In” procedure [79]. The COT track is extrapolated inside the SVX and all the silicon r-ϕ hits found within the cone of a given size around the track are progressively added to the track. Every time a new hit is found, the covariance matrix of the track is updated. After all the r-ϕ silicon layers are taken into account, the z information from the silicon stereo layers is added.

If there is more than one track candidate found, with different combinations of SVX hits attached to the same set of COT hits, then the track candidate with the largest number of SVX layers is chosen.

Because the energy losses are not accounted for in the tracking algorithms we have to re-fit the reconstructed tracks during the analysis with the particle hypothesis of interest. The re-fit procedure is described in Section 3.1. During the re-fit we drop the hits found by L00, because this system has not been fully calibrated yet.

2.2.3 Muon Systems

Muons do not interact hadronically so that they do not have to loose their energy interacting with nuclei. Muons are about 200 times heavier than electrons and their bremsstrahlung radiation is therefore about 40000 times smaller. Thus, muons can travel inside material further than any other charged particle and the muon chambers can be placed in the outermost location of the detector.

There are four systems of scintillators and proportional chambers used in CDF for muon detection: the Central MUon detector (CMU), the Central Muon uPgrade (CMP), the Central Muon eXtension (CMX) and the Intermediate MUon detector (IMU). They cover the region $|\eta| < 2.0$. The muon chambers in the CMP and CMX are placed together with scintillators, which are used to suppress the backgrounds coming from the interactions in the beampipe material. The scintillator systems are called CSP and CSX, correspondingly. The technical specifications of all these systems are given in Table 2.3. The pion interaction lengths and multiple scattering are quoted for a reference angle of $\theta = 90°$ in CMU and CMP/CSP, for an angle of $\theta = 55°$ in

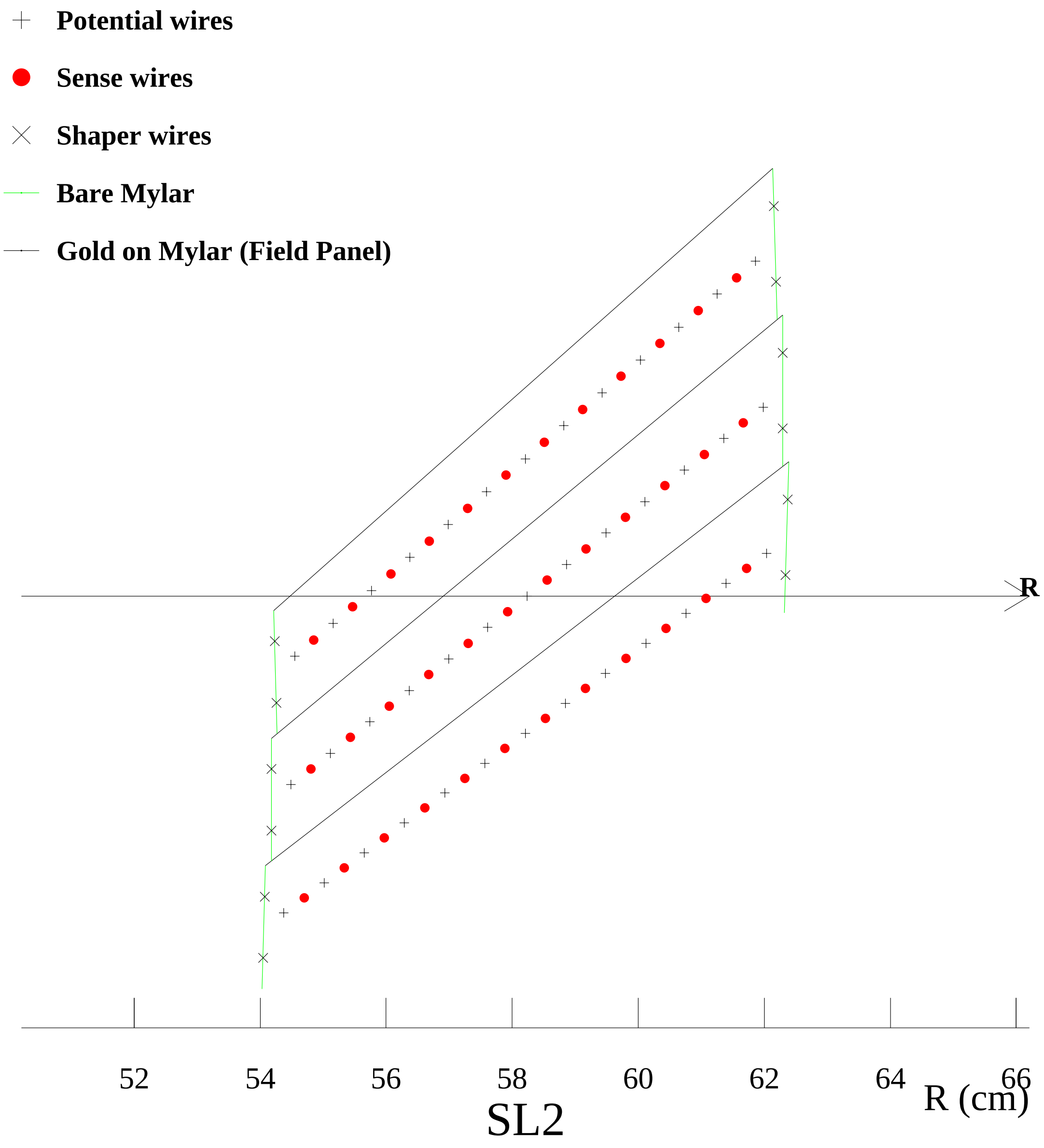

Figure 2-10: The cell layout for superlayer 2 at COT.

CMX/CSX and show the range of values for IMU. The Figure 2-11 displays how the coverage of the muon detectors was extended from the Run I to Run II.

	CMU	CMP/CSP	CMX/CSX	IMU
Pseudorapidity coverage	$\|\eta\| < 0.6$	$\|\eta\| < 0.6$	$0.6 < \|\eta\| < 1.0$	$1.0 < \|\eta\| < 2.0$
Drift tube cross-section	2.7×6.4 cm^2	2.5 cm^2	2.5 cm^2	2.5.4 cm^2
Drift tube length	226 cm	640 cm	180 cm	363 cm
Maximum drift time	800 ns	1.4 μs	1.4 μs	800 ns
# of drift tubes	2304	1076	2208	1728
Scint. counter thickness		2.5 cm	1.5 cm	2.5 cm
Scint. counter width		30 cm	$30 - 40$ cm	17cm
Scint. counter length		320 cm	180 cm	180cm
# of counters		269	324	864
Pion interaction length	5.5	7.8	6.2	6.2-20
Minimum muon p_t	1.4 GeV/c	2.2 GeV/c	1.4 GeV/c	$1.4 - 2.0$ GeV/c
Multiple scat. resolution	12 cm/p_t	15 cm/p_t	13 cm/p_t	13-25 cm/p_t

Table 2.3: The technical specifications of the CDF muon systems.

Muons are detected in the muon chambers by leaving small track segments, called *muon stubs*. Not all the stubs actually come from muons, some may be due to hadronic punch-throughs (hadrons getting beyond the hadronic calorimeter) or because of the electronics' noise. The stubs found are matched to the tracks previously found in COT. To do so for each stub we extrapolate all the tracks with $p_t > 1.3$ GeV/c to the radial position of the stub. If the distance between the track and the stub in the CMU or CMP is smaller than 30 cm (50 cm for CMX), this track is added to the candidate list for the stub. Then, the stub-track pair with the smallest relative distance is chosen as a muon candidate, and this track is removed from the candidate lists for all other stubs. The procedure is repeated while the stub-track pairs are available.

The shielding, provided by the parts of the detector on the way of the muons, plays both positive and negative roles. The positive effect is that it gives us "clean" muons, removing all the other particles coming from the primary vertex. Among the negative effects is the fact that it does not allow muons below certain p_t threshold to reach the muon chambers. But this not a big problem, because the interesting muons, *i.e.* the muons which we are triggering upon, should have a large p_t anyway. Another negative issue is the multiple Coulomb scattering which may randomly deflect the muons from their initial trajectory. It complicates a little the procedure of stub-track matching, but the roughly gaussian and narrow mismatch can be taken into account, as described in Section 2.2.6.

Below, each of the muon systems described in more detail.

CMU

The Central MUon (CMU) detector is placed at the radius 347 cm around the hadron calorimeter. Only muons with p_t greater than about 1.4 GeV/c can reach it. The CMU is divided into 24 ϕ wedges covering 15° each. The working part of the wedge covers only 12.6°, so that the CMU has 24 gaps, 2.4° each. Also, there is about an 18 cm gap between the East and the West halves of the CMU.

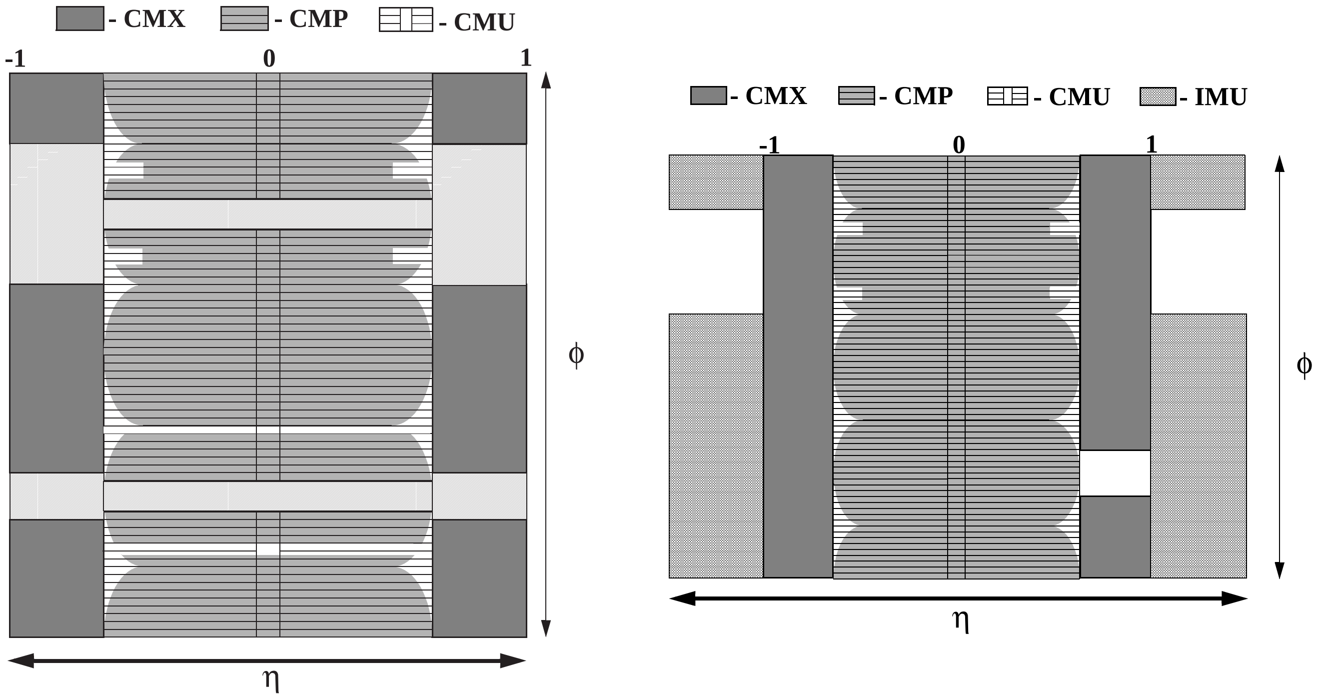

Figure 2-11: Muon coverage for Run I (left) and Run II (right).

A wedge consists of three chambers of angular coverage 4.2°. Each of them has 16 rectangular drift cells, arranged into 4 layers, as shown in Figure 2-12. The cells are filled with same Argon-Ethane gas mixture as the COT. The voltage on the aluminum cathodes of the cells is is -2500 V, while the stainless steel sense wires are kept at $+2325$ V. Two of the four cell layers are oriented along a radial plane passing through the z axis, while the other two are laid along the parallel plane, offseted by 2 mm from the first one. The offset is measured at the midpoint of the chamber. This arrangement allows us to know on which side of the sense wires a track is, by looking at which sense wire got the signal first.

The z position of the hit on a sense wire is determined from the charge division between the ends of the wire. The resolution in the CMU chambers is about 250 μm in the r-ϕ plane and about 1 mm in z.

Reference [80] has a more detailed description of the CMU system.

CMP

The Central Muon uPgrade (CMP) also covers the central region of the detector. It is shielded by an additional steel absorber to reduce hadronic punch-through contamination which the CMU suffers from. The path of the muons is effectively increased by this absorber to 7.8 interaction lengths. Only muons with p_t above 2.2 GeV/c can get to CMP.

The CMP approximately has a shape of a rectangular box with the walls of equal lengths in z. The r-ϕ view of the CMP system is shown in Figure 2-13. Due to such shape the CMP covers the CMU's gaps in ϕ. For Run II the CMP coverage in ϕ was extended, as shown in Figure 2-11. Both systems — CMU and CMP — help us to obtain clean muon selection in the central region of the detector.

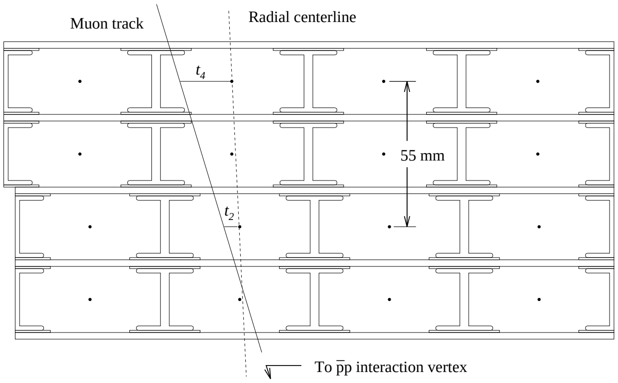

Figure 2-12: The stack of 4 cells in the CMU system.

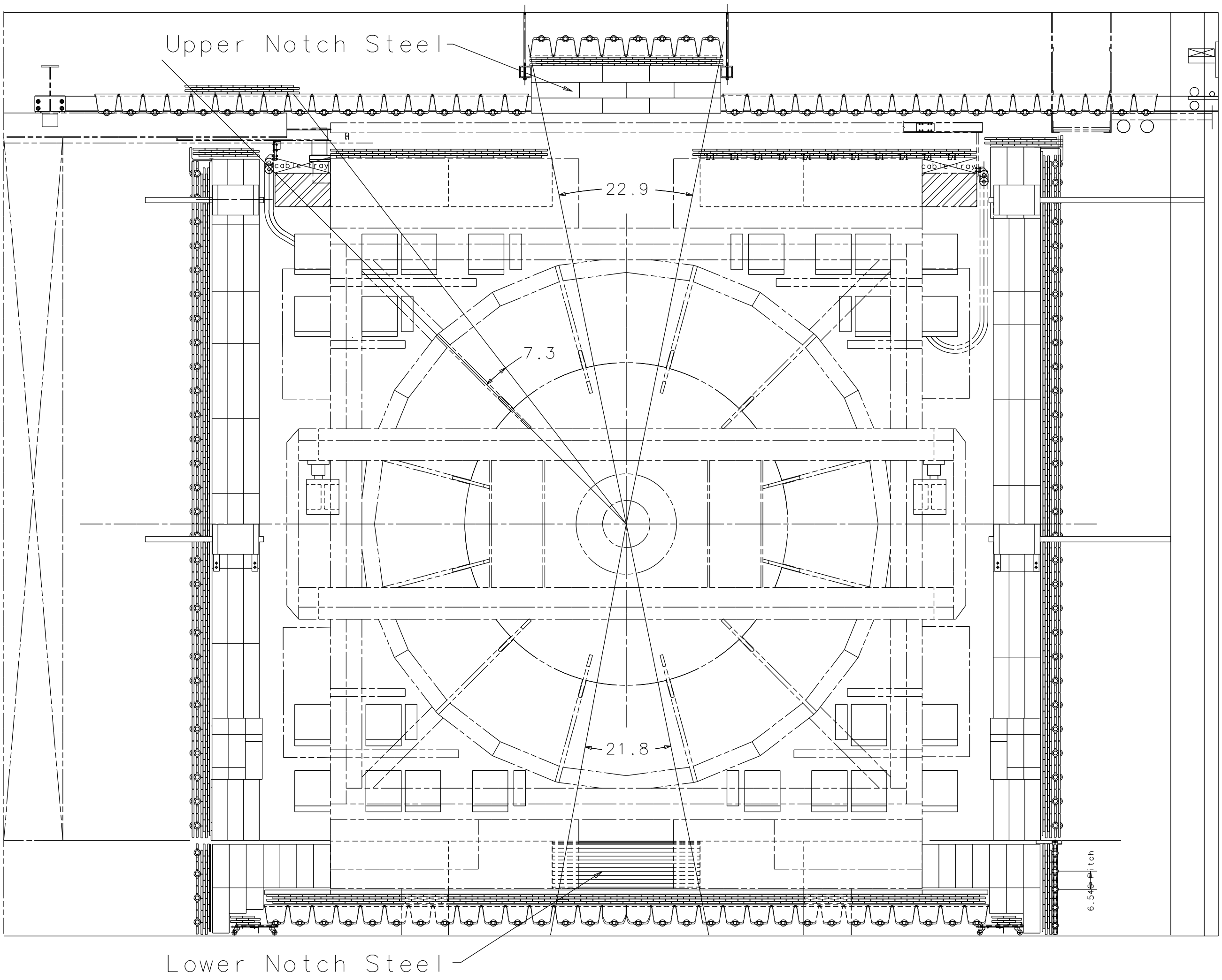

Figure 2-13: The $r-\phi$ view of the CMP system looking at the end of the CDF detector.

The CMP chambers are mounted directly on the absorber. They consist of single-wire tubes 2.5 cm × 15 cm × 640 cm. Some of them are a little bit shorter to allow the cables from the inner parts of the detector go outside. The drift tubes are organized into four layers with each layer being shifted by a half-size of the tube with respect to the neighboring layers.

The CMP is described more completely in Reference [81].

CMX

The Central Muon eXtension (CMX) consists of the wedges, forming a conical shapes on both ends of the detector. Each wedge covers 15° in ϕ and the range $0.6 < |\eta| < 1.0$. The (mentally extrapolated) apexes of the cones lie on the z-axis of the detector and the opening angle of all the cones is about 45°. The elevation view of the CMX system is displayed in Figure 2-14. The IMU barrel chambers and scintillation counters, the toroid counters, and the endwall counters are also shown. In the Run I CMX had a 30° gap at the top on the West end and 90° gap at the bottom in both East and West ends. The first gap was created to make space for the liquid helium lines and the second gap was due to intersection of the conical section with the collision hall floor. For Run II both these gaps are covered by KeyStone and MiniSkirt additions to CMX. The KeyStone consists of two more CMX wedges, while the MiniSkirt has a little bit different geometry, shown in Figure 2-15.

The CMX chambers consist of the same tubes as in CMP with only the length of the tubes being different: 180 cm. Each wedge in the CMX has 48 tubes arranged in 8 layers, each layer has 6 tubes. The layers are staggered so that there are at least 4 tubes in any coverage in ϕ. Figure 2-16 shows the arrangement of the CMX tubes. The layers are placed at a slight stereo angle, which allows for the measurement of the z coordinate.

More information on the CMX can be found in Reference [81].

IMU

The Intermediate MUon system (IMU) covers the region $1.0 < |\eta| < 2.0$ with fine granularity. It was introduced to complement ISL in the reconstruction of the tracks with $|\eta| > 1.0$.

The IMU's drift chambers and counters are placed around the steel toroids on the both ends of the CDF. There are additional counters between the toroids. The detailed section of the IMU Barrel is shown in Figure 2-17 and the complete elevation view of the IMU system – in Figure 2-18. The IMU chambers and scintillators are represented by the outer circle around the toroids. The CMX lower 90° section is also shown. The chambers and counters used in the IMU are the same as those in CMX and CMP, and the electronics is the same too. Reference [82] provides further information on the IMU.

The dimuon trigger was not available for this system at the time when the data for this thesis was collected. For this reason, the IMU is not used in our analysis.

2.2.4 Other Systems

The other systems in the CDF detector include the Time-of-Flight (TOF), the calorimetry and the Cherenkov Luminosity Counters (CLC). They are not used in this analysis, so we will present only a short description.

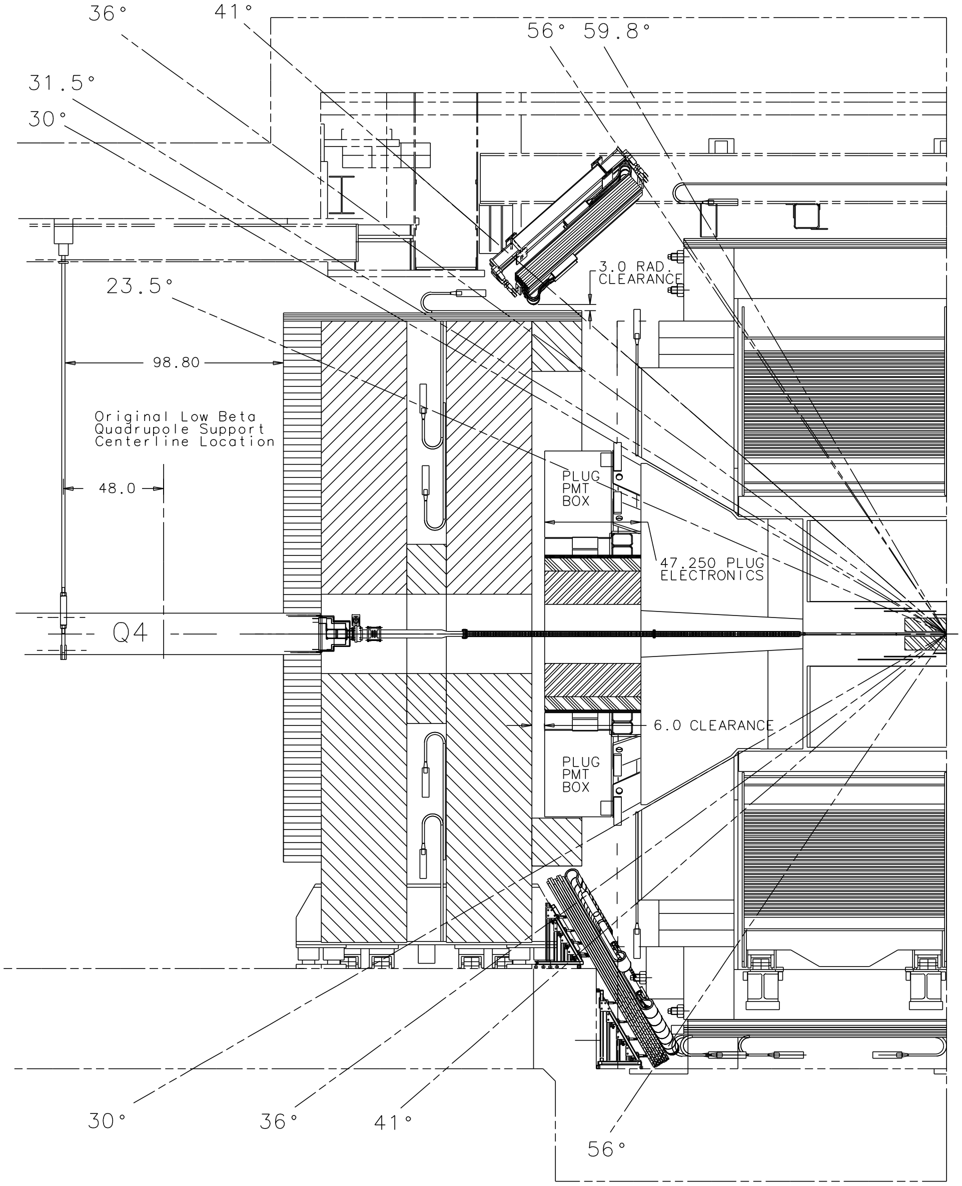

Figure 2-14: The side view of the CDF showing the CMX coverage. The dark blocks spanning between 30°-40° and 56° are the CMX wedges.

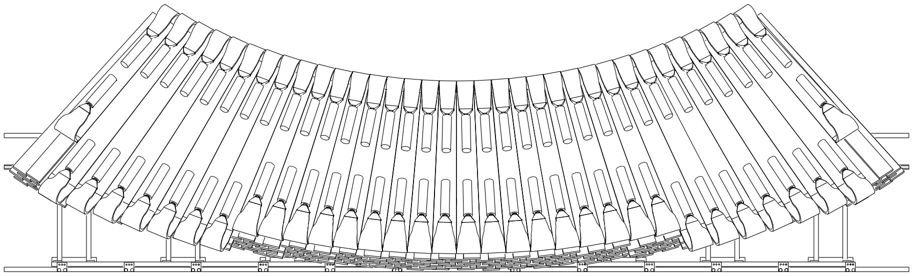

Figure 2-15: The MiniSkirt portion of the CMX system.

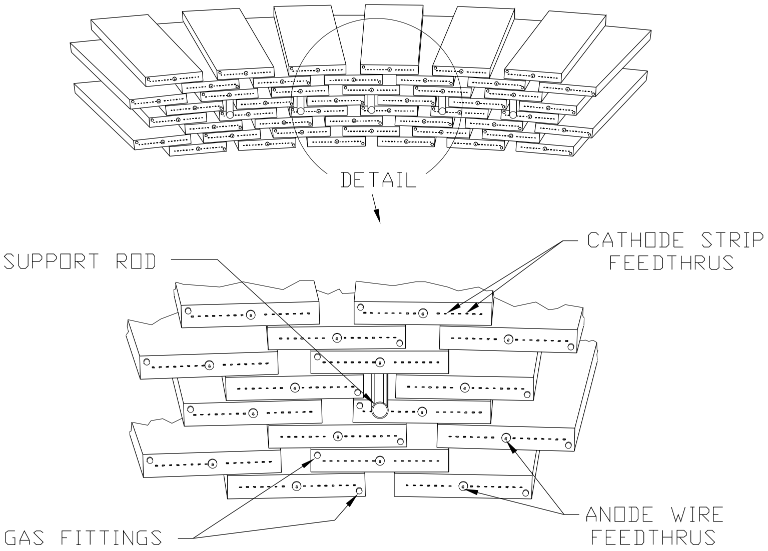

Figure 2-16: The arrangement of the layers in the CMX system.

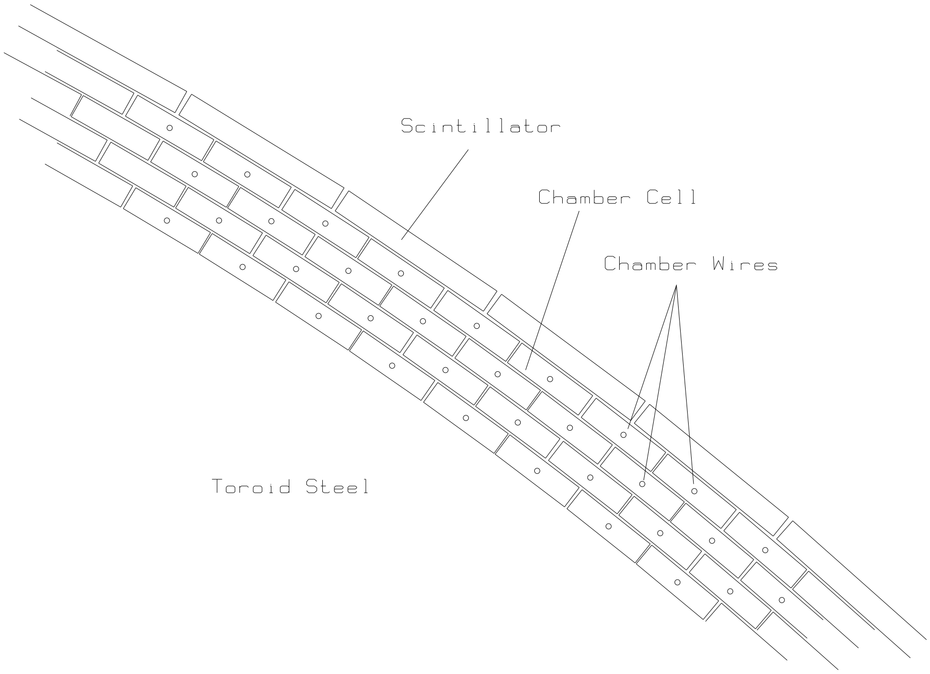

Figure 2-17: A detailed section of the IMU Barrel.

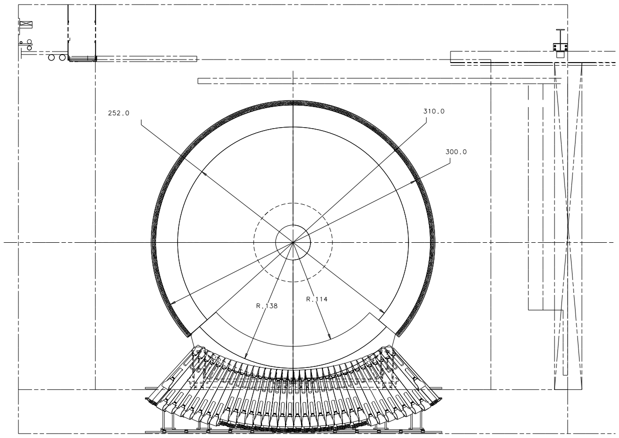

Figure 2-18: The elevation view of the IMU Barrel (thick dark line). The MiniSkirt part of the CMX system is shown too.

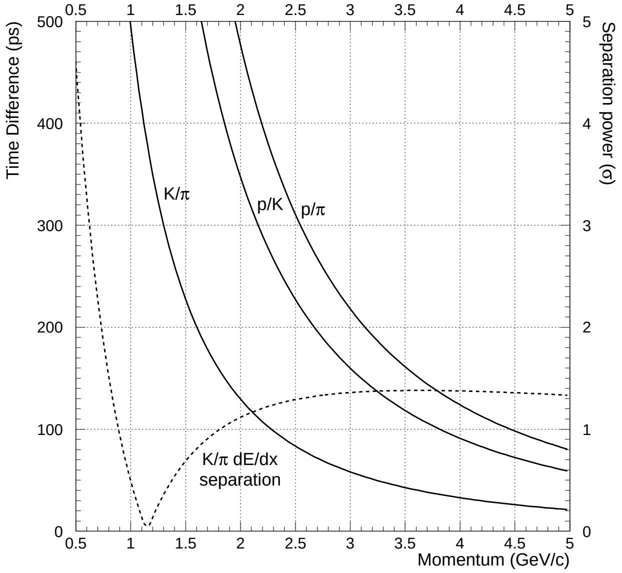

Figure 2-19: The Time-of-Flight performance.

Time-of-Flight

The Time-of-Flight (TOF) system surrounds the COT. It serves to determine the masses m of particles, and thus identify it, with the formula:

$$m = \frac{P}{\gamma\beta c} = \frac{P}{\beta c}\sqrt{1-\beta^2} = \frac{P}{c}\sqrt{\frac{1}{\beta^2} - 1} = \frac{P}{c}\sqrt{\frac{(ct)^2}{L^2} - 1},$$

where t is the time passed from the collision moment, L is the path length and P is the momentum of the particle.

The TOF system is located between the COT and the solenoid magnet, at a radius of 138 cm. It consists of 216 scintillator bars 4 cm × 4 cm × 279 cm. These bars cover the region $|\eta| < 1$. When a particle passes through a bar, the photons from ionized molecules travel to both ends of the bar, where they are detected by fine-mesh photomultiplier tubes. The travel time of the photons determines the position at which the particle crossed the tube. These tubes can operate inside the magnetic field of 1.4 T, created by the solenoid.

The ability of the TOF system to distinguish particles of different mass (*separation power*) is illustrated in Figure 2-19. The time difference between kaons, pions and protons over path of 140 cm as a function of momentum, expressed in terms of picoseconds (left scale) and the separation power σ (right scale) assuming a time resolution 100 ps. This is close to the real value of $\sim$120 ps. The dashed line shows the separation between kaons and pions obtained from the energy loss measurements (dE/dx) in COT.

Reference [83] gives a more detailed discussion of the TOF system.

Calorimetry

The Time-of-Flight system is surrounded by an electromagnetic calorimeter, which, in turn, is surrounded by a thicker hadron calorimeter. Geometrically the calorimeters are divided into

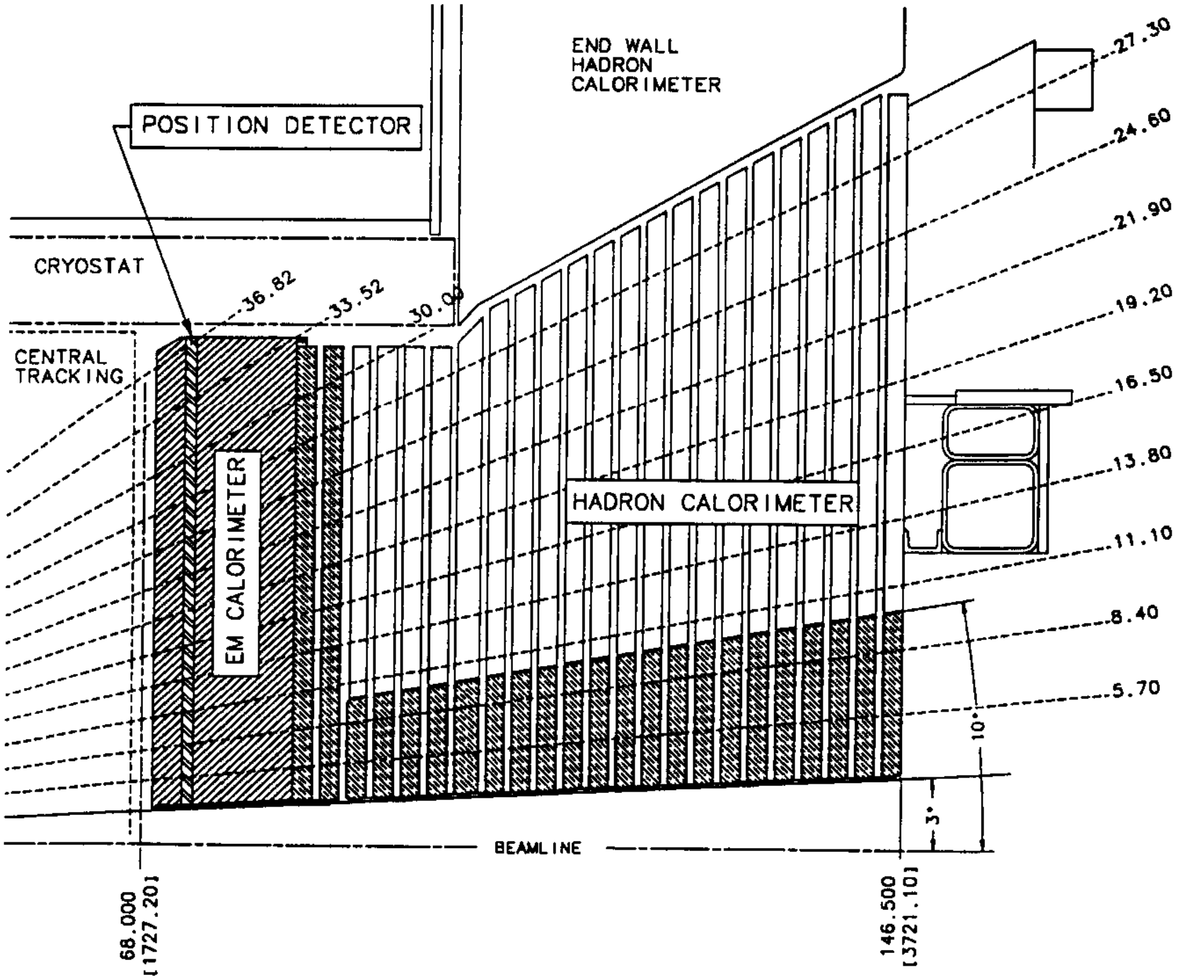

Figure 2-20: The cross-section of upper part of the end plug calorimeter.

central, wall and plug parts. They are called, correspondingly: the Central ElectroMagnetic (CEM), the Central HAdron (CHA), the Wall HAdron (WHA), the Plug ElectroMagnetic (PEM) and Plug HAdron (PHA) calorimeters.

All the calorimeters in CDF are *sampling* calorimeters, which means that they consist of alternating layers of absorber and scintillator. The absorber is necessary to make the passing particle create a shower, while the scintillator gives us the signal, read out by phototubes. The CEM and PEM use lead as the absorber.

The central parts cover the region $|\eta| < 1.1$ for EM and $|\eta| < 1.3$ for hadron calorimeters. They are divided into towers of equal size: 15° in ϕ and 0.1 in η. The plug calorimeters extend down to $\eta = 3.6$ and have variable segmentation. The schematic view of the plug calorimeters is shown in Figure 2-4 and the cross-section in Figure 2-20.

Both the CEM and PEM have electromagnetic strips called CES and PES, respectively. These are gas proportional chambers with the wires inside being perpendicular to the strips outside. This configuration allows us to measure both ϕ and z coordinates of the particle shower. The

Calorimeter	Thickness	Number of layers: thickness	Resolution (E in GeV)
CEM	19 X_0	20-30 lead:3 mm, scintillator:5 mm	$2\% \oplus 13.5\%/\sqrt{E\cdot\sin\theta}$
PEM	21 X_0	22 lead:4.5 mm, scintillator:4 mm + preshower scint. layer 10 mm	$0.7\% \oplus 14.4\%/\sqrt{E\cdot\sin\theta}$
CHA/WHA	$4.7/4.5\lambda_0$	32/15 iron:25/50 mm, scintillator:10 mm	$3\% \oplus 75\%/\sqrt{E\cdot\sin\theta}$
PHA	7 λ_0	23 iron:51 mm, scintillator:6 mm	$5\% \oplus 80\%/\sqrt{E\cdot\sin\theta}$

Table 2.4: The basic properties of the calorimeters at CDF

spatial resolution is about 2 mm in both directions for the CES and about 1 mm for the PES.

The CES and PES are located inside the calorimeters, to give us the transverse shower profile measurement at the place where it is the largest, *i.e.* at the depth of about 6 radiation lengths X_0. They measure the position of the shower, so that it could be matched to COT tracks. This way electrons can be distinguished from photons and neutral pions.

The CEM is preceded by a Central PReshower (CPR) multiwire proportional chamber. It was introduced because of the delayed initiation of γ-showers. The PEM has no such chamber, only its first scintillator layer, called PPR, is much thicker than the others, and has an individual read out.

The hadron calorimeters are located after the electromagnetic calorimeters. They use iron as the absorber which makes the incident hadrons create showers. The hadron and electromagnetic calorimeters are similar, differing from each mainly by the depths. The basic properties of the calorimeters are given in the Table 2.4.

More information about calorimetry in CDF can be found in References [82] and [84].

Luminosity Counters

The Cherenkov Luminosity Counter (CLC) serves to determine the instantaneous luminosity $\mathcal{L}$ of the Tevatron at the CDF interaction point by the formula:

$$\mathcal{L} = \frac{\mu \cdot f_{bc}}{\sigma_{p\bar{p}}},$$

where μ is the average number of interactions per bunch crossing, f_{bc} is the rate of the bunch crossings at the Tevatron and $\sigma_{p\bar{p}}$ is the total $p\bar{p}$ cross-section at $\sqrt{s} = 1.96$ TeV, scaled [85] to this energy from the results of the previous measurements [86].

According to Poisson statistics, the probability to have an empty bunch crossing, *i.e.* a bunch crossing with no $p\bar{p}$ collisions, is $P = e^{-\mu}$. The CLC actually measures the number of such empty bunch crossings. This measurement is based on the well-known Cherenkov effect: a charged particle traveling in some media with a speed higher than the speed of light in this media radiates light in a narrow cone around its direction. If the total amount of the collected light is below a threshold, the CLC counts it as an empty crossing. The measured fraction of these crossings, corrected for the CLC acceptance, is used to calculate μ.

The Cherenkov counters are located in the gaps of the Plug Calorimeter, between the Plug Calorimeter and the beamline. They are directed towards the interaction point, so that the particles coming from this point would generate the largest amount of light into the counters. The time resolution of the CLC system is about 50 ps, which makes it possible to distinguish between particles coming from different interactions. The precision of the luminosity measurement at

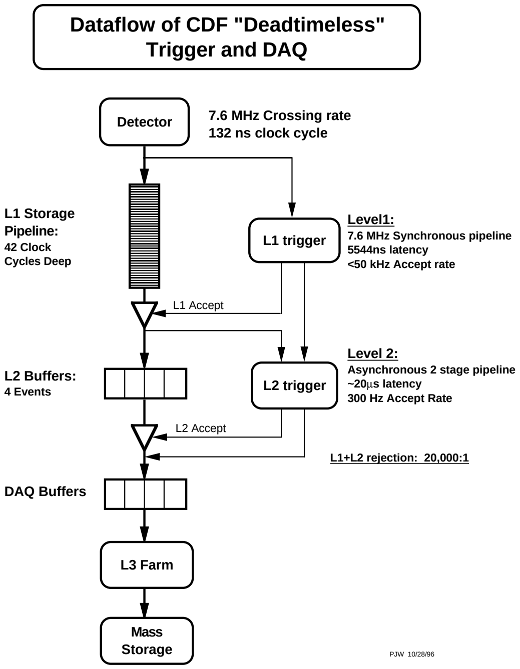

Figure 2-21: The trigger and DAQ system functional block diagram.

CDF is about 5%.

More details about the CLC may be found in Reference [87].

2.2.5 General Triggering

The proton and antiproton bunches cross in the Tevatron every 396 ns at CDF. At the current luminosity of about 10^{31} cm^{-2}s^{-1} we have approximately one p-$\bar{p}$ interaction per bunch crossing. This means that 2.5 million events are produced at CDF every second. Recording all of these events would require an enormous data throughput of 250 GBytes/sec (assuming an average size of an event of 100 KB). It is not only not possible to achieve this rate with existing technology, but it is also not desirable to do so. Even if we managed to record all these data, it would take a very long time to analyze it afterwards. To make the data throughput and the size of the data samples reasonable, we have to somehow select and write to tape only the most interesting events, letting all the others go unrecorded. To decide which events are the most interesting, we look for the specific signatures, such as high-p_t tracks, leptons, jets etc. To do so on-the-fly, a special trigger system was built. Ideally this system has no deadtime, which means that there is no situation when an event can not be recorded because the previous one is still being processed. This is achieved by having three trigger levels (Level-1, Level-2 and Level-3), connected with buffered pipelines. The block scheme of the data acquisition (DAQ) and trigger system at CDF is shown in Figure 2-21.

The Level-1 trigger has only 5.5 μs to make a decision about each event. On average, it accepts only one event out of 250, bringing the event rate down to about 10 KHz. The accepted events go further to Level-2. Level-2 has a little bit more time to decide, about $20-30$ μs per event. If Level-2 accepts the event, the whole detector is read out, and the event goes further, to the Event Builder and Level-3. The event rate at this point is about $200-300$ Hz. In the

Event Builder the data fragments from the different parts of the detector are collected into a single event record, which is submitted to the Level-3. At Level-3, the event is reconstructed and, again, is considered for possible rejection. Level-3 accepts about one event out of 4. The accepted events are transmitted to the mass storage devices at a rate of approximately 75 Hz and get written on a tape.

Below all three levels of the CDF trigger discussed in more detail. Even more information can be found in References [82] and [88].

Level-1

As was mentioned earlier, Level-1 trigger has only 5.5 μs to accept or reject an event. Therefore, it can not do the detailed reconstruction of COT tracks and muon stubs or obtain the details of showers in the calorimeters. Instead, it uses some very crudely reconstructed versions, which are called *primitives*. For example, for the muon stubs we only know which muon chamber has the stub, the stub position and slope are not measured. The muon or calorimeter primitives, being combined with the track primitives give us electrons, muons and jets, which we can trigger upon.

The full list of trigger algorithms can be found in Reference [89]. The most important trigger for this analysis is so-called dimuon trigger based on detecting two muons in the event. It will be described later, in Section 2.2.6.

XFT and XTRP

The eXtremely Fast Tracker (XFT) uses information from only 4 axial superlayers of the COT to identify high-p_t track primitives in the r-ϕ plane. To do so the hits from the COT are separated into two classes, according to their drift time: *prompt* hits with the drift time less than 44 ns and *delayed* hits with longer drift time. Then the hit pattern in the event is compared to a predefined set of patterns for both prompt and delayed hits. This predefined set of patterns helps to find the segments of high-p_t tracks coming from the beamline very fast. For all the found segments the information about the charge, curvature and the ϕ position at the COT superlayer 6 is kept. Then the segments which look like they came from the same track are linked together into the track primitive. Of course, the parameters of the track primitive are estimated very crudely, given the short time which XFT has for this. The information about the found track primitives is given to the eXTRaPolator unit (XTRP) and to Level-2.

The XTRP matches the track primitives from XFT with the muon and calorimeter primitives. A detailed description of this matching utilized in dimuon trigger is given in Section 2.2.6. XTRP also uses a predefined set of patterns to speed up the matching.

The detailed information about XFT and XTRP logic is available in References [90] and [91].

Level-2

The events accepted by Level-1 go to Level-2 for the further processing. The Level-2 uses the primitives from the Level-1 plus some additional information from the calorimetry and from the SVX (see Figure 2-22). The information about r-ϕ hits from the SVX is used to extrapolate the XFT track primitives inside the SVX and to determine the tracks impact parameter, d_0. Some triggers look for tracks with high d_0, *i.e.* for the events with *displaced vertex*. This capability was introduced in Run II.

If the event is accepted, the primitives, constructed at Level-2 are submitted further, to the Event Builder and Level-3.

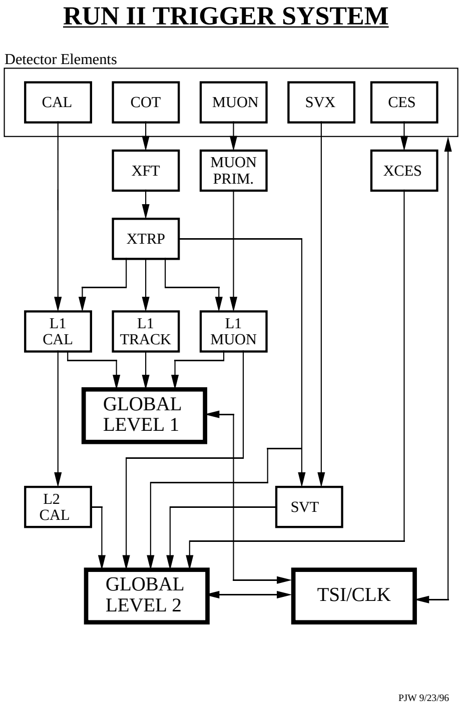

Figure 2-22: The CDF trigger-system block diagram.

Event Builder and Level-3

In the Event Builder system the event fragments from the different parts of the detector are put together and go further as one whole piece. This is done with the aid of an Asynchronous Transfer Mode (ATM) network switch, which takes the event fragments from the Level-2 VME crates, puts them in the proper places and then feeds them to the Level-3 (see Figure 2-23).

The Level-3 consists of 292 computers. They are subdivided into 16 groups (subfarms) of 16-18 computers in each. One computer in each subfarm serves as a *converter node*, accepting the data from the Event Builder and directing it to one of the other computers in the subfarm (*processor node*) for the analysis. The accepted events go to the *output nodes* and then further to the mass storage device. Each output node is shared by two subfarms.

The processor nodes transform the event fragments into a united event record, which has all the information about the event from all the parts of the detector. The Level-1 and Level-2 have to deal with crudely reconstructed primitives because of the lack of time. The Level-3 has enough time to fully reconstruct tracks, muons, electrons, jets, *etc*and to apply the final trigger requirements to them. The parallel data handling of Level-3 allows for this time to make the decision about each event.

More information about the Event Builder and Level-3 is available in Reference [92].

2.2.6 Dimuon Trigger

The dimuon trigger at CDF looks for events with two muons. One of the muons should be from the CMU, another can be either from CMU or from the CMX. Let us first consider the case when the second muon also comes from the CMU. For this scenario the trigger is called

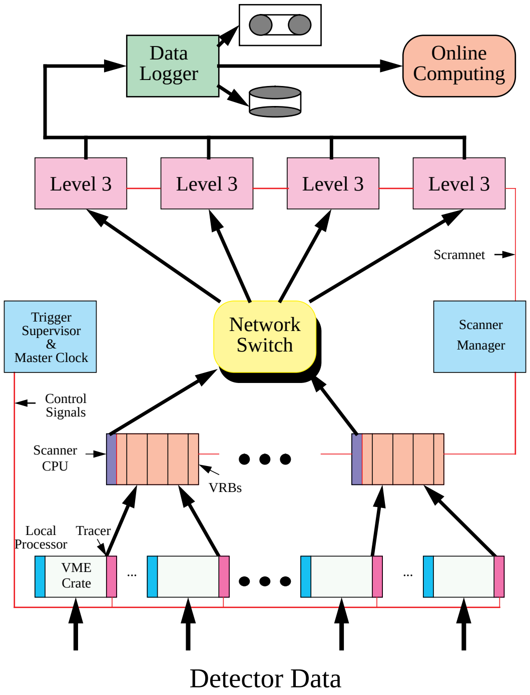

Figure 2-23: The block scheme of the Event Builder and Level-3 system.

“L1_TWO_CMU_PT1.5”, because only muons with $p_t > 1.5$ GeV/c can get to the CMU.

The muon chambers in the CMU are organized in stacks of four. Each end of the detector has 288 such stacks. The stack may have a *stub* — a track segment in which the hits in the cells 1 & 3 or cells 2 & 4 are separated in time by no more than 396 ns. The adjacent stacks are logically assembled into pairs, called *towers*. If at least one stack in the tower has a stub, the tower has fired. Otherwise, the tower is empty.

The information from muon chambers is linked to the tracking information as follows. First, the XFT reports the charge, p_t and ϕ (measured at the 6th COT superlayer) of the tracks to the XTRP. The latter extrapolates the tracks (assuming they came from the beam line) to the inner radius of the CMU - 347.8 cm. The multiple scattering in the detector material leads to an uncertainty in the determination of the position of the track at this radius. So that, for each track a ϕ window is determined, where the track could end up with 99.5% (3σ) probability. This window in ϕ is called a *footprint*.

If a fired CMU tower is covered by at least one track footprint, it is called *muon tower*. The event gets accepted by Level-1 dimuon trigger if it has at least two muon towers. These towers, though, must be separated by at least two other towers (which may or may not be empty), or to be on the different ends of the detector. If the muon towers are separated by a 2.4° gap between CMU wedges, this is also counted as a tower. This requirement ensures that there is a separation in ϕ between the two muons.

If one muon in the event comes from the CMU while another muon comes from the CMX, the trigger has a different name, “L1_CMU_PT1.5_CMX_PT2.2”, which reflects the fact that only muons with $p_t > 2.2$ GeV/c can reach CMX. Another difference is that the CMU and CMX muon towers require no separation in ϕ. There is no requirement for the muons to be of the opposite charge at Level-1.

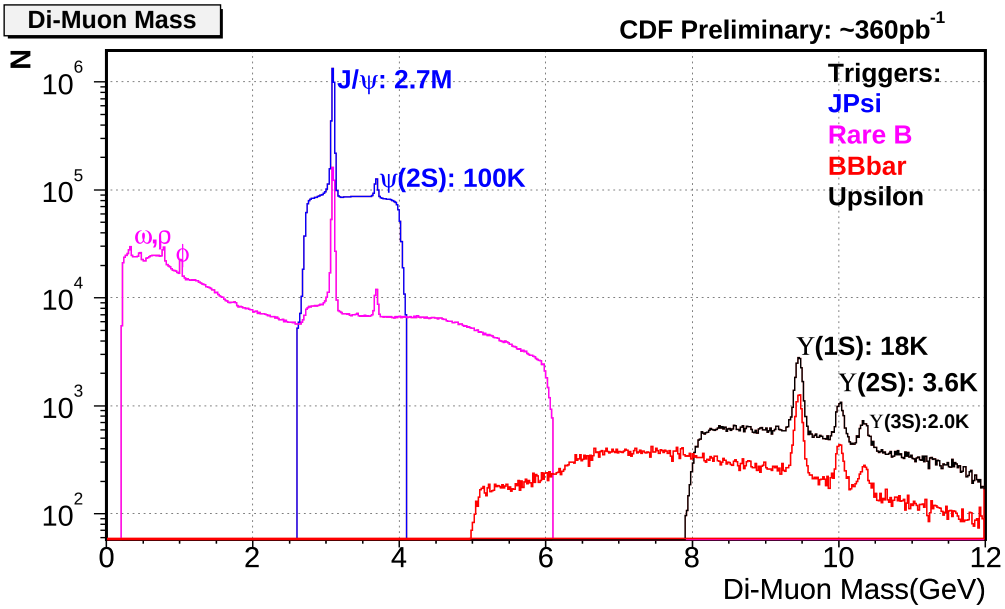

Figure 2-24: The mass spectrum of muon pairs obtained via different triggers at CDF. The dimuon trigger used in this analysis is called "JPsi".

Reference [93] give more information about the Level-1 dimuon trigger. Figure 2-24 shows the mass spectrum of the muon pairs obtained with different triggers in CDF. The described here dimuon trigger is called "JPsi" on this plot.

Level-2 does not impose any additional cuts on the dimuons, and the events accepted by Level-1 trigger proceed directly to Level-3. At Level-3 the muons are required to have opposite charge. The invariant mass of both muons should be between 2.7 GeV$/c^2$ and 4.0 GeV$/c^2$ (selecting J/ψ and $\psi(2S)$), the difference in z_0 should be smaller than 5 cm and the opening angle between them less than 130°.

2.3 Offline Data Handling

The data obtained from the Level-3 are split into ten "streams" which are called by first ten letters of the alphabet: "A", "B"... "J". The events passing the requirements of the dimuon trigger go into the stream "J". These events are written to tape in real time mode, *i.e.* online. Further manipulations of the data are performed offline. The data on the tape is written in the form of the raw data banks from different parts of the detector. One needs to unpack these banks and produce the objects for actual physics analysis, such as tracks, muons, electrons, etc. This procedure is called *production*. The data for this analysis was produced with a production version 5.3.3. The data after the production is split into so-called *datasets*, containing the events satisfying a particular set of trigger requirements. These datasets are given to the end users to do the physics analysis. There are 35 datasets in CDF. This analysis is done with the `jpmm0c` dataset, which contained the events with dimuon candidates found by the detector. The events in this dataset are "stripped" by removing the banks and objects not needed for the further analysis. The compressed version of our dataset is called `xpmm0c`. The stripping greatly speeds up the analysis, because much of the time is usually taken reading the data files, rather than actually processing the data. The stripped data is subject to a further reduction by applying some loose cuts. This is called *skimming.* The skimmed data files contain mostly the interesting events and it takes quite a short time to apply tighter cuts to them and extract the final results.

The amount of data in the final datasets is usually measured not in the number of events, but rather in the inverse units of the cross-section. In this way the users can multiply the size of the dataset by the cross-section of the process they are interested in to obtain the expected number of the events of this type in the dataset. The total size of the dataset used for this analysis is about 360 pb^{-1}.

A few words should be said about the format of the data in the data files. After production, the data files contain the collections of tracks, muons, electrons *etc.* During the analysis though, it is more convenient to work with the collections of J/ψ candidates, $X(3872)$ candidates *etc.* For this purpose a special framework is developed, in which the particle candidates can be created, put into collections and stored in a special kind of ntuple — *stntuple.* This framework allows one to handle the particle candidates faster and in more convenient way. More details about the stntuples can be found in Reference [94].

Chapter 3

Data Sample and Selection Cuts

The dataset used in this analysis is collected via the dimuon trigger. This dataset comprises Runs 138425 through 186598, corresponding to an integrated luminosity of 360 pb^{-1}.

The CDF detector consists of many different subsystems which may be turned on or off during the data taking. In particular, the silicon part of the tracking system, the muon systems and the parts of triggering system may not be fully activated for a particular set of runs. The shift crew marks the detector subsystems for each run as "good" or "bad". We use only the data from the runs for which all the crucial subsystems for the analysis were marked as "good". We call these runs "good". We loose about 10-20% of the total luminosity because of this requirement. More information about the good run system is given in Reference [95].

3.1 Track Preparation

After the basic algorithm of the track reconstruction has been performed there are a number of additional refinements to the track parameters introduced for the analysis. Some of them are performed during the production stage. Others, are done in a special module called `TrackRefitter` [96, 97] which is applied during the analysis stage. This module takes the raw tracks from COT and refits them introducing the necessary changes.

During the track reconstruction at the production stage, the hits coming from the L00 are not included in the fit, because this tracking subsystem was not yet completely calibrated at the time when this analysis was performed. The `TrackRefitter` also excludes the L00 hits from the fit. Though this is not a change with respect to the production stage, it is an important part of the track treatment at CDF, and we mention it here.

Another feature of the track reconstruction at CDF is the correction of the track parameters for the small non-uniformities in the magnetic field produced by the CDF solenoid, which were well known from Run I [99]. Another effect, related to the magnetic field, is the correction for the nominal value of the field. To take these effects into account, the magnetic field was measured in different places in the solenoid and the data was fit with smooth functions to provide the field map for the whole CDF detector. The full magnetic map is taken into account during the track reconstruction. This correction is performed for all the tracks during the production stage.

The parameters of the tracks in CDF are calculated with respect to the detector coordinate system with the origin in the center of the COT (Section 2.2.1). To obtain a consistent picture from both the COT and the SVX, one needs to take into account possible angular and translational misalignments between the COT and the SVX coordinate systems. These misalignments are found empirically and are corrected for during the track reconstruction. This is mostly done during the production stage and after this we only introduce small corrections for the refinements obtained after the production has run.

And the last, but probably the most important, correction is the correction for the energy loss in the detector material. The CDF detector appears to have more material than it should according to *a priori* tabulations. To obtain the correct parameters of the track one needs to take into account all this material. This is achieved by introducing into GEANT simulation of the detector a number of special cylindrical layers of silicon, so that the integrated effects of the additional detector material on the passing particles would be simulated [96, 97, 98]. The widths of these layers are tuned, so that the Monte Carlo track parameter distributions correspond to that of the tracks in the data. During the production stage the parameters of the tracks are corrected for the presence of these layers, assuming the mass of a charged pion for each track. After the production, during the analysis stage the `TrackRefitter` module performs these corrections for other mass assignments – charged kaon, proton, muon *etc.*

To select only good quality tracks for the analysis we require each track to have r-ϕ hits in at least three distinct SVX layers. As for the COT-related requirements, we want to use only tracks which do not leave the COT before they cross superlayer 6. Also, all the pion tracks used in this analysis must have the total of at least 10 axial hits and at least 10 stereo hits in COT. The transverse momentum p_t of these tracks has to be higher than 400 MeV/c.

3.2 Muon Preparation

The muons in CDF consist of muon stubs from the muon subsystems (CMU, CMP *etc*) matched to COT tracks. These tracks must be the trigger tracks, *i.e.* the XFT must have found them. Though, in our analysis we do not verify explicitly that the muons in the sample satisfy the trigger. Also these tracks must have hits in at least three SVX layers in r-ϕ plane.

We require that in the muons reported by the CMU the stub and the COT track have the matching $\chi^2 < 9$. The muons found in CMP and CMX do not have this requirement, because of the much lower level of noise. Also, there is a cut on the offline p_t of the muons, reconfirming the cut imposed by the XFT, $p_t > 1.5$ GeV/c^2. These cuts are summarized in Table 3.1.

3.3 J/ψ Reconstruction

In our dataset only those events are present which have been collected via the dimuon trigger, *i.e.* which have two muons of the opposite charge satisfying the trigger cuts. These two muons are required to form a J/ψ candidate. The muon tracks in this candidate are forced to come from a common vertex in three dimensions. The parameters of these tracks are adjusted accordingly.

The mass of the J/ψ candidate is required to be within a window of ± 60 MeV/c^2 around the nominal J/ψ mass 3096.87 MeV from the PDG [100]. To have a high-quality μ^+-μ^- vertex we require the χ^2 of the vertex fit to be smaller than 15. The p_t of the μ^+-μ^- system must be greater than 4 GeV/c. The full list of cuts applied to the J/ψ candidates is given in Table 3.1.

3.4 $J/\psi\,\pi^+\pi^-$ Sample

To reconstruct $J/\psi\,\pi^+\pi^-$ candidates, we use the J/ψ candidates constructed out of two muons and two additional oppositely-charged tracks, assigned with the mass of a charged π meson.

Cut	Value
Single muons:	
Number of SVX layers with a hit in r-ϕ plane	> 2
χ^2 for track-stub match (CMU only)	< 9.0
$p_t(\mu)$	> 1.5 GeV/c
$\mu^+\mu^-$ *system:*	
$p_t(\mu^+\mu^-)$	> 4.0 GeV/c
3D vertex fit χ^2 for $\mu^+\mu^-$	< 15
Mass window	$\lvert M(\mu^+\mu^-) - M(J/\psi)\rvert < 60$ MeV/c^2

Table 3.1: The J/ψ reconstruction cuts.

First, the raw mass of the candidate is calculated based on the track momenta, and candidates are only accepted within a loose mass window between the kinematic limit of 3.3 GeV/c^2 and 6.5 GeV/c^2. Then the three-dimensional vertex fit is performed.

The vertex fitting package used in CDF [101] allows one to put constraints on some of the parameters of the fit, *e.g.* to fix the total invariant mass of two tracks or to make track point into a specific place. For the reconstruction of the J/ψ candidates we do not apply any pointing or mass constraints. The only requirement at that point is that the fit converges. For the $\mu^+\mu^-\pi^+\pi^-$ reconstruction, though, we constrain the mass of the dimuon to the PDG value of the J/ψ mass. We want the χ^2 from the vertex fit to be smaller than 25, ensuring the good quality of the vertex.

The $X(3872)$ mesons produced in CDF are highly boosted and its daughter tracks are expected to be relatively close to each other. To suppress background in the $J/\psi\,\pi^+\pi^-$ reconstruction we only consider the pion tracks lying in the narrow cone $\Delta R \equiv \sqrt{\Delta\phi^2 + \Delta\eta^2} < 0.7$ around the momentum of the $X(3872)$ candidate.

We need to correct our data for the acceptance and inefficiency of the detector and selection, and therefore want to stay away from kinematic regions in which the detector's acceptance is low and our modeling of the detector's efficiency is poor. For this reason we impose fiducial cuts $p_t(\psi'/X) > 6$ GeV/c^2 and $|\eta(\psi'/X)| < 0.6$. These cuts keep 66% of the $\psi(2S)$'s.

The final cut values are mostly taken from the analysis presented in Reference [2]. We slightly divert from that analysis by imposing the just described additional fiducial cuts, and by releasing the cut on the number of the candidates per event described in Reference [2]. By releasing this cut we slightly decrease the significance of the $X(3872)$ peak in the full $J/\psi\,\pi^+\pi^-$ sample, but the significance of the $X(3872)$ peak in the $J/\psi\,\pi^+\pi^-$ sample after the cut $m_{\pi\pi} > 500$ MeV/c^2 grows. Because we mostly care about this $m_{\pi\pi}$ range, we choose to release the number of candidates cut in this analysis.

In the analysis presented in Reference [2], the cuts are optimized by improving the signal-to-noise ratio for the $X(3872)$, where the rescaled $\psi(2S)$ signal is used to mimic the $X(3872)$ signal. The final cut values, obtained this way, are summarized in the Table 3.2. This table includes the cuts used for the J/ψ reconstruction already listed in Table 3.1.

The mass distribution of $J/\psi\,\pi^+\pi^-$ after all these cuts is shown in the top part of Figure 3-1. This is the full $J/\psi\,\pi^+\pi^-$ sample which we use for this analysis. For the $X(3872)$ mass measurement we impose another cut, $m_{\pi\pi} > 500$ MeV/c^2, which selects only the most important for the analysis events [2]. The mass distribution of $J/\psi\,\pi^+\pi^-$ after this cut is shown in the

Cut	Value
Pion tracks:	
Number of hits in axial COT superlayers	≥ 10
Number of hits in stereo COT superlayers	≥ 10
Number of SVX layers with a hit in $r-\phi$ plane	> 2
$p_t(\pi)$	> 0.4 GeV/c
Single muons:	
Number of SVX layers with a hit in $r-\phi$ plane	> 2
χ^2 for track-stub match (CMU only)	< 9.0
$p_t(\mu)$	> 1.5 GeV/c
$\mu^+\mu^-$ *system:*	
$p_t(\mu^+\mu^-)$	> 4 GeV/c
3D vertex fit χ^2 for $\mu^+\mu^-$	< 15
Mass window	$\lvert M(\mu^+\mu^-) - M(J/\psi)\rvert < 60$ MeV/c^2
$J/\psi\,\pi^+\pi^-$ *system:*	
ΔR, cone around $X(3872)$ candidate momentum containing both pions	< 0.7
3D vertex fit χ^2 for $J/\psi\,\pi^+\pi^-$	< 25
Fiducial cuts:	
$p_t(J/\psi\,\pi^+\pi^-)$	> 6 GeV/c^2
$\lvert\eta(J/\psi\,\pi^+\pi^-)\rvert$	< 0.6

Table 3.2: The $J/\psi\,\pi^+\pi^-$ reconstruction cuts.

bottom part of Figure 3-1. The second histogram in the lower plot, fitted with dashed line, shows the events rejected by the $m_{\pi\pi}$ cut.

We fit the $J/\psi\,\pi^+\pi^-$ mass distribution using a double Gaussian with a common mean for the $\psi(2S)$ peak and a single gaussian for the $X(3872)$ peak. The background is approximated by a quadratic polynomial $ax^2 + bx + c$, where x stands for the measured $J/\psi\,\pi^+\pi^-$ mass.

The double Gaussian for the $\psi(2S)$ peak is parametrized in the following way:

$$N_{\psi(2S)}\Big[(1-N_{rel})\frac{1}{\sqrt{2\pi}\sigma}\exp\big(-\frac{(x-m_{\psi(2S)})^2}{2\sigma^2}\big)+N_{rel}\frac{1}{\sqrt{2\pi}\sigma_{rel}\sigma}\exp\big(-\frac{(x-m_{\psi(2S)})^2}{2\sigma_{rel}^2\sigma^2}\big)\Big]. \quad (3.1)$$

With this parametrization the fit automatically determines the error on the $\psi(2S)$ yield $N_{\psi(2S)}$. One Gaussian is σ_{rel} times wider than the other one. We call the width of the narrow one, $\sigma_{\text{narrow}} \equiv \sigma$, a *narrow width* and the width of the wide one, $\sigma_{\text{wide}} \equiv \sigma_{rel}\sigma$, a *wide width.* The $m_{\psi(2S)}$ here is a common mean of both Gaussians. All the parameters are floating during the fit.

The fit of the full $J/\psi\,\pi^+\pi^-$ sample yields 11503 ± 221 $\psi(2S)$ candidates and 929 ± 154 $X(3872)$ candidates before the cut on $m_{\pi\pi}$. After the cut, the number of $\psi(2S)$ candidates goes down to 6813 ± 131, while the number of $X(3872)$ candidates grows up to 1262 ± 134. To understand this growth, we fit the $J/\psi\,\pi^+\pi^-$ mass distribution of the events rejected by the cut $m_{\pi\pi} > 500$ MeV/c^2, shown in Figure 3-1. The mass and width of the $X(3872)$ are fixed during this fit. We observe a little depletion of 147 ± 88 candidates in the signal region which is compatible with a background fluctuation. This depletion explains part of the growth in the $X(3872)$ yield. Another reason for the $X(3872)$ yield increase is that the $X(3872)$ width after the $m_{\pi\pi}$ cut also grows from 4.7 to 5.0 MeV/c^2. The complete results of the mass fits for the full sample and for the sample after the $m_{\pi\pi}$ cut are presented in Table 3.3. Table 3.4 gives the full correlation matrices for both fits.

Quantity	No cut on $m_{\pi\pi}$	After cut on $m_{\pi\pi}$	Rejected by cut on $m_{\pi\pi}$
$\psi(2S)$ total yield, $N_{\psi(2S)}$	11503 ± 221	6813 ± 131	5030±208
$\psi(2S)$ mass, $m_{\psi(2S)}$ [MeV/c^2]	3685.9 ± 0.1	3686.0 ± 0.1	3685.9±0.1
$\psi(2S)$ narrow width, σ [MeV/c^2]	2.3 ± 0.3	2.4 ± 0.3	2.9±0.2
$\psi(2S)$ double Gaussian area ratio, N_{rel}	0.37 ± 0.07	0.32 ± 0.09	0.31±0.05
$\psi(2S)$ double Gaussian width ratio, σ_{rel}	2.95 ± 0.27	2.53 ± 0.26	5.00±0.37
$X(3872)$ yield, N_X	929 ± 154	1262 ± 134	-147±88
$X(3872)$ mass, m_X [MeV/c^2]	3873.0 ± 1.0	3872.2 ± 0.6	fixed to 3872.2
$X(3872)$ width, σ_X [MeV/c^2]	4.7 ± 0.7	5.0 ± 0.6	fixed to 5.0
Fit χ^2	116.3	78.2	40.4
Number of degrees of freedom	73	61	70
$S/\sqrt{B}$ for $X(3872)$ in mass region $(3.858, 3.886)$ GeV/c^2	7.9	9.9	–

Table 3.3: The results of the fit in Figure 3-1 (statistical errors only).

The *residuals* of the fit, which are the differences between the fitted distribution and the data, divided by the error on the fitted distribution are shown in Figure 3-2. The upper-left plot has no cut on $m_{\pi\pi}$, the upper-right plot has a cut of $m_{\pi\pi} > 500$ MeV/c^2. The vertical lines on the upper

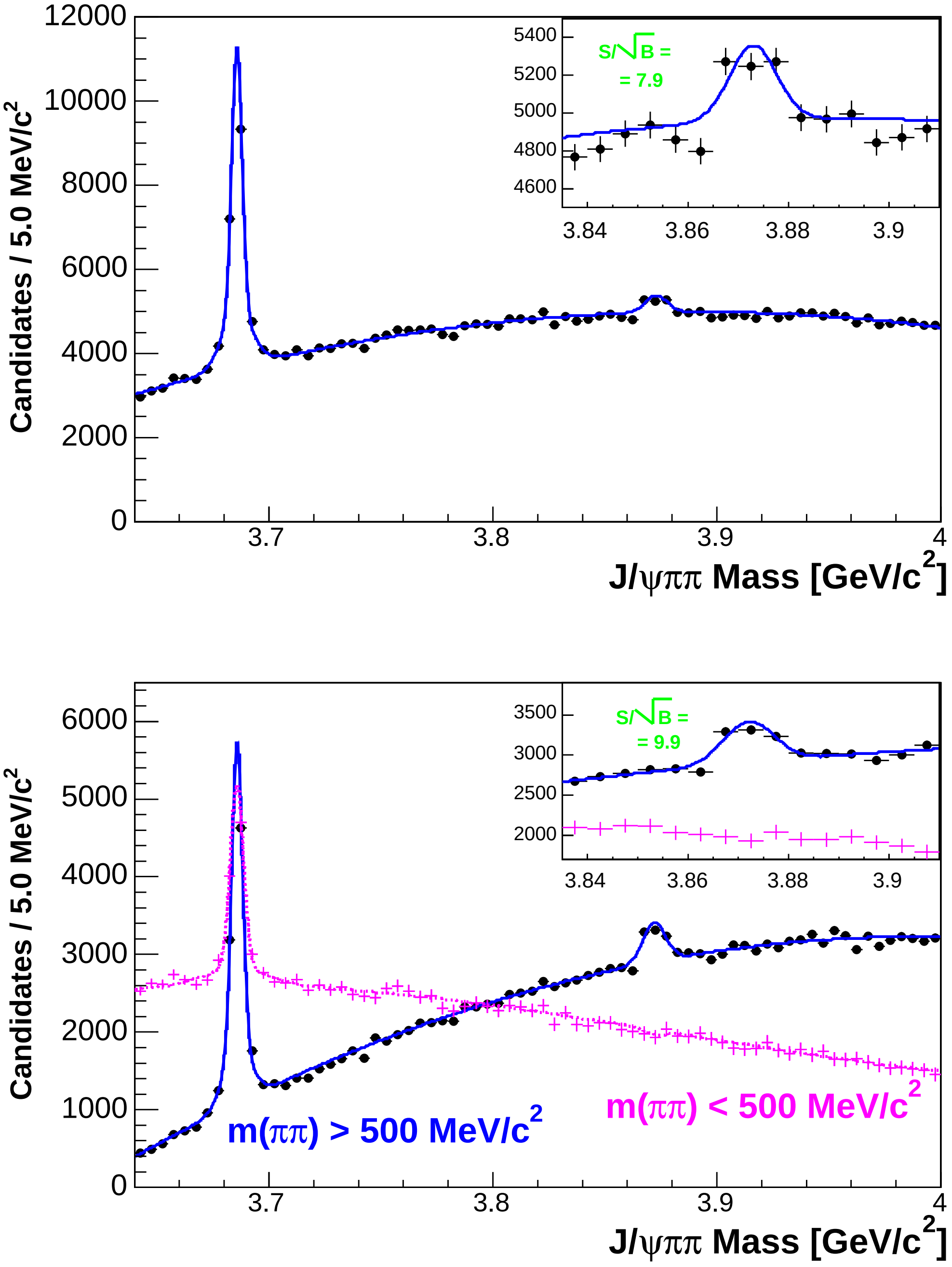

Figure 3-1: Mass distributions of the $J/\psi\,\pi^+\pi^-$ sample after fiducial cuts without (top) and with (bottom) a $m_{\pi\pi} > 500$ MeV$/c^2$ cut.

Full-sample fit:

PARAMETER		CORRELATION COEFFICIENTS										
NAME	NO.	1	2	3	4	5	6	7	8	9	10	12
$N_{\psi(2S)}$	1	1.000	0.163	0.253	0.032	0.001	0.014	0.085	-0.007	-0.081	-0.217	0.407
$m_{\psi(2S)}$	2	0.163	1.000	0.772	0.008	0.000	0.004	0.013	-0.002	-0.012	-0.656	-0.299
σ	3	0.253	0.772	1.000	0.012	0.000	0.005	0.024	-0.003	-0.023	-0.927	-0.222
N_X	4	0.032	0.008	0.012	1.000	0.077	0.430	-0.070	-0.003	0.069	-0.010	0.016
m_X	5	0.001	0.000	0.000	0.077	1.000	0.176	-0.011	0.000	0.009	-0.000	0.000
σ_X	6	0.014	0.004	0.005	0.430	0.176	1.000	-0.032	-0.001	0.032	-0.004	0.007
a	7	0.085	0.013	0.024	-0.070	-0.011	-0.032	1.000	-0.893	0.594	-0.021	0.048
b	8	-0.007	-0.002	-0.003	-0.003	0.000	-0.001	-0.893	1.000	-0.892	0.002	-0.004
c	9	-0.081	-0.012	-0.023	0.069	0.009	0.032	0.594	-0.892	1.000	0.020	-0.046
N_{rel}	10	-0.217	-0.656	-0.927	-0.010	-0.000	-0.004	-0.021	0.002	0.020	1.000	-0.028
σ_{rel}	12	0.407	-0.299	-0.222	0.016	0.000	0.007	0.048	-0.004	-0.046	-0.028	1.000

χ^2/DoF = 116.295/73, Prob = 0.0665231%

After $m_{\pi\pi} > 500$ MeV/c^2:

PARAMETER		CORRELATION COEFFICIENTS										
NAME	NO.	1	2	3	4	5	6	7	8	9	10	12
$N_{\psi(2S)}$	1	1.000	0.107	0.188	0.027	0.002	0.015	0.157	-0.007	-0.162	-0.176	0.430
$m_{\psi(2S)}$	2	0.107	1.000	0.662	0.006	0.001	0.003	0.013	-0.001	-0.013	-0.566	-0.053
σ	3	0.188	0.662	1.000	0.009	0.001	0.005	0.040	-0.002	-0.041	-0.930	0.098
N_X	4	0.027	0.006	0.009	1.000	0.170	0.534	-0.118	-0.000	0.111	-0.008	0.019
m_X	5	0.002	0.001	0.001	0.170	1.000	0.298	-0.028	0.001	0.027	-0.001	0.001
σ_X	6	0.015	0.003	0.005	0.534	0.298	1.000	-0.069	0.000	0.065	-0.005	0.010
a	7	0.157	0.013	0.040	-0.118	-0.028	-0.069	1.000	-0.753	0.122	-0.040	0.118
b	8	-0.007	-0.001	-0.002	-0.000	0.001	0.000	-0.753	1.000	-0.744	0.002	-0.005
c	9	-0.162	-0.013	-0.041	0.111	0.027	0.065	0.122	-0.744	1.000	0.041	-0.123
N_{rel}	10	-0.176	-0.566	-0.930	-0.008	-0.001	-0.005	-0.040	0.002	0.041	1.000	-0.350
σ_{rel}	12	0.430	-0.053	0.098	0.019	0.001	0.010	0.118	-0.005	-0.123	-0.350	1.000

χ^2/DoF = 78.2306/61, Prob = 6.57205%

Table 3.4: The full correlation matrices for the combined $\psi(2S)$ and $X(3872)$ mass fits.

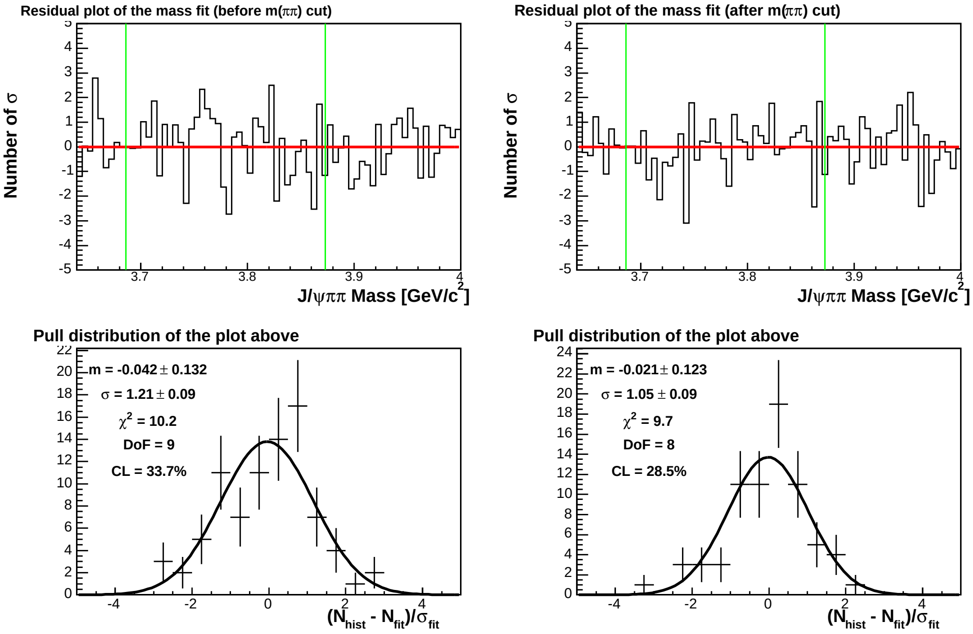

Figure 3-2: The residual plots and the pull distributions of the mass fits in Figure 3-1.

plots display the positions of the $\psi(2S)$ and the $X(3872)$ peaks. The bottom plots represent the *pull distributions* which show how many standard deviations the data points in each bin are away from the expected values of the fit. The pull distributions are fitted with Gaussians which, for correct statistical behavior, ought to have a mean of zero and a width of one. As we can see, the fitted values are consistent with these ideal quantities, which indicates that the fits describe the data well.

The $X(3872)$ mass measured in our sample (after $m_{\pi\pi}$ cut) is equal to

$$m_{X(3872)} = 3872.2 \pm 0.6(\text{stat.})\ \text{GeV}/c^2.$$

This result is consistent with the values obtained in other measurements [1, 2, 3, 4].

Chapter 4

Dipion Mass Spectrum Measurement

As we can see in Figure 3-1, the combinatorial background in the $J/\psi\,\pi^+\pi^-$ sample is quite high. For this reason the $m_{\pi\pi}$ distribution obtained with a conventional sideband-subtraction technique would have large errors and, therefore, poorly constrained its shape. We use a different method to measure the $m_{\pi\pi}$ spectrum. We divide our sample into slices of the dipion mass, fit the mass histogram of $J/\psi\,\pi^+\pi^-$ candidates in each slice and plot the dependence of the yield versus $m_{\pi\pi}$.

The $J/\psi\,\pi^+\pi^-$ mass distribution has two peaks: the larger one corresponds to the $\psi(2S)$ and the smaller one to the $X(3872)$. Our goal is to obtain the $m_{\pi\pi}$ spectrum for the $X(3872)$, and we use the $\psi(2S)$ as a well-studied convenient testbed with a large number of events. For this reason, we first apply our slicing method to the $\psi(2S)$ and compare its $m_{\pi\pi}$ spectrum to the equivalent spectra obtained in other experiments. Then we apply the same technique to the $X(3872)$.

The produced $X(3872)$ and $\psi(2S)$ mesons are not always registered in the detector. Sometimes their daughter tracks lie outside of the regions where they can be found by the detector tracking systems, *i.e.* outside of the detector *acceptance*. This is true, for example, for the tracks with very low p_t or very high $|\eta|$. Also, the tracks inside the detector acceptance regions may be not registered properly, due to the imperfect *efficiency* of the detector. To compare our $m_{\pi\pi}$ spectrum to the spectra obtained in other experiments, we need to take these effects into account. This is done with the aid of Monte Carlo simulation of the detector's efficiency in the acceptance region. We generate Monte Carlo samples of the events before detector effects and after the detector is simulated, and calculate the detector's efficiency for each $m_{\pi\pi}$ slice. For this analysis it is important that the p_t, η, and $m_{\pi\pi}$ distributions of the $\psi(2S)$ and the $X(3872)$ in the data are properly described by the Monte Carlo simulation.

The following few subsections describe how we measure the p_t spectra for both $\psi(2S)$ and $X(3872)$, how we generate the Monte Carlo samples using these spectra, and how we calculate the detector efficiency corrections. Then we describe how we fit the $J/\psi\,\pi^+\pi^-$ mass histograms in the $m_{\pi\pi}$ slices, obtain the $m_{\pi\pi}$ spectrum, and apply the efficiency corrections to it.

4.1 Measurement of the p_t Spectra

The p_t spectrum for the $\psi(2S)$ is fairly well studied, but is *a priori* unknown for the $X(3872)$. If the $X(3872)$ is a charmonium state one might be prepared to accept using the $\psi(2S)$ p_t distribution, but we cannot assume that. If, for example, the $X(3872)$ is a fragile molecular state, it could have a quite different p_t spectrum, as it tends to be more difficult to make complex and weakly bound states in hard fragmentation. For this reason we obtain the p_t spectrum for the $X(3872)$ from the data, independently of the one for the $\psi(2S)$.

Our data sample has a large number of $\psi(2S)$ mesons, so that it is easy to obtain the $\psi(2S)$ p_t spectrum by a regular sideband-subtraction technique. But for the $X(3872)$ it is not so easy, because of the low event yields and the large combinatorial background. We divide our data into a few p_t slices and do a binned likelihood fit of the $J/\psi\,\pi^+\pi^-$ mass distribution in each of them, with the fitting function being integrated over the bin range. In this way we obtain the $\psi(2S)$ and the $X(3872)$ yields for each p_t slice. The individual mass fits for the $\psi(2S)$ are given in Appendix A, and for the $X(3872)$ in Appendix B.

Figure 4-1 displays the sliced p_t spectra, overlaid on top of the sideband-subtracted ones, in both normal and logarithmic scales. The spectra are normalized to have the same number of events. We find that the slicing technique reduces the uncertainties compared to the sideband subtraction – by about 10-20% for the $\psi(2S)$ and by about 50-60% for the $X(3872)$.

The $\psi(2S)$ and $X(3872)$ p_t spectra are overlaid on top of each other in Figure 4-2 in both linear and logarithmic scales. As we can see, they are the same within the uncertainties. We use the respective p_t spectra to derive the input for the Monte Carlo generation for the $\psi(2S)$ and the $X(3872)$.

4.2 Detector Efficiency Corrections

In our Monte Carlo simulation the $X(3872)$ particle is generated by a program, called HeavyQuarkGen [102] developed in CDF, and then decayed with the QQ [103] program, created in CLEO. The decay products are put through a special filter (`HepgFilter` [104]), which uses generator level information without taking into account the detector smearing, efficiency *etc.* This filter keeps only the events with the $X(3872)$ decay products within the *fiducial* region, which means that the particles should have $p_t > 1.4$ GeV/c and low pseudorapidity $|\eta|$. The latter requirement translates into a cut on the distance from the beamline to the point at which the particle crosses the COT end cap, *i.e.* the *exit radius* from the COT of $R_{exit} > 1010$ mm. For the Monte Carlo generation most of the unknown $X(3872)$ properties are taken from the $\psi(2S)$, except for the mass, of course. The details of Monte Carlo generation are given in Appendix C, similar to Reference [76].

We need to make sure that the Monte Carlo sample kinematically reflects the data, *i.e.* has the same p_t and η distributions. To do this we start generating Monte Carlo samples with a flat p_t-η distribution. Each event goes through the GEANT simulation of the detector, the simulation of the trigger, production and the reconstruction code. The output p_t distribution is an *efficiency curve* for the detector. For each p_t bin it gives the fraction of the $\psi(2S)$'s or $X(3872)$'s initially generated in the fiducial volume in which all the daughter tracks are registered by the detector and reconstructed in our analysis.

To avoid using the bins with low number of events, and keep the true distributions reasonable and trustworthy, we constrain ourselves to the region $p_t(\psi(2S)) > 6$ GeV/c^2 and $p_t(X(3872)) > 6$ GeV/c^2. The pseudorapidities of both $\psi(2S)$ and $X(3872)$ are also constrained to $|\eta| < 0.6$. The true η distribution is considered flat within this region. The histograms for the Monte Carlo generation are produced in a little bit wider region $p_t > 5$ GeV/c^2 and $|\eta| < 0.7$ to allow for smearing at the boundaries. These additional margins are chosen to be significantly larger than the resolutions on p_t and η.

We want to make sure that the $m_{\pi\pi}$ distribution in the Monte Carlo simulation adequately

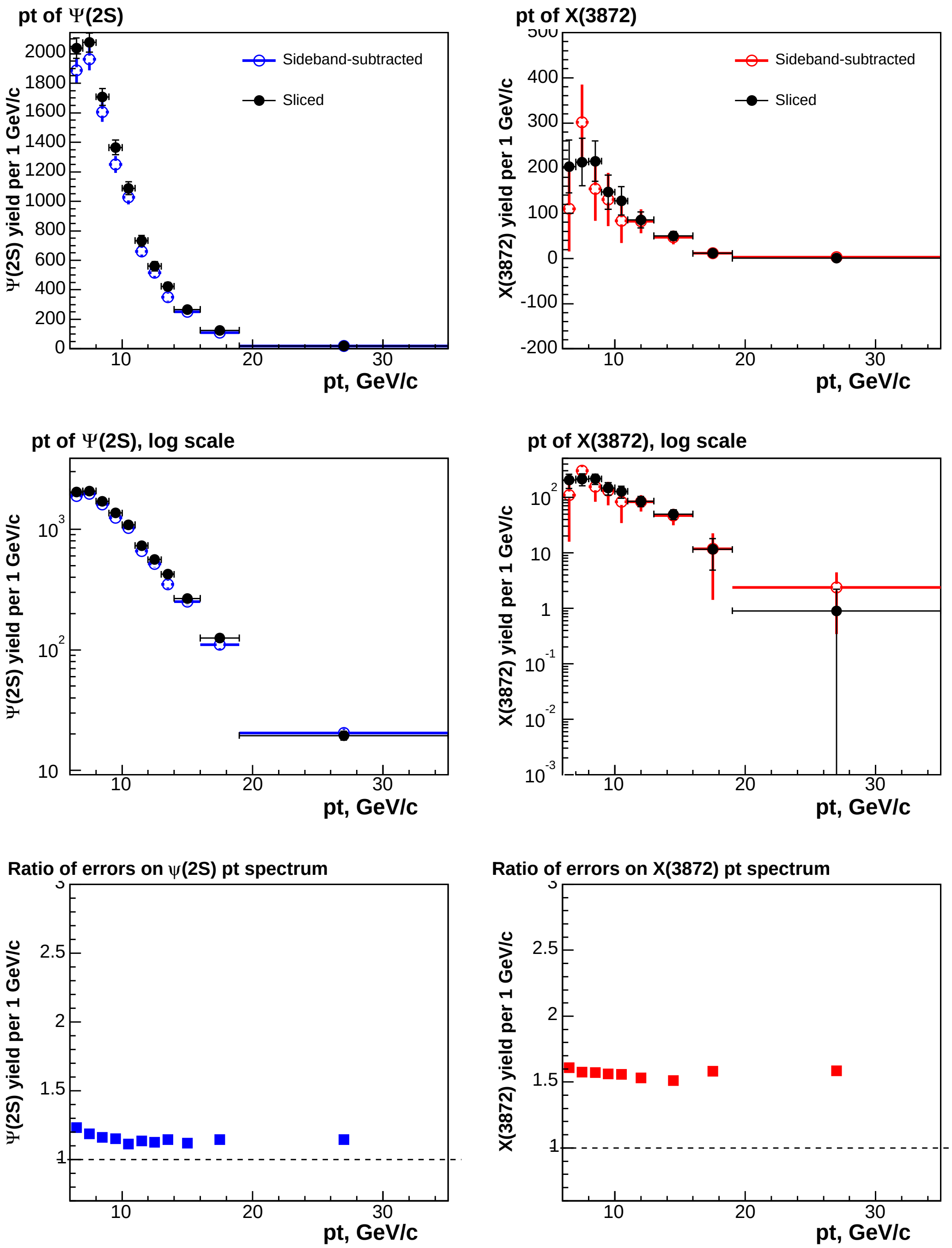

Figure 4-1: The p_t spectra of the $\psi(2S)$ (left) and the $X(3872)$ (right) obtained with regular sideband-subtraction and with the slicing technique on linear (top) and logarithmic (middle) scales. Bottom: the ratio of the uncertainties obtained with these two methods.

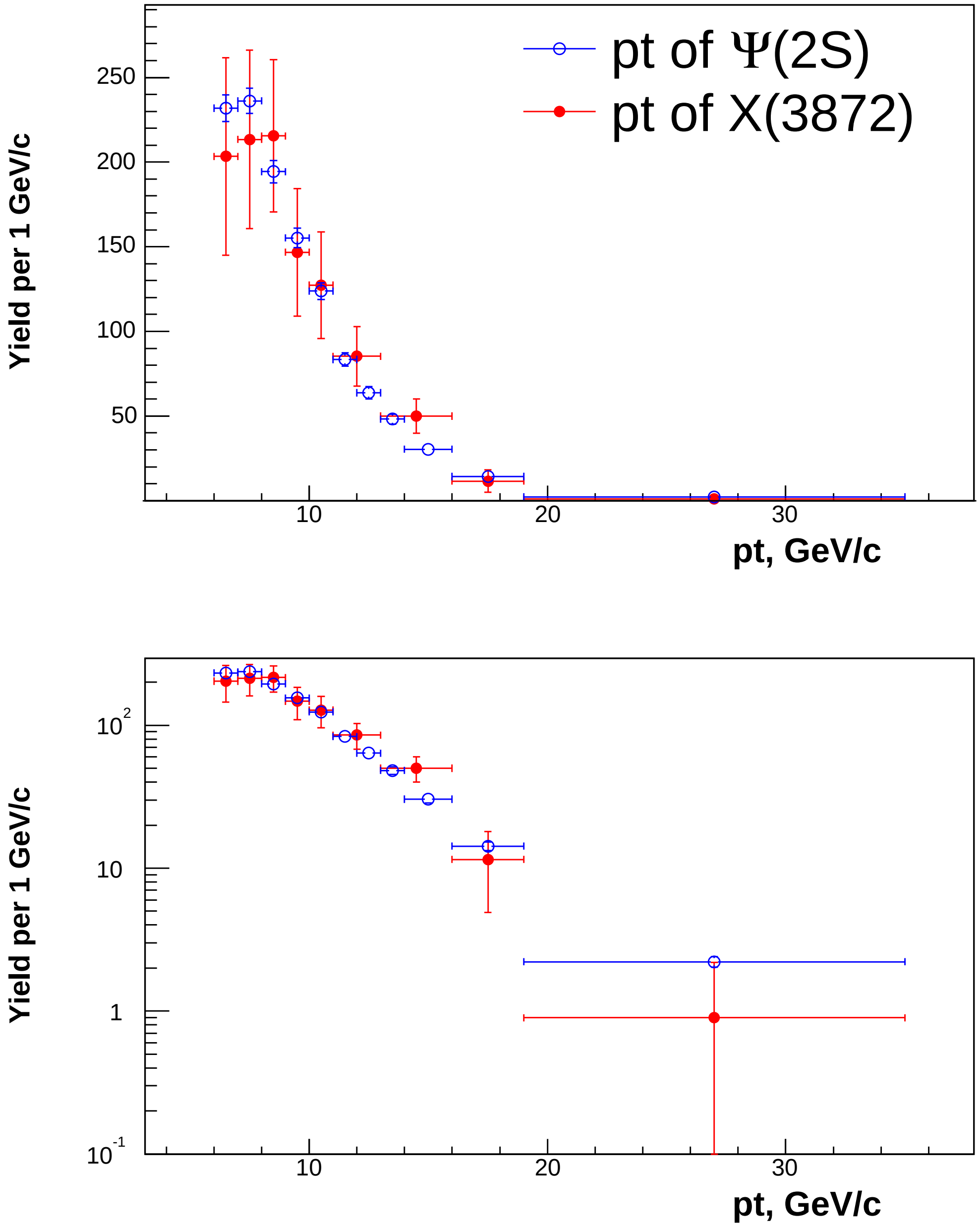

Figure 4-2: The $\psi(2S)$ and $X(3872)$ “sliced” p_t-spectra overlaid on top of each other on linear (top) and logarithmic (bottom) scales. The $\psi(2S)$ p_t spectrum is normalized to the same number of candidates as the $X(3872)$ one.

describes the data. The shape of the $m_{\pi\pi}$ spectrum for the $\psi(2S)$ decay is well known from measurements. We call this shape *S-wave*, because the $\psi(2S)$ is a $^3S_1$ charmonium state. A good description for it is given by:

$$\frac{dN}{dm_X} \sim (m_{\pi\pi}^2 - 4m_\pi^2)^{2.5}\sqrt{(m_{\psi(2S)}^2 - m_{J/\psi}^2 - m_{\pi\pi}^2)^2 - 4m_{J/\psi}^2 m_{\pi\pi}^2}. \tag{4.1}$$

This parametrization was used, in particular, in a CDF Run I analysis [105] and by the MARK III Collaboration [106]. While we know the shape of the $m_{\pi\pi}$ distribution for the $\psi(2S)$, it is *a priori* unknown for the $X(3872)$ – this is what we wish to determine in this analysis. So, to generate the proper Monte Carlo $m_{\pi\pi}$ spectrum for the $X(3872)$ we have to bootstrap ourselves by feeding our measured $m_{\pi\pi}$ distribution into the Monte Carlo and then iterating, to obtain a better approximation. It is reasonable to use the S-wave $m_{\pi\pi}$ spectrum as an input for the first iteration. It turns out that this shape is a quite good approximation already. For this reason we do not actually iterate and simply use the S-wave parametrization for the $m_{\pi\pi}$ spectrum of the $X(3872)$. We will assign a systematic uncertainty to our imperfect knowledge of the true shape of the $m_{\pi\pi}$ distribution.

The ratios of the measured p_t-distributions for the $\psi(2S)$ and the $X(3872)$ to the efficiency curves give us the *true* p_t spectra, not distorted by the detector effects and by our selection. In Figures 4-3 (for the $\psi(2S)$) and 4-4 (for the $X(3872)$) the upper-left plot represents the raw measured p_t, the upper-right plot the efficiency curve, and the two lower plots their ratio (true p_t) in linear and logarithmic scales. The true p_t-distributions for both the $\psi(2S)$ and the $X(3872)$ are parametrized by the function $\exp(a_0 + a_1(p_t - p_{t0}) + a_2(p_t - p_{t0})^2)$, where p_{t0} is a convenient expansion point of the polynomial exponent. This point is chosen to minimize the correlation amongst the fit parameters, *i.e.* it is near the p_t-centroid of the data. The parameter a_0 is a normalization and has no physical meaning. The parameters a_1 and a_2 determine the shape of the p_t spectrum. The fits are also given in Figures 4-3 (for the $\psi(2S)$) and 4-4 (for the $X(3872)$).

We use the result of these fits to produce new p_t-η histograms, which correspond to the true p_t-η distributions. These new histograms are used in HeavyQuarkGen to generate a new set of Monte Carlo samples. In these samples the output p_t and η spectra are quite close to the measured ones, as shown in Figures 4-5 and 4-6. In principle, this process may be repeated a few times in an attempt to achieve even better coincidence of Monte Carlo and data. But the next iterations are not very much different from the last one, so that we stop here.

Having matched the p_t and η distributions for both the $\psi(2S)$ and the $X(3872)$, and the $m_{\pi\pi}$ distribution for the $\psi(2S)$ in Monte Carlo and in data, we calculate the detector efficiency for the $m_{\pi\pi}$ spectrum. Actually, we obtain the *inverse* detector efficiency, $\xi(m_{\pi\pi})$, which we find more convenient to use than the detector efficiency $\epsilon = 1/\xi(m_{\pi\pi})$. To find the $\xi(m_{\pi\pi})$ we divide the $m_{\pi\pi}$ distribution before the detector $\zeta(m_{\pi\pi})$ by the $m_{\pi\pi}$ distribution after the detector and trigger simulation, production, reconstruction, and selection cuts, $\overline{\zeta}(m_{\pi\pi})$. We use a quadratic polynomial $\xi(m_{\pi\pi})$ to parametrize this ratio.

All these distributions and functions are shown in Figure 4-7 for both the $\psi(2S)$ and the $X(3872)$. Each plot in this figure shows the $m_{\pi\pi}$ spectra before (triangles) and after (boxes) detector simulation and event selection. The solid dots with error bars give the ratio of the former to the latter (*i.e.* the inverse efficiency). This ratio is to be read on the scale at the right-hand side of the plot. The fitting quadratic function $\xi(m_{\pi\pi})$ of this ratio (dashed line) is also shown in each plot. The parameters of the fits are given in Table 4.1. These respective functions $\xi(m_{\pi\pi})$ are used to correct the raw $m_{\pi\pi}$ spectra for the $\psi(2S)$ and the $X(3872)$.

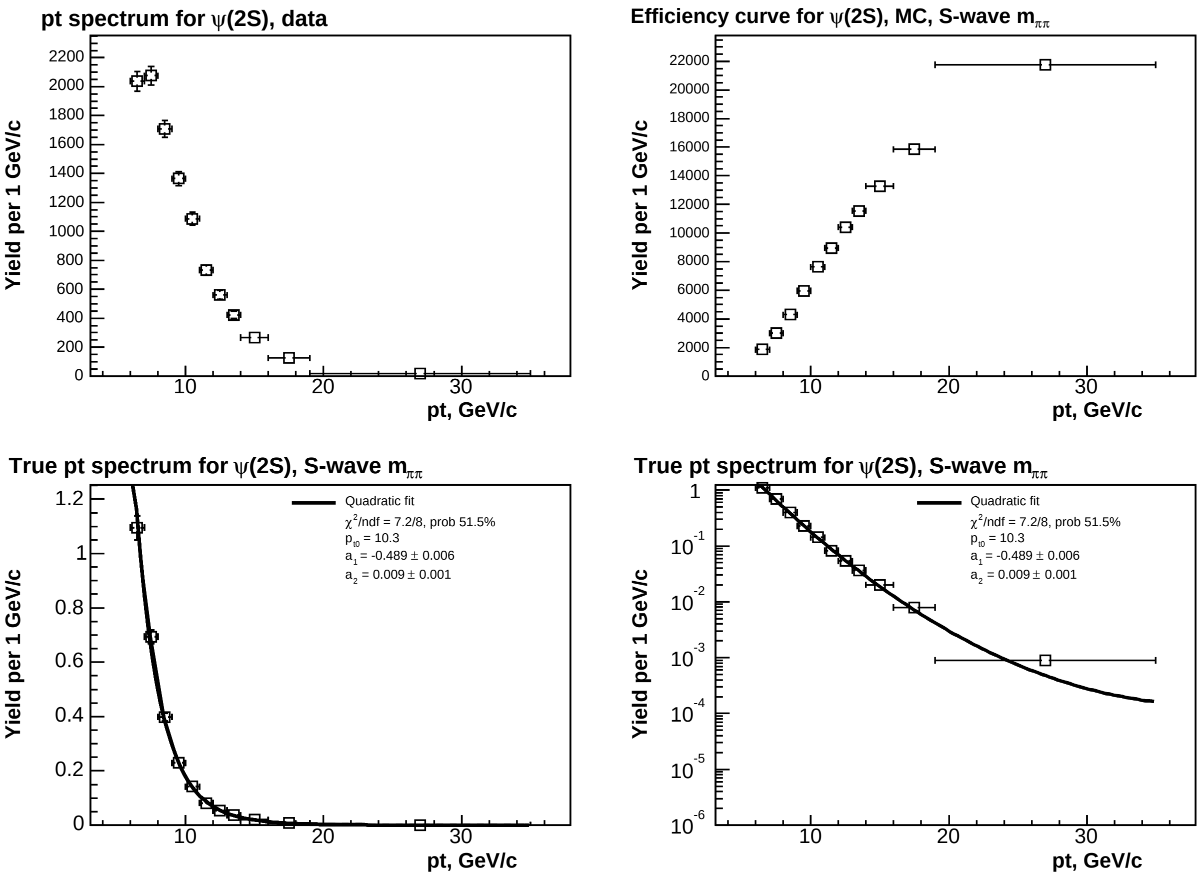

Figure 4-3: The p_t distributions of $\psi(2S)$. Upper-left plot: raw data. Upper-right plot: the detector efficiency curve. Two lower plots are the ratio of the data and the efficiency curve in both linear and logarithmic scales. The $m_{\pi\pi}$ parametrization for Monte Carlo simulation in this figure is S-wave (Equation 4.1).

4.3 Measurement of the $m_{\pi\pi}$ Spectrum for the $\psi(2S)$

To obtain the $m_{\pi\pi}$ spectrum for the $\psi(2S)$ we do a bin-integrated likelihood fit of the $J/\psi\,\pi^+\pi^-$ mass histogram in each $m_{\pi\pi}$ slice. To fit the signal we use the same function as for the mass fit of the full sample, a double Gaussian for the $\psi(2S)$ and a single Gaussian for the $X(3872)$. Because we are subdividing our sample, each slice will have a considerably reduced number of events, and thus larger uncertainties. We stabilize the results by fixing mass and width parameters of the slice fits to the values obtained in full-sample fits for the $\psi(2S)$, and for the $X(3872)$ to the values from the fits of the sample after the $m_{\pi\pi} > 500$ MeV$/c^2$ cut.

The double Gaussian for the $\psi(2S)$ is parametrized in the form of Equation 3.1. The common mean and the widths of both Gaussians, σ and $\sigma\sigma_{rel}$, are fixed to the values obtained from the full-sample fit. Their relative normalization, N_{rel}, is also fixed to the value extracted from the same source. The total area of both Gaussians $N_{\psi(2S)}$ is allowed to be both positive and negative, to take into account possible negative fluctuations in the background dominated fits, and thereby not bias the yield. The $J/\psi\,\pi^+\pi^-$ background is parametrized with the following function:

$$A \cdot \frac{(\alpha+1)(x-x_0)^{\alpha}}{(x_{up}-x_{low})^{\alpha+1}} \cdot \frac{\beta e^{-\beta x}}{e^{-\beta x_{low}} - e^{-\beta x_{up}}}, \tag{4.2}$$

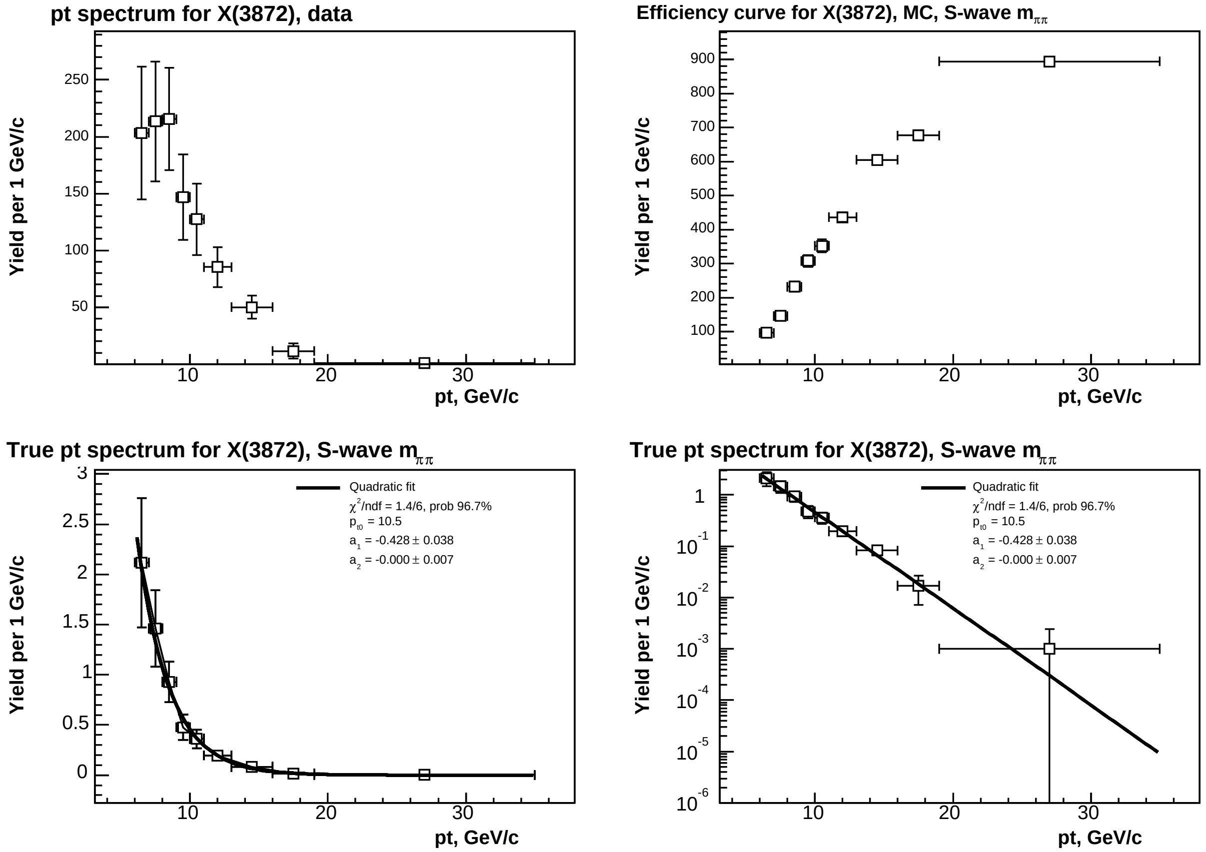

Figure 4-4: The p_t distributions of $X(3872)$. Upper-left plot: raw data. Upper-right plot: the detector efficiency curve. Two lower plots are the ratio of the data and the efficiency curve in both linear and logarithmic scales. The $m_{\pi\pi}$ parametrization for Monte Carlo simulation in this figure is S-wave (Equation 4.1).

where x stands for the $J/\psi\,\pi^+\pi^-$ invariant mass, A is a normalization coefficient, α and β are shape parameters and x_0 is a turn-on parameter. The background is set to be equal to zero for values of $x < x_0$. This turn-on value is constrained to be close to the kinematic limit "$M_{J/\psi}$ + minimum $m_{\pi\pi}$" for each $m_{\pi\pi}$ slice. The parameters A, α and β float freely in the fit. The parameters x_{up} and x_{low} denote the upper and the lower boundary for the fit and are fixed for each individual mass fit. The expressions in the denominator are introduced to normalize the power function and the exponent.

The $J/\psi\,\pi\pi$ mass fits for the $\psi(2S)$ in each $m_{\pi\pi}$ slice are given in Appendix D. The fit range normally starts 100 MeV/c^2 below the mass of $\psi(2S)$, and is kept to be 200 MeV/c^2 wide. However, as we move to higher $m_{\pi\pi}$, the kinematic threshold increases and when the turn-on reaches the window the right boundary increases correspondingly to maintain a 200 MeV/c^2 window with data in it. The last few $m_{\pi\pi}$ slices have a somewhat smaller fit window, 180 MeV/c^2, to avoid fitting the $X(3872)$ peak. We always ensure that the fit range starts and ends at the bin boundaries.

The first five $m_{\pi\pi}$ slices are 20 MeV/c^2 wide in an effort to pool together the data and to be sensitive to the low $\psi(2S)$ yield at low $m_{\pi\pi}$ values. Most of the rest of the slices after the first five are 10 MeV/c^2 wide, giving reasonable yields and maintaining fairly fine resolution. The exception is the few last slices, which are made 5 MeV/c^2 wide to better resolve the rapid

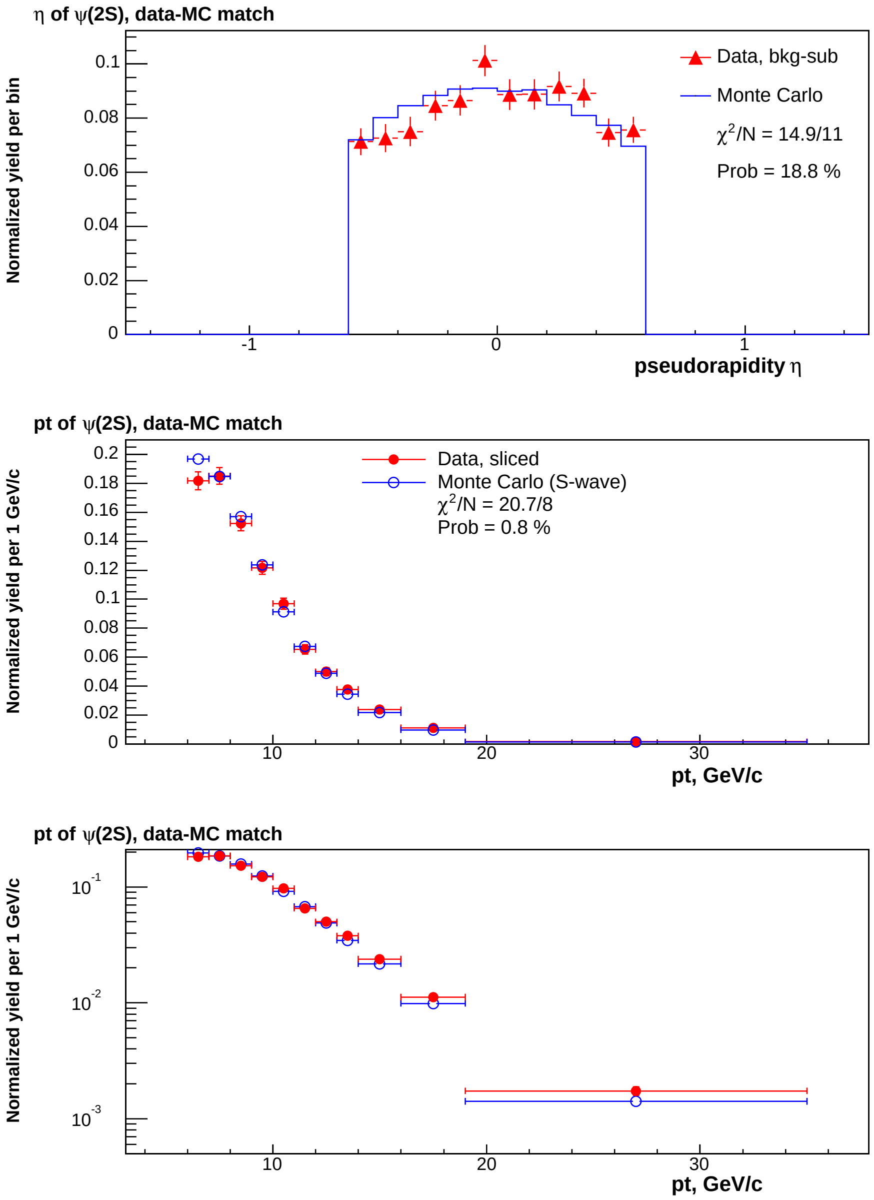

Figure 4-5: Top: comparison between the η distributions of $\psi(2S)$ in raw data and after Monte Carlo simulation, generated with S-wave $m_{\pi\pi}$ parametrization (Equation 4.1); middle and bottom: the comparison between the p_t distributions in linear and logarithmic scales.

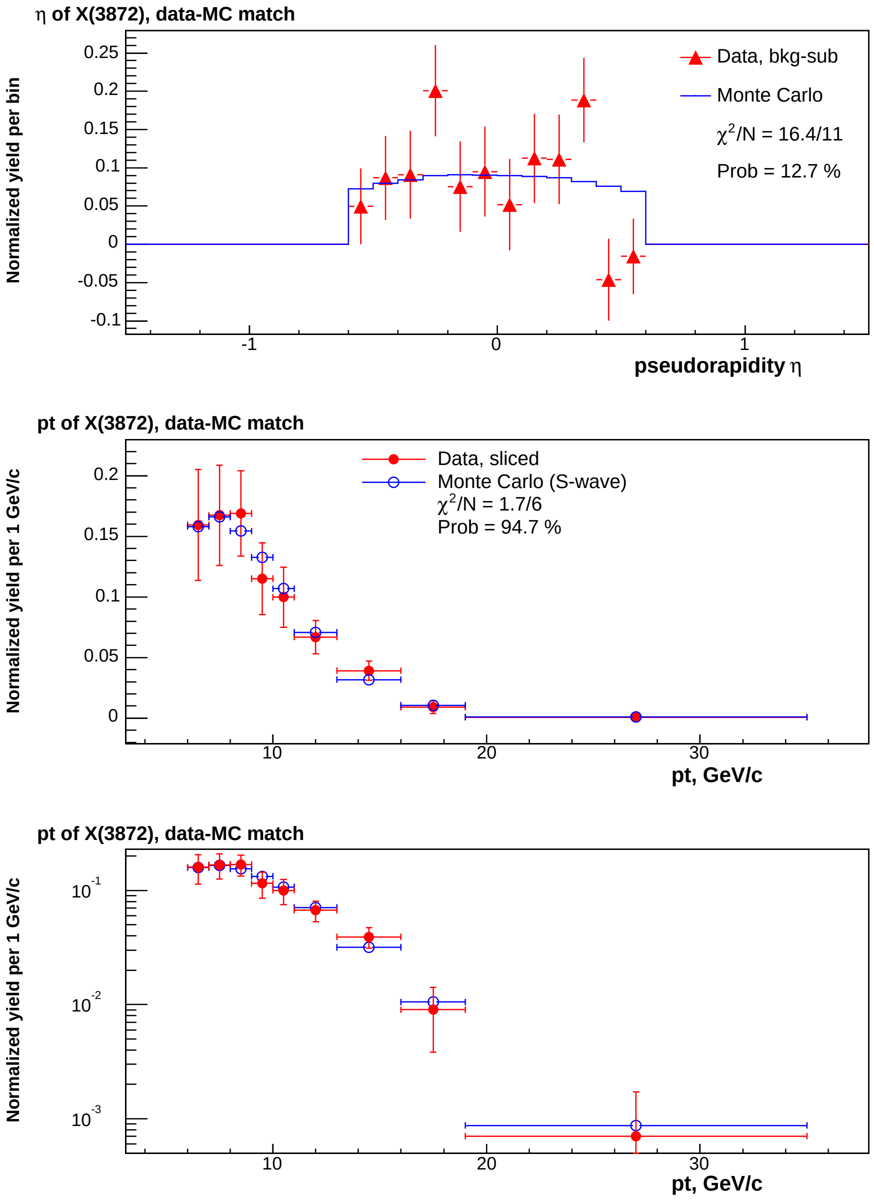

Figure 4-6: Top: the comparison between the η distributions of the $X(3872)$ in raw data and after Monte Carlo simulation, generated with S-wave $m_{\pi\pi}$ parametrization (Equation 4.1); middle and bottom: the comparison between the p_t distributions in linear and logarithmic scales.

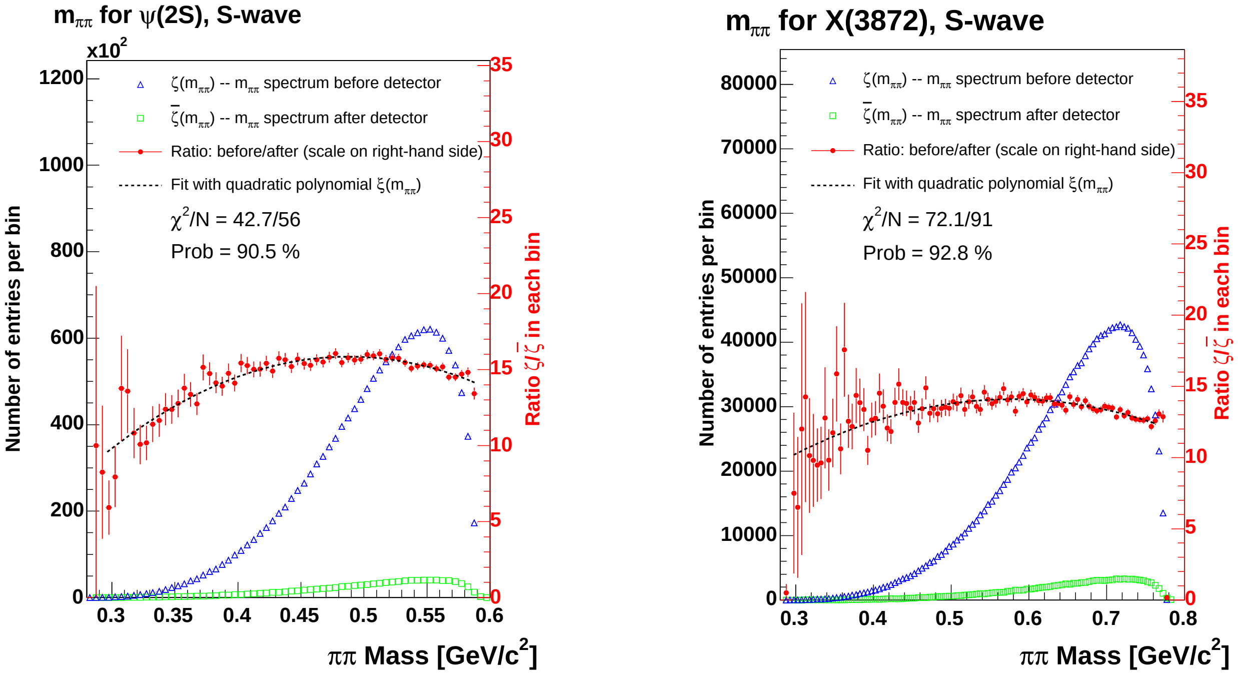

Figure 4-7: The ratios (points) of pre-detector (triangles) to post-detector (boxes) $m_{\pi\pi}$ distributions (*i.e. inverse* efficiency) for the $\psi(2S)$, left; and for the $X(3872)$, right.

	$\psi(2S)$	$X(3872)$
$\xi^{(0)}$	-24.80±2.71	-2.51±1.71
$\xi^{(1)}$	166.54±11.38	57.51±5.62
$\xi^{(2)}$	-170.60±11.79	-49.79±4.57

Table 4.1: The parameters of the fitted inverse detector efficiency correction functions $\xi(m_{\pi\pi}) = \xi^{(0)} + \xi^{(1)} m_{\pi\pi} + \xi^{(2)} m_{\pi\pi}^2$ for both the $\psi(2S)$ and the $X(3872)$.

fall-off of the spectrum. The normalization to 10 MeV/c^2 per slice is chosen to give the reader the generally correct impression of the total raw yields over most of the slices.

We fix the means and widths for most of the $\psi(2S)$ fits in order to better constrain the results. Though for the last two slices they are allowed to float, because of the following reason. By taking a slice of data near the upper kinematic limit we are potentially biasing the $J/\psi\,\pi^+\pi^-$ mass. A candidate that has fluctuated to a high value of $m_{\pi\pi}$ most likely will also have a high $J/\psi\,\pi^+\pi^-$ mass. In normal slices candidates can fluctuate in and out of the slice from both low and high mass slices. In the slices near the kinematic limit, though, entries are only lost to the low side. This results in a shift in the peak position. Appendix F describes this in more detail.

Another effect, unique to the last few slices near the kinematic limit, is that the turn-on is very close to the peak, so that it becomes hard for the fitter to determine the position of the turn-on precisely. In Chapter 5 we will assign a systematic uncertainty due to this effect. Also, in the last slice the turn-on comes so closely to the peak that the peak shape is distorted. For this reason we fit it with a single Gaussian rather than the double one. This effect is also taken into account with a systematic uncertainty. This is discussed into more detail in Appendix F.

We calculate the fit probabilities in the individual $m_{\pi\pi}$ slices for the full fit range. They are shown in Figure 4-8. The points on this plot are uniformly scattered, producing neither trends nor clusters. The fit probability for the full fit range is generally dominated by the background distribution. For this reason we also compute the probability in the narrow region between 3.675 GeV/c^2 and 3.695 GeV/c^2, roughly corresponding to a six standard deviations window centered around the $\psi(2S)$ mass value. This probability shows how well the $\psi(2S)$ peak itself is described. The probability for each $m_{\pi\pi}$ slice is shown in Figure 4-9. This plot also manifests a quite uniform distribution of the points.

The resulting plot of the yield versus $m_{\pi\pi}$ for $\psi(2S)$ is given in Figure 4-10, both before and after the detector efficiency corrections. The efficiency corrections have a quite small effect over the range where the $\psi(2S)$ yield is significant. The yields after the correction in the i-th $m_{\pi\pi}$ slice are obtained by multiplying the yield before correction, N_i, by the integrated-average, ξ_i, of the nominal correction function, $\xi(m_{\pi\pi})$, over the i-th $m_{\pi\pi}$ slice range:

$$N_i^{corr} = N_i \cdot \frac{1}{b_i - a_i} \int_{a_i}^{b_i} \xi(m_{\pi\pi})\, dm_{\pi\pi} = N_i \cdot \xi_i. \tag{4.3}$$

Here a_i and b_i denote the lower and upper boundaries of the i-th $m_{\pi\pi}$ slice. The inverse efficiency correction factors, ξ_i, are globally rescaled as to preserve the *total* number of candidates. The same data in tabular form are given in Chapter 5 (Table 5.1) after the determination of the systematic uncertainties.

One should notice that our $m_{\pi\pi}$ spectrum for the $\psi(2S)$ after the detector efficiency correction matches the S-wave parametrization from Equation 4.1 quite well, as shown in Figure 4-11. In Chapter 5 we assign the systematic uncertainties due to our imperfect knowledge of the $m_{\pi\pi}$ shape for the Monte Carlo generation.

4.4 Measurement of the $m_{\pi\pi}$ Spectrum for the $X(3872)$

We apply the same fitting procedure to obtain the $m_{\pi\pi}$ spectrum for the $X(3872)$. We change the binning of the $J/\psi\,\pi^+\pi^-$ mass histograms from 2.5 MeV per bin to 5.0 MeV per bin because we have a weaker and broader signal. For the same reason we fit the signal with a single Gaussian

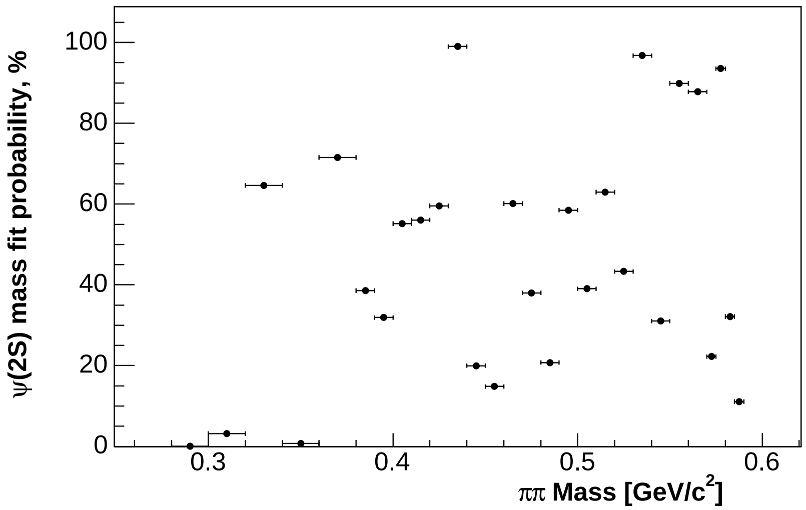

Figure 4-8: The $\psi(2S)$ mass fit probability for the full mass range versus $m_{\pi\pi}$.

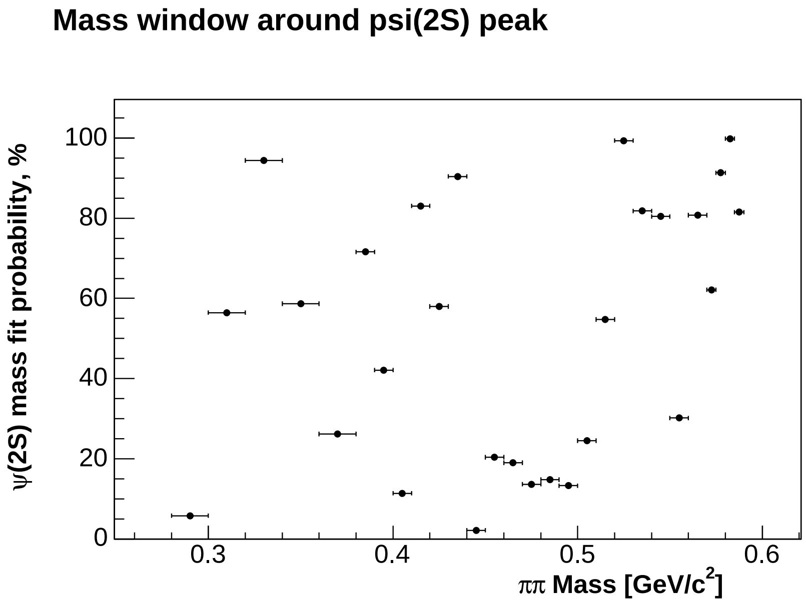

Figure 4-9: The $\psi(2S)$ mass fit probability within a narrow window from 3.675 GeV$/c^2$ to 3.695 GeV$/c^2$ around the $\psi(2S)$ peak versus $m_{\pi\pi}$.

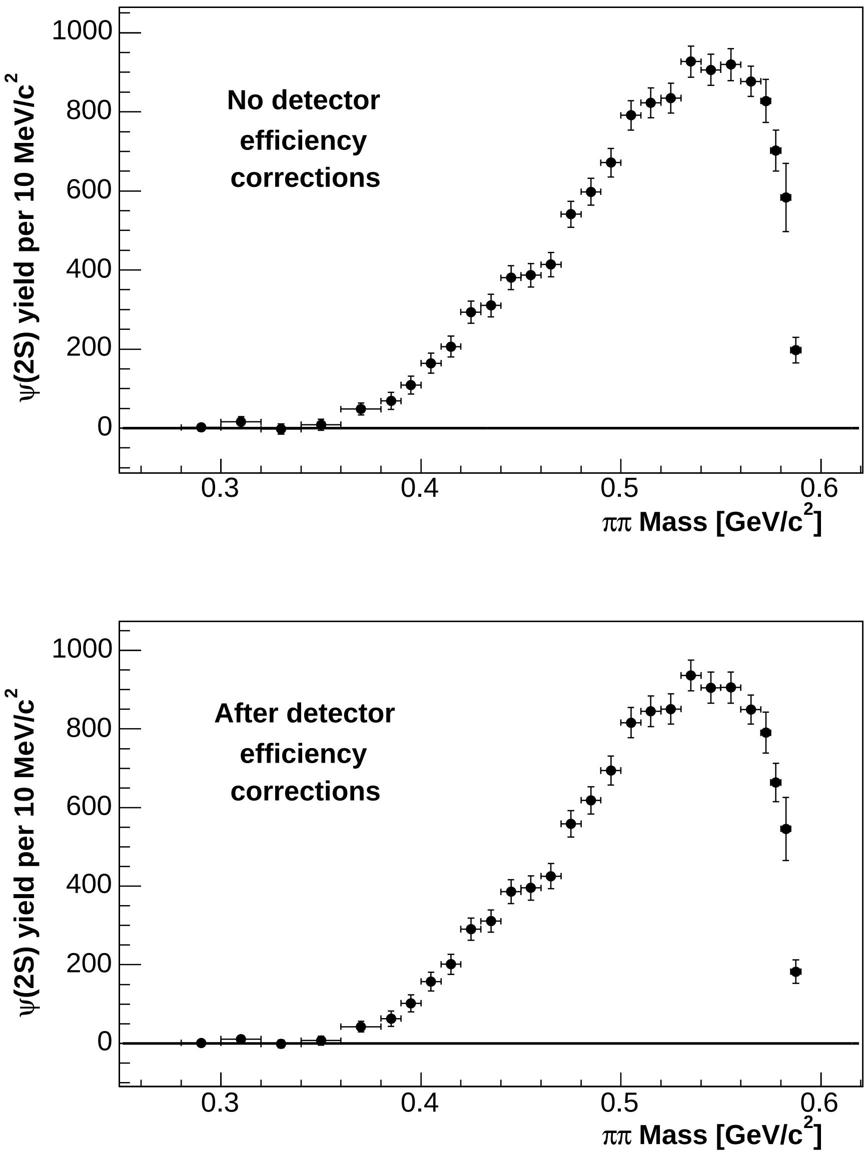

Figure 4-10: The $\psi(2S)$ yield vs. $m_{\pi\pi}$, both before (top) and after (bottom) detector efficiency corrections. The efficiency corrections are rescaled so that the plot after the correction have same area under the curve, *i.e.* the same total number of events.

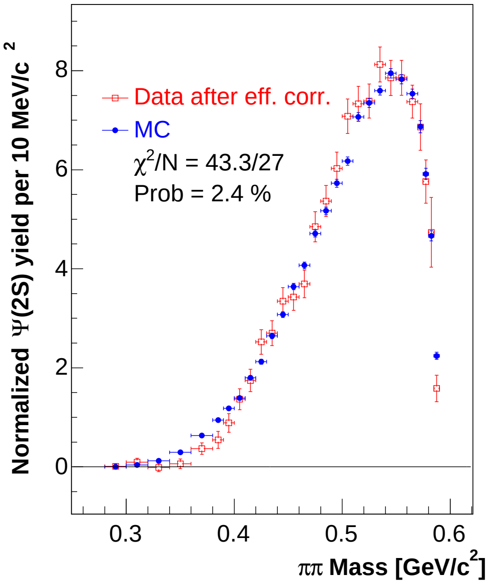

Figure 4-11: The comparison between the $m_{\pi\pi}$ spectrum for $\psi(2S)$ in data, corrected for the detector efficiency, and from Monte Carlo simulation, generated from Equation 4.1 with no detector effects simulated.

for the $X(3872)$. The $X(3872)$ mass and width are fixed to the values from the whole-sample fit after the $m_{\pi\pi} > 500$ MeV$/c^2$ cut as listed in Table 3.3.

Just as in the case of the $\psi(2S)$ fits, we start each individual fit about 100 MeV$/c^2$ below the mass of the $X(3872)$, keeping the size of the fit window to be 200 MeV$/c^2$. Similar to the $\psi(2S)$, the last three $m_{\pi\pi}$ slices require somewhat special handling because of the biases and uncertainties that arise near the kinematic cutoff. The $X(3872)$ yield in the last slice is quite low on top of a relatively large background. Due to these reasons we allow the width of the $X(3872)$ to float in the last slices, constraining it to be greater than 3.0 MeV$/c^2$. Another special feature of the last slices is the concern that the value of the turn-on parameter, x_0 from Equation 4.2, cannot be reliably determined from the data. The fitter has trouble varying this parameter in the minimization when background turn-on starts nearly under the Gaussian signal, *i.e.* it becomes strongly correlated with the background and signal shape parameters. The resulting $X(3872)$ yield in the slice changes depending on the position of the turn-on. To independently constrain the value of the x_0 we extrapolate from the turn-on information from the previous slices. The second half of Appendix F has more details.

The individual fits for each $m_{\pi\pi}$ slice are given in Appendix E. They show reasonable agreement between the fit functions and the data. The plot of the fit probability for the full fit range is given in Figure 4-12. Just as in the $\psi(2S)$ case, the points in the plot are distributed uniformly, making neither clusters nor trends. The plot in Figure 4-13 shows the fit probabilities for the description of the $X(3872)$ peak itself. They are computed in the narrow window between 3.855 GeV$/c^2$ and 3.885 GeV$/c^2$, which roughly corresponds to a six standard deviations window centered on the $X(3872)$. This plot displays a uniform distribution of the points too.

The final plot of the $X(3872)$ yield versus $m_{\pi\pi}$ is given in Figure 4-14. Just as for the

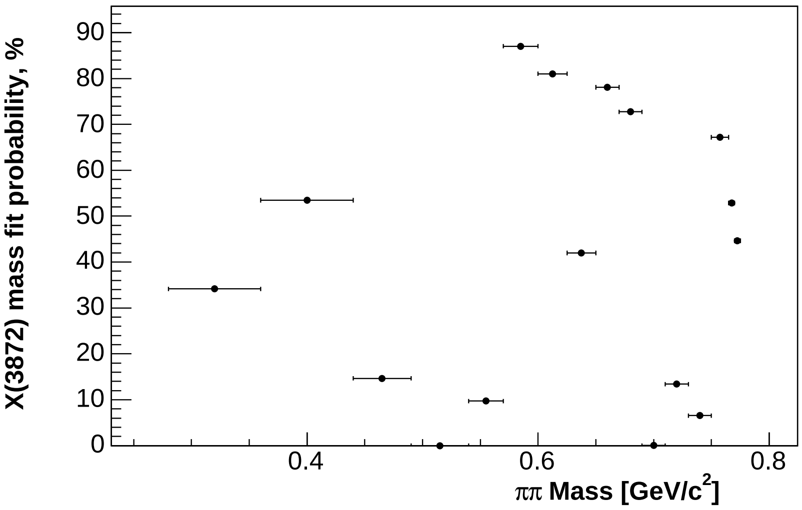

Figure 4-12: The $X(3872)$ mass fit probability for the full mass range versus $m_{\pi\pi}$.

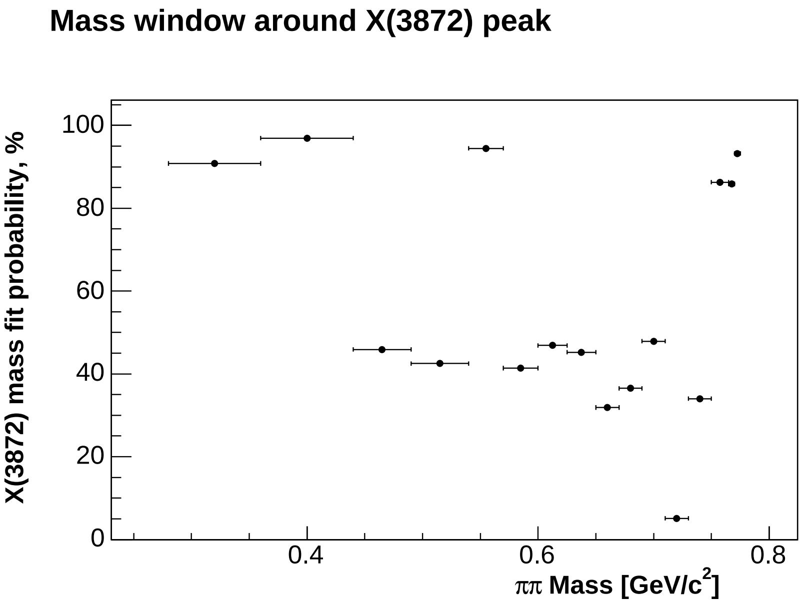

Figure 4-13: The $X(3872)$ mass fit probability for the range from 3.855 GeV/c^2 to 3.885 GeV/c^2 around $X(3872)$ mass peak.

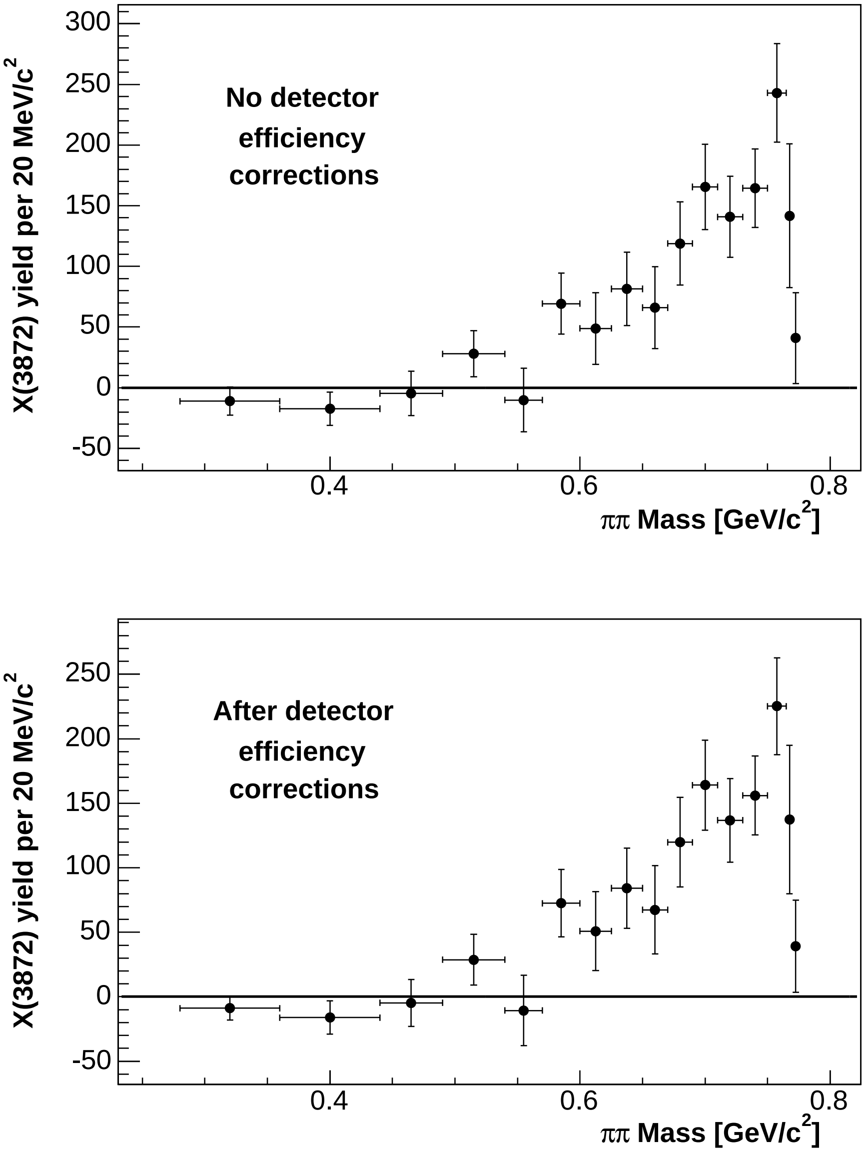

Figure 4-14: The $X(3872)$ yield vs. $m_{\pi\pi}$ before (top) and after (bottom) the detector efficiency corrections. The efficiency corrections are rescaled so that the total number of events is preserved.

$\psi(2S)$, the inverse efficiency correction factors, ξ_i, are rescaled so that the total number of the events is the same before and after the corrections. The net effect of the efficiency corrections is quite small. The results in tabular form are given in Chapter 5 (Table 5.2) after we obtain the systematic uncertainties.

The $m_{\pi\pi}$ spectrum for the $X(3872)$ looks similar to that for the $\psi(2S)$. It also favors high dipion masses and falls off rapidly at the upper kinematical limit. In Chapter 6 we will fit this spectrum with different theoretical models.

Chapter 5

Systematic Uncertainties

The systematic uncertainty in our analysis is very small with respect to the statistical one. This is explained by the fact that the $X(3872)$ peak is found on top of a quite large background so that the statistical uncertainty of this background dominates the total statistical uncertainty.

As for the systematic uncertainty, there are two main contributions: uncertainties on the yields N_i in each of the individual $m_{\pi\pi}$ slices, and uncertainties on the efficiency corrections $\xi(m_{\pi\pi})$. The determination of the uncertainty on the yield $\sigma^{\text{syst}}(N_i)$ is further separated into issues surrounding the signal and the background parametrizations. The uncertainties on the efficiency corrections $\xi(m_{\pi\pi})$ are subdivided into components related to the assumed $m_{\pi\pi}$ spectrum, and to that of the p_t spectrum. We will consider all these categories separately.

Our systematic errors are grouped into two sets of uncertainties: correlated and uncorrelated ones. Correlations in the efficiency uncertainties originate from the fact that we are concerned with the shape of the distribution, *i.e.* the efficiency in a given $m_{\pi\pi}$ slice is correlated with that of its neighbors. This distinction is neglected when we plot the $m_{\pi\pi}$ spectra or quote a total systematic error, but it is exploited when we fit the data with various theoretical models.

5.1 Yield Systematics

The models we chose for the signal and background may have a systematic bias in the yields. To estimate the systematic uncertainty arising from this bias for the majority of the $m_{\pi\pi}$ slices we perform a few variations of the fit model and compare the changed yields with the nominal ones. The last few slices require special handling because of the effects unique to the upper kinematic limit, discussed in Chapter 4. We will assign these points with special systematics later, in Section 5.1.4.

5.1.1 Systematics from Modeling the Signal

For the systematic uncertainty from the signal model for the $\psi(2S)$ we exploit three variations of this model. In the first variation we calculate the number of the events in the peak obtained from simply counting bin entries. Specifically, we first obtain the number of background events under the peak from our background parametrization, and then subtract it from the total number of the events in the peak region. The peak region used for this estimate is chosen to be from 3.675 GeV/c^2 to 3.695 GeV/c^2. This range roughly corresponds to a six standard deviations window centered around the $\psi(2S)$ mass. The thus obtained number of events is compared to the nominal one, and the yield differences δN_i for each $m_{\pi\pi}$ slice are plotted in the upper part of Figure 5-1. The nominal and alternate yields are determined from the same sample, therefore the nominal uncertainties on each of them are highly correlated. For this reason we only use the nominal uncertainties from one set of yields for the error bars, rather than double count them by adding the two sets of uncertainties in quadrature. Nevertheless, this is still a gross over estimate of the true uncertainty of the difference between two highly correlated measurements. Thus, the fluctuations of the yield differences in this plot are much smaller than the error bars.

We focus our attention on the high-mass part of the $m_{\pi\pi}$ spectrum which has significant yields, whereas the low-mass slices are dominated by noise rather than the signal. The significant points are plotted with the large circles in Figure 5-1, and the ones we ignore with the small symbols. For this set of the large points we compute the mean value $\nu = \langle \delta N \rangle$, the RMS spread $\theta = \sqrt{\langle(\delta N - \nu)^2\rangle}$ and the sample variance $\sigma_\nu = \frac{1}{\sqrt{n-1}}\sqrt{\langle(\delta N - \nu)^2\rangle}$, which is used as an estimate of the uncertainty on the mean value ν. The last two points in the middle and bottom plots in Figure 5-1 are also shown in small symbols, because they are excluded from the calculations of the mean, RMS and sample variance. As was mentioned earlier, these points will be assigned special systematics later.

If there were a clear systematic bias, systematic trends should be apparent among the large points. Given the seemingly random scatter, we use the mean value ν of the differences δN_i to quantify a possible bias, and use the uncertainty on the mean σ_ν to judge if the mean is significantly different from zero. There is no clear evidence of a bias, but arguably we cannot exclude the presence of a bias any smaller than the uncertainty on the mean, $\sigma_\nu = \pm 2.7$ candidates for the $\psi(2S)$ and $\sigma_\nu = \pm 4.9$ candidates for the $X(3872)$. Thus we take these values as our yield systematic for the signal model. These are quite small numbers, and clearly if this were a large effect we should have more judiciously separated out any remaining statistical contributions, or have better understood our model.

In the next two variations of the signal model we shift the width σ and the relative normalization N_{rel} of the $\psi(2S)$, which are fixed in the slice fits, by plus (minus) one standard deviation from the central value, as determined by the mass fit of the whole sample. The increases (decreases) in the yields with the changed models turn out to be proportional to the yields themselves. The *fractional* differences between the changed and the nominal yields are displayed in the middle plot in Figure 5-1 for the shift in the relative normalization N_{rel}, and in the bottom plot for the shift in the width σ. The plots show that the yields change by $\sim 2.7\%$ for the relative normalization and by $\sim 1.7\%$ for the width. These are clear and well defined systematic shifts. However, we are only concerned with shape differences, and the uniform fractional shifts are of no significance to our result. Multiplication of all the points by the same number does not change the shape at all. We only care about the residual variation within this global shift, which is less than about 0.5%, and we neglect it.

In the case of the $X(3872)$, the corresponding systematic plots are shown in Figure 5-2. The top plot displays the difference in the yields between the fitted and the counted numbers of the entries in the peak. The range for the counting is chosen to be from 3.855 GeV/c^2 to 3.885 GeV/c^2, which roughly corresponds to a six standard deviation window centered on the $X(3872)$ mass.

The general picture manifested by the yield difference distribution for the $X(3872)$ is similar to that of the $\psi(2S)$: modest fluctuations, with a relatively small mean. We again take the value of the sample variance, $\sigma_\nu = \pm 4.9$ candidates, as an upper bound on the size of the systematic.

The next two plots in Figure 5-2 show the fractional yield differences for the $X(3872)$ mass[1]

---

[1] We do not vary the $\psi(2S)$ mass, because due to the large number of $\psi(2S)$'s in the sample one standard

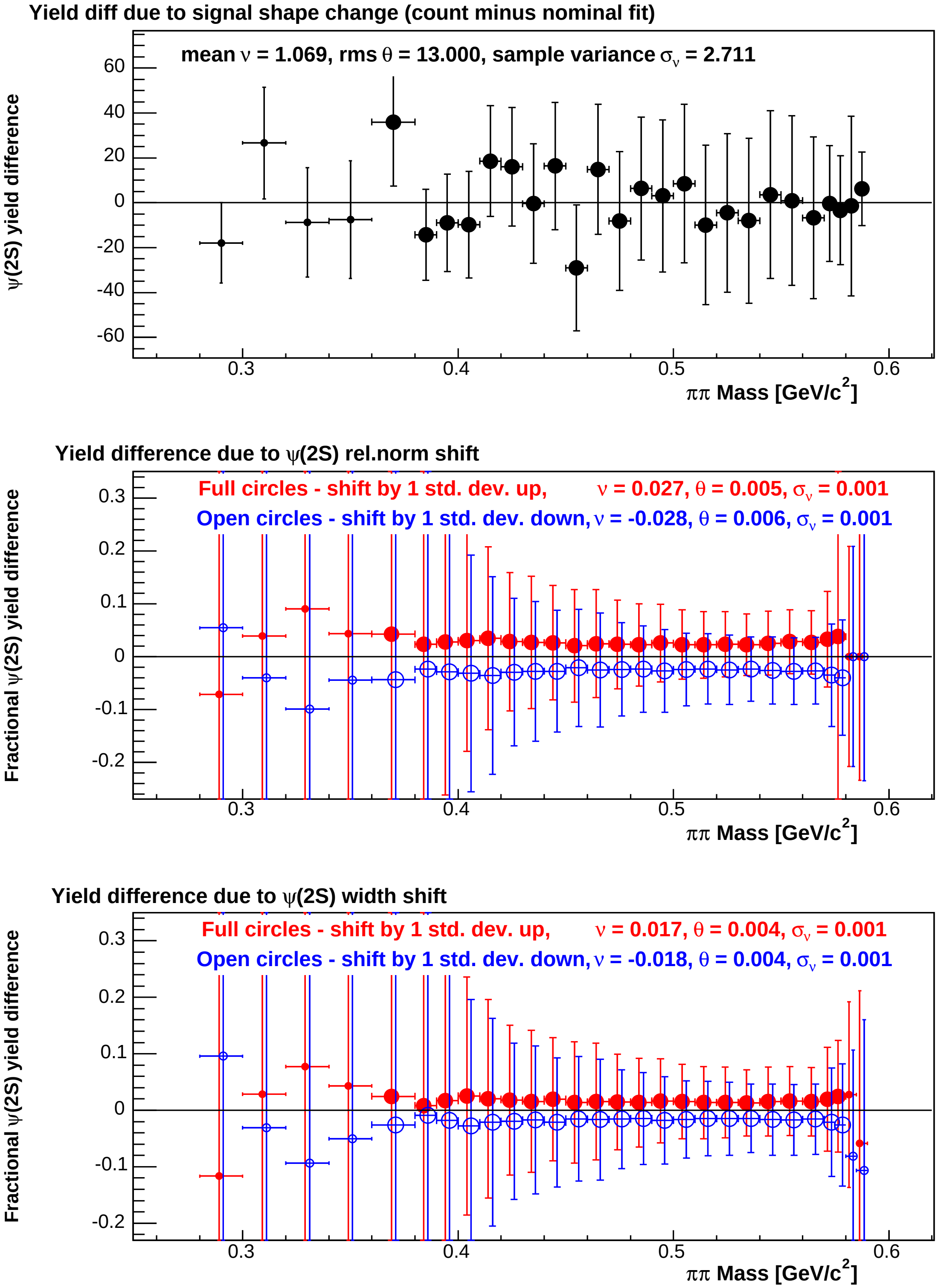

Figure 5-1: TOP: The yield differences (variation minus nominal) for the $\psi(2S)$ yield vs. $m_{\pi\pi}$ for the first signal model variation, counting bin entries. The first four points are drawn in small symbols to reflect the fact that they are excluded from the calculation of the mean ν, the RMS spread θ and the sample variance σ_ν. MIDDLE and BOTTOM: The *fractional* yield differences for two other variations, shift in $\psi(2S)$ relative normalization and $\psi(2S)$ width by one standard deviation up and down. The last two points in the middle and the bottom plots are given special treatment and for this reason also excluded from the mean, RMS and sample variance.

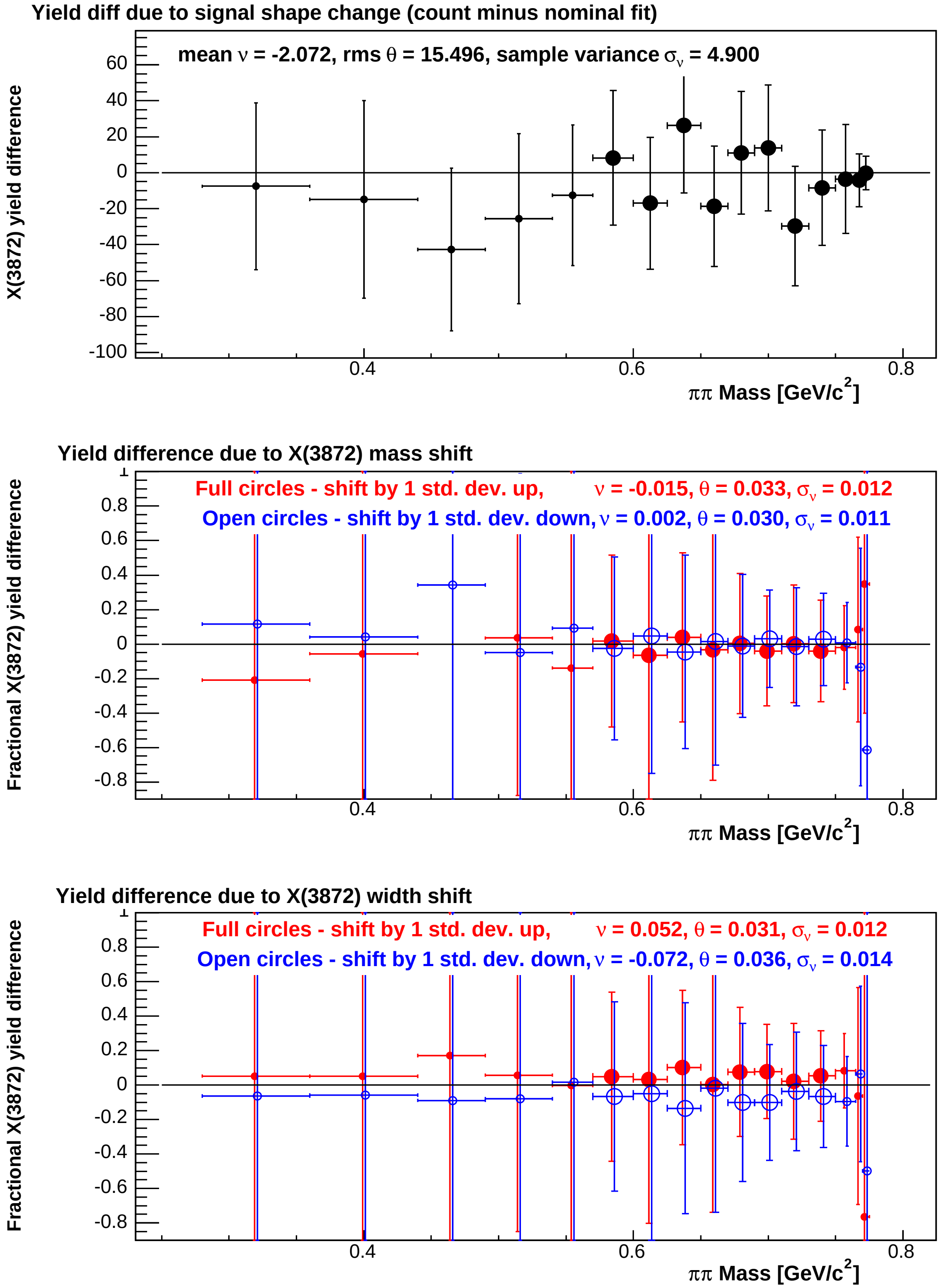

Figure 5-2: TOP: The yield differences (variation minus nominal) for the $X(3872)$ yield vs. $m_{\pi\pi}$ for the first signal model variation, counting bin entries. The first five points are drawn in small symbols to show that they are excluded from the calculation of the the mean ν, RMS θ and sample variance σ_ν. MIDDLE and BOTTOM: The *fractional* yield differences for two other variations, shift in $X(3872)$ mass and $X(3872)$ width by one standard deviation up and down. The last three points are made smaller in size to show that they are also excluded from the mean, RMS and sample variance.

and width shifted by plus or minus one standard deviation from the central value. They show systematic trends, but the statistical fluctuations start to wash out the clear pattern observed in the $\psi(2S)$. We apply the lesson from the $\psi(2S)$ and take the effect of these variations to be the universal fractional shifts, and assign no systematic for them.

5.1.2 Systematics from Modeling the Background

To obtain the systematic uncertainty coming from the background shape, we consider three different variations of the background modeling: the background shape parametrization, the size of the fit window and the number of the points skipped in the beginning of the turn-on.

To change the background shape parametrization we replace the background fitting function from Equation 4.2 with a polynomial. We rely upon the high-mass sideband to largely fix the background polynomial and do not fit the low-mass sideband, to allow for greater freedom in the low mass shape which varies more. To do so we shift the left boundary of the fit range from the nominal value of 100 MeV/c^2 lower than the $X(3872)$ mass, to just a few standard deviations below the peak. For the $\psi(2S)$, which has two Gaussians, we use: $m(\psi(2S)) - 4.0\sqrt{N_{rel}\sigma^2_{\text{wide}} + (1 - N_{rel})\sigma^2_{\text{narrow}}}$. For the $X(3872)$ the lower limit of the fit range is $m(X) - 3.5\sigma(X)$. The background shape can not be well described with a polynomial when the turn-on comes close to the mass peak, so that we do not use the polynomial for the very last $m_{\pi\pi}$ slices.

The top plots in Figure 5-3 and Figure 5-4 show the differences between the yields with nominal and alternate background parametrization for the $\psi(2S)$ and the $X(3872)$, respectively. For the $\psi(2S)$ the yield variations are dominated by statistical fluctuations, no clear systematic trend is observed. We take the uncertainty on the mean σ_ν as an upper bound on the systematic from the background parameterization. The picture, and our conclusion for the $X(3872)$ in Figure 5-4 is similar.

The other major check of systematics is the variation of the exact starting point of the fit window. Looking through the $J/\psi\,\pi^+\pi^-$ mass distributions in the $m_{\pi\pi}$ slices we see occasional hills and valleys in the data below the mass peaks that are potentially systematic deviations from our background model. Depending on where the window edge falls these features may distort the yields. To make alternate versions of the fit we visually inspect the fits and add or drop the points from the fits by hand if we have a reason to believe that adding or dropping certain points produces a significant effect on the yield. The bottom plots in Figures 5-3 and 5-4 show the graphs of the yield differences for the $\psi(2S)$ and the $X(3872)$, respectively. The plot with open markers is for the case of the fit window starting at a bit lower mass, to include certain points. The other plot corresponds to the beginning of the fit window moved to a bit higher mass value to drop certain points from the fit. For the $\psi(2S)$, where we have good statistics, the mean ν and the sample variance σ_ν are fairly small. They are a little bit larger, though, than the previously alloted systematics, and we take this slightly larger value, ±2.4 candidates, as a final estimate of the background systematic uncertainty. Likewise for the $X(3872)$, this systematic uncertainty coming from the background shape modeling is ±6.8 candidates.

---

deviation is quite small and shifting the mass value by it would cause a negligible effect, whereas the $X(3872)$ mass has a larger uncertainty.

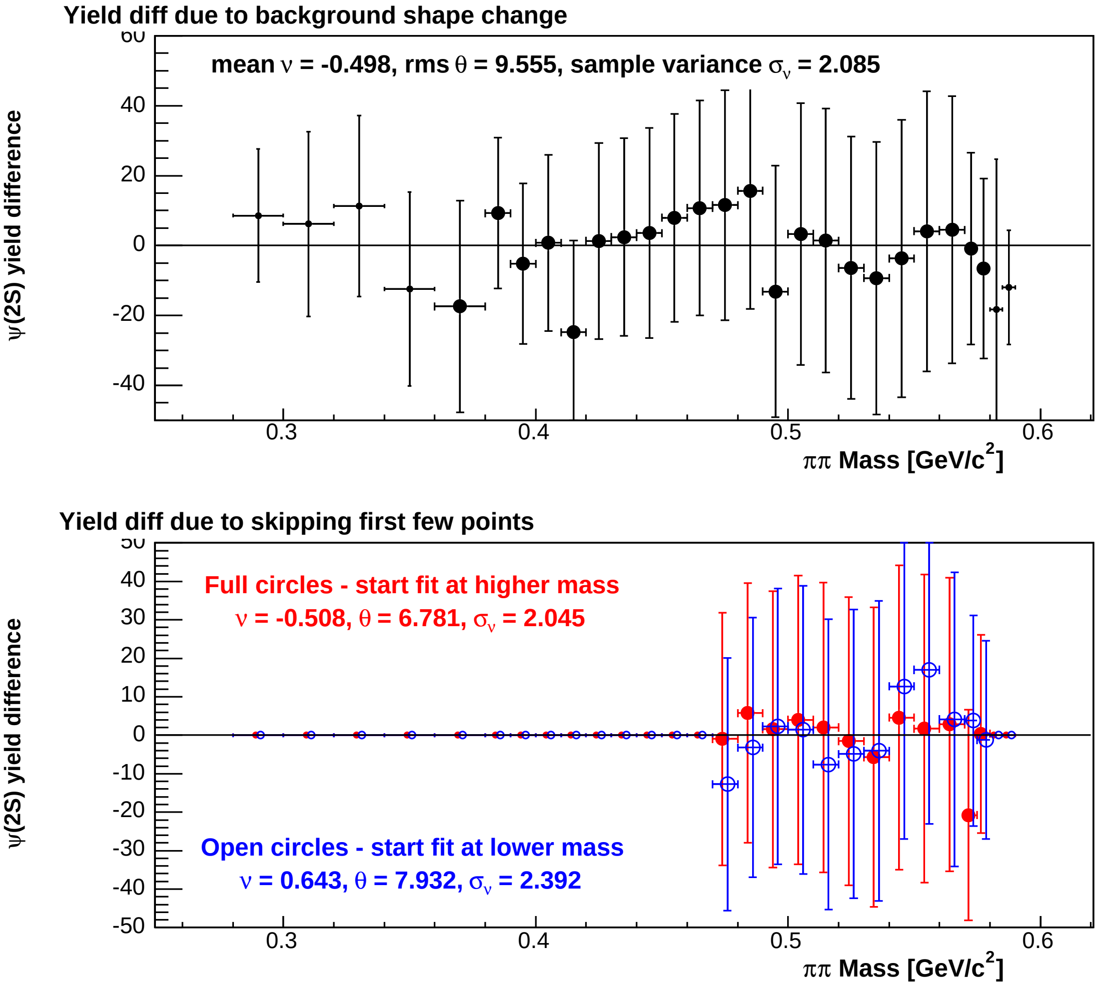

Figure 5-3: The yield differences (variation minus nominal) for the $\psi(2S)$ yield vs. $m_{\pi\pi}$ for the background shape variation – polynomial background (top) and shifting the beginning of the fit range (bottom). The first four points and the last two are drawn in small symbols to show that they are excluded from the calculation of the mean ν, the RMS θ and the sample variance σ_ν.

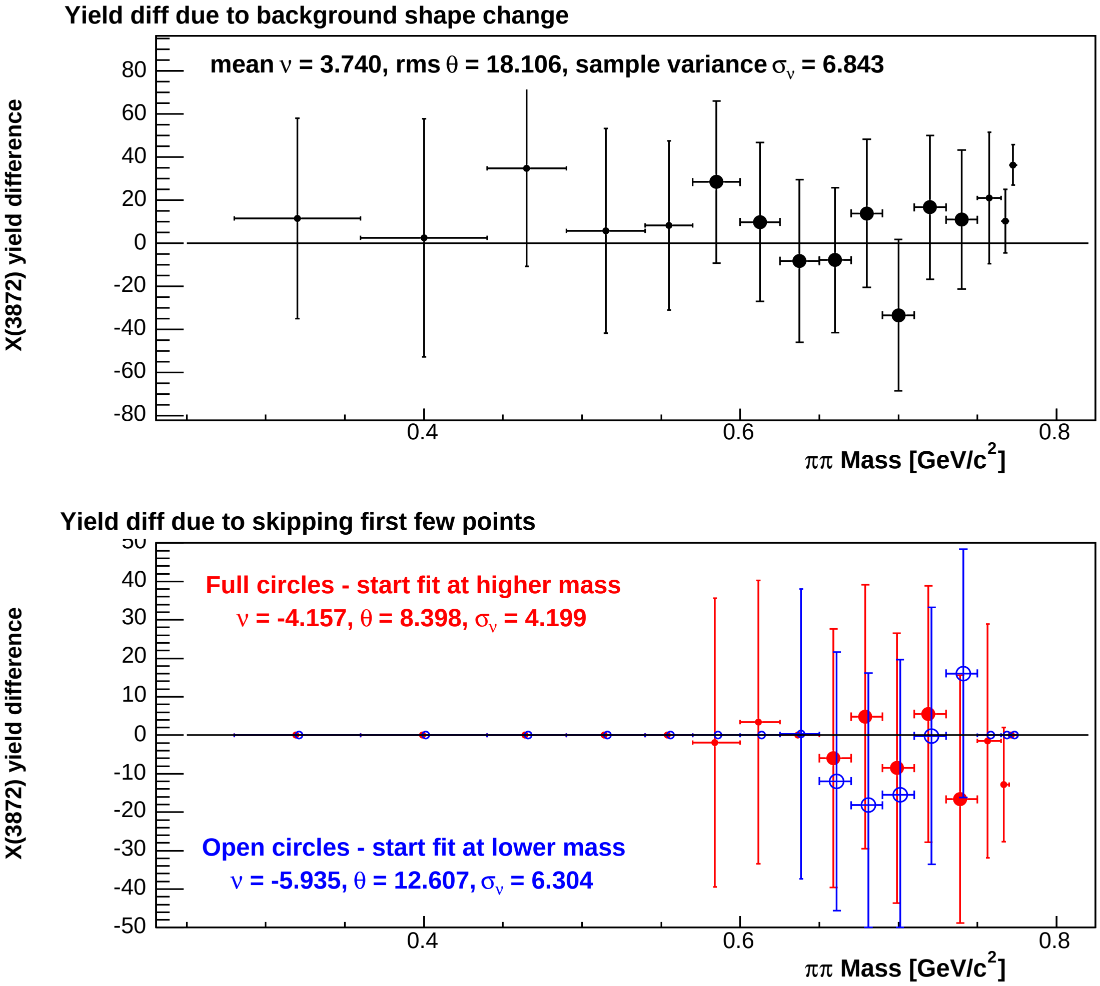

Figure 5-4: The yield differences (variation minus nominal) for the $X(3872)$ yield vs. $m_{\pi\pi}$ for the background shape variation – polynomial background (top) and shifting the beginning of the fit range (bottom). The first five points and the last three are drawn in small symbols to show that they are excluded from the calculation of the mean ν, the RMS θ and the sample variance σ_ν.

5.1.3 Final Systematics from Signal and Background

To obtain the total *uncorrelated* systematic uncertainty for the yields for each $m_{\pi\pi}$ slice we add the signal and the background uncertainties in quadrature. These are: ±3.6 candidates for the $\psi(2S)$, and ±8.4 candidates for the $X(3872)$. These values are utilized in all $m_{\pi\pi}$ slices with the exception of some slices at the end of the spectra.

5.1.4 Systematics for Yields in the Last Few $m_{\pi\pi}$ Slices

As alluded to earlier, the last few points in the $m_{\pi\pi}$ spectra for both $\psi(2S)$ and $X(3872)$ merit special handling. To determine the systematic uncertainty on these points we perform a variety of special fits and monitor the stability of the yields under different assumptions. The various fits are shown in Appendix F, and since the process is somewhat involved we leave most of the details there. But the major issues that we contend with are:

- Near the upper kinematic limit, the selection bias of taking a narrow $m_{\pi\pi}$ slice may bias the mass and width of the $J/\psi\,\pi^+\pi^-$ signal Gaussian;
- As the kinematic turn-on reaches the lower range of the signal Gaussian the background turn-on is more difficult for the fit to determine.

To grapple with these issues we experiment with letting the mass and width parameters of the fit float, and we use the lower $m_{\pi\pi}$ slices to extrapolate the turn-on point of the background in the problematic slices. In the end we finally assign the following systematic uncertainties:

$$\begin{aligned} N_{\psi}^{\mathrm{last}} &= 99 \pm 16\,(\mathrm{stat.})^{+13}_{-10}\,(\mathrm{syst.}), \\ N_{\psi}^{\mathrm{last}-1} &= 292 \pm 43\,(\mathrm{stat.})^{+12}_{-22}\,(\mathrm{syst.}), \\ N_{X}^{\mathrm{last}} &= 10 \pm 9\,(\mathrm{stat.})^{+8}_{-2}\,(\mathrm{syst.}), \\ N_{X}^{\mathrm{last}-1} &= 35 \pm 15\,(\mathrm{stat.})^{+3}_{-21}\,(\mathrm{syst.}), \\ N_{X}^{\mathrm{last}-2} &= 182 \pm 30\,(\mathrm{stat.})^{+15}_{-16}\,(\mathrm{syst.}). \end{aligned}$$

5.2 Efficiency Systematics

5.2.1 Uncertainty in the $m_{\pi\pi}$ Spectra

In Section 4.2 we obtained the detector efficiency correction based on the S-wave $m_{\pi\pi}$ spectra $\xi(m_{\pi\pi})$. This efficiency correction depends on the p_t distribution, as shown in Figure 5-5 for the $\psi(2S)$ and Figure 5-6 for the $X(3872)$. The $\xi(m_{\pi\pi})$ curves in different p_t slices are different. Figures 5-5 and 5-6 also manifest that in our Monte Carlo simulation the $m_{\pi\pi}$ distribution itself is correlated with the p_t. Because of these correlations, the detector efficiency correction $\xi(m_{\pi\pi})$ is also correlated to the $m_{\pi\pi}$ distribution in the Monte Carlo simulation itself. To obtain the correct $\xi(m_{\pi\pi})$ we must make sure that the $m_{\pi\pi}$ distribution assumed in the Monte Carlo generation is the same as in the data. An incorrectly simulated $m_{\pi\pi}$ results in a distorted p_t spectrum, leading to a distorted $m_{\pi\pi}$ efficiency.

The S-wave $m_{\pi\pi}$ distribution reflects the data very well for the $\psi(2S)$, but for the $X(3872)$ it does not have to be so. We introduce a systematic for our ignorance of the true shape of the $m_{\pi\pi}$ distribution for the $X(3872)$. Fortunately, the efficiency $\xi(m_{\pi\pi})$ is not very sensitive to the exact $m_{\pi\pi}$ shape, and we may change this shape quite dramatically to quantify an uncertainty

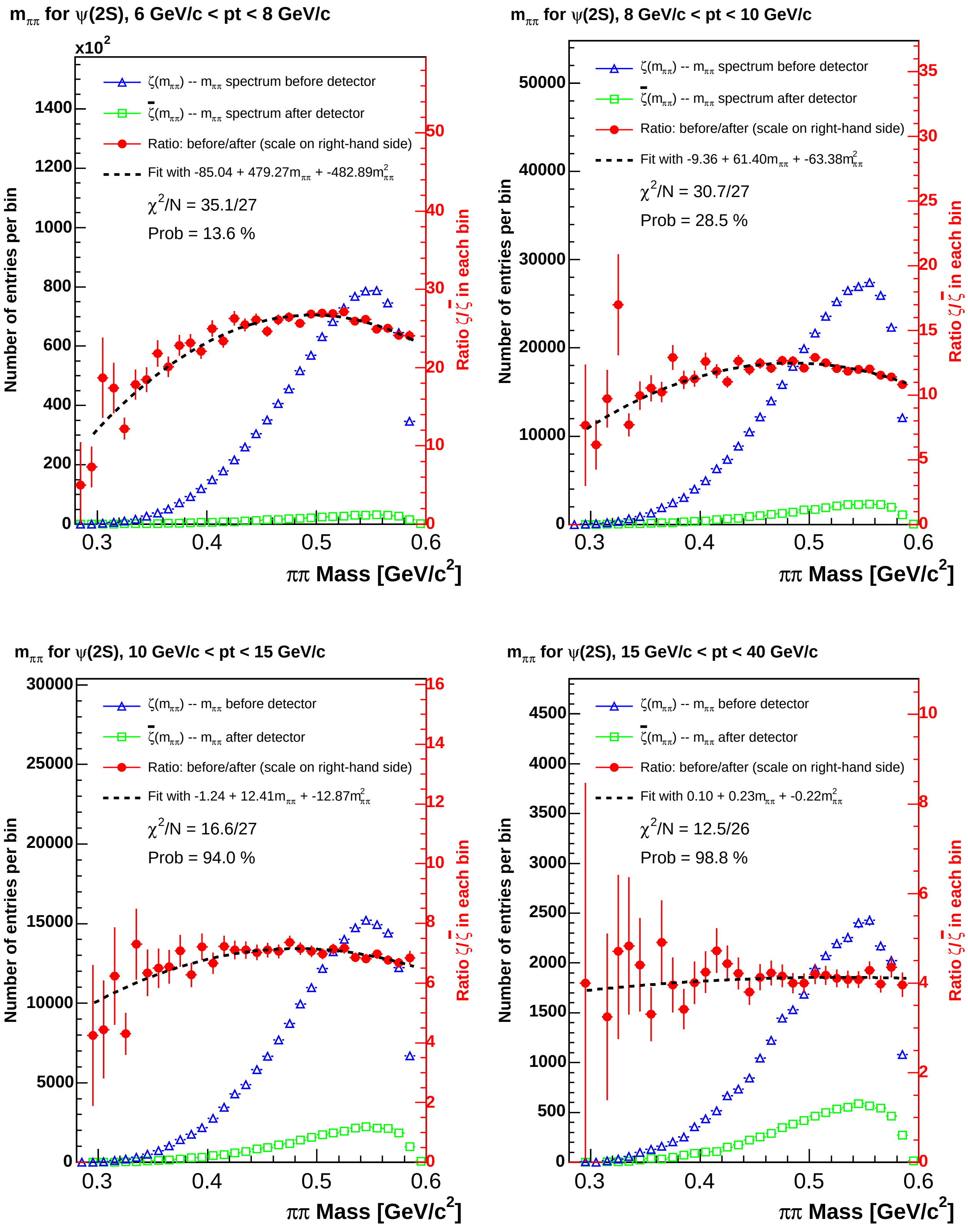

Figure 5-5: The S-wave $m_{\pi\pi}$ spectra for $\psi(2S)$ in different ranges of p_t.

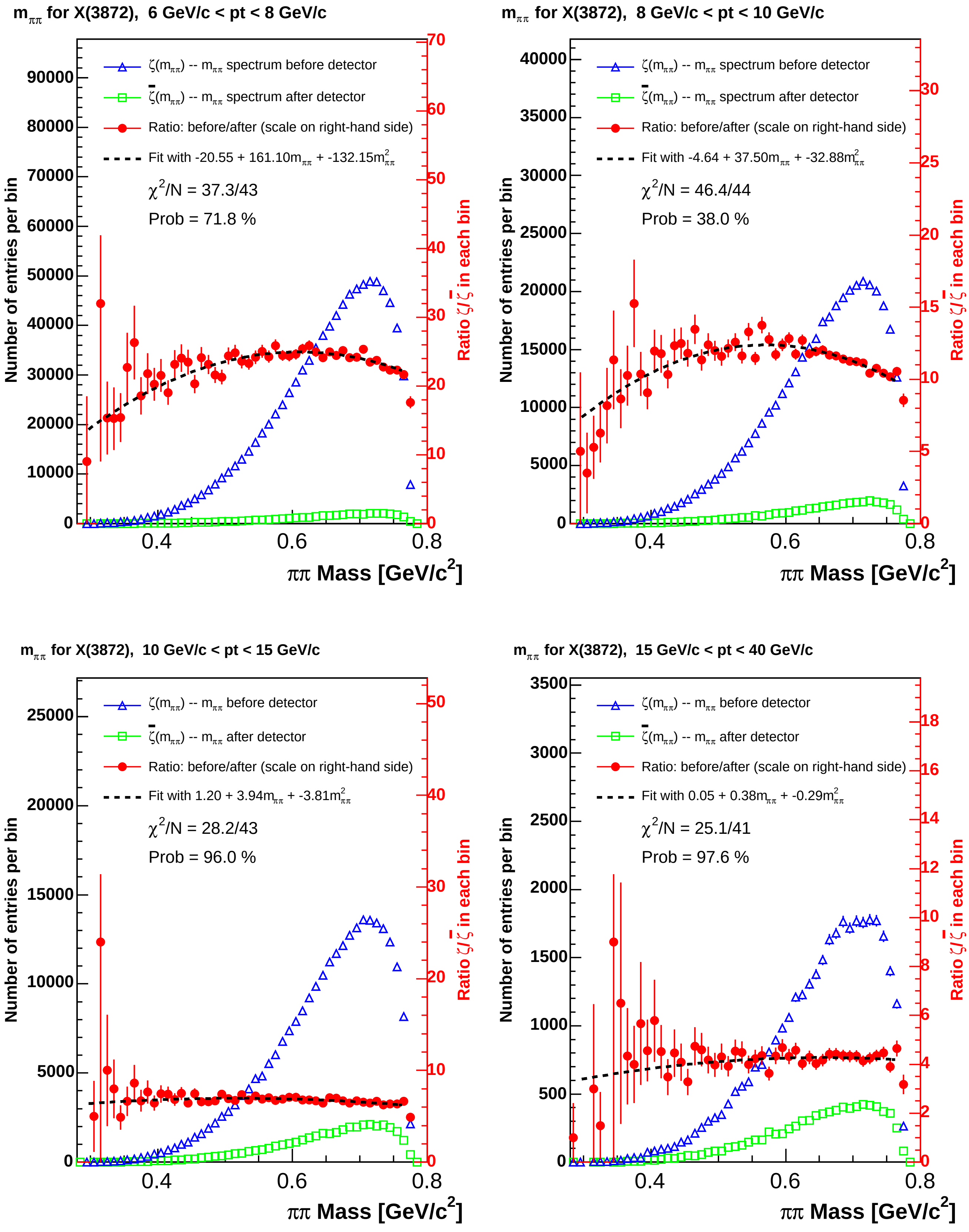

Figure 5-6: The S-wave $m_{\pi\pi}$ spectra for $X(3872)$ in different ranges of p_t.

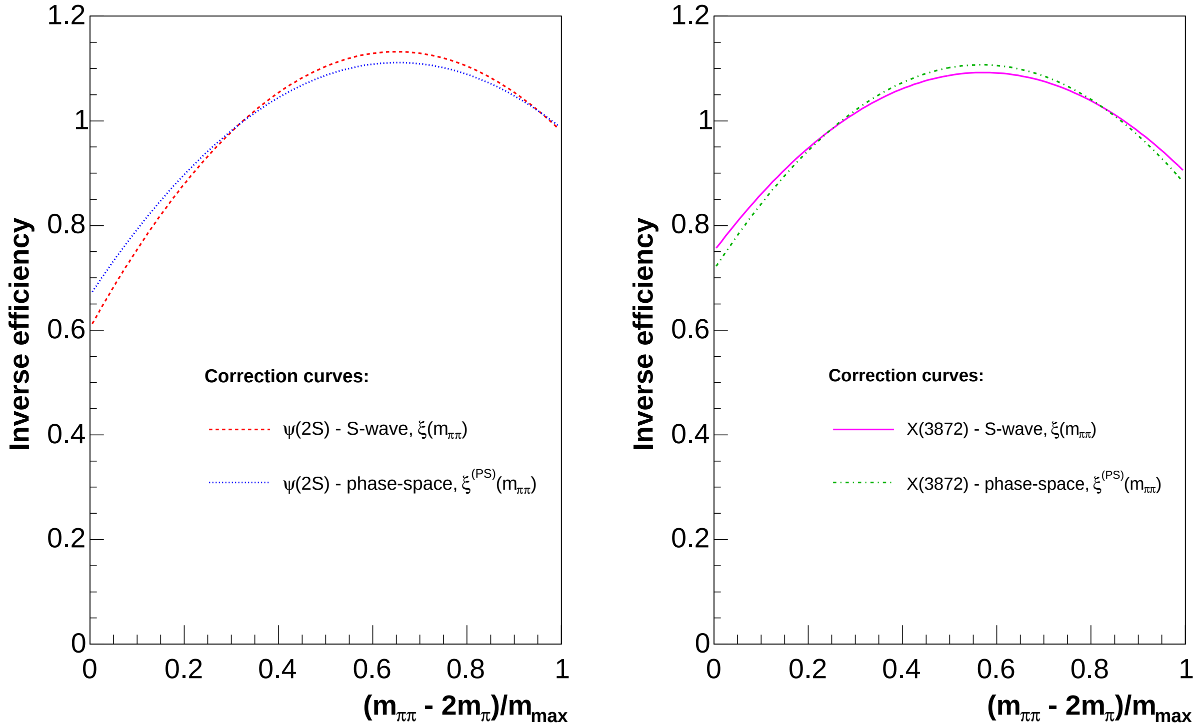

Figure 5-7: The inverse detector efficiency fitted curves $\xi(m_{\pi\pi})$ for both the $\psi(2S)$ (left) and the $X(3872)$ (right) based on the S-wave and phase-space models.

on our nominal S-wave model. The model which we adopt as a gross alternative to the S-wave is to distribute dipion masses according to phase space:

$$PS = \sqrt{\frac{(m_{\pi\pi}^2 - 4m_\pi^2)((M_{\psi(2S)}^2 - M_{J/\psi}^2)^2 - 2(M_{\psi(2S)}^2 + M_{J/\psi}^2)m_{\pi\pi}^2 + m_{\pi\pi}^4)}{2M_{\psi(2S)}}}. \tag{5.1}$$

The details of the Monte Carlo generation for this *phase space model* are given in Appendix G. The resulting inverse efficiency correction curves $\xi^{PS}(m_{\pi\pi})$ are compared to the nominal $\xi(m_{\pi\pi})$ in Figure 5-7 for both the $\psi(2S)$ and the $X(3872)$. We see that the shapes of $\xi(m_{\pi\pi})$ and $\xi^{PS}(m_{\pi\pi})$ are practically the same for both the $\psi(2S)$ and the $X(3872)$. Given these small variations it is unnecessary to try and achieve a better approximation for the $m_{\pi\pi}$ spectrum for the $X(3872)$, as could be done by feeding the measured spectrum back into the Monte Carlo generation and iterating.

To determine the systematic uncertainty for the $\psi(2S)$ and for the $X(3872)$ we take the ratio of the phase space correction factor to that from the S-wave distribution (Equation 4.1) that serves as our default:

$$\gamma^{PS}(m_{\pi\pi}) = \frac{\xi^{PS}(m_{\pi\pi})}{\xi(m_{\pi\pi})}. \tag{5.2}$$

This ratio $\gamma^{PS}(m_{\pi\pi})$ is shown in Figure 5-8 for both $\psi(2S)$ and $X(3872)$. We are only interested

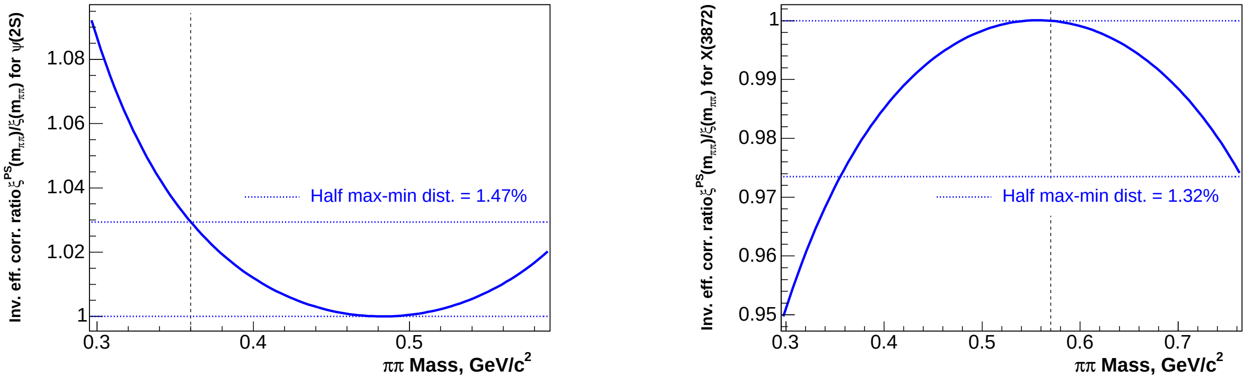

Figure 5-8: Variations in $\psi(2S)$ (left) and $X(3872)$ (right) efficiency correction factors due to the form of the $m_{\pi\pi}$ parametrization. Using the maximum and minimum of the variations over the mass range of prime interest (lower bound is indicated by the vertical dashed lines) we get the values quoted in the figure. These, however, are not the errors finally used, but only an overall estimate (See text for details).

in *shape* changes, so that the absolute normalization of this ratio is chosen arbitrarily. We choose it so that the extremum value of $\gamma^{PS}(m_{\pi\pi})$ is 1.0.

We see that low dipion masses have a more rapidly changing shape of the correction, because this is where the correction factor has the most significant change itself. We are primarily concerned with the uncertainty in the high mass region, and if we restrict ourselves to the variation above 360 MeV/c^2 for $\psi(2S)$ and 570 MeV/c^2 for the $X(3872)$, and use half of the maximum-to-minimum span over the above mass ranges as a systematic estimator we get something like $\pm 1.5\%$ for both the $\psi(2S)$ and the $X(3872)$. Since this systematic is clearly correlated across $m_{\pi\pi}$ slices, we use the whole shape determined from the efficiency ratio $\gamma^{PS}(m_{\pi\pi})$, rather than the maximum-to-minimum span estimators. Thus, when quoting tabulated numbers of yields per i-th slice and their uncertainties, we will add in a systematic uncertainty on the efficiency $\sigma^{PS}_{syst}(\xi_i)$ obtained by averaging this efficiency ratios over the slice range:

$$\frac{\sigma^{PS}_{syst}(\xi_i)}{\xi_i} = \gamma^{PS}_i - 1 = \frac{1}{b_i - a_i}\int_{a_i}^{b_i} \gamma^{PS}(m_{\pi\pi})\, dm_{\pi\pi} - 1, \tag{5.3}$$

where a_i and b_i are the lower and upper boundaries of the i-th $m_{\pi\pi}$ slice. But given that these uncertainties are correlated from slice to slice, we will fold the full polynomial parametrization into the fits of various theories to our $m_{\pi\pi}$ spectra.

5.2.2 Uncertainty in the p_t Spectrum

There is one more potentially important source of systematic uncertainty for the $m_{\pi\pi}$ shape for the $X(3872)$. The detector efficiency determined from the Monte Carlo is dependent on the p_t spectrum used in the generation. To verify the efficiency corrections we match the Monte Carlo output p_t spectrum to the one observed in the data, but this is only done to the statistical precision of our data. Therefore, we assign a systematic uncertainty to the resulting detector efficiency corrections based on the uncertainty of the fitted slope of the p_t spectrum.

The p_t spectrum for Monte Carlo generation is parameterized with $\exp(a_0 + a_1 p_t + a_2 p_t^2)$.

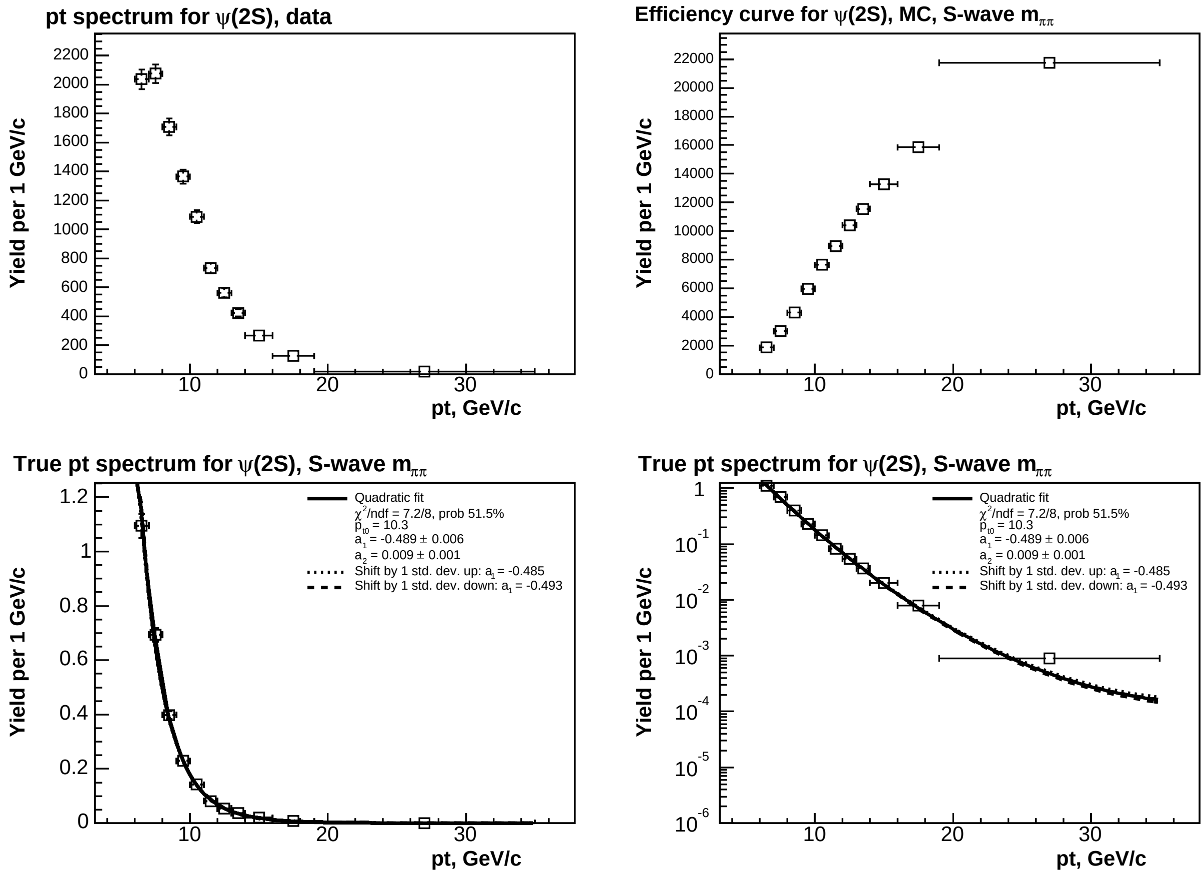

Figure 5-9: The p_t distributions of the $\psi(2S)$. Upper-left plot: raw data. Upper-right plot: the detector efficiency curve. Two lower plots are the ratio of the data and the efficiency curve in both linear and logarithmic scales, fitted with the normal parametrization functions and the ones "shifted" by 1 standard deviation.

We determine the parameters a_0, a_1 and a_2 from the fit of the ratio of the data to the detector efficiency curve shown in Figure 4-4. The quadratic term a_2 turns out to be not very important and to simplify our systematic study we fix it. Since the parameter a_0 is a normalization, only the slope a_1 has relevance to the shape. Therefore, to obtain the systematic uncertainties on the shape we shift the parameter a_1 by one standard deviation up and down, as determined from the above mentioned fit to p_t data. The fits with shifted a_1 parameters are shown in Figures 5-9 for the $\psi(2S)$ and 5-10 for the $X(3872)$. In the case of the $\psi(2S)$ these shifts, plotted as dotted and dashed lines, only appear as a slight thickening of the default fitted curve (solid line). For the $X(3872)$ the slope variations are more apparent due to the larger statistical uncertainties of the $X(3872)$-data.

With these variations of the p_t spectra we can determine the corresponding inverse detector efficiency corrections $\xi^{\pm 1\sigma}(m_{\pi\pi})$. The ratios of these curves to the nominal curve

$$\gamma^{\pm 1\sigma}(m_{\pi\pi}) = \frac{\xi^{\pm 1\sigma}(m_{\pi\pi})}{\xi(m_{\pi\pi})} \tag{5.4}$$

are plotted in Figure 5-11 for the $X(3872)$. The dashed curve in this figure represents $\gamma^{+1\sigma}(m_{\pi\pi})$, and the solid curve $\gamma^{-1\sigma}(m_{\pi\pi})$. Just as in the case of the shape variations for different $m_{\pi\pi}$

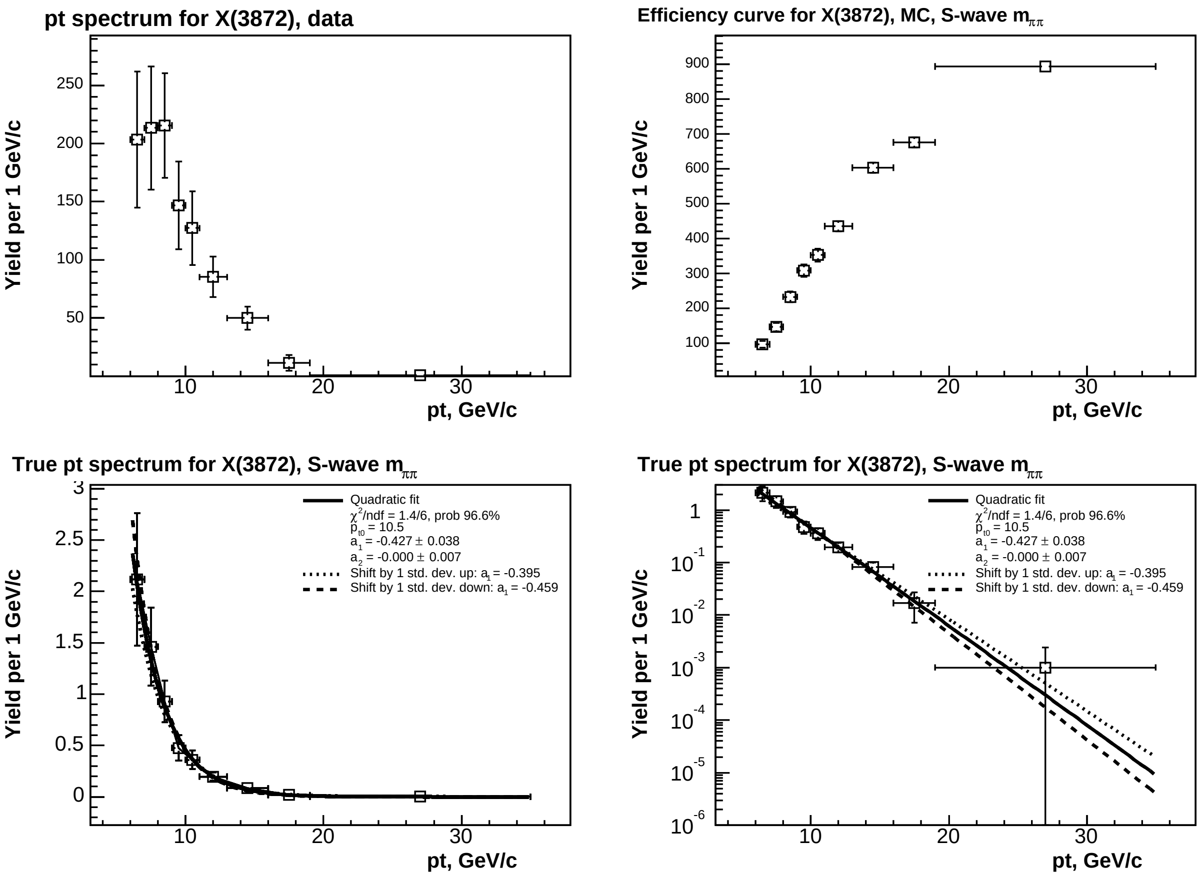

Figure 5-10: The p_t distributions of $X(3872)$. Upper-left plot: data. Upper-right plot: the detector efficiency curve. Two lower plots are the ratio of the data and the efficiency curve in both linear and logarithmic scales, fitted with normal parametrization functions and the ones "shifted" by 1 standard deviation.

parametrization, the absolute normalization is arbitrary and we choose it so that the maximum values of $\gamma^{\pm 1\sigma}(m_{\pi\pi})$ are equal to one. The horizontal lines show the maximum and minimum ratios for masses above 570 MeV/c^2, the prime range of interest for the systematic variation. The crude estimator of half of the maximum-to-minimum for this $m_{\pi\pi}$ range gives less than 1%. But even though it is so small, we follow the approach adopted in the previous section and use the full polynomial parametrization of the efficiency uncertainty due to p_t in the theory fits of the $X(3872)$ dipion spectrum described in Chapter 6.

To estimate the systematic uncertainty for the $\psi(2S)$ due to p_t spectrum parametrization in Monte Carlo we do exactly the same thing. The ratios of the $m_{\pi\pi}$ parametrizations $\gamma^{\pm 1\sigma}(m_{\pi\pi})$ are shown in Figure 5-12 with the crude estimation of the systematic uncertainty in the region above 360 MeV/c^2 being less than 1.5%. The dashed curve in this figure represents $\gamma^{+1\sigma}(m_{\pi\pi})$, the solid curve $\gamma^{-1\sigma}(m_{\pi\pi})$ for $\psi(2S)$. The normalization of both curves is chosen so that the minimum is equal to one.

Our crude estimation of the systematic uncertainty for the $\psi(2S)$ is actually larger than that for the $X(3872)$ because the inverse detector efficiency curve is flatter for the $X(3872)$.

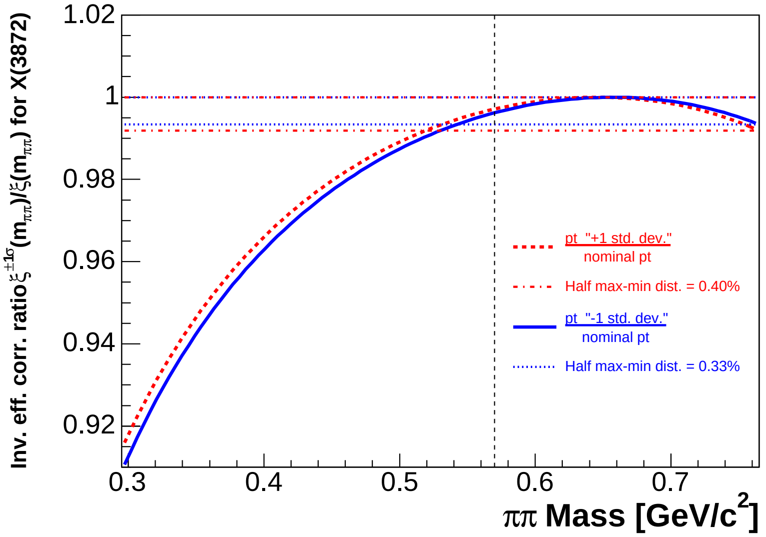

Figure 5-11: The systematic variation in detector efficiency for the $X(3872)$ coming from the parametrization of the Monte Carlo p_t spectrum.

5.3 Final Yields and Uncertainties

We combine the various sources of uncertainties on the $\psi(2S)$ and $X(3872)$ yields in Tables 5.1 and 5.2. In the second column we show the raw yields per slice with their statistical and *uncorrelated* systematic uncertainties. The third column gives the yields, rescaled appropriate to the number of MeV$/c^2$ per slice. These yields (per MeV$/c^2$) are used when we plot the spectra. The per slice inverse efficiency correction factors with their *correlated* uncertainties appear in the fourth column, although we necessarily treat them as uncorrelated here. The uncorrelated uncertainties are scaled in such a way that the yields after the correction have the same area under the curve as before the correction. In mathematical language, the expression in fourth column is given by:

$$\xi_i \left(1 \pm \sqrt{(\gamma_i^{PS} - 1)^2 + (\gamma_i^{-1\sigma} - 1)^2}\right) = \xi_i \left(1 \pm \frac{\sqrt{(\sigma_{syst}^{PS}(\xi_i))^2 + (\sigma_{syst}^{-1\sigma}(\xi_i))^2}}{\xi_i}\right) = \xi_i \left(1 \pm \frac{\sigma_{syst}(\xi_i)}{\xi_i}\right).$$

This equation gives the systematic uncertainty $\sigma_{syst}(\xi_i)$ on the inverse efficiency correction factor ξ_i in the i-th $m_{\pi\pi}$ slice used in the table. The numbers γ_i^{PS} and $\gamma_i^{-1\sigma}$ are calculated from the continuous functions $\gamma^{PS}(m_{\pi\pi})$ and $\gamma^{-1\sigma}(m_{\pi\pi})$ just as shown in Equation 5.3. We use $\gamma_i^{-1\sigma}$ and not $\gamma_i^{+1\sigma}$ because it gives us more conservative estimation of the systematic uncertainty. We will discuss this in detail later, in Section 6.2. The fifth column gives the efficiency corrected yields with the systematic uncertainties now being a sum of the correlated and uncorrelated systematics in quadratures, $(\sigma_{syst}^{corrected})_i = \xi_i \sqrt{\left(\sigma_{syst}(N_i)\right)^2 + N_i^2 \left(\frac{\sigma_{syst}(\xi_i)}{\xi_i}\right)^2}$. The last column gives the final numbers used for displaying the $m_{\pi\pi}$ spectrum.

$m_{\pi\pi}$ range GeV/c^2	Uncorr. $\psi(2S)$ yield per slice (stat. & syst. error)	Uncorr. $\psi(2S)$ yield per 10 MeV/c^2 (stat. & syst. error)	inv. eff. corr. factor, $\xi_i(1 \pm \frac{\sigma^{syst}(\xi_i)}{\xi_i})$ (syst. error only)	Corr. $\psi(2S)$ yield per slice (stat. & syst. error)	Corr. $\psi(2S)$ yield per 10 MeV/c^2 (stat. & syst. error)
280 - 300	$3.7 \pm 19.0 \pm 3.6$	$1.9 \pm 9.5 \pm 1.8$	$0.597(1 \pm 0.138)$	$2.2 \pm 11.3 \pm 2.2$	$1.1 \pm 5.7 \pm 1.1$
300 - 320	$31.9 \pm 26.4 \pm 3.6$	$15.9 \pm 13.2 \pm 1.8$	$0.681(1 \pm 0.098)$	$21.7 \pm 18.0 \pm 3.2$	$10.9 \pm 9.0 \pm 1.6$
320 - 340	$-4.1 \pm 25.9 \pm 3.6$	$-2.0 \pm 12.9 \pm 1.8$	$0.756(1 \pm 0.069)$	$-3.1 \pm 19.5 \pm 2.7$	$-1.5 \pm 9.8 \pm 1.4$
340 - 360	$17.6 \pm 27.7 \pm 3.6$	$8.8 \pm 13.9 \pm 1.8$	$0.822(1 \pm 0.049)$	$14.4 \pm 22.8 \pm 3.1$	$7.2 \pm 11.4 \pm 1.5$
360 - 380	$96.5 \pm 30.3 \pm 3.6$	$48.2 \pm 15.2 \pm 1.8$	$0.879(1 \pm 0.034)$	$84.8 \pm 26.6 \pm 4.3$	$42.4 \pm 13.3 \pm 2.1$
380 - 390	$68.7 \pm 21.6 \pm 3.6$	$68.7 \pm 21.6 \pm 3.6$	$0.916(1 \pm 0.025)$	$62.9 \pm 19.8 \pm 3.7$	$62.9 \pm 19.8 \pm 3.7$
390 - 400	$108.9 \pm 23.0 \pm 3.6$	$108.9 \pm 23.0 \pm 3.6$	$0.938(1 \pm 0.020)$	$102.2 \pm 21.5 \pm 3.9$	$102.2 \pm 21.5 \pm 3.9$
400 - 410	$164.3 \pm 25.2 \pm 3.6$	$164.3 \pm 25.2 \pm 3.6$	$0.958(1 \pm 0.016)$	$157.3 \pm 24.1 \pm 4.2$	$157.3 \pm 24.1 \pm 4.2$
410 - 420	$206.2 \pm 26.2 \pm 3.6$	$206.2 \pm 26.2 \pm 3.6$	$0.975(1 \pm 0.012)$	$201.1 \pm 25.6 \pm 4.3$	$201.1 \pm 25.6 \pm 4.3$
420 - 430	$293.5 \pm 28.1 \pm 3.6$	$293.5 \pm 28.1 \pm 3.6$	$0.990(1 \pm 0.009)$	$290.6 \pm 27.8 \pm 4.4$	$290.6 \pm 27.8 \pm 4.4$
430 - 440	$310.1 \pm 28.3 \pm 3.6$	$310.1 \pm 28.3 \pm 3.6$	$1.003(1 \pm 0.006)$	$311.0 \pm 28.4 \pm 4.1$	$311.0 \pm 28.4 \pm 4.1$
440 - 450	$380.4 \pm 30.1 \pm 3.6$	$380.4 \pm 30.1 \pm 3.6$	$1.014(1 \pm 0.004)$	$385.7 \pm 30.5 \pm 4.0$	$385.7 \pm 30.5 \pm 4.0$
450 - 460	$386.6 \pm 29.8 \pm 3.6$	$386.6 \pm 29.8 \pm 3.6$	$1.022(1 \pm 0.003)$	$395.3 \pm 30.4 \pm 3.8$	$395.3 \pm 30.4 \pm 3.8$
460 - 470	$413.8 \pm 30.7 \pm 3.6$	$413.8 \pm 30.7 \pm 3.6$	$1.029(1 \pm 0.002)$	$425.6 \pm 31.6 \pm 3.8$	$425.6 \pm 31.6 \pm 3.8$
470 - 480	$541.0 \pm 32.9 \pm 3.6$	$541.0 \pm 32.9 \pm 3.6$	$1.033(1 \pm 0.001)$	$558.6 \pm 33.9 \pm 3.8$	$558.6 \pm 33.9 \pm 3.8$
480 - 490	$597.9 \pm 33.7 \pm 3.6$	$597.9 \pm 33.7 \pm 3.6$	$1.034(1 \pm 0.000)$	$618.5 \pm 34.9 \pm 3.7$	$618.5 \pm 34.9 \pm 3.7$
490 - 500	$671.3 \pm 35.9 \pm 3.6$	$671.3 \pm 35.9 \pm 3.6$	$1.034(1 \pm 0.000)$	$694.2 \pm 37.1 \pm 3.7$	$694.2 \pm 37.1 \pm 3.7$
500 - 510	$791.2 \pm 37.5 \pm 3.6$	$791.2 \pm 37.5 \pm 3.6$	$1.031(1 \pm 0.001)$	$816.0 \pm 38.7 \pm 3.8$	$816.0 \pm 38.7 \pm 3.8$
510 - 520	$823.2 \pm 37.7 \pm 3.6$	$823.2 \pm 37.7 \pm 3.6$	$1.026(1 \pm 0.002)$	$845.0 \pm 38.7 \pm 4.0$	$845.0 \pm 38.7 \pm 4.0$
520 - 530	$834.7 \pm 37.5 \pm 3.6$	$834.7 \pm 37.5 \pm 3.6$	$1.019(1 \pm 0.003)$	$850.9 \pm 38.2 \pm 4.5$	$850.9 \pm 38.2 \pm 4.5$
530 - 540	$926.9 \pm 39.0 \pm 3.6$	$926.9 \pm 39.0 \pm 3.6$	$1.010(1 \pm 0.005)$	$936.2 \pm 39.4 \pm 5.8$	$936.2 \pm 39.4 \pm 5.8$
540 - 550	$906.3 \pm 39.6 \pm 3.6$	$906.3 \pm 39.6 \pm 3.6$	$0.998(1 \pm 0.007)$	$905.0 \pm 39.5 \pm 7.3$	$905.0 \pm 39.5 \pm 7.3$
550 - 560	$919.4 \pm 40.1 \pm 3.6$	$919.4 \pm 40.1 \pm 3.6$	$0.985(1 \pm 0.010)$	$905.3 \pm 39.4 \pm 9.4$	$905.3 \pm 39.4 \pm 9.4$
560 - 570	$877.1 \pm 38.2 \pm 3.6$	$877.1 \pm 38.2 \pm 3.6$	$0.969(1 \pm 0.013)$	$849.7 \pm 37.0 \pm 11.4$	$849.7 \pm 37.0 \pm 11.4$
570 - 575	$413.8 \pm 27.4 \pm 3.6$	$827.6 \pm 54.8 \pm 7.2$	$0.955(1 \pm 0.016)$	$395.3 \pm 26.2 \pm 7.1$	$790.6 \pm 52.3 \pm 14.1$
575 - 580	$351.0 \pm 25.8 \pm 3.6$	$702.1 \pm 51.5 \pm 7.2$	$0.946(1 \pm 0.018)$	$331.9 \pm 24.4 \pm 6.8$	$663.9 \pm 48.7 \pm 13.5$
580 - 585	$291.8 \pm 43.0 ^{+12.0}_{-22.0}$	$583.5 \pm 85.9 ^{+24.0}_{-44.0}$	$0.935(1 \pm 0.020)$	$272.9 \pm 40.2 ^{+12.5}_{-21.3}$	$545.8 \pm 80.4 ^{+24.9}_{-42.6}$
585 - 590	$98.7 \pm 16.4 ^{+13.0}_{-10.0}$	$197.4 \pm 32.7 ^{+26.0}_{-20.0}$	$0.925(1 \pm 0.022)$	$91.3 \pm 15.1 ^{+12.2}_{-9.5}$	$182.5 \pm 30.3 ^{+24.4}_{-18.9}$

Table 5.1: The $\psi(2S)$ yields before (uncorr.) and after (corr.) detector efficiency corrections with their statistical and systematic uncertainties. The inverse detector efficiency correction factors ξ_i are rescaled so that the total number of events remains the same after correction. The yields are given with an artificial level of precision, because we want to show the dynamics of the yield change and to treat all the $m_{\pi\pi}$ slices equally, and therefore keep an excessive number of digits.

$m_{\pi\pi}$ range GeV/c^2	Uncorr. $X(3872)$ yield per slice (stat. & syst. error)	Uncorr. $X(3872)$ yield per 20 MeV/c^2 (stat. & syst. error)	inv. eff. corr. factor, $\xi_i(1 \pm \frac{\sigma^{syst}(\xi_i)}{\xi_i})$ (syst. error only)	Corr. $X(3872)$ yield per slice (stat. & syst. error)	Corr. $X(3872)$ yield per 20 MeV/c^2 (stat. & syst. error)
280 - 360	-44.3 ± 46.5 ± 8.4	-11.1 ± 11.6 ± 2.1	0.800(1 ± 0.086)	-35.4 ± 37.2 ± 7.4	-8.9 ± 9.3 ± 1.8
360 - 440	-69.3 ± 55.3 ± 8.4	-17.3 ± 13.8 ± 2.1	0.929(1 ± 0.041)	-64.4 ± 51.3 ± 8.2	-16.1 ± 12.8 ± 2.1
440 - 490	-11.7 ± 45.4 ± 8.4	-4.7 ± 18.2 ± 3.4	0.999(1 ± 0.020)	-11.7 ± 45.4 ± 8.4	-4.7 ± 18.2 ± 3.4
490 - 540	69.6 ± 47.5 ± 8.4	27.8 ± 19.0 ± 3.4	1.032(1 ± 0.010)	71.8 ± 49.0 ± 8.7	28.7 ± 19.6 ± 3.5
540 - 570	-15.3 ± 39.2 ± 8.4	-10.2 ± 26.1 ± 5.6	1.045(1 ± 0.005)	-15.9 ± 41.0 ± 8.8	-10.6 ± 27.3 ± 5.9
570 - 600	103.9 ± 37.6 ± 8.4	69.3 ± 25.0 ± 5.6	1.047(1 ± 0.003)	108.8 ± 39.3 ± 8.8	72.5 ± 26.2 ± 5.9
600 - 625	61.0 ± 36.8 ± 8.4	48.8 ± 29.4 ± 6.7	1.042(1 ± 0.002)	63.6 ± 38.4 ± 8.8	50.9 ± 30.7 ± 7.0
625 - 650	101.8 ± 37.7 ± 8.4	81.5 ± 30.2 ± 6.7	1.033(1 ± 0.003)	105.2 ± 39.0 ± 8.7	84.2 ± 31.2 ± 7.0
650 - 670	66.0 ± 33.6 ± 8.4	66.0 ± 33.6 ± 8.4	1.022(1 ± 0.006)	67.4 ± 34.3 ± 8.6	67.4 ± 34.3 ± 8.6
670 - 690	118.9 ± 34.3 ± 8.4	118.9 ± 34.3 ± 8.4	1.008(1 ± 0.008)	119.8 ± 34.6 ± 8.5	119.8 ± 34.6 ± 8.5
690 - 710	165.5 ± 35.1 ± 8.4	165.5 ± 35.1 ± 8.4	0.991(1 ± 0.012)	164.1 ± 34.8 ± 8.6	164.1 ± 34.8 ± 8.6
710 - 730	140.8 ± 33.4 ± 8.4	140.8 ± 33.4 ± 8.4	0.972(1 ± 0.016)	136.8 ± 32.4 ± 8.5	136.8 ± 32.4 ± 8.5
730 - 750	164.4 ± 32.2 ± 8.4	164.4 ± 32.2 ± 8.4	0.949(1 ± 0.020)	156.0 ± 30.6 ± 8.6	156.0 ± 30.6 ± 8.6
750 - 765	$182.2 \pm 30.4\ ^{+15.0}_{-16.0}$	$243.0 \pm 40.5\ ^{+20.0}_{-21.3}$	0.927(1 ± 0.025)	$168.9 \pm 28.2\ ^{+14.5}_{-15.4}$	$225.3 \pm 37.6\ ^{+19.4}_{-20.6}$
765 - 770	$35.4 \pm 14.8\ ^{+3.0}_{-21.0}$	$141.6 \pm 59.3\ ^{+12.0}_{-84.0}$	0.970(1 ± 0.028)	$34.3 \pm 14.4\ ^{+3.1}_{-20.4}$	$137.3 \pm 57.5\ ^{+12.3}_{-81.6}$
770 - 775	$10.2 \pm 9.3\ ^{+8.0}_{-2.0}$	$40.9 \pm 37.3\ ^{+32.0}_{-8.0}$	0.956(1 ± 0.030)	$9.8 \pm 8.9\ ^{+7.7}_{-1.9}$	$39.1 \pm 35.7\ ^{+30.6}_{-7.7}$

Table 5.2: The $X(3872)$ yields before (uncorr.) and after (corr.) detector efficiency corrections with their statistical and systematic uncertainties. The inverse efficiency correction factors ξ_i are rescaled so that the total number of events remains the same after the correction. The yields are given with an artificial level of precision, because we want to show the dynamics of the yield change and to treat all the $m_{\pi\pi}$ slices equally, and therefore keep an excessive number of digits.

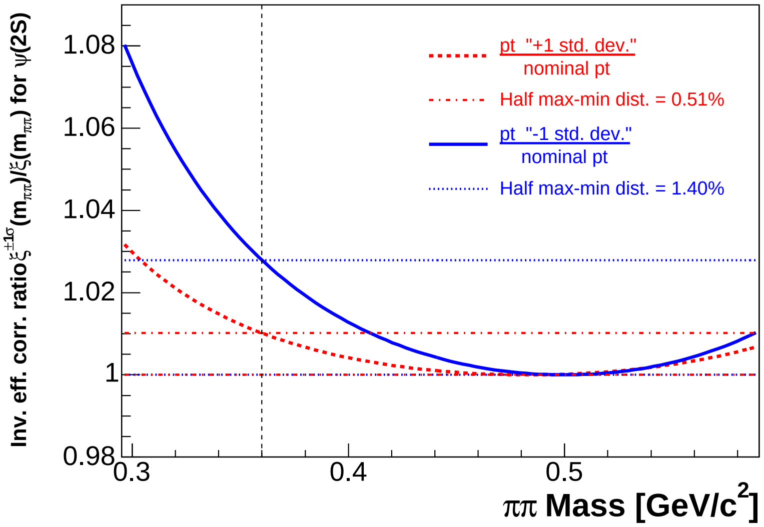

Figure 5-12: The systematic variation in efficiency for the $\psi(2S)$ coming from the parametrization of the Monte Carlo p_t spectrum.

Chapter 6

Fitting $\psi(2S)$ and $X(3872)$ $m_{\pi\pi}$ Spectra with Theoretical Models

6.1 Models for the $m_{\pi\pi}$ Spectra of Charmonia

The dipion mass spectrum for the $\psi(2S)$ is very well studied theoretically and a few models [15, 107, 108, 109, 110] have been developed to describe its shape. References [111, 112] are very helpful in providing explicit formulae for them. We will give a short overview of these models and then apply them to our $\psi(2S)$ data, to see that the shape of our $m_{\pi\pi}$ spectrum for $\psi(2S)$ is in accord with the previous knowledge about it. As was discovered back in 1975 with the data collected by the MARK II experiment, this shape is very far from a simple phase-space distribution [107, 113].

The models start their calculations with the *matrix element* M for the transition between the initial charmonium states and the final state $J/\psi\,\pi^+\pi^-$, or, in spectroscopic notations, ${}^3S_1\pi^+\pi^-$. The square of the absolute value of this quantity gives a prediction for the dipion mass distribution $\frac{dN}{dm_{\pi\pi}}$. Reference [15] calculates the matrix element with the help of a multipole expansion of the QCD Lagrangian. The model from Reference [108] gives a phenomenological analysis of the shape of the $m_{\pi\pi}$ spectrum in the decay $\psi(2S) \to J/\psi\pi^+\pi^-$. The other models [107, 109, 110] which we consider calculate the matrix element by applying current algebra and the partial conservation of axial-vector currents to the chiral QCD Lagrangian. References [109] and [110] also include some multipole-expansion techniques. A brief review of these models follows.

6.1.1 Yan Model

Our baseline model is that of Yan [15]. This model is based on a Taylor series expansion of the QCD Lagrangian. The idea behind the multipole expansion is the realization that one may consider the process of the hadronic transition between the initial heavy-quark state Φ' and the final one Φ as a two-step process: first the gluons are emitted from the heavy quark system and then they are converted into light hadrons, $\Phi' \to \Phi + gg$, $gg \to$ light hadrons. We will be considering the heavy-quark system in the external fields generated by the light quarks. The heavy-quark system moves slowly and has a much smaller size than the emitted light-quark system [114]. Therefore, one can treat the heavy quarks non-relativistically, and the Taylor series expansion of the color field converges quickly for heavy enough quark masses.

The author assumes that the multipole expansion is compatible with the hypothesis of partial conservation of axial-vector currents, parametrizes the matrix element in terms of a few free parameters, and calculates the $m_{\pi\pi}$ spectrum for ${}^3S_1$, ${}^1P_1$, ${}^3D_{1,2,3}$ initial states decaying into ${}^3S_1\pi^+\pi^-$.

We fit our $m_{\pi\pi}$ spectrum of the $\psi(2S)$ with the formula for the ${}^3S_1$ initial state. Reference [111] explicitly gives the $m_{\pi\pi}$ spectrum for this case as:

$$\frac{d\sigma}{dm_{\pi\pi}} = (PS)\times\left[(m_{\pi\pi}^2-2m_\pi^2)^2+\frac{B}{3A}(m_{\pi\pi}^2-2m_\pi^2)\left(m_{\pi\pi}^2-4m_\pi^2+2K^2\left(1+\frac{2m_\pi^2}{m_{\pi\pi}^2}\right)\right)+\mathcal{O}\left(\frac{B^2}{A^2}\right)\right], \tag{6.1}$$

where

$$K = \frac{M_{\psi(2S)}^2 - M_{J/\psi}^2 + m_{\pi\pi}^2}{2M_{\psi(2S)}},$$

and PS is the 3-body $J/\psi\,\pi\pi$ phase space from Equation 5.1. The parameters A and B are free parameters of the theory. The term $\mathcal{O}(B^2/A^2)$ is a higher-order correction, which was originally derived in Reference [15], but Reference [112] develops an explicit term:

$$\mathcal{O}\left(\frac{B^2}{A^2}\right) = \frac{1}{20}\frac{B^2}{A^2}\left[(m_{\pi\pi}^2-4m_\pi^2)^2+\frac{4}{3}(m_{\pi\pi}^2-4m_\pi^2)(m_{\pi\pi}^2+6m_\pi^2)\frac{K^2}{{m_{\pi\pi}}^2}+\right.$$
$$\left.+\frac{8}{3}(m_{\pi\pi}^4+2m_\pi^2m_{\pi\pi}^2+6m_\pi^4)\frac{K^4}{m_{\pi\pi}^4}\right]. \tag{6.2}$$

In our fits we use both forms of the model — with and without the higher-order correction.

6.1.2 Brown – Cahn Model

The Brown – Cahn model [107] preceded the Yan model. Yan's model in fact includes some of its techniques. Reference [107] does not use the multipole expansion techniques because they were not yet available at that time. Instead they base their calculations on a chiral Lagrangian approach. The details of the model are given in Reference [107]. Here we constrain ourselves to the main conclusions. Neglecting chiral symmetry breaking, Reference [107] expresses the matrix element for the $\psi(2S)\to J/\psi\,\pi^+\pi^-$ decay as:

$$M = F_\pi^{-2}\{\vec{\epsilon}\cdot\vec{\epsilon'}[-q_1^\mu q_{2\mu}A+q_1^0q_2^0B]+(\vec{\epsilon}\cdot\vec{q_1}\vec{\epsilon'}\cdot\vec{q_2}+\vec{\epsilon}\cdot\vec{q_2}\vec{\epsilon'}\cdot\vec{q_1})C\},$$

where F_π is the pion decay constant, $\vec{\epsilon}$ and $\vec{\epsilon'}$ are purely spatial polarizations of the J/ψ and the $\psi(2S)$, q_1^μ and q_2^μ are the pions' four-momenta, and A, B, and C are parameters. Both the J/ψ and $\psi(2S)$ are treated non-relativistically. The relativistic corrections are assumed to be small, as well as the momentum-dependent variations of A, B and C. According to Reference [107], the only significant corrections possibly may come from the S-wave pion-pion rescattering.

The parameters A and B turn out to be the same as for the Yan model. The terms associated with parameters B and C have strong angular correlations between the momentum of the dipion system and the momentum of the J/ψ. Such correlations were experimentally not detected at the time [113], and therefore Reference [107] assumed that $B = C = 0$. The $m_{\pi\pi}$ spectrum in this model is given by:

$$\frac{dN}{dm_{\pi\pi}} \sim (PS)\times\left(m_{\pi\pi}^2-2m_\pi^2\right)^2, \tag{6.3}$$

where PS denotes the $J/\psi\,\pi\pi$ phase space. This formula has no parameters except for the normalization factor. It is important to notice that Equation 6.3 is obtained from Equation 6.1

if the parameter B is set to zero.

6.1.3 Pham – Pire – Truong Model

The authors of this model [108] calculated the matrix element M of the $\psi(2S) \to J/\psi\,\pi^+\pi^-$ transition starting from the general assumption:

$$M = f(\epsilon' \cdot \epsilon) + g(\epsilon \cdot (q_1 + q_2))(\epsilon' \cdot (q_1 + q_2)) + h(\epsilon \cdot (q_1 - q_2))(\epsilon' \cdot (q_1 - q_2)),$$

where ϵ and ϵ' are polarizations of J/ψ and ψ', q_1 and q_2 are are the pions four-momenta and f, g and h are the scalar functions of the masses and energies of the involved particles.

The $m_{\pi\pi}$ spectrum obtained from this matrix element did not agree with the data [115], and therefore the authors reduced the matrix element to the simplest possible form:

$$M = (\epsilon' \cdot \epsilon)(f_1 + f_2 q_1 \cdot q_2).$$

The $m_{\pi\pi}$ spectrum obtained from this matrix element is

$$\frac{dN}{dm_{\pi\pi}} \sim (PS) \times ({m_{\pi\pi}}^2 - \lambda m_\pi^2)^2, \tag{6.4}$$

where λ is a free parameter. This formula is a generalization of Brown – Cahn Equation 6.3.

6.1.4 Voloshin – Zakharov Model

The Voloshin – Zakharov [109] model is based on a chiral Lagrangian approach and utilizes some multipole-expansion techniques to calculate the parameters of the Lagrangian. The matrix element in this model is initially calculated in the chiral limit $m_\pi = 0$ and then a phenomenological term λm_π^2 is added. Reference [111] quotes the differential cross-section for this model as:

$$\frac{dN}{dm_{\pi\pi}} \sim (PS) \times ({m_{\pi\pi}}^2 - \lambda m_\pi^2)^2, \tag{6.5}$$

where PS stands for $J/\psi\,\pi\pi$ phase space. Equations 6.5 and 6.4 are mathematically the same, so that we unify them under the same name “PPT/VZ model”. It is worth noting that this formula (Equation 6.4 or Equation 6.5) for $\lambda = 4$ is what we use in the Monte Carlo generation in this analysis as the S-wave parametrization of Chapter 4.

6.1.5 Novikov – Shifman Model

The Novikov – Shifman model [110] is a more elaborate version of Voloshin – Zakharov analysis [109], published just a few months later. This model includes smaller terms, formally of order α_s, which Reference [109] has neglected in the leading order. Reference [111] puts matrix element M for this model in a simple, easy-to-use form:

$$M \sim \left\{q^2 - \kappa(\Delta M)^2\left(1 + \frac{2m_\pi^2}{q^2}\right) + \frac{3}{2}\kappa[(\Delta M)^2 - q^2]\left(1 - \frac{4m_\pi^2}{q^2}\right)\left(\cos^2\theta_\pi^* - \frac{1}{3}\right)\right\},$$

where q is the four momentum of the dipion system in $\psi(2S)$ reference frame, θ_π^* is the angle between the J/ψ direction and the π^+ in the $\psi(2S)$ rest frame, and $\Delta M = M_{\psi(2S)} - M_{J/\psi}$.

The parameter κ is a free parameter of the theory. Reference [116] predicts κ to be about $0.15 \sim 0.20$. The parameter κ is expected to be different for $\psi(2S)$ and for other charmonia states. The differential cross-section is:

$$\frac{dN}{dm_{\pi\pi} d\cos\theta^*_\pi} \sim (PS) \times M^2,$$

where PS is the phase space. The $m_{\pi\pi}$ spectrum is given by [111]:

$$\frac{dN}{dm_{\pi\pi}} \sim |\vec{q}|\sqrt{q^2 - 4m_{\pi\pi}{}^2}\Big\{\big[q^2 - \kappa(\Delta M)^2\big(1 + \frac{2m_\pi^2}{q^2}\big)\big]^2 + \frac{\kappa^2}{5}[(\Delta M)^2 - q^2]^2\big(1 - \frac{4m_\pi^2}{q^2}\big)^2\Big\}. \quad (6.6)$$

This model predicts a small D-wave admixture to the predominantly S-wave dipion system. The matrix element consists of three terms, the first two correspond to S-wave contributions and the last one to the D-wave. A non-zero κ means that there is some D-wave component, but this is a small effect because the coefficient $\frac{\kappa^2}{5}$ is small.

6.2 Fitting the $m_{\pi\pi}$ Spectrum of the $\psi(2S)$

We want to apply the reviewed models to our $m_{\pi\pi}$ spectrum to be able to compare our data to the existing knowledge about its shape. We do a bin-integrated χ^2 fit to our data with the theoretical models described above. The naïve χ^2 would be:

$$\chi^2_{\text{naïve}} = \sum \left(\frac{N_i\xi_i - T_i}{\sigma(N_i)\xi_i}\right)^2,$$

where $N_i \pm \sigma(N_i)$ is the raw yield in the i-th $m_{\pi\pi}$ slice, ξ_i is the nominal detector efficiency correction function $\xi(m_{\pi\pi})$, integrated over the i-th $m_{\pi\pi}$ slice, and T_i is the theoretical yield prediction for i-th slice, also integrated over the i-th $m_{\pi\pi}$ slice.

But because we have shape-related correlations in the uncertainty of the detector efficiency, *i.e.* correlations in the uncertainties of the corrections $\sigma^{syst}(\xi_i)$ between neighboring $m_{\pi\pi}$ slices, we need to include them in this χ^2. Namely, we want to take into account the correlated systematic uncertainty due to variations in the shapes of the assumed $m_{\pi\pi}$ and p_t spectra. We cannot do this by propagating the error along with $\sigma(N_i)$ in the denominator of the χ^2, because in that case the errors would be treated as uncorrelated. So, we take a different approach. Let us consider the $m_{\pi\pi}$ parametrization first.

To account for the correlated systematic uncertainty in the variation of the $m_{\pi\pi}$ shape we change this shape from the nominal S-wave parametrization to the phase-space one. In mathematical language, we substitute the nominal correction function $\xi(m_{\pi\pi})$ by the changed function $\xi^{PS}(m_{\pi\pi})$, introduced in Section 4. We consider this change in shapes to correspond to a one standard deviation variation. To include this change into the fit we create a new floating parameter a, governing the $m_{\pi\pi}$ shape. This parameter continuously controls the change of this shape from S-wave (at $a = 0$) to phase-space (at $a = 1$). Mathematically this means that we multiply the yields N_i by a factor $[1 + a(\gamma_i^{PS} - 1)]$. The expression γ_i^{PS} here denotes the average of the continuous function from Equation 5.2, $\gamma^{PS}(m_{\pi\pi}) \equiv \xi^{PS}(m_{\pi\pi})/\xi(m_{\pi\pi})$, over the i-th $m_{\pi\pi}$ slice range. The parameter a is allowed to float, but is nominally constrained to have zero central value and a standard deviation of one.

The χ^2 function properly including the correlated systematics uncertainty on the $m_{\pi\pi}$ spectrum parametrization looks like:

$$\chi^2 = \sum \left(\frac{N_i \xi_i [1 + a(\gamma_i^{PS} - 1)] - T_i}{\sigma(N_i) \xi_i [1 + a(\gamma_i^{PS} - 1)]} \right)^2 + a^2 \tag{6.7}$$

where the term a^2 should be interpreted as $\left(\frac{a-0}{1}\right)^2$. This term introduces one more degree of freedom and one more parameter, so that the total number of the degrees of freedom does not change.

Having included such a correction for the change of the $m_{\pi\pi}$ shape into the χ^2, we do the same for the p_t shape. We change the p_t spectrum parametrization from the nominal $e^{a_0 + a_1 p_t + a_2 p_t^2}$ to the functions $\xi^{\pm 1\sigma}(m_{\pi\pi})$, defined in the Section 5.2.2. These functions are considered as corresponding to the variation of the shape by one standard deviation up and down ($\pm 1\sigma$). Then we introduce one more floating parameter, b, controlling the change of the shape of the correction function from the nominal (at $b = 0$) to the changed (at $b = 1$). Mathematically, we multiply the yields by one more factor, $[1 + b(\gamma_i^{\pm 1\sigma} - 1)]$. The expression $\gamma_i^{\pm 1\sigma}$, again, means the ratio of the correction functions from Equation 5.4, $\gamma^{\pm 1\sigma}(m_{\pi\pi}) = \xi^{\pm 1\sigma}(m_{\pi\pi}) / \xi(m_{\pi\pi})$, integrated over the i-th $m_{\pi\pi}$ slice. The parameter b is also allowed to float but constrained to have a central value of zero and a standard deviation of one.

The full χ^2 function properly including the correlated systematics uncertainty looks like:

$$\chi^2 = \sum \left(\frac{N_i \xi_i [1 + a(\gamma_i^{PS} - 1)][1 + b(\gamma_i^{\pm 1\sigma} - 1)] - T_i}{\sigma(N_i) \xi_i [1 + a(\gamma_i^{PS} - 1)][1 + b(\gamma_i^{\pm 1\sigma} - 1)]} \right)^2 + a^2 + b^2. \tag{6.8}$$

We have obtained two systematic variations for the p_t spectrum, $\gamma^{+1\sigma}$ and $\gamma^{-1\sigma}$, corresponding to the change of the shape of the p_t spectrum by one standard deviation steeper and shallower in p_t as determined in Section 5.2.2. It is a somewhat delicate matter of how to handle two asymmetric p_t variations into one uncertainty. Fortunately, the effects we are concerned with are small and we simplify things by taking the variation which has the largest impact on the shape, and use it to get a conservative estimate of the systematic uncertainty. In order to choose between $\gamma^{+1\sigma}$ and $\gamma^{-1\sigma}$ let us temporarily put $a = 0$. If there were no p_t variation (*i.e.* coefficient b were fixed to zero) the fitted χ^2 would necessarily be greater than with such a variation (*i.e.* non-zero b). For the systematic variation we want to use the p_t shape which is the furthest from the nominal one. We look at the change in the fit χ^2 to find out which shape is the furthest. Table 6.1 shows the χ^2 values for using the $\gamma^{+1\sigma}$ and $\gamma^{-1\sigma}$ in the χ^2 from Equation 6.8, and with the theoretical function T_i being Yan's formula for S-state with higher-order corrections. One can see that the biggest change in χ^2 value between the naïve χ^2 fit ($a = b = 0$) and the full χ^2 fit is achieved when $\gamma^{-1\sigma}$ is used. For this reason we take $\gamma^{-1\sigma}$ for the analysis.

The use of the fit χ^2 for the selection of $\gamma^{-1\sigma}$ over $\gamma^{+1\sigma}$ may in principle bias our fit results, but we expect this bias to be small. The change in χ^2 due to using $\gamma^{+1\sigma}$ instead of $\gamma^{-1\sigma}$ is less than 0.5 unit and the change in the fit result is small too: the B/A parameter is different by a tiny fraction of statistical uncertainty. Also, the $\psi(2S)$ fit is only used to obtain the already known shape of the $m_{\pi\pi}$ spectrum for $\psi(2S)$, we do not extract any new physics information from this fit, so that we neglect the possible small bias.

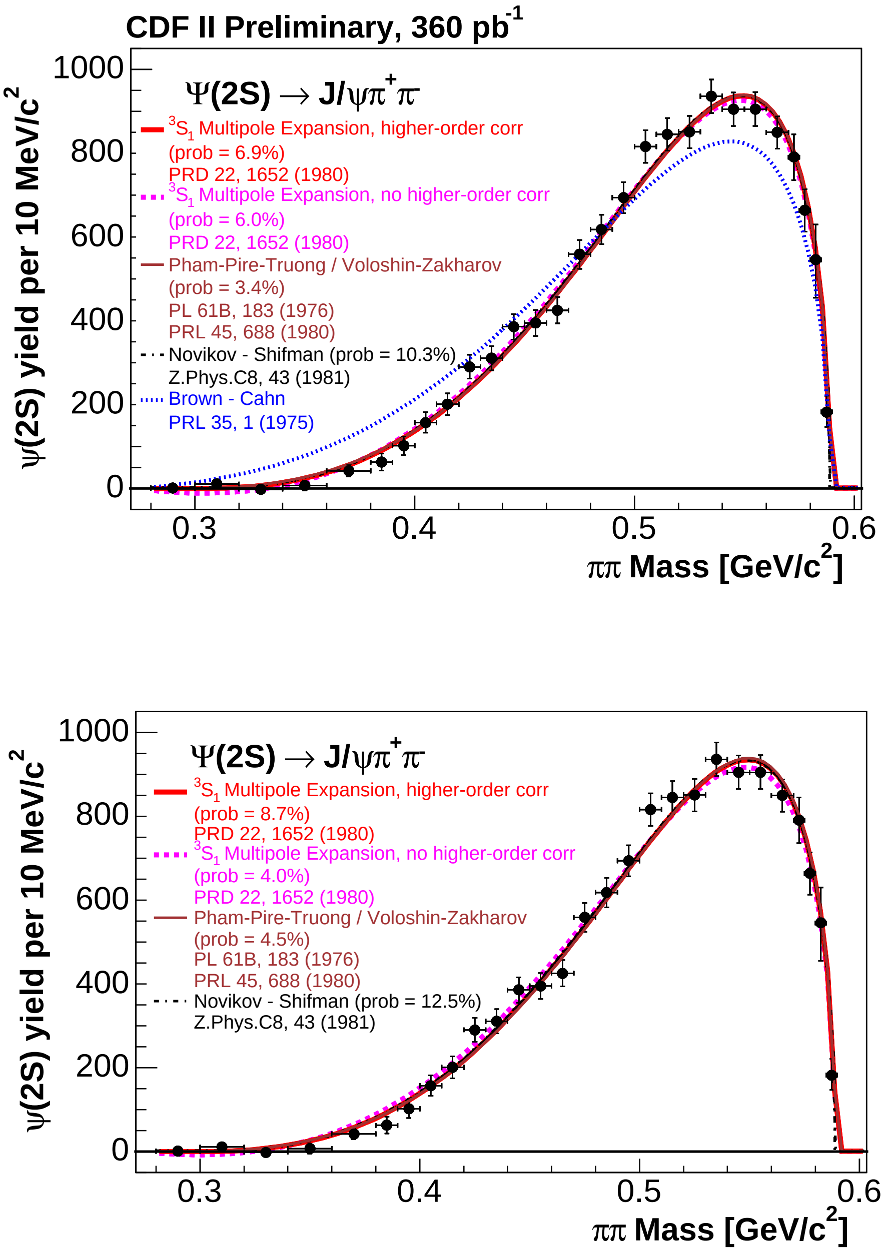

Figure 6-1: Fit of the $m_{\pi\pi}$ spectrum for $\psi(2S)$ with theoretical curves from References [15, 107, 108, 109, 110]. TOP: the fits with all the parameters floating. BOTTOM: the fits with only normalizations floating and all other parameters are fixed to the values from BES [111].

Parameter b	$\gamma^{+1\sigma}$ or $\gamma^{-1\sigma}$?	Parameter a	Fit χ^2	B/A
Floats: 0.64 ± 0.56	Using $\gamma^{+1\sigma}$	Fixed to zero	39.8234	-0.343 ± 0.021
Floats: 0.75 ± 0.48	Using $\gamma^{-1\sigma}$	Fixed to zero	39.3317	-0.341 ± 0.022
Floats: 0.62 ± 0.58	Using $\gamma^{+1\sigma}$	Floats: 0.89 ± 1.40	37.8277	-0.344 ± 0.022
Floats: 0.73 ± 0.50	Using $\gamma^{-1\sigma}$	Floats: 0.89 ± 0.39	$\chi^2_{min} = 37.3978$	-0.342 ± 0.022
Fixed to zero	–	Fixed to zero	$\chi^2_{naïve} = 40.3365$	-0.347 ± 0.021
Fixed to zero	–	Floats: 0.90 ± 1.40	38.2782	-0.344 ± 0.021

Table 6.1: The naïve and the full χ^2 with $\gamma^{\pm 1\sigma}$, obtained from the $m_{\pi\pi}$ spectrum fit for $\psi(2S)$.

6.3 Fit Results for the $\psi(2S)$

The top part of Figure 6-1 displays our $\psi(2S)$ data fitted with the different theoretical models. The Yan model for the ${}^3S_{1^{--}}$ state without higher-order correction describes the data reasonably well, with a 6.0% fit probability. The inclusion of the higher-order correction diminishes the χ^2 by one unit and thus increases the fit probability to 6.9%. The PPT/VZ model also describes the data, with a fit probability of 3.4%. The Novikov – Shifman model yields an even higher fit probability of 10.3%. All these fits are very close to each other, except for the Brown – Cahn model. This model does not describe the data, because of its assumption that $B = 0$. The fit χ^2 of 226 is so large for the given number of the degrees of freedom of 27 that we do not even calculate the tiny probability for this fit.

The complete results of these fits are given in the Table 6.2. This table also compares the parameters in our fits with those obtained by the BES Collaboration [111] for the $\psi(2S) \to J/\psi\,\pi^+\pi^-$ decay. Their sample is quite large [23k of $\psi(2S)$] and they fit the $m_{\pi\pi}$ spectrum with all the same models as we do, except the Brown—Cahn model. The BES data and fits are given in Figure 6-2. All four curves in this picture are very much alike. From Table 6.2 we conclude that our fit results are very close to the BES ones — less than one standard deviation away. The numbers in the last column of Table 6.2 are obtained by fitting CDF data with the theoretical parameters fixed to the BES values, with only the normalization left to float. By fixing a parameter we loose a degree of freedom, so that the fit probabilities in the last column may be higher than the original ones. These fit probabilities are reasonable, and this fact confirms, that our data is in good agreement to that of the BES. The actual fits of our data with the theory parameters fixed to the BES values are shown in the bottom part of Figure 6-1.

Since our $m_{\pi\pi}$ spectrum for the $\psi(2S)$ is close to that from the large BES sample, we conclude that our technique of obtaining the $m_{\pi\pi}$ spectrum, including the detector efficiency corrections, are vindicated.

6.4 Models Used for the $X(3872)$

Unlike the $\psi(2S)$, the quantum numbers of the $X(3872)$ are unknown. We do not even know whether it is a $c\bar{c}$ state. As pointed out in Section 1.3, the properties of the $X(3872)$ could be inferred from the quantum numbers of the dipion system in the $X(3872) \to J/\psi\,\pi^+\pi^-$ decay. According to Equation 1.17, the dipion system may be considered either 0^{++} or 1^{--}, where we ignore the less likely possibility of D-wave pions.

	Our result	Result from BES [111]	Difference	Our result with parameters fixed to BES value
Yan model [15] $^3S_1$ state with higher-order corr.	$B/A = -0.342 \pm 0.022$ $\chi^2/NDF = 37/26$ Prob = 6.9%	$B/A = -0.336 \pm 0.009 \pm 0.019$ $\chi^2/NDF = 60/45$ Prob = 6.4%	-0.006 ± 0.024 (0.2σ)	$B/A = -0.336$ $\chi^2/NDF = 41/27$ Prob = 8.7%
Yan model [15] $^3S_1$ state no higher-order corr.	$B/A = -0.245 \pm 0.011$ $\chi^2/NDF = 38/26$ Prob = 6.0%	$B/A = -0.225 \pm 0.004 \pm 0.028$ $\chi^2/NDF = 84/45$ Prob = 0.02%	-0.020 ± 0.030 (0.7σ)	$B/A = -0.225$ $\chi^2/NDF = 37/27$ Prob = 4.0%
Brown-Cahn model [107]	$\chi^2/NDF = 226/27$	–	–	–
PPT/VZ model [108, 109]	$\lambda = 4.34 \pm 0.15$ $\chi^2/NDF = 41/26$ Prob = 3.4%	$\lambda = 4.35 \pm 0.06 \pm 0.17$ $\chi^2/NDF = 69/45$ Prob = 1.0%	-0.01 ± 0.24 (0.04σ)	$\lambda = 4.35$ $\chi^2/NDF = 41/27$ Prob = 4.5%
Novikov - Shifman model [110]	$\kappa = 0.189 \pm 0.007$ $\chi^2/NDF = 35/26$ Prob = 10.3%	$\kappa = 0.186 \pm 0.003 \pm 0.006$ $\chi^2/NDF = 55/45$ Prob = 14.6%	0.003 ± 0.010 (0.3σ)	$\kappa = 0.186$ $\chi^2/NDF = 36/27$ Prob = 12.5%

Table 6.2: The results of the different theoretical fits of $m_{\pi\pi}$ spectrum for $\psi(2S)$ compared to those obtained by BES Collaboration [111].

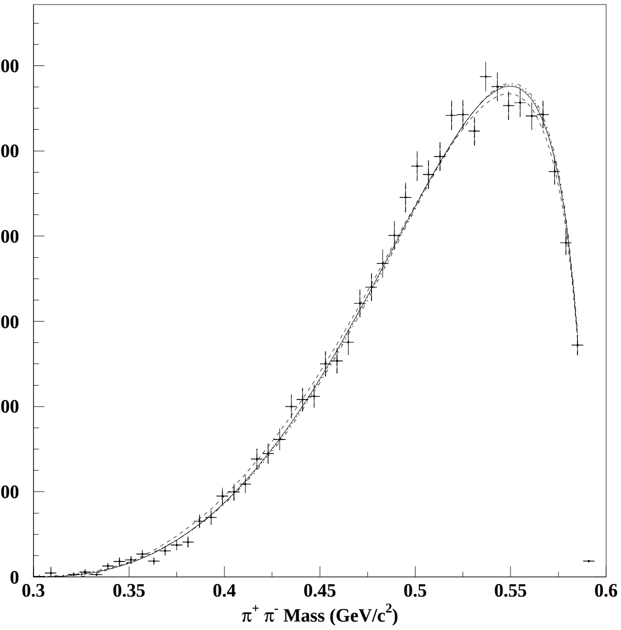

Figure 6-2: The $m_{\pi\pi}$ distribution for the $\psi(2S)$ produced by the BES collaboration [111]. The solid curve is the Novikov-Shifman model, the long-dashed and short-dashed are the Yan's ${}^3S_1$ model with and without the higher-order corrections, respectively, and the dash-dotted curve is the PPT/VZ model.

The 0^{++} dipions must come from C-negative states, either conventional charmonia or exotic. To check if the $X(3872)$ could be a C-negative charmonium state we fit our $m_{\pi\pi}$ spectrum with the multipole expansion predictions from Yan [15] described in Section 6.1.1. They are developed for ${}^3S_{1--}$, ${}^1P_{1+-}$, and ${}^3D_{1,2,3--}$ charmonia. Unfortunately, we have no predictions for the shape of the $m_{\pi\pi}$ spectrum for C-negative exotic states.

As for the 1^{--} dipions, they come from C-positive states, again, either conventional charmonia or exotics. As we saw at the end of Section 1.2, the two pions in the 1^{--} state must have isospin $I = 1$. But charmonium has isospin $I = 0$, so that the charmonium decays to $J/\psi\,(\pi^+\pi^-)_{(1--)}$ are isospin violating, and should normally be highly suppressed. However, we still take this option into account. The states that decay into 1^{--} dipions proceed through a virtual ρ^0, and we describe their dipion mass spectra by a Breit-Wigner resonance for the ρ^0 modulated with the $J/\psi\,\pi^+\pi^-$ phase space. This shape, though, does not distinguish between the hypotheses of the $X(3872)$ being a conventional C-positive charmonium and an exotic state.

6.4.1 0^{++} Dipions

The formula for the multipole expansion of Yan for the ${}^3S_1 \to {}^3S_1\pi^+\pi^-$ transitions is given in Equation 6.1. Of course, it should be modified to accommodate the different masses of the $\psi(2S)$ and the $X(3872)$.

The prediction for the ${}^1P_1 \to {}^3S_1\pi^+\pi^-$ transition is obtained in the following way. Reference [117] gives the multipole expansion prediction for the ${}^3S_1 \to {}^1P_1\pi^+\pi^-$ transition. However, in the non-relativistic approximation of the multipole expansion the spin and angular momentum components are decoupled and the expansion only depends on the orbital components. This means that the $m_{\pi\pi}$ distribution for the ${}^3S_1 \to {}^1P_1\pi^+\pi^-$ is the same as for the ${}^1P_1 \to {}^3S_1\pi^+\pi^-$

transition [118]. The $m_{\pi\pi}$ distribution for the ${}^1P_1$ is:

$$\begin{aligned}\frac{dN}{dm_{\pi\pi}} \sim\ & K\sqrt{M_{\pi\pi}^2 - 4m_\pi^2}\left\{(M_{\pi\pi}^2 - 4m_\pi^2)^2\left[4\frac{K_0^4}{M_{\pi\pi}^4} - 3\frac{K_0^2}{M_{\pi\pi}^2} - 1\right]\right. \\ & \left. +40(M_{\pi\pi}^2 - m_\pi^2)m_\pi^2\frac{K_0^2}{M_{\pi\pi}^2}\left[\frac{K_0^2}{M_{\pi\pi}^2} - 1\right]\right\}, \qquad (6.9)\end{aligned}$$

where

$$K = \frac{\sqrt{[(M_X + M_{J/\psi})^2 - M_{\pi\pi}^2][(M_X - M_{J/\psi})^2 - M_{\pi\pi}^2]}}{2M_X}, \quad \text{and} \qquad (6.10)$$

$$K_0 = \frac{M_X^2 - M_{J/\psi}^2 + M_{\pi\pi}^2}{2M_X}. \qquad (6.11)$$

For the three D-wave states, ${}^3D_{1,2,3^{--}} \to {}^3S_{1^{--}}\pi^+\pi^-$, the multipole expansion gives:

$$\frac{dN}{dm_{\pi\pi}} \sim K\sqrt{M_{\pi\pi}^2 - 4m_\pi^2}\left\{(M_{\pi\pi}^2 - 4m_\pi^2)^2\left[1 + \frac{2}{3}\frac{K^2}{M_{\pi\pi}^2}\right] + \frac{8}{15}\frac{K^4}{M_{\pi\pi}^4}(M_{\pi\pi}^4 + 2M_{\pi\pi}^2 m_\pi^2 + 6m_\pi^4)\right\}, \qquad (6.12)$$

where K is defined as before (Equation 6.10) [15].

6.4.2 1^{--} Dipions

The remaining (C-positive) charmonia states fall under the $J/\psi\,\rho^0$ heading. This case is also what is expected from the C-positive exotic interpretation of the $X(3872)$. As noted above, we assume that the dipion spectrum follows the ρ^0 Breit-Wigner distribution modulated by the 3-body $J/\psi\,\pi\pi$ phase space PS from Equation 5.1:

$$\frac{dN}{dm_{\pi\pi}} \sim \frac{\Gamma}{(m_{\pi\pi} - M_\rho)^2 + \Gamma_\rho^2/4} \times (PS). \qquad (6.13)$$

To see the effect of the Breit-Wigner resonance in this formula more clearly, we also fit the $X(3872)$ data with the simple 3-body $J/\psi\,\pi\pi$ phase space.

6.5 Fitting the $m_{\pi\pi}$ Spectrum of the $X(3872)$

When we fit the $X(3872)$ data we use the same method as for the $\psi(2S)$, namely we minimize the χ^2 from Equation 6.8. Just as in the $\psi(2S)$ case we pick one of the systematic variations to use for the p_t spectrum: $\gamma^{+1\sigma}$ or $\gamma^{-1\sigma}$. The Table 6.3 helps us to make this decision in favor of $\gamma^{-1\sigma}$, the same as for the $\psi(2S)$. This variation gives us the greatest change in the shape relative to the naïve χ^2 fit, which is reflected in the largest χ^2 change, *i.e.* lowest χ^2 value. The theory function chosen for these comparison fits is the same as for the $\psi(2S)$ case : Yan's formula for the ${}^3S_1$ state with higher-order corrections. And just as for the $\psi(2S)$ case, even though the choice of $\gamma^{-1\sigma}$ and not $\gamma^{+1\sigma}$ may introduce a bias into the fit, this bias is small. The changes in both χ^2 and the shape (the B/A parameter) are negligible. Also, this bias is formally only present in the Yan's formula for the ${}^3S_1$ state, the fit with the $J/\psi\,\rho^0$ hypothesis, which will be the most interesting result for the $X(3872)$, was not utilized in selecting which systematic to use.

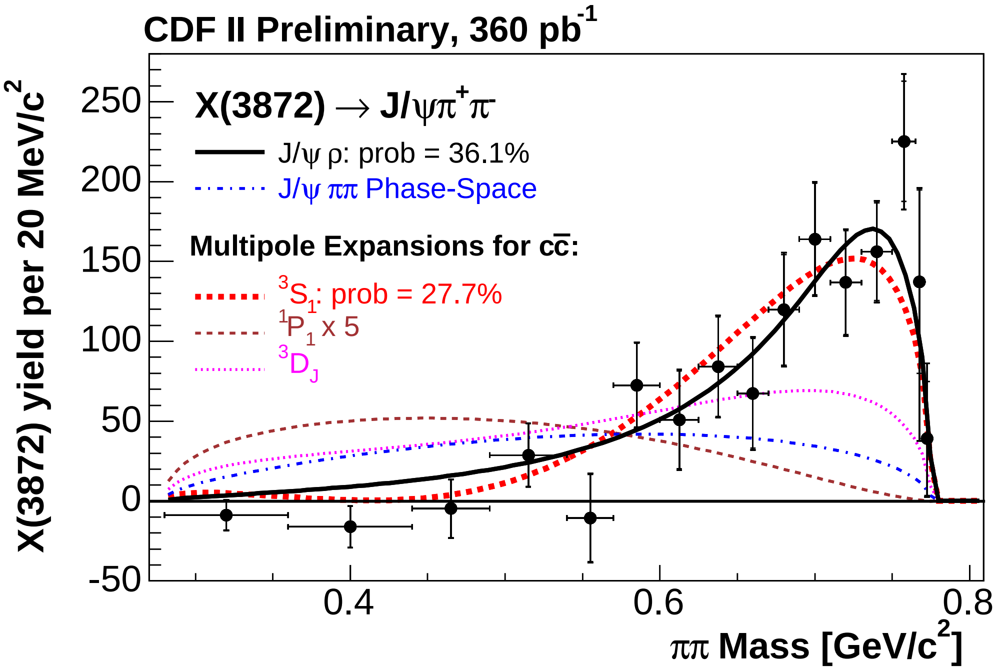

Figure 6-3: Fits of the $m_{\pi\pi}$ spectrum for $X(3872)$ with $J/\psi\,\rho^0$ hypothesis (Equation 6.13), with simple $J/\psi\,\pi\pi$ phase-space (Equation 5.1), and with multipole expansion for $c\bar{c}$ for the ${}^3S_1, {}^1P_1$ and ${}^3D_{1,2,3}$ cases [15, 117].

6.6 Fit Results for the $X(3872)$

Figure 6-3 displays the fits of the $X(3872)$ $m_{\pi\pi}$ spectrum with all formulae from Section 6.4: the $c\bar{c}$ multipole expansion predictions for C-negative S-wave, P-wave and D-wave, the simple 3-body $J/\psi\,\pi\pi$ phase-space hypothesis, and with the ρ^0 resonance modified by phase-space. The results of the fit are summarized in Table 6.4. The parameter B/A there is free parameter of the Yan model. The $J/\psi\,\rho^0$ hypothesis and $c\bar{c}$ multipole expansion for the ${}^3S_1$ give the best descriptions of the data. The fit probabilities are 36.1% and 27.7%, respectively. The $c\bar{c}$ multipole expansions for the ${}^1P_1$ and ${}^1D_J$ and the simple $J/\psi\,\pi\pi$ phase-space model are incompatible with the data. The fit χ^2 in these fits is so large for the given number of degrees of freedom that we do not even calculate the infinitesimal fit probability.

The similar $m_{\pi\pi}$ plot from the Belle Collaboration is given in Figure 1-1, together with fits for the ${}^3S_1$ drawn with dashed line and ${}^3D_J$ shown by solid line dipion states (Equations 6.1 and 6.12). One can see that the data are peaking somewhat stronger than both theory curves, but the error bars are too large to make any firm conclusions.

6.7 Discussion of Theoretical Implications

Now let us discuss the implications of our fit results for the $X(3872)$. We will consider separately the 0^{++} and 1^{--} dipion systems. First, we consider the charmonium options for the $X(3872)$.

Parameter b	$\gamma^{+1\sigma}$ or $\gamma^{-1\sigma}$?	Parameter a	Fit χ^2	B/A
Floats: -0.03 ± 1.29	Using $\gamma^{+1\sigma}$	Fixed to zero	16.6985	-0.582 ± 0.145
Floats: -0.22 ± 1.32	Using $\gamma^{-1\sigma}$	Fixed to zero	16.6913	-0.587 ± 0.110
Floats: -0.01 ± 1.14	Using $\gamma^{+1\sigma}$	Floats: 0.40 ± 1.52	16.6203	-0.582 ± 0.145
Floats: -0.22 ± 1.32	Using $\gamma^{-1\sigma}$	Floats: 0.40 ± 1.52	$\chi^2_{min} = 16.6133$	-0.584 ± 0.111
Fixed to zero	–	Fixed to zero	$\chi^2_{naïve} = 16.6985$	-0.585 ± 0.124
Fixed to zero	–	Floats: 0.40 ± 1.52	16.6203	-0.582 ± 0.108

Table 6.3: The naïve and the full χ^2 with $\gamma^{(\pm 1\sigma)}$, obtained from the $m_{\pi\pi}$ spectrum fit for $X(3872)$.

Model		Fit results for $X(3872)$
Multipole Expansion for $c\bar{c}$	Yan [15] $^3S_1$, higher-order corr.	$B/A = -0.584 \pm 0.111$ $\chi^2/NDF = 17/14$ Prob = 27.7%
	Yan [117] $^1P_1$	$\chi^2/NDF = 127/15$
	Yan [15] ^3D_J	$\chi^2/NDF = 76/15$
	$J/\psi\,\pi\pi$ Phase-Space	$\chi^2/NDF = 102/15$
	$X(3872) \to J/\psi\,\rho^0$ (Breit-Wigner × PS)	$\chi^2/NDF = 16/15$ Prob = 36.1%

Table 6.4: The results of the different theoretical fits of the $m_{\pi\pi}$ spectrum for the $X(3872)$.

$n^{2s+1}\ell_{J^{PC}}$	Known	Mass	J^{PC} of $\pi^+\pi^-$	Comments
1^1S_{0-+}	$\eta_c(1S)$	2980		
1^3S_{1--}	J/ψ	3097		
1^1P_{1+-}	$h_c(1P)$	3525	0^{++}	
1^3P_{0++}	$\chi_{c0}(1P)$	3415	1^{--}	
1^3P_{1++}	$\chi_{c1}(1P)$	3510	1^{--}	
1^3P_{2++}	$\chi_{c2}(1P)$	3556	1^{--}	
1^1D_{2-+}		3838	1^{--}	← **$m_{\pi\pi}$ allowed** (isospin violating)
1^3D_{1--}	$\psi(3770)$	3770	0^{++}	
1^3D_{2--}		3830	0^{++}	← ME prediction incompatible with data
1^3D_{3--}		3868	0^{++}	← ME prediction incompatible with data
2^1S_{0-+}	$\eta_c(2S)$	3638	1^{--}	
2^3S_{1--}	$\psi(2S)$	3686	0^{++}	
2^1P_{1+-}		3968	0^{++}	← ME prediction incompatible with data, also can be excluded on other grounds
2^3P_{0++}		3932	1^{--}	← $m_{\pi\pi}$ allowed (isospin violating), but can be excluded on other grounds (not seen in $\gamma\gamma$ fusion)
2^3P_{1++}		4008	1^{--}	← **$m_{\pi\pi}$ allowed** (isospin violating)
2^3P_{2++}		3966	1^{--}	← $m_{\pi\pi}$ allowed (isospin violating), but can be excluded on other grounds (not seen in $\gamma\gamma$ fusion)
3^1S_{0-+}			1^{--}	← $m_{\pi\pi}$ allowed (isospin violating), can be excluded on other grounds
3^3S_{1--}	$\psi(4040)$	4040	0^{++}	← ME prediction compatible with data, but can be excluded on other grounds

Table 6.5: Summary of standard charmonium states with the measured/predicted masses and the J^{PC} of dipion system in the decay into $J/\psi\,\pi^+\pi^-$. The comments about possible assignments for the $X(3872)$ in light of the measured $m_{\pi\pi}$ spectrum shape are also given.

6.7.1 Charmonium

Table 6.5 summarizes the spin-parities of the standard $c\bar{c}$ states, the names of the known corresponding particles and their masses and the spin-parities of the dipion system in the decay into $J/\psi\,\pi^+\pi^-$. The masses of the unobserved states come from Reference [32]. The states $2D$, $3P$, $3D$ and higher, and the states with $L > 2$ are not included, because they are expected to be too heavy for the $X(3872)$ [32]. The options for the $X(3872)$ are evaluated in the last column in Table 6.5.

0^{++} Dipions

In Section 1.4 we considered a list of possible $c\bar{c}$ options for the $X(3872)$ and found four viable candidates: 1^1D_{2-+}, 1^3D_{2--}, 1^3D_{3--} and 2^3P_{1++}. Two of them, 1^3D_{2--} and 1^3D_{3--}, are C-negative and decay into 0^{++} dipions. But our shape of the $m_{\pi\pi}$ spectrum clearly disfavors the D-wave charmonium, based on the multipole-expansion predictions. The data favors the $^3S_{1--}$ state. But all the low-level $^3S_{1--}$ states are known already: 1^3S_{1--} is J/ψ, 2^3S_{1--} is $\psi(2S)$ and

$3^3S_{1^{--}}$ is $\psi(4040)$. The $4^3S_{1^{--}}$ state must be even heavier than $\psi(4040)$, *i.e.* much heavier than the $X(3872)$. We, therefore, exclude the $^3S_{1^{--}}$ option for the $X(3872)$, even though its $m_{\pi\pi}$ spectrum is compatible with the multipole expansion predictions.

A word of caution is in order. One may question whether the multipole expansion is a reliable theory. Just like any other theory, it is based on a series of assumptions and approximations. The question about its dependability is discussed in the literature [119, 120, 121, 122]. The main point of this discussion is that the multipole expansion model does not have a very firm grounding in experimental verifications. Despite several successes, its predictions are known to clearly fail for $\Upsilon(3S) \rightarrow \Upsilon(1S)\pi^+\pi^-$ transition [123, 124]. This is a standing problem in quarkonia physics.

In summary, we found no viable conventional charmonium options for the $X(3872)$ decaying into 0^{++} dipions based on the multipole expansion predictions. But the multipole expansion model itself is not completely understood yet.

1^{--} Dipions

If the $X(3872)$ is a conventional charmonium state decaying into a 1^{--} dipion system then the pions in the final state must have isospin $I = 1$. Since charmonium has $I = 0$, such a decay would be isospin violating and, therefore, should be significantly suppressed. To consider the 1^{--} dipion for a conventional charmonium the $X(3872)$ one needs to accept the isospin violation. In principle, this is a plausible option if one takes into account the proximity of the $X(3872)$ to $D^0\overline{D}^{*0}$ and open channel coupling between these two states. The $D^0\overline{D}^{*0}$ system is not an isospin eigenstate, so that we can "bypass" the isospin conservation law by virtual coupling to this state.

Another feature of the decay into a 1^{--} dipion is that this spin-parity coincides with the spin-parity of the ρ^0-meson, and that the decay proceeds via a ρ^0. The upper kinematic boundary for the $m_{\pi\pi}$ spectrum is below the nominal ρ^0 mass and only because of its large width [21] can the ρ^0 extend down into the allowed region. Figure 6-3 shows that our data are compatible with the $J/\psi\,\rho^0$ hypothesis. There are two $c\bar{c}$ states available: the $1^1D_{2^{-+}}$ and the $2^3P_{1^{++}}$.

If the $X(3872)$ is a $1^1D_{2^{-+}}$ then the isospin-conserving decay into $\eta_c\pi^+\pi^-$ is expected to have a much higher branching ratio than the observed isospin-violating decay $X(3872) \rightarrow J/\psi\,\pi^+\pi^-$. Belle is searching for $X(3872) \rightarrow \eta_c\pi^+\pi^-$, but has not reported anything yet. Although, this fact by itself cannot be considered as a strong objection against the $1^1D_{2^{-+}}$ assignment for the $X(3872)$, because the η_c is quite hard to isolate. We conclude that the $1^1D_{2^{-+}}$ charmonium is a viable option for the $X(3872)$.

The $2^3P_{1^{++}}$ state, being assigned a mass of 3872 MeV/c^2, is expected to have a narrow width 1-2 MeV [13], which is consistent with the limit on the $X(3872)$ width. The dominant decays of the $2^3P_{1^{+-}}$ state are predicted to be $J/\psi\,\gamma$ and $\psi(2S)\,\gamma$, where the former contradicts Belle's measurement (Equation 1.6). Also, the predicted mass of the $2^3P_{1^{+-}}$ is $\sim$ 80 MeV/c^2 higher than $X(3872)$'s observed one [13]. Nevertheless we consider the $2^3P_{1^{++}}$ as a viable charmonium option for the $X(3872)$ too.

Our conclusion is that if the $X(3872)$ is a $c\bar{c}$ state decaying with isospin violation into 1^{--} dipion, then it must be either the $1^1D_{2^{-+}}$ or the $2^3P_{1^{++}}$.

6.7.2 Exotica

Now let us consider the implications of the $X(3872)$ $m_{\pi\pi}$ measurement performed in this thesis for different exotic models described in the Introduction. These models consider the $X(3872)$ as glueball, hybrid, cusp and molecule (including other 4-quark states). Our main result, relevant for these models, is that the $m_{\pi\pi}$ spectrum is consistent with $J/\psi\,\rho^0$ hypothesis, which implies the positive C-parity of the $X(3872)$.

The positive C-parity of the $X(3872)$ invalidates the glueball model from Section 1.7 which predicts the $X(3872)$ with $J^{PC} = 1^{--}$. For the case of the hybrid model, our results favor the available C-positive option 1^{-+}, but does not answer the question if the $X(3872)$ is a hybrid or not. The same statement is true about the cusp hypothesis: our measurement is consistent with predicted $J^{PC} = 1^{++}$, but conveys no further information as to whether the $X(3872)$ is a real bound state or a dynamic cusp in the rescattering amplitude at the $D^0\overline{D}^{0*}$ threshold.

Speaking of the molecular hypotheses, we conclude that our measurement is consistent with the models from the References [42] and [46], proposing molecular models with positive C-parity, and disfavors the model from the Reference [12], considering the C-negative mixture of molecule with $c\bar{c}$.

The diquark-antidiquark model developed in Reference [48] predicts the J^{PC} of the $X(3872)$ to be 1^{++}, which is compatible with our $m_{\pi\pi}$ measurement. Although, the $X(3872)$ isospin doublet, predicted by this model is not observed in our data (there is no “double-hump” structure in the $X(3872)$ peak), unless we see an unresolved mixture of both members of the doublet.

Chapter 7

Conclusion

In August 2003 the Belle Collaboration announced discovery of a new state $X(3872)$ found in the exclusive decay $B^+ \to K^+ X(3872) \to K^+ J/\psi\,\pi^+\pi^-$. A few models were proposed to explain the properties of this state — from conventional charmonium state to D-$\overline{D}^*$ "molecules" and other exotic hypotheses. To investigate the viability of these models, a wide net of searches for other decay modes of the $X(3872)$ was cast, mostly with negative results. The shape of the mass distribution of the two pions in the decay $X(3872) \to J/\psi\,\pi^+\pi^-$ may also shed light on the puzzling nature of the $X(3872)$.

In this thesis we measure the distribution of dipion masses by using a 360 pb^{-1} sample of dimuon triggers collected at CDF during the Tevatron's Run II.

For comparison, and as a control, we have also extracted the $m_{\pi\pi}$ spectrum for the $\psi(2S) \to J/\psi\,\pi^+\pi^-$ decay using the same technique. It is shown in Figure 4-10. This $m_{\pi\pi}$ spectrum is well-studied experimentally and theoretically. Our measurement is consistent with prior measurements [111], and confirms theoretical models described in References [15, 108, 109, 110]. The model from Reference [107] has noticeable shortcomings due to an improper assumption about the absence of strong angular correlations.

The measured $m_{\pi\pi}$ spectrum for the $X(3872)$ is shown in Figure 7-1. The detector efficiency corrections, which have a relatively minor effect on the shape of the $m_{\pi\pi}$ spectrum, have been applied. The prior dipion mass spectrum measurements are given in Figures 1-1 (Belle) and 1-2 (BaBar). Both have rather large uncertainties on the data points, which make it hard to determine the shape precisely. We confirm Belle's original report [1] that the $m_{\pi\pi}$ spectrum peaks at high mass values.

We fit the $m_{\pi\pi}$ spectrum with theoretical models, based on a multipole expansion of QCD Lagrangian for $c\bar{c}$, for different $c\bar{c}$ quantum states. The ${}^3S_1$ charmonium fits the data quite well, with the fit probability 27.7%. Although the ${}^3S_1$ charmonium hypothesis must be excluded on other grounds. The multipole expansions for the ${}^1P_1$ and the ${}^3D_{1,2,3}$ charmonia are in clear disagreement with the data.

We also test the hypothesis that the dipion originates from a ρ^0 by fitting the spectrum with a Breit-Wigner resonance multiplied by the 3-body $J/\psi\,\pi\pi$ phase space factor. This hypothesis fits the data very well, with the fit probability 36.1%. We conclude that our $m_{\pi\pi}$ distribution for the $X(3872)$ is compatible with $J/\psi\,\rho^0$ hypothesis. This hypothesis, in turn, implies that the $X(3872)$ has positive C-parity.

The C-positive $X(3872)$ is consistent with Belle's evidence of the decay $X(3872) \to J/\psi\,\pi^+\pi^-\pi^0$, with the tripion being interpreted as the ω meson [11]. Also, the positive C-parity of the $X(3872)$ is strongly confirmed by another result from Belle announced after the completion of this work:

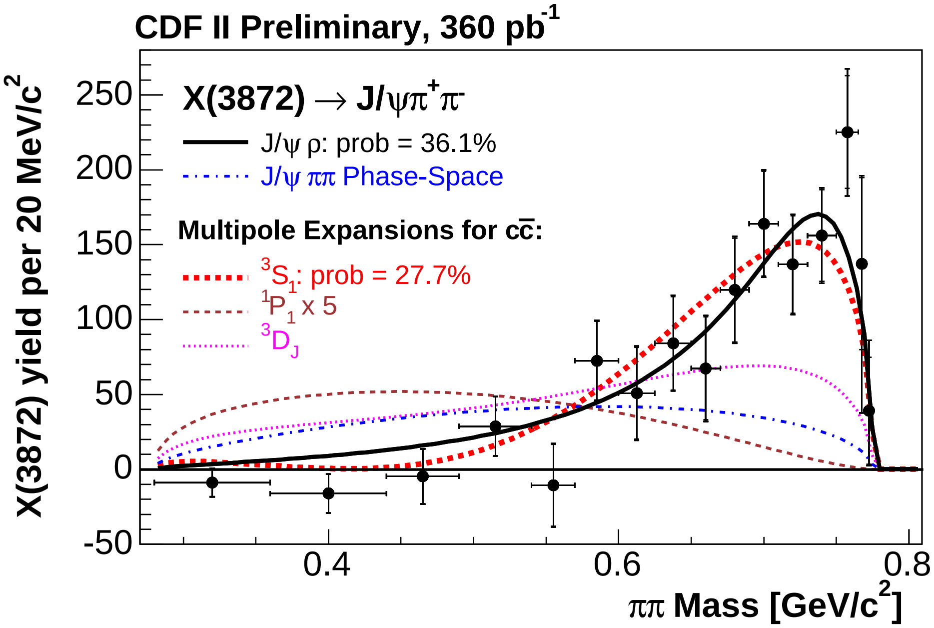

Figure 7-1: The measured $m_{\pi\pi}$ spectrum for $X(3872)$ fitted with different theoretical models described in Chapter 6.

the observation of the decay $X(3872) \to J/\psi\,\gamma$ [17].

As for the nature of the $X(3872)$ we can argue that it could be either a 1^1D_{2-+} or 2^3P_{1++} charmonium decaying into $J/\psi\,\pi^+\pi^-$ with non-conservation of isospin, or C-positive exotic state, such as a D^0-$\overline{D}^{*0}$ molecule.

Bibliography

[1] S.-L. Choi *et al.* (Belle Collaboration), *Observation of a Narrow Charmonium-Like State in Exclusive* $B^{\pm} \rightarrow K^{\pm} - \pi^{+}\pi^{-}J/\psi$ *Decays*, Phys. Rev. Lett. **91** 262001 (Dec 2003);
see also: K. Abe *et al.* (Belle Collaboration), hep-ex/0308029, revised version hep-ex/0309032.

[2] D. Acosta *et al.* (CDF II Collaboration), *Observation of the Narrow State* $X(3872) \rightarrow J/\psi\pi^{+}\pi^{-}$ *in* $p\bar{p}$ *Collisions at* $\sqrt{s} = 1.96$ TeV, Phys. Rev. Lett. **93**, 072001 (2004) [hep-ex/0312021].

[3] V. M. Abazov *et al.* (D0 Collaboration), *Observation and Properties of the* $X(3872)$ *Decaying to* $J/\psi\pi^{+}\pi^{-}$ *in* $p\bar{p}$ *Collisions at* $\sqrt{s} = 1.96$ TeV, Phys. Rev. Lett. **93**, 162002 (2004) [hep-ex/0405004].

[4] B. Aubert *et al.* (BaBar Collaboration), *Study of the* $B^{-} \rightarrow J/\psi K^{-}\pi^{+}\pi^{-}$ *Decay and Measurement of the* $B^{-} \rightarrow X(3872)K^{-}$ *Branching Fraction*, Phys. Rev. **D71**, 071103 (2005), [hep-ex/0406022].

[5] S.-K. Choi (Belle Collaboration), *Lake Louise Winter Institute*, Lake Louise, Alberta, Canada, 15-21 Feb 2004 [hep-ex/0405014];
see also Reference [1].

[6] B. Aubert *et al.*, (BaBar Collaboration), *Properties of the X(3872) at Belle*, hep-ex/0402025.

[7] R. Chistov, *et al.*, (Belle Collaboration), Phys. Rev. Lett. **93**, 051803 (2004) [hep-ex/0307061].

[8] C. Z. Yuan, X. H. Mo and P. Wang, *The upper limit of the* $e^{+}e^{-}$ *partial width of* $X(3872)$, Phys. Lett. **B579** 74 (2004) [hep-ph/0310261].

[9] S. Dobbs *et al.* (CLEO Collaboration), *Search for* $X(3872)$ *in* $\gamma\gamma$ *Fusion and Radiative Production at CLEO*, Phys. Rev. Lett. **94**, 032004 (2005) [hep-ex/0410038];
Z. Metreveli *et al.* (CLEO Collaboration), *Search for* $X(3872)(3872)$ *in Untagged* $\gamma\gamma$ *Fusion and Initial State Radiation Production with CLEO III*, presented at ICHEP, Aug 16-22, 2004, Beijing, China [hep-ex/0408057].

[10] B. Aubert *et al.* (BaBar Collaboration), contribution to ICHEP04, hep-ex/0408083.

[11] Belle Collaboration, contribution to ICHEP04, hep-ex/0408116 (August 2004).

[12] S. Pakvasa and M. Suzuki, *On the hidden charm state at* 3872 MeV/c^{2}, hep-ph/0309294.

[13] T. Barnes, S. Godfrey, *Charmonium Options for the $X(3872)$*, Phys. Rev. **D69** 054008 (2004) [hep-ph/0311162].

[14] T. Skwarnicki, *Heavy Quarkonium*, hep-ph/0311243, (Dec 2003).

[15] T.-M. Yan, Phys. Rev. **D22**, 1652 (1980);
see also: Y.-P. Kuang *et al., ibid.* **37** 1210 (1988).

[16] B. Aubert *et al.* (BaBar Collaboration), [hep-ex/0406022].

[17] B. Yabsley, *Charm Physics at Belle*, presented at XIII International Workshop on Deep Inelastic Scattering (DIS 2005), Madison, WI, USA, April 27 - May 1, 2005. `http://agenda.hep.wisc.edu/askArchive.php?base=agenda&categ=a058&id=a058s6t11/transparencies`

[18] See, for example: F. Halzen, A. Martin, *Quarks and Leptons: An Introductory Course in Modern Particle Physics*, John Wiley & Sons, Inc. (1984) Ch. 2, §5.

[19] See, for example: S. Eidelman *et al.*, *Review of particle physics*, Phys. Lett. **B592**, 1 (2004), §35.

[20] M. B. Voloshin, Phys. Lett. **B579**, 316 (2004) [hep-ph/0309307].

[21] S. Eidelman *et al.*, *Review of particle physics*, Phys. Lett. **B592**, 1 (2004).

[22] M. Deutsch, Phys. Rev. **82**, 455 (1951).

[23] C. Edwards *et al.* (Crystal Ball Collaboration), Phys. Rev. Lett. **48**, 70 (9182).

[24] S.-K. Choi *et al.* (Belle Collaboration), Phys. Rev. Lett. **89**, 102001 (2002), Erratium *ibid.* **89**, 129901 (2002);
K. Abe *et al.* (Belle Collaboration), Phys. Rev. Lett. **89**, 142001 (2002); K. Abe *et al.*, BELLE-PREPRINT-2003-7, KEK-PREPRINT-2003-24, hep-ex/0306015.

[25] B. Aubert *et al.* (BaBar Collaboration), Phys. Rev. Lett. **92**, 142002 (2004);
see also: G. Wagner, *Recent results on two-photon and tau physics at BaBar*, hep-ex/0305083.

[26] C. Bagin *et al.* (R704 Collaboration), Phys. Lett.**B171**, 135 (1986);
T. A. Armstrong *et al.* (E760 Collaboration), Phys. Rev. Lett. **69**, 2337 (1992);
L. Antoniazzi *et al.* (E705 Collaboration), Phys. Rev. **D50**, 4258 (1994).

[27] C. Patrignani (2004), *E835 at FNAL: Charmonium Spectroscopy at $p\bar{p}$ Annihilations*, presented at BEACH'04, Chicago, June 27 - July 3, 2004, `http://capp.iit.edu/beach04/`
see also: D. Bettoni, *Study of charmonium states formed in $p\bar{p}$ annihilations: results from Fermilab E835*, `http://www.ep1.rub.de/~panda/db/talksDB/bettoni_gsioct00.pdf`

[28] A. Tomaradze (CLEO Collaboration), hep-ex/0410090.

[29] L. Antoniazzi *et al.* (E705 Collaboration), Phys. Rev. **D50**, 4258 (1994).

[30] A. Gribushin *et al.* (E672 Collaboration), S. Blusk *et al.* (E706 collaboration), Phys. Rev. **D53**, 4723 (1996).

[31] J. Z. Bai *et al.* (BES Collaboration), Phys. Rev. **D57**, 3854 (1998).

[32] C. Quigg, *The Lost Tribes of Charmonium*, hep-ph/0407124;
see also E. J. Eichten, K. Lane and C. Quigg, *Charmonium levels near threshold and the narrow state* $X(3872) \to \pi^+\pi^- J/\psi$ Phys. Rev. **D69**, 094019 (2004).

[33] S. E. Ackleh, T. Barnes, Phys. Rev. **D45** 232 (1992).

[34] E. Eichten, K. Gottfried, T. Kinoshita, K. Lane and T.-M. Yan, *Charmonium: Comparison with Experiment*, Phys. Rev. **D21**, 203 (1980).

[35] W. Buchmüller and S.-H. H. Tye, Phys. Rev. **D24** 132 (1981).

[36] S. Olsen (Belle Collaboration), *Search for a Charmonium Assignment for the* $X(3872)$, presented at MESON2004 Workshop [hep-ex/0407033].

[37] C. N. Yang, Phys. Rev. **77**, 242 (1950);
L. D. Landau, Dok. Akad. Nauk USSR **60**, 207 (1948).
see also H. Aihara *et al.* (TPC/Two-Gamma Collaboration), Phys. Rev. **D38**, 1 (1988).

[38] A. Astier *et al.*, Phys. Lett. **B25**, 294 (1967).

[39] A. B. Wicklund *et al.*, Phys. Rev. Lett. **45** 1469 (1980);
see also: J. Weinstein and N. Isgur, Phys. Rev. Lett. **48**, 659 (1982); Phys. Rev. **D27**, 588 (1983); *ibid* **41**, 2236 (1990).

[40] M. B. Voloshin and L. B. Okun, Pis'ma Zh. Eksp. Teor. Fiz. **23** 369 (1976) [JETP Lett. **23**, 333 (1976)];
A. De Rújula, H. Georgi and S. L. Glashow, Phys. Rev. Lett. **38**, 317 (1977);
M. Bander, G. L. Shaw, P. Thomas and S. Meshkov, Phys. Rev. Lett. **36**, 695 (1976).

[41] V. A. Novikov, L. B. Okun, M. A. Shifman, A. I. Vainshtein, M. B. Voloshin and V. I. Zakharov, Phys. Rept. **C41**, 1 (1978).

[42] N. Törnqvist, Phys. Rev. Lett. **67**, 556 (1991).

[43] A. V. Manohar and M. B. Wise, Nucl. Phys. **B339**, 17 (1993);
T. E. O. Ericsson and G. Karl, Phys. Lett. **B309**, 426 (1993).

[44] F. E. Close and P. R. Page, *The* $D^{*0}\bar{D}^0$ *threshold resonance*, Phys. Lett. **B578** 119-123 (2004) [hep-ex/0309253].

[45] E. Braaten and M. Kusunoki, *Low-energy Universality and the New Charmonium Resonance at 3870 MeV*, Phys.Rev. **D69** 074005 (2004), [hep-ph/0311147].

[46] E. S. Swanson, Phys. Lett. **B588**, 189 (2004) [hep-ph/0311229].

[47] S. L. Olsen, *New Particles from Belle*, hep-ex/0412068.

[48] L. Maiani, F. Piccini, A. D. Polosa, V. Riquer, Phys. Rev. **D71**, 014028 (2005).

[49] K. Abe *et al.* (Belle Collaboration), in *Proceedings on the 32nd International Conference on High-Energy Physics (ICHEP 04)*, Beijing, China, 2004, [hep-ex/0408126].

[50] A. V. Evdokimov *et al.* (SELEX Collaboration), Phys. Rev. Lett. **93**, 242001 (2004).

[51] B. A. Li, Phys. Lett. **B605**, 306 (2005) [hep-ph/0410264].

[52] D. Horn and J. Mandula, Phys. Rev. **D17**, 898 (1978).

[53] F. E. Close and S. Godfrey, Phys. Lett. **B574**, 210 (2003) [hep-ph/0305285].

[54] G. Chiladze, A. F. Falk and A. A. Petrov, Phys. Rev. **D58**, 034013 (1998);
N. Isgur and J. Paton, Phys. Rev. **D31**, 2910 (1985);
J. Merlin and J. Paton, Phys. Rev. **D35**, 1668 (1987);
T. Barnes, F. E. Close, E. S. Swanson, Phys. Rev. **D52**, 5242 (1995);
L. A. Griffiths, C. Michael, P. E. Rakow, Phys. Lett. **B129**, 351 (1983);
R. C. Giles and S.-H. Tye, Phys. Rev. **D16**, 1079 (1977);
F. E. Close *et al.*, *ibid.* **D57**, 5653 (1998).

[55] X. Liao and T. Manke, hep-lat/0210030.

[56] C. W. Bernard *et al.* (MILC Collaboration), Phys. Rev. **D56**, 7039 (1997) [hep-lat/9707008].

[57] S. Perantonis, C. Michael, Nucl. Phys. **B347**, 854 (1990).

[58] Y.-P. Kuang, T.-M. Yan, Phys. Rev. **D24**, 2874 (1981).

[59] F. E. Close and J. J. Dudek, hep-ph/0304243.

[60] S. Godfrey and J. L. Rosner, Phys. Rev. **D66**, 014012 (2002).

[61] K. K. Seth, hep-ph/0411122.

[62] C. J. Morningstar and M. Peardon, Phys. Rev. **D60** (1990) 034509.

[63] D. V. Bugg, Phys. Rev. **D71**, 016006 (2005);
D. V. Bugg, Phys. Lett. **B598**, 8 (2004); *ibid.* **B572** 1 (2003) [Erratum – *ibid.* **B595**, 556 (2004)].

[64] B. Kerbikov, A. Stavinsky, V. Fedotov, hep-ph/0402054.

[65] E. P. Wigner, Phys. Rev. **73**, 1002 (1948)

[66] J. Z. Bai *et al.* (BES Collaboration), Phys. Rev. Lett. **91**, 022001-1 (2003);
see also Reference [64].

[67] K. Abe *et al.* (Belle Collaboration), Phys. Rev. Lett. **88**, 181803 (2002).

[68] K. Abe *et al.* (Belle Collaboration), Phys. Rev. Lett. **89**, 151802 (2002).

[69] P. D. Barnes *et al.*, Phys. Rev. **C62**, 055203 (2000).

[70] D. Eastwood *et al.*, Phys. Rev. **D3**, 2603 (1971);
O. Braun *et al.*, Nucl. Phys. **B124**, 45 (1977).

[71] T. E. Browder, S. Pakvasa and A. A. Petrov, *Comment on the new $D_s^{(*)+}\pi^0$ resonances*, Phys. Lett. **B578** 365-368 (2004) [hep-ph/0307054].

[72] *Details about Fermilab's accelerators*,
`http://www.fnal.gov/pub/inquiring/physics/accelerators/chainaccel.html`

Fermilab Beams Division, *Details about Fermilab's accelerators*,
`http://www-bd.fnal.gov/public/chain.html`

Fermilab Beams Division, *Run II Handbook*,
`http://www-bd.fnal.gov/runII/`

Fermilab Beams Division, *Booster Rookie Book*,
`http://www-bd.fnal.gov/proton/booster/rookie/realrookiebook.html`

[73] Fermilab Beams Division, *Fermilab Linac Upgrade. Conceptual design*,
`http://www-lib.fnal.gov/archive/linac/FERMILAB-LU-ConceptualDesign.pdf`

[74] R. Bilinge, *Booster radius*, FERMILAB-FN-0152 (1968).

[75] C. Hojvat *et al.*, *The multiturn charge exchange injection system for the Fermilab booster accelerator*, FERMILAB-TM-0872 (1979).

[76] K. Anikeev, *Measurement of the lifetimes of B meson mass eigenstates*, Ph.D. Thesis at Massachusetts Institute of Technology (Sep 2004).

[77] A. Korn, *Measurement of B-Hadron Masses at CDF Run II*, Ph.D. Thesis at Massachusetts Institute of Technology (May 2004).

[78] F. Bedeschi *et al.* NIM **A268**, 50-74 (1988).

[79] W.M. Yao and K. Bloom, *Outside In Silicon Tracking at CDF*, CDF Note 5591 (2000);
S. Menzemer *et al.*, *TrackingKal - A Tracking and Alignment Software Package for the CDF II Silicon Detector*, CDF Note 5968 (2002).

[80] G. Ascoli *et al.*, *The CDF Central Muon Detector*, NIM **A268**, 63-67 (1988).

[81] G. Ascoli *et al.* (CDF Collaboration), *The 1992 CDF Muon System Upgrade*, CDF Note 2858 (Oct 1994).

[82] The CDF Collaboration, *The CDF II Detector. Technical Design Report*, FERMILAB-Pub-96/390-E (Oct 1996)

[83] The CDF Collaboration, *Proposal for Enhancement of the CDF II detector: An Inner Silicon Layer and a Time of Flight Detector (P-909)*, `http://www-cdf.fnal.gov/upgrades/PAC/p909.ps` (Oct 1998);
Update to Proposal P-909: Physics Performance of the CDF II with an Inner Silicon Layer and a Time of Flight Detector, `http://www-cdf.fnal.gov/upgrades/btb_update_jan99.ps` (Jan 1999).

[84] L. Balka, *et al.*, *The CDF Central Electromagnetic Calorimeter*, Nucl. Instr. & Meth. **A267**, 272 (1988);
Y. Seiya, *et al.*, Nucl. Instr & Meth. A480 (2002) 524;

F. Abe *et al.*, Phys. Rev. **D44**, 29 (Jul 1991);
F. Abe *et al.*, Phys. Rev. **D48**, 2998 (Oct 1993);
F. Abe *et al.*, Phys. Rev. Lett. **D73**, 2662 (Nov 1994);
J. Strait, *Design Considerations for a Preshower Detector for the CDF End Plugs*, CDF Note 2097 (Jun 1993);
S. Bertolucci, *The CDF Central and Endwall Hadron Calorimeter*, NIMPR A267 301 (1988).

[85] M. M. Block and R. N. Cahn, Rev. Mod. Phys. **57**, 563 (1985).

[86] F. Abe *et al.* (CDF Collaboration), Phys. Rev. **D50**, 5550 (1994);
N. Amos *et al.*, Phys. Rev. Lett. **68**, 2433 (1992);
C. Avila *et al.*, Phys. Lett. **B445**, 419 (1999).

[87] S. Klimenko *et al.*, *The CDF Run II Luminosity Monitor*, CDF Note 4330 (Oct 1998);
S. Klimenko *et al.*, *CLC Production and Mechanical Assembly*, CDF Note 5119 (Oct 1999);
D. Acosta *et al.* *A First Look at the CLC Luminosity Measurements*, CDF Note 6052 (Aug 2002).

[88] H. Frisch *et al.*, *Conceptual Design of a Deadtimeless Trigger for the CDF Trigger Upgrade*, CDF Note 2038 (Dec 1994).

[89] The CDF Collaboration, *CDF Run II Trigger Table and Datasets Plan*, CDF Note 4718 (Dec 2001).

[90] E. Thomson *et al.*,*Online Track Processor for the CDF Upgrade*, IEEE Transactions on Nuclear Science, Vol. 49, No. 3 (Jun 2002).

[91] L. Holloway and J. Strologas, *Determination of the XTRP maps from XFT to CMU and CMX*, CDF Note 4146 (Apr 1997).

[92] K. Anikeev *et al.*,*Event Builder and Level-3 for Aces*, CDF Note 5793 (Dec 2001).

[93] M. Paulini and B. Wicklund, *Summary of Proposal for B Physics Triggers in Run II*, CDF Note 5483 (Dec 2000);
K. Anikeev *et al.*, *Level-1 Di-muon Trigger Study (CMU_CMU)*, CDF Note 5769 (Feb 2002);
M. Bishai *et al.*, *Run II Di-muon Trigger Optimization and Efficiency Measurement*, CDF Note 6004 (Jul 2002).

[94] P. Murat, *Stntulple*, `http://fcdfhome.fnal.gov/usr/cdfopr/Stntuple/Stntuple.html` ;
Ch. Paus, *B - Stntuple*, `http://mit1.fnal.gov/~paus/stn.html`

[95] S. Giagu, *ROOT macros and instructions for accessing DB good run bits*, `http://www-cdf.fnal.gov/internal/physics/bottom/validation/rootmacro.html`

[96] K. Anikeev *et al.* *Calibration of Energy Loss and Magnetic Field using J/ψ Events in Run II*, CDF Note 5958 (June 2002);
G. Bauer, A. Korn, C. Paus, *Update on Calibration of Energy Loss and Magnetic Field using J/ψ Events in Run II*, CDF Note 6355 (March 2003).

[97] M. Campanelli and E. Gerchtein, *Calibration of the momentum scale for Kalman refitter using J/ψ events*, CDF Note 6905 (2004).

[98] L. Vacavant, *GEANT description of the CDF Inner Tracker Passive Material*, CDF Note 5825 (Apr 2002).

[99] C. Newman-Holmes *et al.*, *Fitting the Magnetic Field of the CDF Magnet*, CDF Note 361 (Dec 1985);
R. Yamada, C. Newman-Holmes and E. Schmidt, *Measurement of the Magnetic Field of the CDF Magnet*, CDF Note 346 (Nov 1985);
R. Yamada, C. Newman-Holmes and E. Schmidt, *Measurement of the Magnetic Field of the CDF Magnet*, CDF Note 667 (May 1988);
D. Crane, H. Jensen and C. Newman-Holmes, *Solenoid Magnetic Field in the 1988-1989 Run*, CDF Note 969 (Jul 1989);
C. Newman-Holmes, E. Schmidt and R. Yamada, *Measurement of the Magnetic Field of the CDF Magnet*, NIM **A274**, 443 (1989).

[100] K. Hagiwara *et al.*, *Raeview of particle physics. Particle Data Group*, Phys. Rev. **D66**, 010001 (2002).

[101] J. Marriner, *Secondary vertex fit with mass and pointing constraints (ctvmft)*, CDF Note 1996 (Mar 1993);
see also `http://cdfkits.fnal.gov/CdfCode/source/VertexAlg/src/VertexFit.cc`

[102] S. Gromoll, Ch. Paus, *A Heavy Quark Generator*, CDF Note 5985 (June 2002).

[103] P. Avery, K. Read and G. Trahern, Cornell Internal Note CSN-22, 1985 (unpublished).

[104] See `http://cdfkits.fnal.gov/CdfCode/source/HepgMods/src/HepgFilter.cc`

[105] A. Warburton, *Exclusive Nonleptonic Decays of B Mesons into Final States of Strange Mesons and 1S or 2S Charmonia*, Ph.D. Thesis, p. 70, Eqn. (4.1), Univ. of Toronto (Dec 1997).

[106] D. Coffman *et al.*, *Direct Measurement of the J/ψ Leptonic Branching Fraction*, Phys. Rev. Lett. 68, 282 (1992).

[107] L. S. Brown, R. N. Cahn, *Chiral Symmetry and $\Psi' \to \Psi\pi\pi$ Decay*, Phys. Rev. Lett. **35**, 1 (1975);
see also: R. N. Cahn, *Angular distributions in the decay $\psi' \to \psi\pi\pi$*, Phys. Rev. **D12**, 3559 (1975).

[108] T. N. Pham, B. Pire and T. N. Truong, Phys. Lett. **61B** 183 (1976).

[109] M.B. Voloshin and V. Zakharov, Phys. Rev. Lett. **45**, 688 (1980).

[110] V.A. Novikov and M.A. Shifman, Z. Phys. **C8**, 43 (1981).

[111] J.Z. Bai *et al.*, (BES Collaboration), Phys. Rev. **D62**, 032002.

[112] D. Besson *et al.*, Phys. Rev. **D30** 1433 (1984).

[113] G. S. Abrams *et al.*, Phys. Rev. Lett. **33**, 1453 (1974);
G. S. Abrams *et al.*, Phys. Rev. Lett. **34**, 1181 (1975);
G. S. Abrams in *Proceedings of the International Symposium on Lepton and Photon Interactions at High Energies*, Stanford, California, 1975, edited by W. T. Kirk (SLAC, Stanford, 1976).

[114] K. Gottfried, Phys. Rev. Lett. **40**, 598 (1978).

[115] G. S. Abrams *et al.*, *Preliminary data from LBL-SLAC*, presented by J. A. Kadyk at the 10th Recontre de Moriond, 1975.

[116] M. Shifman, Phys. Rep. **209**, 341 (1991).

[117] Y.-P. Kuang, S. F. Tuan, and T.-M. Yan, Phys. Rev. **D37**, 1210 (1988).

[118] Y.-P. Kuang, private communication.

[119] H. J. Lipkin and S. F. Tuan, Phys. Lett. **B206**, 349 (1988).

[120] P. Moxhay, Phys. Rev. **D39**, 3497 (1989).

[121] H.-Y. Zhou and Y.-P. Kuang, Phys. Rev. **D44**, 756 (1991).

[122] N. Brambilla *et al.*, hep-ph/0412158.

[123] M. Oreglia *et al.* (Crystal Ball Collaboration), Phys. Rev. Lett. **45**, 959 (1980).

[124] F. Butler *et al.* (CLEO Collaboration), Phys. Rev. **D49**, 40 (1994).

[125] T. Sjöstrand, Computer Physics Commun. **82** (1994) 74;
see also `http://www.thep.lu.se/tf2/staff/torbjorn/Pythia.html`

[126] See `http://hepwww.rl.ac.uk/theory/seymour/herwig/`

[127] P. Sphicas, *A $b\bar{b}$ Monte Carlo Generator*, CDF Note 2655 (1999);
K. Anikeev, P. Murat, C. Paus, *Description of Bgenerator II*, CDF Note 5092 (Aug 1999).

[128] R. Brun and F. Carminati, *GEANT Detector Description and Simulation Tool*, CERN – Program Library Long Write-up W5013;
see also: `http://consult.cern.ch/writeup/geant/`

[129] S. D. Auria *et al.*, *CDF B Monte Carlo*,
`http://www-cdf.fnal.gov/internal/physics/bottom/b-montecarlo/`

Appendix A

Mass Fits of p_t Slices for the $\psi(2S)$

This Appendix contains the $J/\psi\,\pi^+\pi^-$ mass histograms for different p_t slices. We fit these histograms to obtain the $\psi(2S)$ p_t spectrum as described in Section 4.1. The resulting p_t spectrum is presented in Figures 4-1 and 4-2.

In all the fits presented here the $\psi(2S)$ peak is approximated by a double Gaussian (Equation 3.1) with a common mean. On each plot are listed the total fitted yield $N_{\psi(2S)}$, the relative fraction of the second gaussian N_{rel}, the common mean value $m_{\psi(2S)}$, the narrow width $\sigma_{\psi(2S)}$ and the ratio of the wide width to the narrow width σ_{rel}. The zero fitted uncertainty means that the parameter was fixed during the fit. The fit χ^2, the number of degrees of freedom DoF and the fit probability are given too.

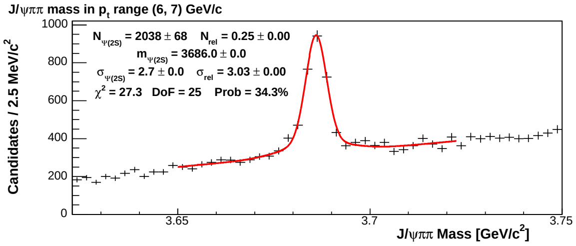

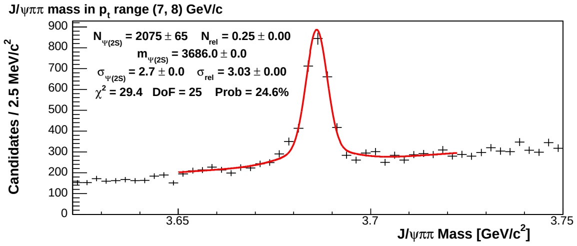

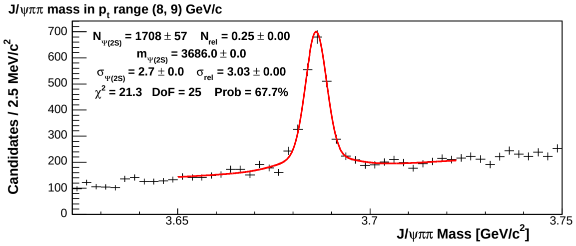

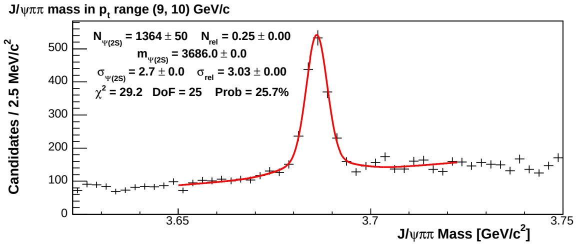

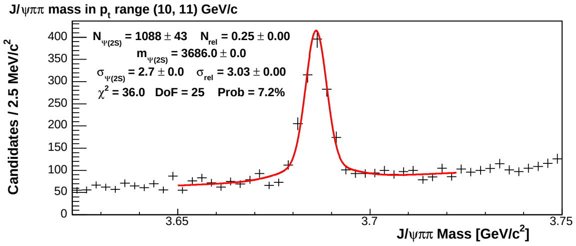

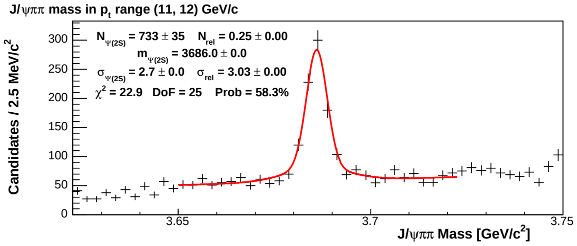

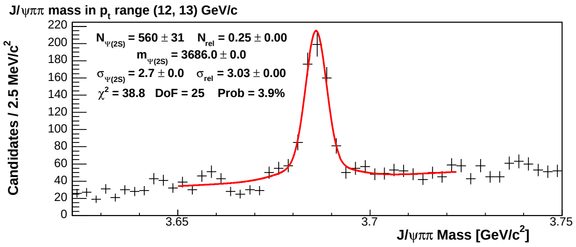
J/ψππ mass in p_t range (12, 13) GeV/c

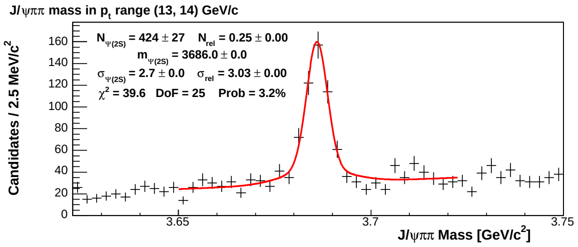
J/ψππ mass in p_t range (13, 14) GeV/c

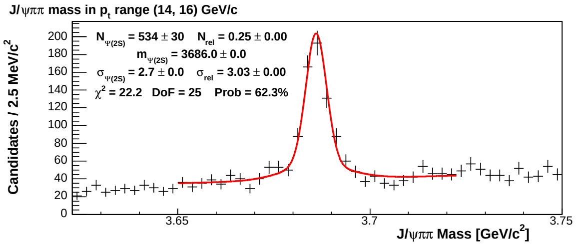
J/ψππ mass in p_t range (14, 16) GeV/c

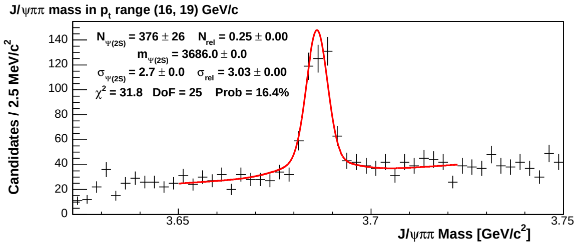
J/ψππ mass in p_t range (16, 19) GeV/c

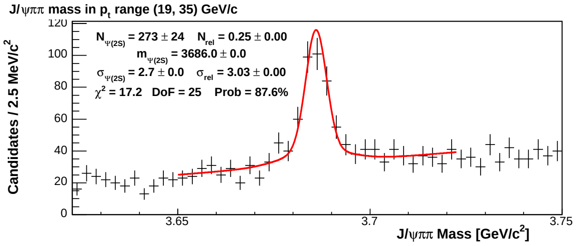
J/ψππ mass in p_t range (19, 35) GeV/c

Appendix B

Mass Fits of p_t Slices for the $X(3872)$

This Appendix, just like the previous one, contains the $J/\psi\,\pi^+\pi^-$ mass histograms in different p_t slices. We fit these histograms to obtain the $X(3872)$ p_t spectrum, as described in Section 4.1. The resulting p_t spectrum is presented in Figures 4-1 and 4-2.

On each plot are listed the total fitted yield N_X, the $X(3872)$ mass and width, the fit χ^2, the number of degrees of freedom DoF and the fit probability. The zero fitted uncertainty means that the parameter was fixed during the fit.

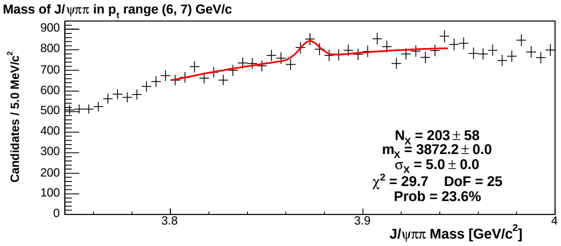

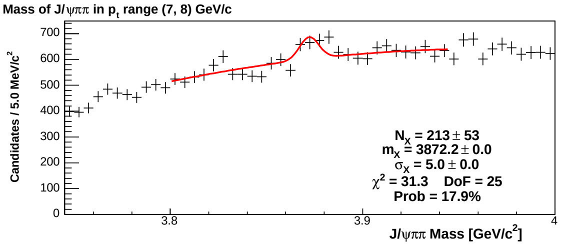

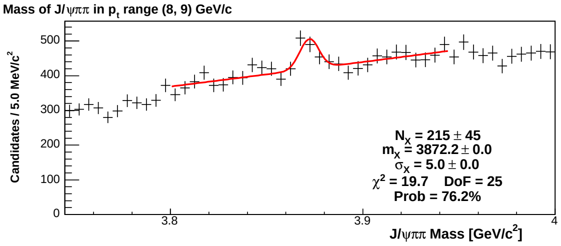

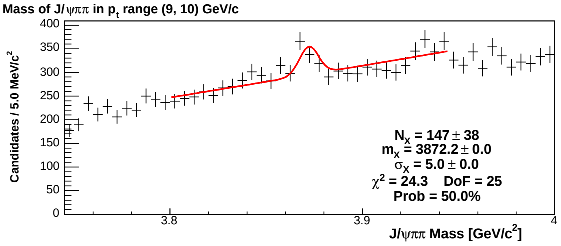

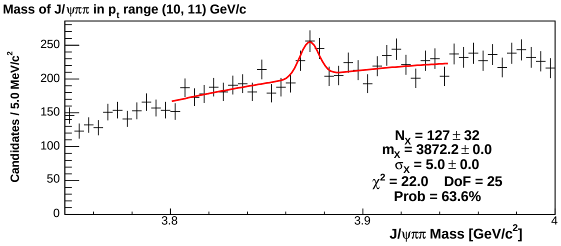

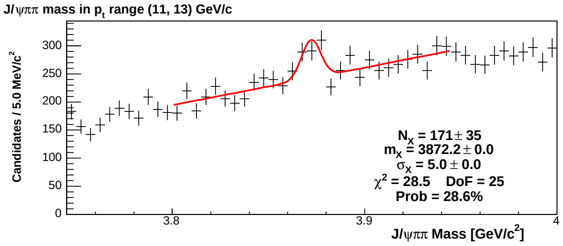

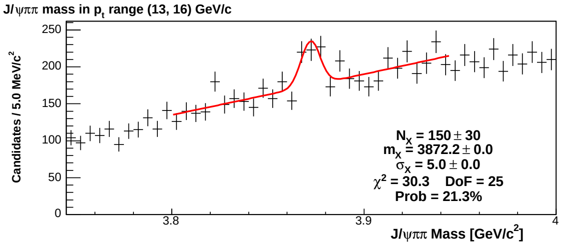
J/ψππ mass in p_t range (13, 16) GeV/c
Candidates / 5.0 MeV/c^2
0
50
100
150
200
250
3.8
3.9
4
J/ψππ Mass [GeV/c^2]
$N_X = 150 \pm 30$
$m_X = 3872.2 \pm 0.0$
$\sigma_X = 5.0 \pm 0.0$
$\chi^2 = 30.3$ DoF = 25
Prob = 21.3%

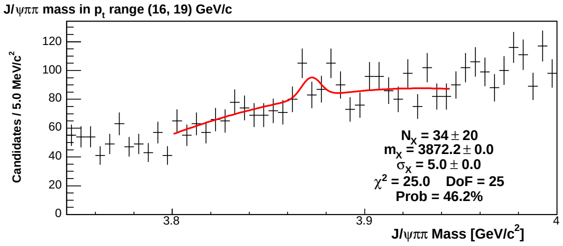
J/ψππ mass in p_t range (16, 19) GeV/c
Candidates / 5.0 MeV/c^2
0
20
40
60
80
100
120
3.8
3.9
4
J/ψππ Mass [GeV/c^2]
$N_X = 34 \pm 20$
$m_X = 3872.2 \pm 0.0$
$\sigma_X = 5.0 \pm 0.0$
$\chi^2 = 25.0$ DoF = 25
Prob = 46.2%

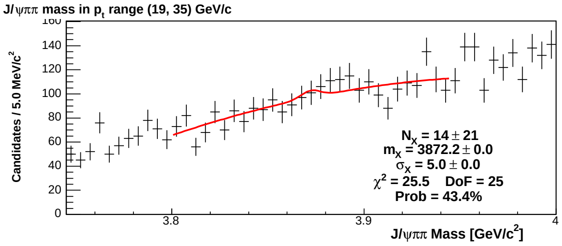
J/ψππ mass in p_t range (19, 35) GeV/c
Candidates / 5.0 MeV/c^2
0
20
40
60
80
100
120
140
160
3.8
3.9
4
J/ψππ Mass [GeV/c^2]
$N_X = 14 \pm 21$
$m_X = 3872.2 \pm 0.0$
$\sigma_X = 5.0 \pm 0.0$
$\chi^2 = 25.5$ DoF = 25
Prob = 43.4%

Appendix C

“Realistic” Monte Carlo Generation

The computer simulation of the physics events occurring in the $p\bar{p}$ collisions and the subsequent processes in the particle detector is used very often in the high-energy physics analyses. Such simulation is based in on random sampling, that is why it is called “Monte Carlo”, after a small principality in Europe known for its casinos.

In physics analysis one may use such computer simulation to model the features which can not be measured by the detectors. For example, in this analysis we use Monte Carlo to calculate how many particles escaped registering. Obviously, no detector can provide us with this information.

To simulate a physics particle, we need to specify all its important characteristics, such as mass, energy, momentum, spin *etc.* Some of them (*e.g.* mass, spin, parity) are constants, which must be setup before the generation. Others (*e.g.* energy, momentum) are, normally, varying for different instances of generated particles. Often they are picked up at random from the distributions prepared in advance. This is usually done by programs called *generators*, such as `PYTHIA` [125], or `HERWIG` [126], or `Bgenerator` [127]. In this analysis we use the package `HeavyQuarkGen` [102] developed at CDF. This package, normally used for single b-quark simulation, or for $b\bar{b}$ pair simulation, was adopted for $X(3872)$ simulation in our analysis.

After creation the particle is decayed into two or more other particles, which means that new particles are also generated with their own masses, spins, parities, energies, momenta *etc.* The program makes sure that all the conservation laws are obeyed during this decay. The quantities which are not strictly determined by these laws, such as, for example, angular correlations, are again selected at random, unless the rules for this selection are provided by the user. In this analysis we use the package QQ [103] developed at CLEO, to decay the generated particle.

The decay products pass through the computer simulation of the detector. To obtain this we use the GEANT package [128], which is designed to describe a very broad range of the detectors. Once the detector is described in GEANT language, practically any kind of particle can be put through it, and GEANT will mimic all the physics processes occurring as the particle passes through the real detector. In particular, GEANT will simulate the responses of different detector subsystems, which may be converted into banks similar to the ones used in data structures for the the real detector.

The next step in Monte Carlo generation is the simulation of the trigger. At this point the data banks from GEANT are fed into the real trigger algorithm (Section 2.2.5) which decides if the event should be accepted or rejected.

After passing the trigger, the events go through the production stage in which the information from the raw data banks is used to create physics objects such as tracks, jets, muons, electrons *etc.*, as described in Section 2.3.

After the Monte Carlo is generated, one would usually compare it to the data, to make sure that they match each other reasonably well. A lot of efforts was invested in CDF into development the Monte Carlo framework, tuning the material description in GEANT and achieving realistic detector resolutions [129]. However, the data taking conditions in CDF were not uniform, particularly in the early phase of Run II operations. This means that during a few years of operation, the detector underwent modifications, and that conditions changed between different runs. To reflect these changes in Monte Carlo, the simulation is supplied with tables of run configurations that truck the changes in data taking conditions. The number of the events generated under particular conditions (taken from a particular run) is proportional to the luminosity of this run. The Monte Carlo generated in this way is called *realistic* and it reflects the changing run conditions.

Appendix D

Mass Fits in $m_{\pi\pi}$ Slices for the $\psi(2S)$

This Appendix contains the $J/\psi\,\pi^+\pi^-$ mass histograms in different $m_{\pi\pi}$ slices. We fit these histograms to obtain the $\psi(2S)$ $m_{\pi\pi}$ spectrum, as described in Section 4.3. The resulting $m_{\pi\pi}$ spectrum is presented in Figure 4-10. See Appendix A for explanation of the numbers on each plot.

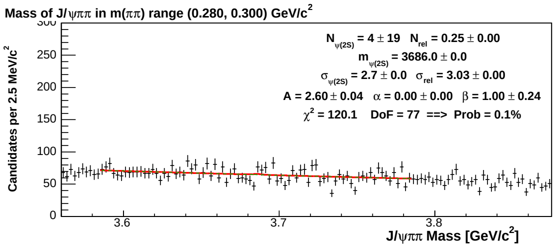

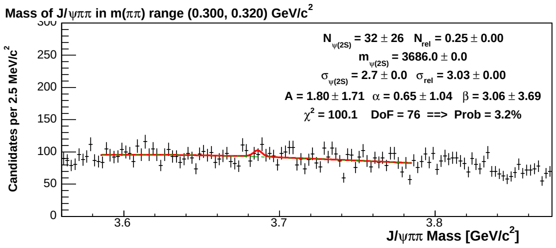

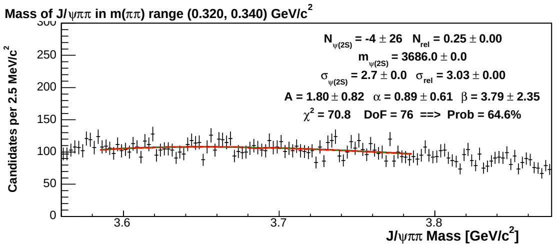

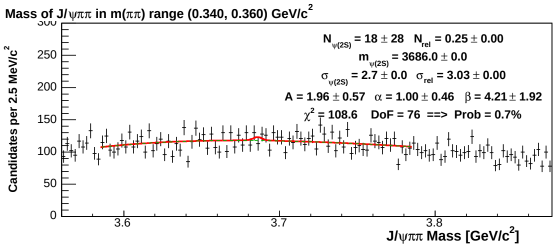

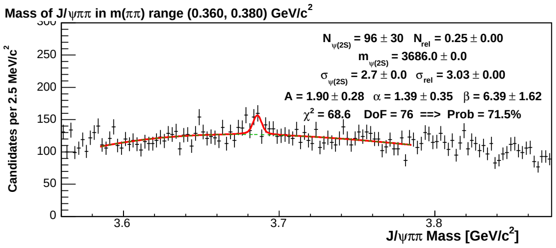

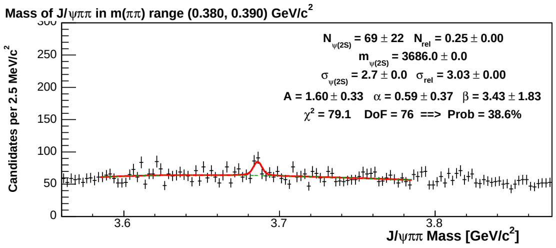

Mass of J/ψππ in m(ππ) range (0.390, 0.400) GeV/c^2

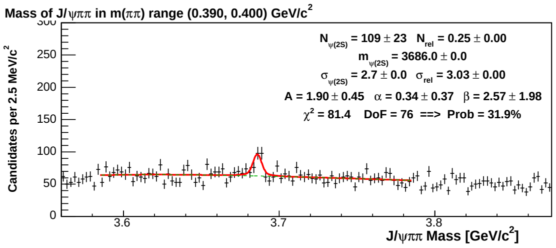

Mass of J/ψππ in m(ππ) range (0.400, 0.410) GeV/c^2

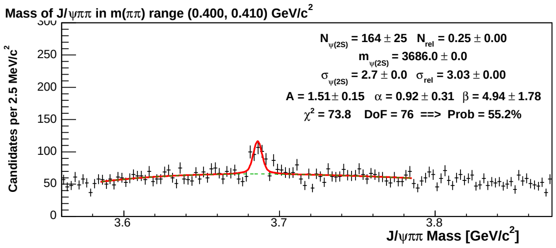

Mass of J/ψππ in m(ππ) range (0.410, 0.420) GeV/c^2

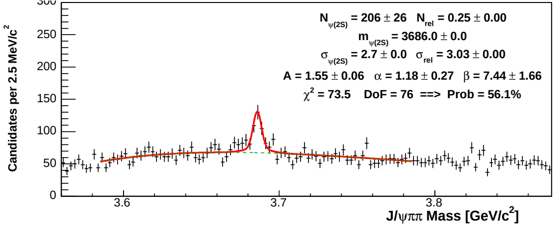

Mass of J/ψππ in m(ππ) range (0.420, 0.430) GeV/c^2

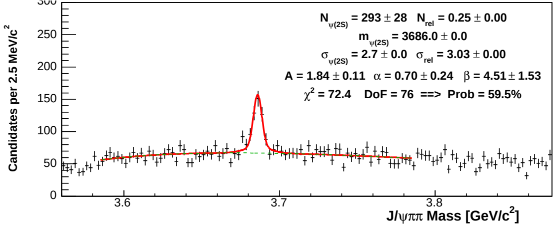

Mass of J/ψππ in m(ππ) range (0.430, 0.440) GeV/c^2

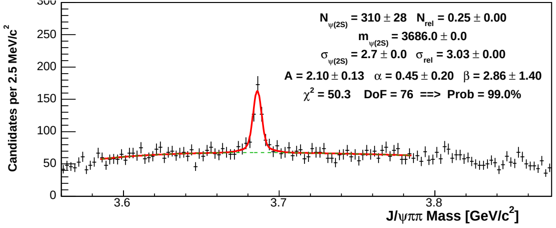

Mass of J/ψππ in m(ππ) range (0.440, 0.450) GeV/c^2

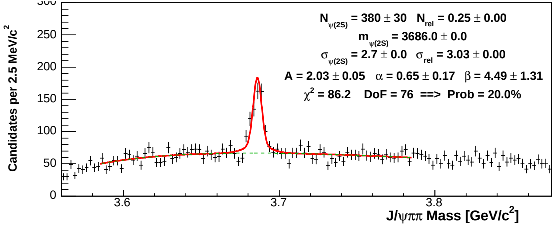

Mass of J/ψππ in m(ππ) range (0.450, 0.460) GeV/c^2

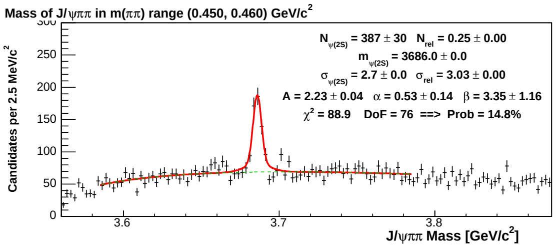

Mass of J/ψππ in m(ππ) range (0.460, 0.470) GeV/c^2

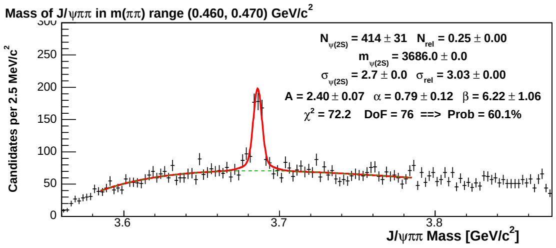

Mass of J/ψππ in m(ππ) range (0.470, 0.480) GeV/c^2

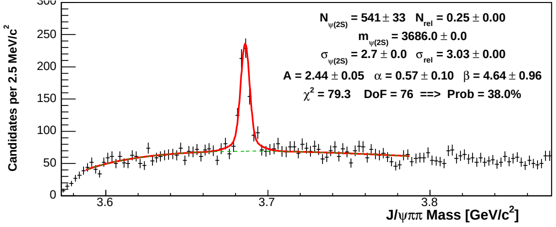

Mass of J/ψππ in m(ππ) range (0.480, 0.490) GeV/c^2

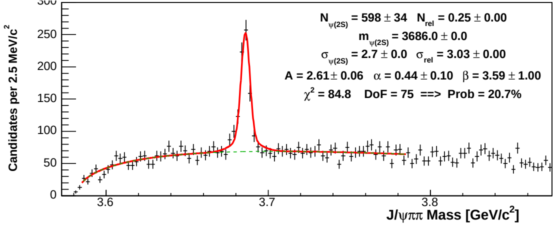

Mass of J/ψππ in m(ππ) range (0.490, 0.500) GeV/c^2

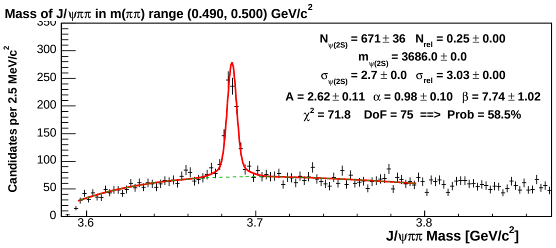

Mass of J/ψππ in m(ππ) range (0.500, 0.510) GeV/c^2

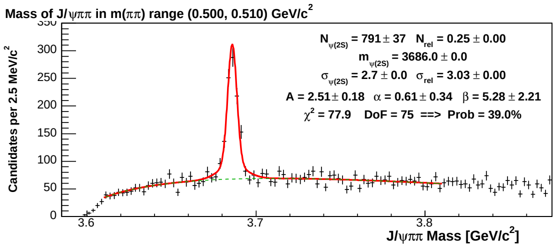

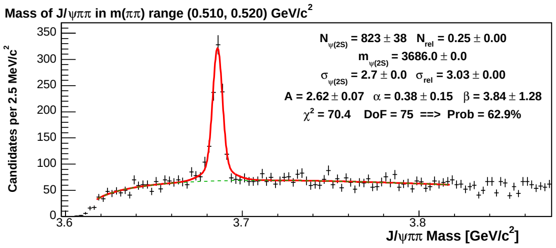

Mass of J/ψππ in m(ππ) range (0.510, 0.520) GeV/c²
N_ψ(2S) = 823 ± 38 N_rel = 0.25 ± 0.00
m_ψ(2S) = 3686.0 ± 0.0
σ_ψ(2S) = 2.7 ± 0.0 σ_rel = 3.03 ± 0.00
A = 2.62 ± 0.07 α = 0.38 ± 0.15 β = 3.84 ± 1.28
χ² = 70.4 DoF = 75 ==> Prob = 62.9%
Candidates per 2.5 MeV/c²
J/ψππ Mass [GeV/c²]

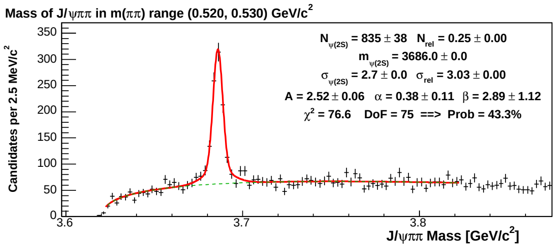

Mass of J/ψππ in m(ππ) range (0.520, 0.530) GeV/c²
N_ψ(2S) = 835 ± 38 N_rel = 0.25 ± 0.00
m_ψ(2S) = 3686.0 ± 0.0
σ_ψ(2S) = 2.7 ± 0.0 σ_rel = 3.03 ± 0.00
A = 2.52 ± 0.06 α = 0.38 ± 0.11 β = 2.89 ± 1.12
χ² = 76.6 DoF = 75 ==> Prob = 43.3%
Candidates per 2.5 MeV/c²
J/ψππ Mass [GeV/c²]

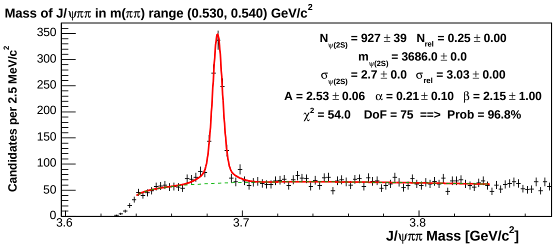

Mass of J/ψππ in m(ππ) range (0.530, 0.540) GeV/c²
N_ψ(2S) = 927 ± 39 N_rel = 0.25 ± 0.00
m_ψ(2S) = 3686.0 ± 0.0
σ_ψ(2S) = 2.7 ± 0.0 σ_rel = 3.03 ± 0.00
A = 2.53 ± 0.06 α = 0.21 ± 0.10 β = 2.15 ± 1.00
χ² = 54.0 DoF = 75 ==> Prob = 96.8%
Candidates per 2.5 MeV/c²
J/ψππ Mass [GeV/c²]

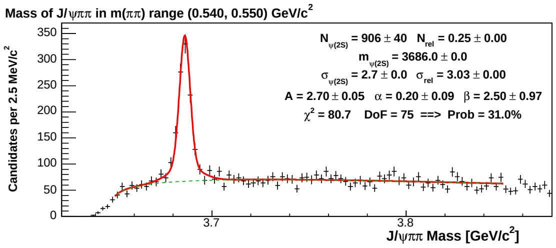

Mass of J/ψππ in m(ππ) range (0.540, 0.550) GeV/c²
N_ψ(2S) = 906 ± 40 N_rel = 0.25 ± 0.00
m_ψ(2S) = 3686.0 ± 0.0
σ_ψ(2S) = 2.7 ± 0.0 σ_rel = 3.03 ± 0.00
A = 2.70 ± 0.05 α = 0.20 ± 0.09 β = 2.50 ± 0.97
χ² = 80.7 DoF = 75 ==> Prob = 31.0%
Candidates per 2.5 MeV/c²
J/ψππ Mass [GeV/c²]

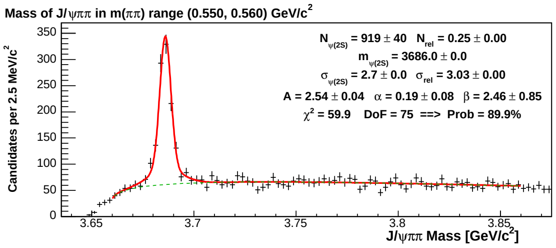

Mass of J/ψππ in m(ππ) range (0.550, 0.560) GeV/c²
N_ψ(2S) = 919 ± 40 N_rel = 0.25 ± 0.00
m_ψ(2S) = 3686.0 ± 0.0
σ_ψ(2S) = 2.7 ± 0.0 σ_rel = 3.03 ± 0.00
A = 2.54 ± 0.04 α = 0.19 ± 0.08 β = 2.46 ± 0.85
χ² = 59.9 DoF = 75 ==> Prob = 89.9%
Candidates per 2.5 MeV/c²
J/ψππ Mass [GeV/c²]

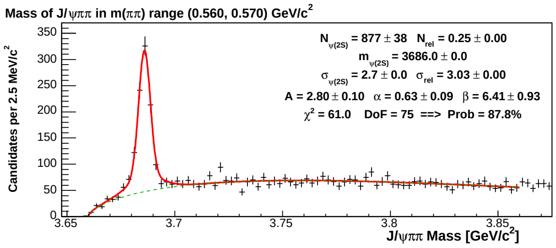

Mass of J/ψππ in m(ππ) range (0.560, 0.570) GeV/c²
N_ψ(2S) = 877 ± 38 N_rel = 0.25 ± 0.00
m_ψ(2S) = 3686.0 ± 0.0
σ_ψ(2S) = 2.7 ± 0.0 σ_rel = 3.03 ± 0.00
A = 2.80 ± 0.10 α = 0.63 ± 0.09 β = 6.41 ± 0.93
χ² = 61.0 DoF = 75 ==> Prob = 87.8%
Candidates per 2.5 MeV/c²
J/ψππ Mass [GeV/c²]

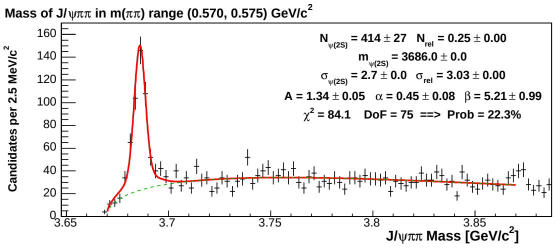

Mass of J/ψππ in m(ππ) range (0.570, 0.575) GeV/c²
N_ψ(2S) = 414 ± 27 N_rel = 0.25 ± 0.00
m_ψ(2S) = 3686.0 ± 0.0
σ_ψ(2S) = 2.7 ± 0.0 σ_rel = 3.03 ± 0.00
A = 1.34 ± 0.05 α = 0.45 ± 0.08 β = 5.21 ± 0.99
χ² = 84.1 DoF = 75 ==> Prob = 22.3%
Candidates per 2.5 MeV/c²
J/ψππ Mass [GeV/c²]

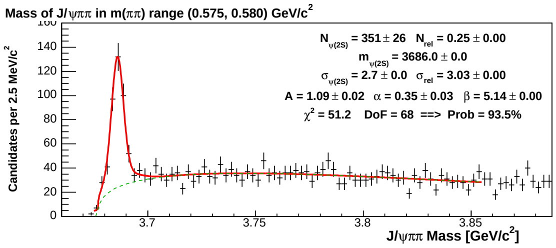

Mass of J/ψππ in m(ππ) range (0.575, 0.580) GeV/c²
N_ψ(2S) = 351 ± 26 N_rel = 0.25 ± 0.00
m_ψ(2S) = 3686.0 ± 0.0
σ_ψ(2S) = 2.7 ± 0.0 σ_rel = 3.03 ± 0.00
A = 1.09 ± 0.02 α = 0.35 ± 0.03 β = 5.14 ± 0.00
χ² = 51.2 DoF = 68 ==> Prob = 93.5%
Candidates per 2.5 MeV/c²
J/ψππ Mass [GeV/c²]

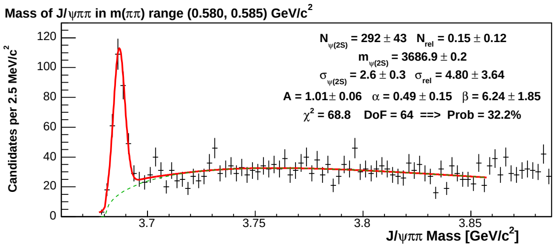

Mass of J/ψππ in m(ππ) range (0.580, 0.585) GeV/c²
N_ψ(2S) = 292 ± 43 N_rel = 0.15 ± 0.12
m_ψ(2S) = 3686.9 ± 0.2
σ_ψ(2S) = 2.6 ± 0.3 σ_rel = 4.80 ± 3.64
A = 1.01± 0.06 α = 0.49 ± 0.15 β = 6.24 ± 1.85
χ² = 68.8 DoF = 64 ==> Prob = 32.2%
Candidates per 2.5 MeV/c²
J/ψππ Mass [GeV/c²]

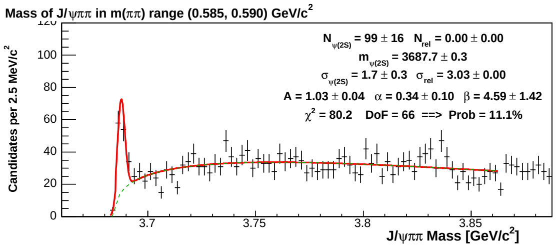

Mass of J/ψππ in m(ππ) range (0.585, 0.590) GeV/c²
N_ψ(2S) = 99 ± 16 N_rel = 0.00 ± 0.00
m_ψ(2S) = 3687.7 ± 0.3
σ_ψ(2S) = 1.7 ± 0.3 σ_rel = 3.03 ± 0.00
A = 1.03 ± 0.04 α = 0.34 ± 0.10 β = 4.59 ± 1.42
χ² = 80.2 DoF = 66 ==> Prob = 11.1%
Candidates per 2.5 MeV/c²
J/ψππ Mass [GeV/c²]

Appendix E

Mass Fits in $m_{\pi\pi}$ Slices for the $X(3872)$

This Appendix, just like the previous one, contains the $J/\psi\,\pi^+\pi^-$ mass histograms in different $m_{\pi\pi}$ slices. We fit these histograms to obtain the $X(3872)$ $m_{\pi\pi}$ spectrum, as described in Section 4.4. The resulting $m_{\pi\pi}$ spectrum is presented in Figure 4-14. See Appendix B for explanation of the numbers on each plot.

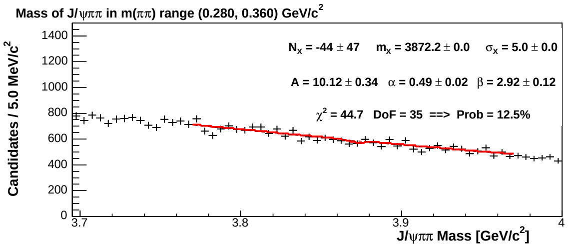

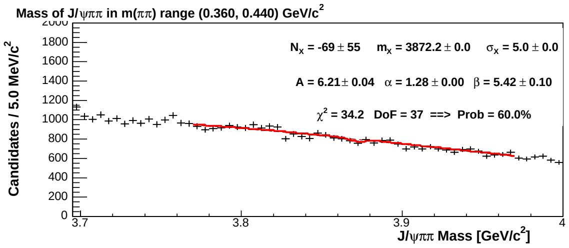

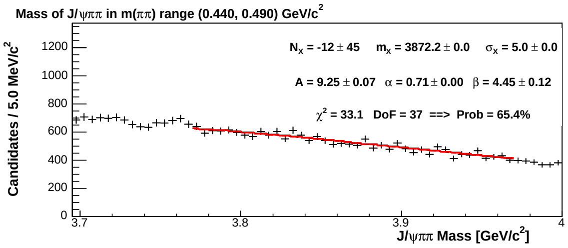

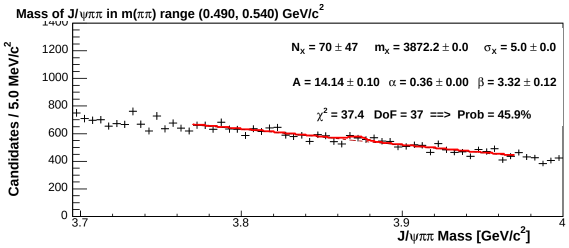

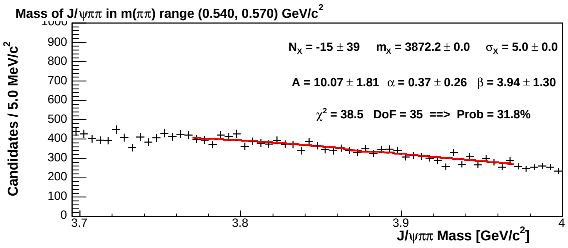

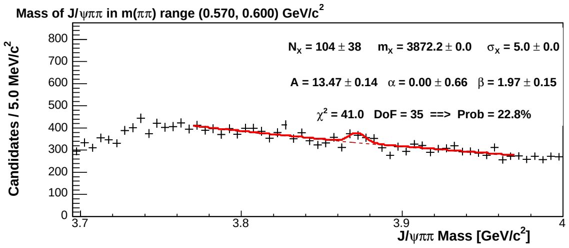

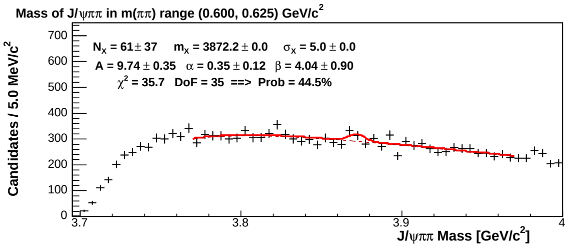
Mass of J/ψππ in m(ππ) range (0.600, 0.625) GeV/c^2
N_x = 61 ± 37 m_x = 3872.2 ± 0.0 σ_x = 5.0 ± 0.0
A = 9.74 ± 0.35   α = 0.35 ± 0.12   β = 4.04 ± 0.90
χ^2 = 35.7   DoF = 35 ==> Prob = 44.5%
Candidates / 5.0 MeV/c^2
0
100
200
300
400
500
600
700
3.7
3.8
3.9
4
J/ψππ Mass [GeV/c^2]

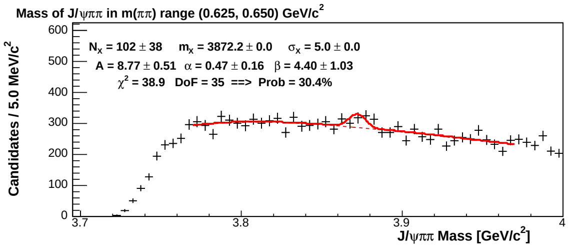
Mass of J/ψππ in m(ππ) range (0.625, 0.650) GeV/c^2
N_x = 102 ± 38 m_x = 3872.2 ± 0.0 σ_x = 5.0 ± 0.0
A = 8.77 ± 0.51   α = 0.47 ± 0.16   β = 4.40 ± 1.03
χ^2 = 38.9   DoF = 35 ==> Prob = 30.4%
Candidates / 5.0 MeV/c^2
0
100
200
300
400
500
600
3.7
3.8
3.9
4
J/ψππ Mass [GeV/c^2]

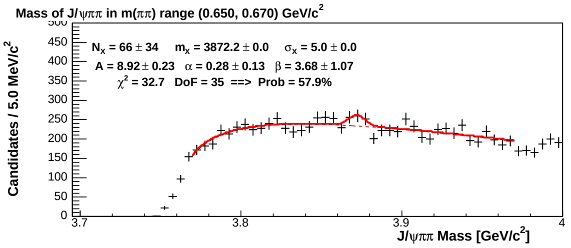
Mass of J/ψππ in m(ππ) range (0.650, 0.670) GeV/c^2
N_x = 66 ± 34 m_x = 3872.2 ± 0.0 σ_x = 5.0 ± 0.0
A = 8.92 ± 0.23   α = 0.28 ± 0.13   β = 3.68 ± 1.07
χ^2 = 32.7   DoF = 35 ==> Prob = 57.9%
Candidates / 5.0 MeV/c^2
0
50
100
150
200
250
300
350
400
450
500
3.7
3.8
3.9
4
J/ψππ Mass [GeV/c^2]

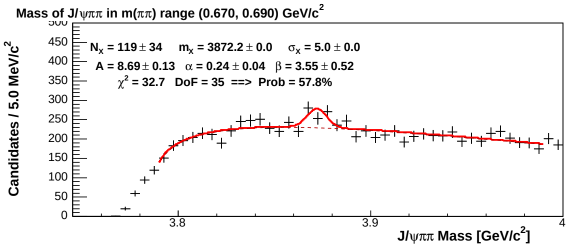
Mass of J/ψππ in m(ππ) range (0.670, 0.690) GeV/c^2
N_x = 119 ± 34 m_x = 3872.2 ± 0.0 σ_x = 5.0 ± 0.0
A = 8.69 ± 0.13   α = 0.24 ± 0.04   β = 3.55 ± 0.52
χ^2 = 32.7   DoF = 35 ==> Prob = 57.8%
Candidates / 5.0 MeV/c^2
0
50
100
150
200
250
300
350
400
450
500
3.8
3.9
4
J/ψππ Mass [GeV/c^2]

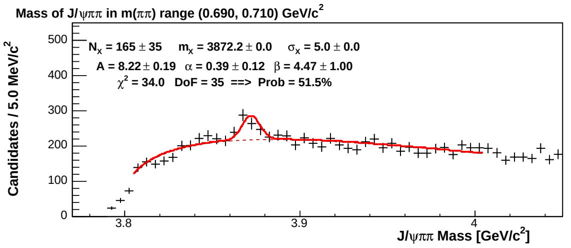
Mass of J/ψππ in m(ππ) range (0.690, 0.710) GeV/c^2
N_x = 165 ± 35 m_x = 3872.2 ± 0.0 σ_x = 5.0 ± 0.0
A = 8.22 ± 0.19   α = 0.39 ± 0.12   β = 4.47 ± 1.00
χ^2 = 34.0   DoF = 35 ==> Prob = 51.5%
Candidates / 5.0 MeV/c^2
0
100
200
300
400
500
3.8
3.9
4
J/ψππ Mass [GeV/c^2]

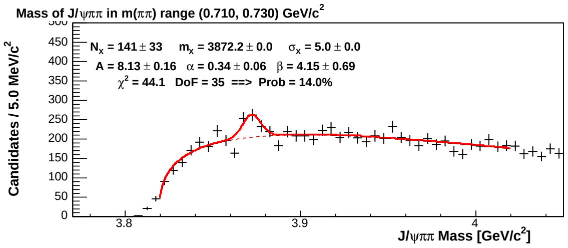
Mass of J/ψππ in m(ππ) range (0.710, 0.730) GeV/c^2
N_x = 141 ± 33 m_x = 3872.2 ± 0.0 σ_x = 5.0 ± 0.0
A = 8.13 ± 0.16   α = 0.34 ± 0.06   β = 4.15 ± 0.69
χ^2 = 44.1   DoF = 35 ==> Prob = 14.0%
Candidates / 5.0 MeV/c^2
0
50
100
150
200
250
300
350
400
450
500
3.8
3.9
4
J/ψππ Mass [GeV/c^2]

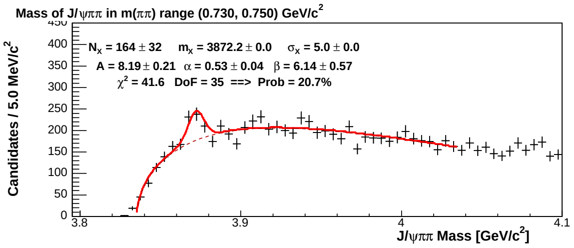
Mass of J/ψππ in m(ππ) range (0.730, 0.750) GeV/c^2
N_x = 164 ± 32 m_x = 3872.2 ± 0.0 σ_x = 5.0 ± 0.0
A = 8.19 ± 0.21   α = 0.53 ± 0.04   β = 6.14 ± 0.57
χ^2 = 41.6   DoF = 35 ==> Prob = 20.7%
Candidates / 5.0 MeV/c^2
0
50
100
150
200
250
300
350
400
450
3.8
3.9
4
4.1
J/ψππ Mass [GeV/c^2]

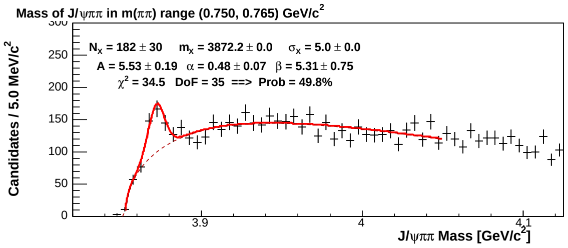
Mass of J/ψππ in m(ππ) range (0.750, 0.765) GeV/c^2
N_x = 182 ± 30 m_x = 3872.2 ± 0.0 σ_x = 5.0 ± 0.0
A = 5.53 ± 0.19   α = 0.48 ± 0.07   β = 5.31 ± 0.75
χ^2 = 34.5   DoF = 35 ==> Prob = 49.8%
Candidates / 5.0 MeV/c^2
0
50
100
150
200
250
300
3.9
4
4.1
J/ψππ Mass [GeV/c^2]

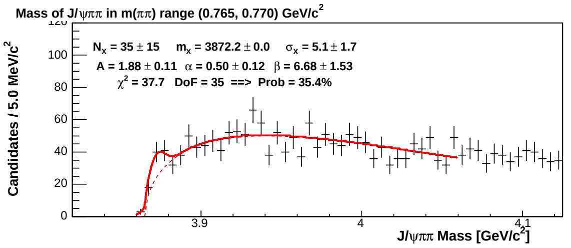
Mass of J/ψππ in m(ππ) range (0.765, 0.770) GeV/c^2
N_x = 35 ± 15 m_x = 3872.2 ± 0.0 σ_x = 5.1 ± 1.7
A = 1.88 ± 0.11   α = 0.50 ± 0.12   β = 6.68 ± 1.53
χ^2 = 37.7   DoF = 35 ==> Prob = 35.4%
Candidates / 5.0 MeV/c^2
0
20
40
60
80
100
120
3.9
4
4.1
J/ψππ Mass [GeV/c^2]

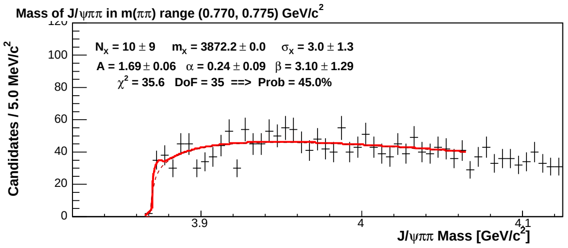
Mass of J/ψππ in m(ππ) range (0.770, 0.775) GeV/c^2
N_x = 10 ± 9 m_x = 3872.2 ± 0.0 σ_x = 3.0 ± 1.3
A = 1.69 ± 0.06   α = 0.24 ± 0.09   β = 3.10 ± 1.29
χ^2 = 35.6   DoF = 35 ==> Prob = 45.0%
Candidates / 5.0 MeV/c^2
0
20
40
60
80
100
120
3.9
4
4.1
J/ψππ Mass [GeV/c^2]

Appendix F

Systematic Uncertainty on the Last Few Slices in the $m_{\pi\pi}$ Spectra

During the $J/\psi\,\pi^+\pi^-$ mass fits in the $m_{\pi\pi}$ slices we fix the means and widths of the signals to the values obtained from the whole-sample mass fit in all the slices except the last a few. In normal slices the entries can smear in and out of the slice from both low and high mass neighboring slices. In the last slices the entries can only smear in one direction, thus biasing the mean value towards higher mass. If we allow the mean and width to float in all the slices, they indeed remain quite constant throughout the whole $m_{\pi\pi}$ range, except the last a few slices, as shown in Figure F-1 for the $\psi(2S)$.

Another special feature of the last a few slices in the $m_{\pi\pi}$ spectra is that the mass peaks in them are very close to the turn-on of the background. As a result, the fit may have difficulty in determining the background turn-on point.

To determine the systematic uncertainty on the yield in these slices coming from the variation of the background parametrization, we perform a few special fits, in addition to the normal ones and see how much the $\psi(2S)$ yield changes. These additional fits include, *e.g.*, the shift of the turn-on value x_0 up and down, because for the last slices this may significantly change the yield. Such variation need not to be done for the regular slices in the $m_{\pi\pi}$ spectra. Some fit variations for these special slices are skipped, *e.g.* we do not try to fit the background with a polynomial, because the polynomial does not work very well in the vicinity of the turn-on.

Special treatment is given for the last three (14th, 15th and 16th) slices in the $X(3872)$ $m_{\pi\pi}$ spectrum and the last two (27th and 28th) slices in the $\psi(2S)$ $m_{\pi\pi}$ spectrum. Below are given the fits with the following variations for each slice:

- Fit “A” for each $m_{\pi\pi}$ slice represents the nominal fit, except for 15th and 16th slices for the $X(3872)$.

- Fits “C” and “D” show the mass fits with the $X(3872)$ width or $\psi(2S)$ *narrow* width shifted up and down by one standard deviation from the fixed nominal value. The standard deviation is determined from the fit of the $X(3872)$ or $\psi(2S)$ peak in the whole sample.

- Fits “C1” and “D1” show the mass fits with the $X(3872)$ mass or $\psi(2S)$ relative normalization N_{rel} shifted up and down by one standard deviation from the fixed nominal value. The standard deviation is, again, determined from the fit of the $X(3872)$ or $\psi(2S)$ peak in the whole sample.

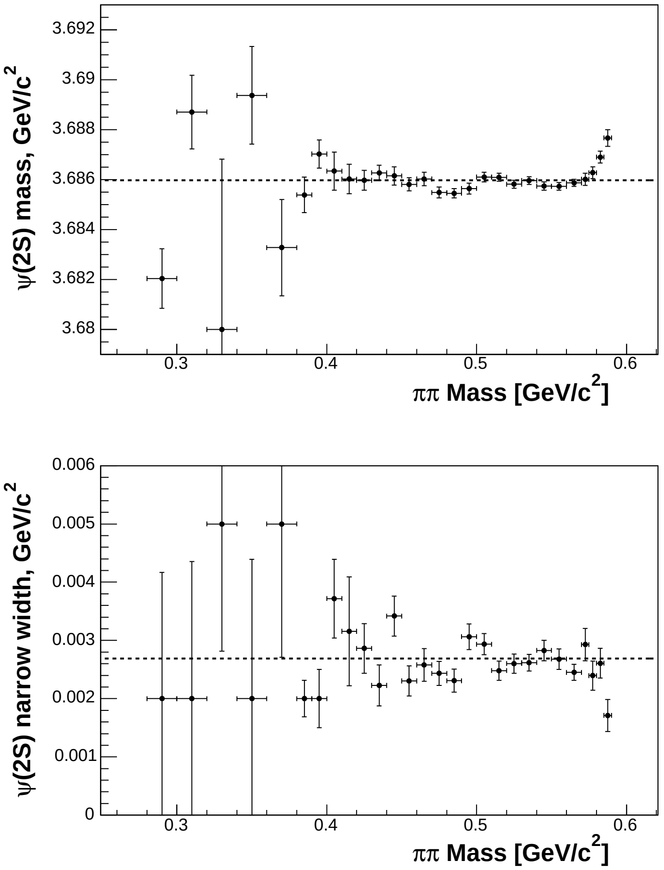

Figure F-1: The $\psi(2S)$ mass (top) and narrow width (bottom) versus $m_{\pi\pi}$. Both of them are almost constant from one $m_{\pi\pi}$ slice to another, except for the last a few slices, where a clear bias is seen in the top plot.

- Fits "E" and "F" display the fit over the different mass range: 150 MeV$/c^2$ and 250 MeV$/c^2$, correspondingly, instead of the nominal fit range 200 MeV$/c^2$.

- Fits "G","H" and "I" are performed with a floating $X(3872)$ mass, a floating $X(3872)$ width and floating both $X(3872)$ mass and width, correspondingly. For the last (16th) and second to the last (15th) slices the $X(3872)$ width is floating by default, so that the fit "H" displays the case of *fixed* $X(3872)$ width. There is no fit "I" for these two slices. For the $\psi(2S)$ the fit "G" corresponds to the fixed N_{rel} and σ_{rel}; the fit "H" – to the fixed $\psi(2S)$ narrow width; the fit "H1" – to the fixed $\psi(2S)$ mass.

- In fits "J" and "K" a few points in the beginning of the range are skipped from the fit or added to the fit to see what effect will this cause. Not all the considered bins have these fits. We look at the fits individually to determine if these fit variations are worth consideration.

- Fits "M" – "Q" are related to the changes in the background turn-on point x_0. These fits will be discussed next. Fits "O" are accepted as nominal ones for 15th and 16th slices for the $X(3872)$.

- Fit "R" is done only for the last (28th) $m_{\pi\pi}$ slice for the $\psi(2S)$. It will be discussed later.

The background turn-on point x_0 is normally allowed to float in the fit within ± 20 MeV$/c^2$ around the kinematic limit of the $m_{\pi\pi}$ mass: mass of J/ψ plus the low boundary of the $m_{\pi\pi}$ slice. But in the last few slices the turn-on comes very close to the mass peak and it becomes hard for the fit to determine its value and uncertainty for it. This is an especially delicate problem for the $X(3872)$, due to the poor signal-to-noise ratio it is unclear what kind of signal is present. In the last $\psi(2S)$ slices at least there is unequivocal signal present, but one might debate how much. Being in such an uncertain situation, we used the results of the lower $m_{\pi\pi}$ slices to *project* an appropriate turn-on point, and an uncertainty on it, for the nominal fit of the last X slices.

To obtain the turn-on point and a reasonable systematic for the associated uncertainty in each $m_{\pi\pi}$ slice, we plot the dependence of x_0 on $m_{\pi\pi}$, fit it with the straight line $x_0(m_{\pi\pi}) = A + B(m_{\pi\pi} - m^0_{\pi\pi})$ and determine the projected value of x_0 at a given point $m^0_{\pi\pi}$ (where the value of x_0 is simply equal to A) as well as the projected uncertainty on A. The $m^0_{\pi\pi}$ is chosen to be the low edge of the given $m_{\pi\pi}$ slice.

The linear fits are shown in Figure F-2, where the last two points are not included in the straight-line fit (the last three in the bottom plot) because we do not trust them, but we still plot them as open circles as a check that they are not too far off the fitted straight-line. Each of the three plots in Figure F-2 have the identical data, the only difference is that the linear fits are performed around different expansion points $m^0_{\pi\pi}$ for different slices, which are indicated by the large filled circles. The text in the plots lists numerical details of the fit results. Notice that we found it more convenient to measure x_0 from an arbitrarily chosen reference point of 3.7 MeV$/c^2$.

These linear fits provide us with a projection A of the expected turn-on point x_0, and the fitted standard deviation σ_A defines a plausible range for the precision with which we may know the turn-on value. This range for the turn-on is unconnected with what the $J/\psi\pi^+\pi^-$ spectrum for that particular slice tells us. We study the "validity" of the projected standard deviation σ_A value by varying the turn-on in the $J/\psi\pi^+\pi^-$ fit by $\pm 1\sigma_A$ while at the same time monitoring the fit χ^2. Nominally the systematic uncertainty on x_0, when we fix it to the projected x_0, is obtained by shifting the projection by one σ_A up and down.

Now we consider this method in detail. First, let us look at the very last slice (slice 16) in the $m_{\pi\pi}$ spectrum for the $X(3872)$. Fit "F-16-A" would normally be a nominal one. If we shift the x_0 value by one nominal standard deviation up or down (Fits "F-16-M" and "F-16-N") the χ^2 practically does not change, though one would expect it to increase by 1 unit. From this we conclude that the normal fit grossly underestimates the uncertainty on the turn-on value x_0. Because of the unreliability of the "would-be" nominal value (and "would-be" nominal standard deviation) of the turn-on, we adopt the projected value of the x_0 $(3.7 + 169.604/1000)$ (Fit "F-16-O") and the projected standard deviation as the nominal ones. If the x_0 value is shifted by plus or minus one projected standard deviation (Fits "F-16-P" and "F-16-Q") then the $X(3872)$ yield changes from 10 ± 9, up to 15 ± 9, and down to 8 ± 11. This variation gives a systematic uncertainty on the yield due to x_0 of $^{+5}_{-2}$ candidates. However, the full yield systematic we adopt is based on the whole ensemble of variations, and we find other effects that will give a larger uncertainty on the high side.

The same procedure is followed for the second-to-last (15th) slice. In this case the fitter fails to find the minimum in the nominal fit at all, because the χ^2 curve looks like a steep wall going into very shallow valley. To prevent the fitter from wandering in this valley and finally giving us some random result, we again fix the turn-on to its projected value (Fit "F-15-O") instead of its "would-be" nominal value (Fit "F-15-A") and vary it by a projected standard deviation up and down (Fits "F-15-P" and "F-15-Q") instead of the "would-be" nominal standard deviation (Fits "F-15-M" and "F-15-N"). The change in the $X(3872)$ yield from 35 ± 15, up to 38 ± 15,

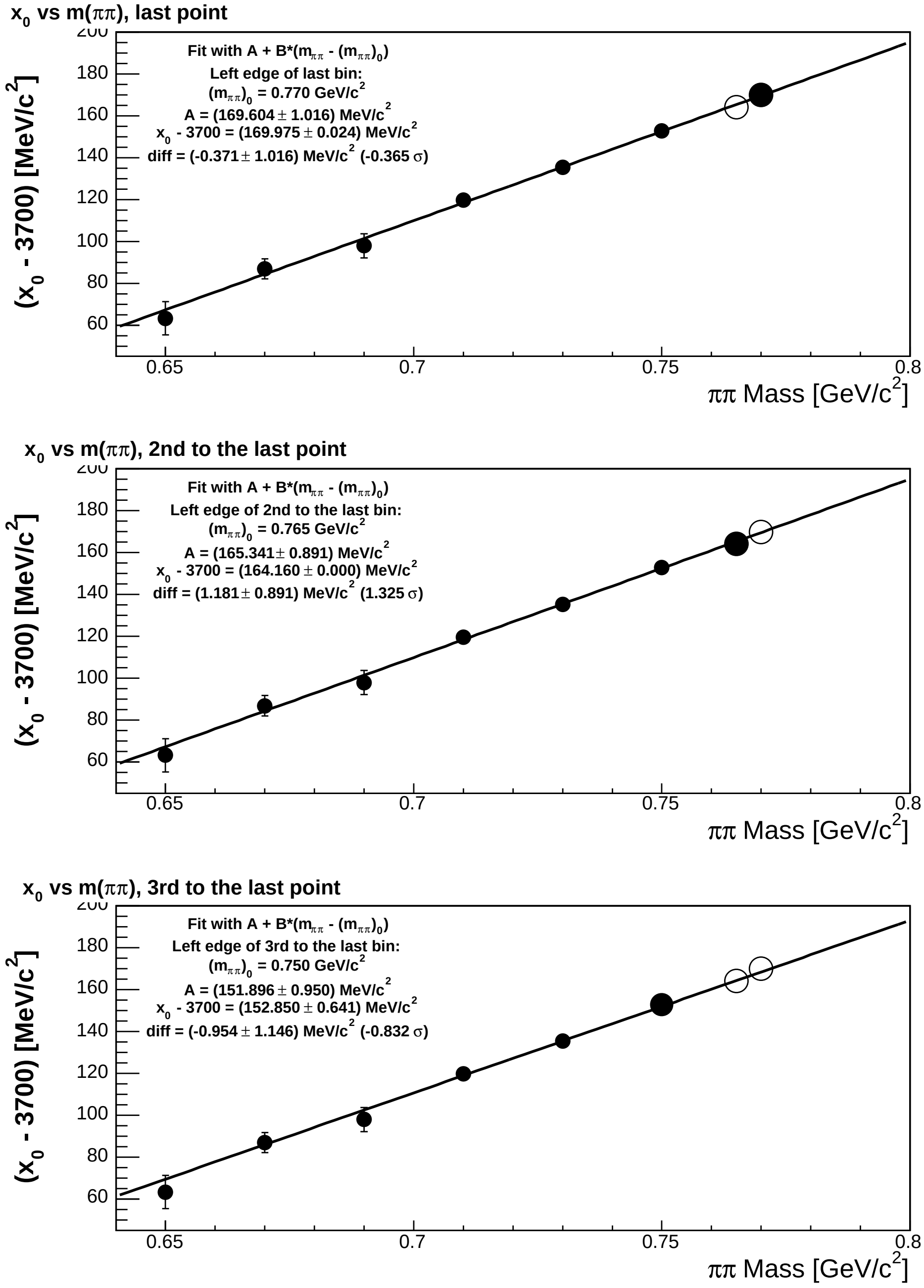

Figure F-2: The linear fits for the projected turn-on value of the $J/\psi\,\pi^+\pi^-$ mass distributions for $m_{\pi\pi}$ slices. In each plot the first few lower $m_{\pi\pi}$ slices (small full circles) determine the line, and the big full circle is compared to the projected value on this line. The big full circle itself is not included in the fit. The big open circles are not included in the fit too, they are only drawn for the comparison's sake.

x_0 value	χ^2	$\psi(2S)$ yield
3.68493 ± 0.00001	80.2	99
3.68551 (= 3.68493 + 50σ)	81.2	101
3.68415 (= 3.68493 - 67σ)	81.2	97

Table F.1: The x_0 scan for the last (28th) slice in the $\psi(2S)$ $m_{\pi\pi}$ spectra. The first line shows the x_0 value with its reported uncertainty. The hand-made scan shows that the value is right; but our manual shift for change in χ^2 by one unit corresponds to what MINUIT reports as a $^{+50}_{-67}$ standard deviations shift.

x_0 value	χ^2	$\psi(2S)$ yield
3.68045 ± 0.00092	68.8	292
3.96682 (= 3.68045 + 4σ)	69.8	304
3.67889 (= 3.68045 - 1.7σ)	69.8	278

Table F.2: The x_0 scan for the second-to-last (27th) slice in the $\psi(2S)$ $m_{\pi\pi}$ spectra. The first line shows the x_0 value and the nominal uncertainty for it. The hand-made scan shows that the value is right; but our manual shift for change in χ^2 by one unit corresponds to what MINUIT reports as a $^{+4.0}_{-1.7}$ standard deviations shift.

and down to 31 ± 16, gives us an estimate of the systematic uncertainty on the yield of only a few candidates. The effects of the other systematic fit variations, though, will be much more important.

For the $\psi(2S)$ we treat the uncertainty related to the x_0 position differently. The main problem here is that the error matrix, calculated by MINUIT, is not complete, though the fit converges. This results in a gross underestimation of the nominal uncertainty on the x_0 value. The x_0 values and the uncertainties on them for both last (28th) and last-but-one (27th) $m_{\pi\pi}$ slices are given in the first lines of Tables F.1 and F.2. Fits "F-27-A" and "F-28-A" are produced with these x_0 values. Had the uncertainties on x_0 been correct, we would vary x_0 by plus-minus one standard deviation, and then compare the changed $\psi(2S)$ yields to the nominal one, just as for the $X(3872)$. But because the reported uncertainties on the x_0 values are extremely low, we determine them by hand. Namely, we do a scan of the fit χ^2, re-minimizing at each point of the scan. Then we find the χ^2 minimum and the places which correspond to the increase of the χ^2 by one unit (*i.e.* true standard deviations). These standard deviations for x_0 are adopted as the nominal ones. The nominal value for x_0 does not get "re-defined". Having done that we determine the systematic uncertainty by varying the x_0 by plus-minus one nominal standard deviation and looking at the respective $\psi(2S)$ yields. The bottom two lines in the Tables F.1 and F.2 show the positions of the true standard deviations. The corresponding fits are Fits "F-27-M", "F-27-N", "F-28-M" and "F-28-N".

For the last (28th) $m_{\pi\pi}$ slice for the $\psi(2S)$ we do one more novel systematic variation. Being so close to the kinematic limit the Gaussian shape of the signal might undergo more dramatic types of distortion, and for the $\psi(2S)$ there is enough signal that we might actually be sensitive to such an effect. In particular, by chopping the data into slices we may distort the simple Gaussian into some other shape. We consider this by fitting the peak with an *asymmetric* Gaussian, *i.e.* a Gaussian with different widths above and below the peak. The results of this is shown in

Fit "F-28-R". The fit actually prefers to zero out the low-mass half of the Gaussian. But some residual mass smearing is going to take place anyhow and a vanishing low-side σ is not physical. We limit the fit so that the lower half of the Gaussian must have $\sigma \geq 1.5$ MeV/c^2, and the turn-on is fixed to the value found in Table F.1. The fit comes to this limiting value, but still maintains a respectable χ^2, which is in fact better than what our nominal fit (Fit "F-28-A") gives for this slice.

The purpose of all these fit variations is to see how much the yield changes among them. For each $m_{\pi\pi}$ slice we find what are, generally,[1] the highest and the lowest yields, calculate how far they are from the default fit, and assign this difference as an asymmetric systematic uncertainty to the yield from the nominal fit. The final systematic results are summarized in Table F.3, which also indicates from which fits the uncertainties are derived.

Slice #	$m_{\pi\pi}$ range GeV/c^2	Default yield / Fit #	Highest yield / Fit #	Lowest yield / Fit #
$X(3872)$ 14th	0.730 - 0.750	182 ± 30 / F-14-A	197 / F-14-O	166 / F-14-D
$X(3872)$ 15th	0.750 - 0.765	35 ± 15 / F-15-O	38 / F-15-C	14 / F-15-F
$X(3872)$ 16th	0.765 - 0.775	10 ± 9 / F-16-O	18 / F-16-C1	8 / F-16-Q
$\psi(2S)$ 27th	0.580 - 0.585	292 ± 43 / F-27-A	304 / F-27-M	270 / F-27-D
$\psi(2S)$ 28th	0.585 - 0.590	99 ± 16 / F-28-A	112 / F-28-R	89 / F-28-D

Table F.3: The default, lowest and highest yields in the last slices in the $m_{\pi\pi}$ spectra.

F.1 Fits for the Last Three Slices in $m_{\pi\pi}$ Spectrum for $X(3872)$

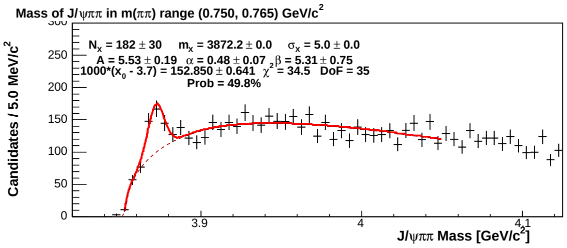

Fit F-14-A: nominal mass fit ($X(3872)$ mass and width are fixed)

---

[1] We consider on a case-by-case basis whether variations do indeed show plausible changes. There are occasionally variations for which we have reasons to doubt their suitability, but this turns out to rarely, if ever, impact our final systematic.

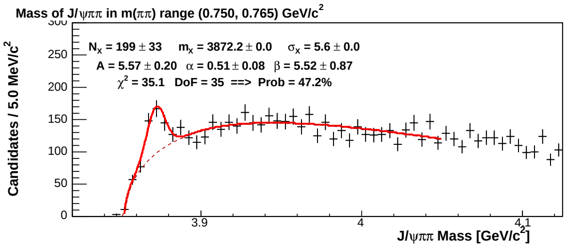

Fit F-14-C: the $X(3872)$ width is shifted by one standard deviation up from the nominal value

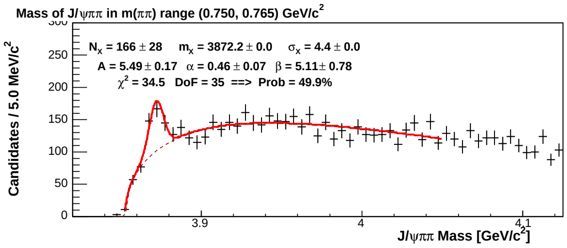

Fit F-14-D: the $X(3872)$ width is shifted by one standard deviation down from the nominal value

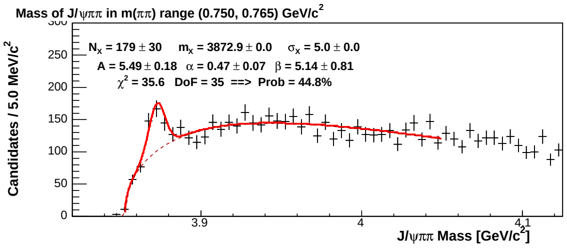

Fit F-14-C1: the $X(3872)$ mass is shifted by one standard deviation up from the nominal value

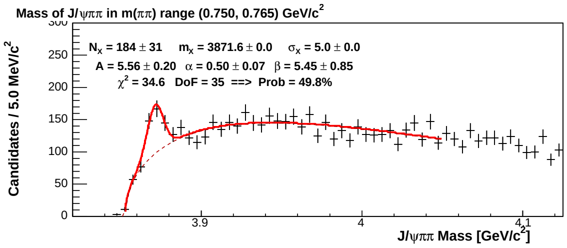

Fit F-14-D1: the $X(3872)$ mass is shifted by one standard deviation down from the nominal value

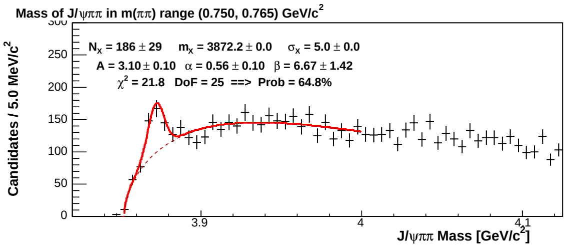

Fit F-14-E: mass fit with the fit range decreased to 150 MeV/c^2

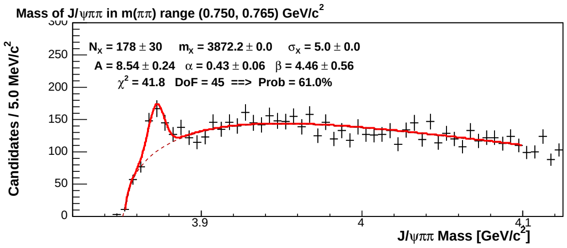

Fit F-14-F: mass fit with the fit range increased to 250 MeV/c^2

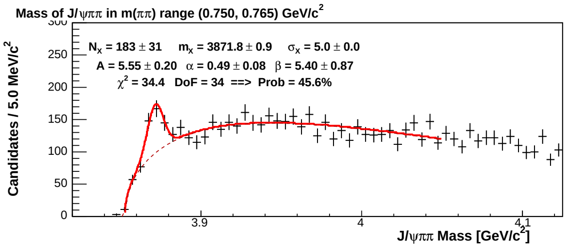

Fit F-14-G: mass fit with $X(3872)$ mass floating

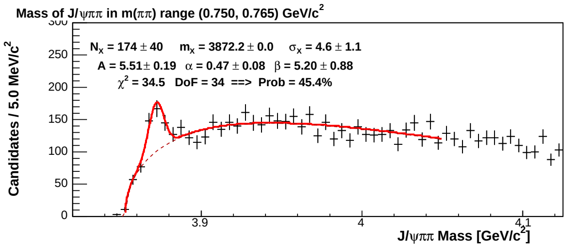

Fit F-14-H: mass fit with $X(3872)$ width floating

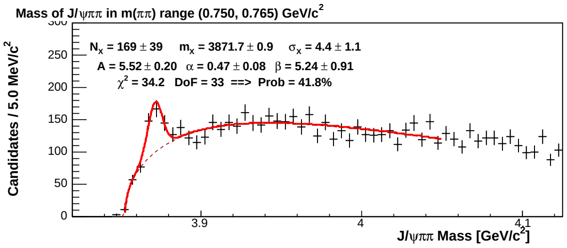

Fit F-14-I: mass fit with both $X(3872)$ mass and width floating

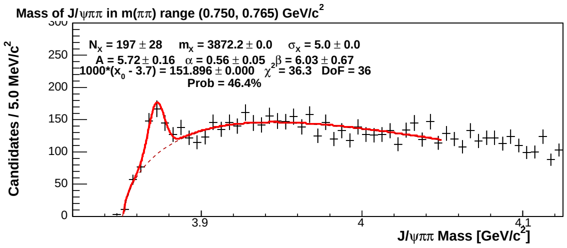

Fit F-14-O: the turn-on is fixed to the projected value.

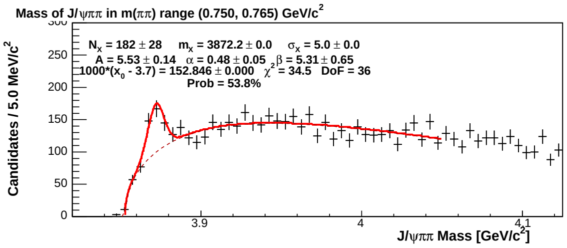

Fit F-14-P: the turn-on is shifted by one projected standard deviation up from the projected value.

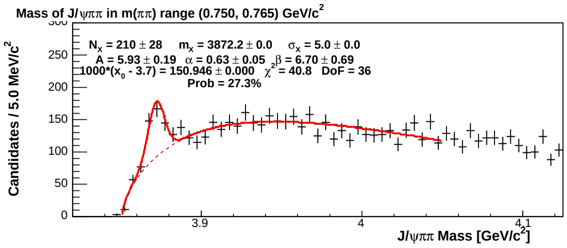

Fit F-14-Q: the turn-on is shifted by one projected standard deviation down from the projected value.

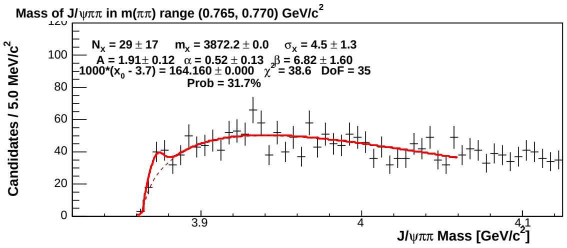

Fit F-15-A: fit **without x_0 projection** ($X(3872)$ mass fixed, $X(3872)$ width floating above 3.0 MeV/c^2). Had we accepted this x_0 value, this fit would be nominal.

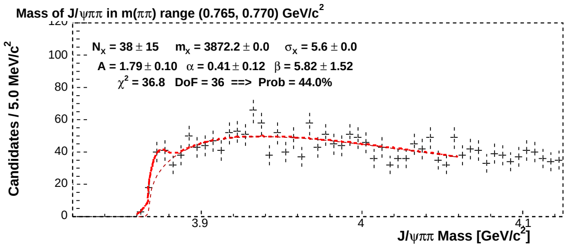

Fit F-15-C: the $X(3872)$ width is shifted by one standard deviation up from the nominal value.

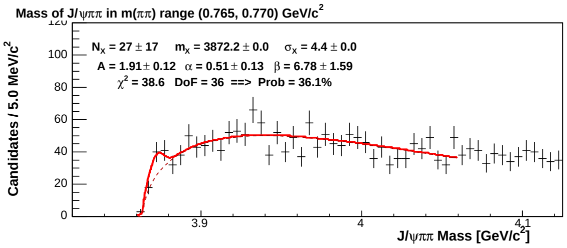

Fit F-15-D: the $X(3872)$ width is shifted by one standard deviation down from the nominal value.

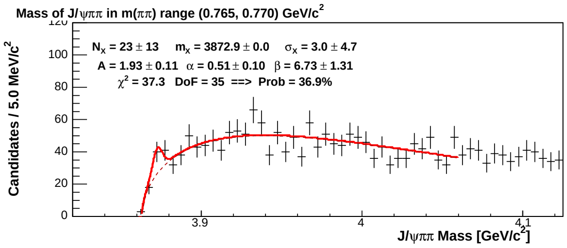

Fit F-15-C1: the $X(3872)$ mass is shifted by one standard deviation up from the nominal value.

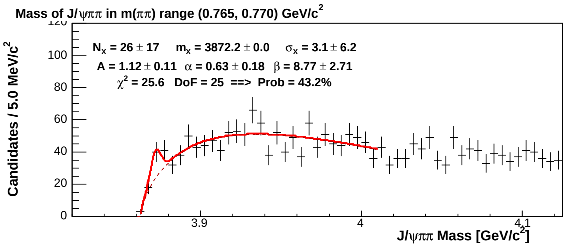

Fit F-15-E: mass fit with the fit range decreased to 150 MeV/c^2.

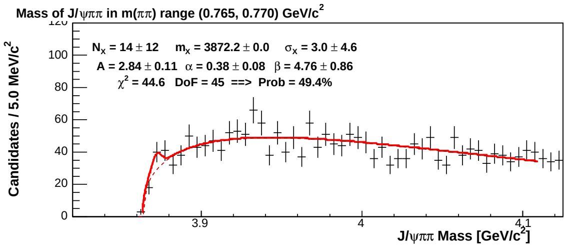

Fit F-15-F: mass fit with the fit range increased to 250 MeV/c^2.

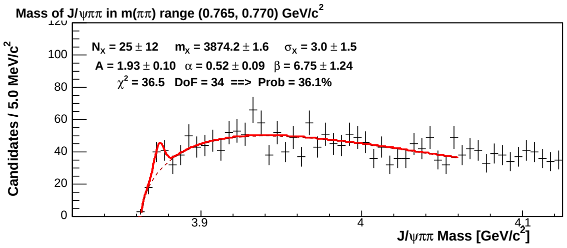

Fit F-15-G: mass fit with $X(3872)$ mass floating.

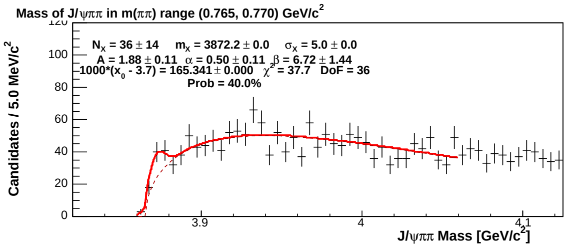

Fit F-15-H: mass fit with $X(3872)$ width fixed.

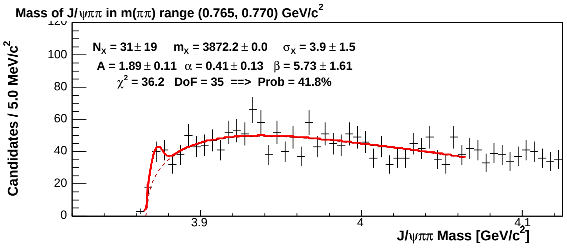

Fit F-15-J: mass fit with skipped point.

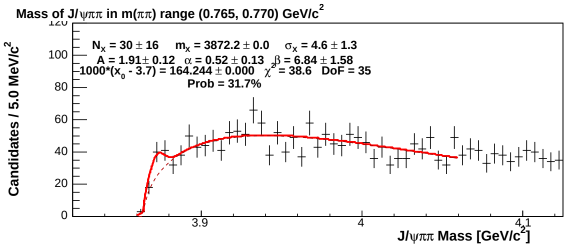

Fit F-15-M: the turn-on is shifted up from the fitted value by one standard deviation (as reported by MINUIT which drastically underestimates it).

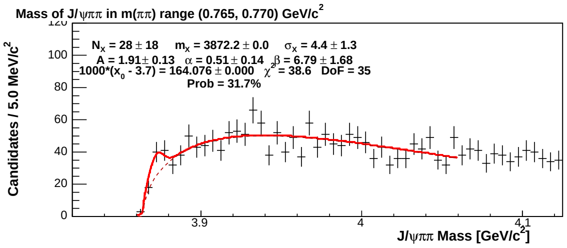

Fit F-15-N: the turn-on is shifted down from the fitted value by one standard deviation (as reported by MINUIT which drastically underestimates it).

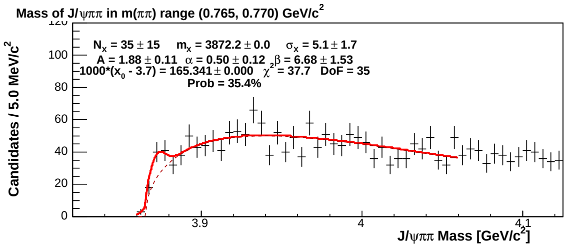

Fit F-15-O: the turn-on is fixed to the projected value - **the nominal fit**.

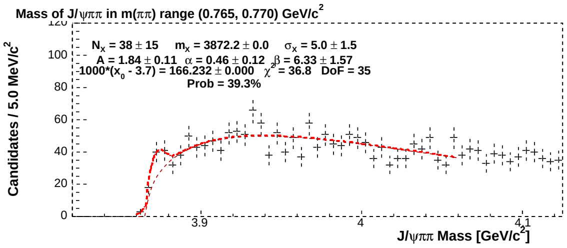

Fit F-15-P: the turn-on is shifted by one projected standard deviation up from the projected value.

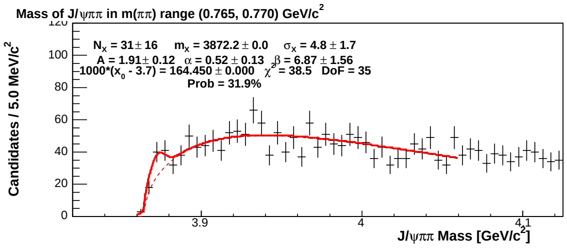

Fit F-15-Q: the turn-on is shifted by one projected standard deviation down from the projected value.

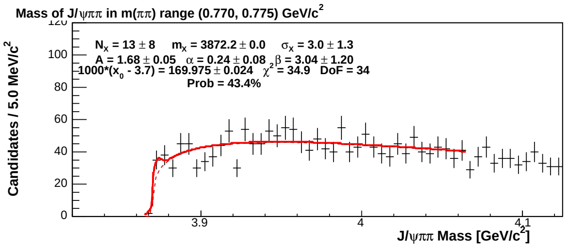

Fit F-16-A: fit **without x_0 projection** ($X(3872)$ mass fixed, $X(3872)$ width floating above 3.0 MeV/c^2). Had we accepted this x_0 value, this fit would be nominal.

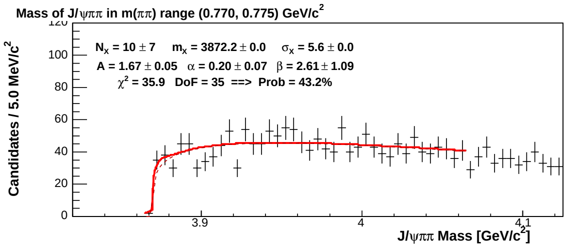

Fit F-16-C: the $X(3872)$ width is shifted by one standard deviation up from the nominal value.

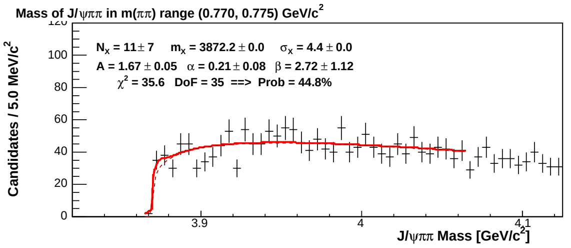

Fit F-16-D: the $X(3872)$ width is shifted by one standard deviation down from the nominal value.

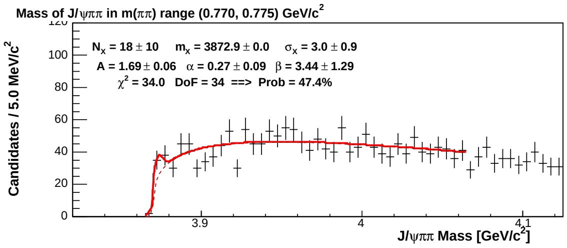

Fit F-16-C1: the $X(3872)$ mass is shifted by one standard deviation up from the nominal value.

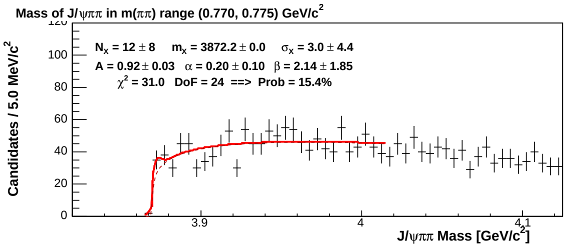

Fit F-16-E: mass fit with the fit range decreased to 150 MeV/c^2.

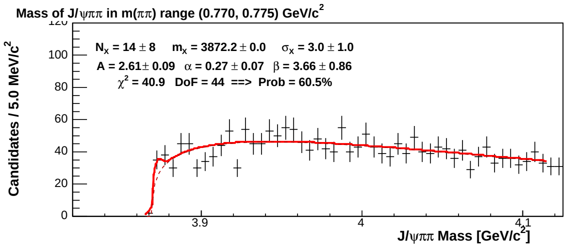

Fit F-16-F: mass fit with the fit range increased to 250 MeV/c^2.

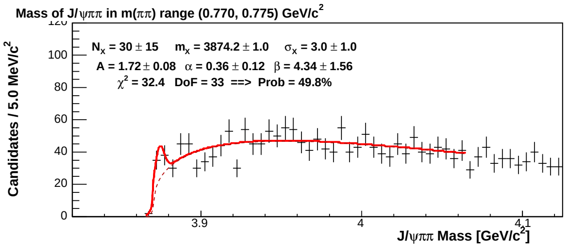

Fit F-16-G: mass fit with $X(3872)$ mass floating.

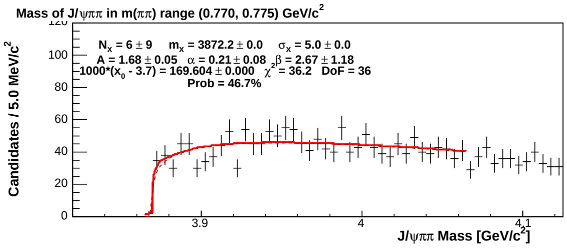

Fit F-16-H: mass fit with $X(3872)$ width fixed.

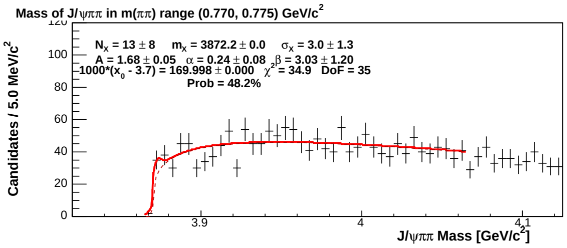

Fit F-16-M: the turn-on is shifted by one standard deviation up from the fitted value.

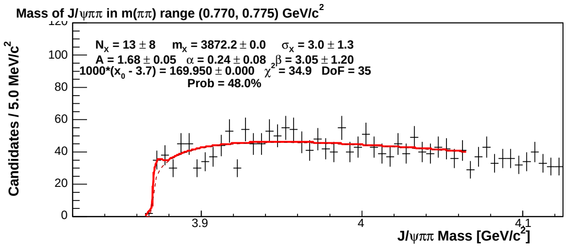

Fit F-16-N: the turn-on is shifted by one standard deviation down from the fitted value.

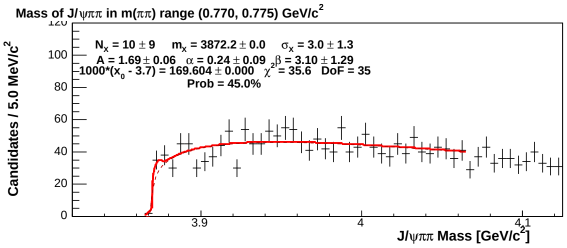

Fit F-16-O: the turn-on is fixed to the projected value – **the nominal fit**.

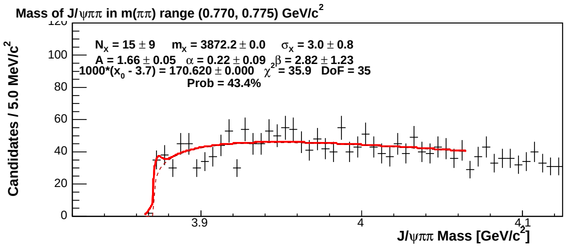

Fit F-16-P: the turn-on is shifted by one projected standard deviation up from the projected value.

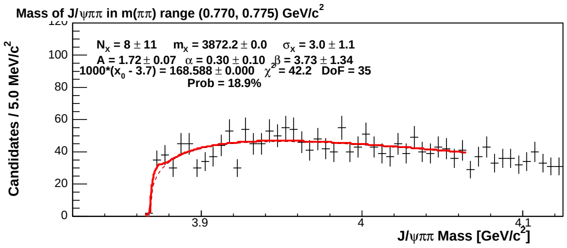

Fit F-16-Q: the turn-on is shifted by one projected standard deviation down from the projected value.

F.2 Fits for the Last Two Slices in $m_{\pi\pi}$ Spectrum for $\psi(2S)$

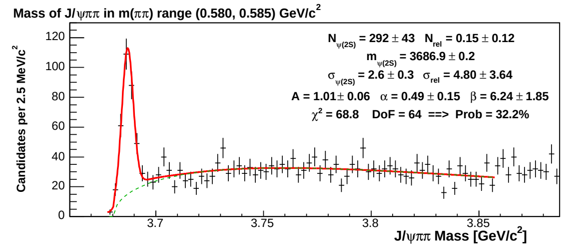

Fit F-27-A: nominal mass fit (N_{rel}, σ_{rel}, mass and width of $\psi(2S)$ are floating).

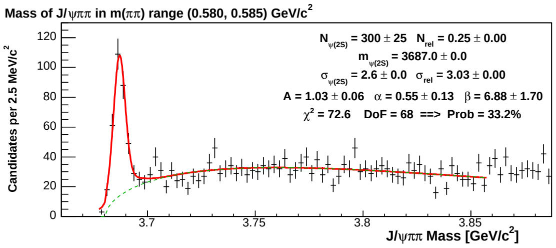

Fit F-27-C: the $\psi(2S)$ width is shifted by one standard deviation up from the nominal value.

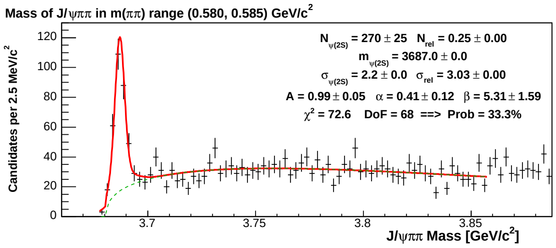

Fit F-27-D: the $\psi(2S)$ width is shifted by one standard deviation down from the nominal value.

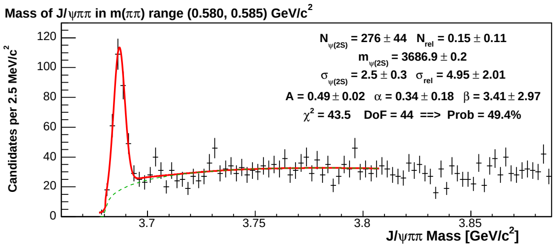

Fit F-27-E: mass fit with the fit range decreased to 150 MeV/c^2.

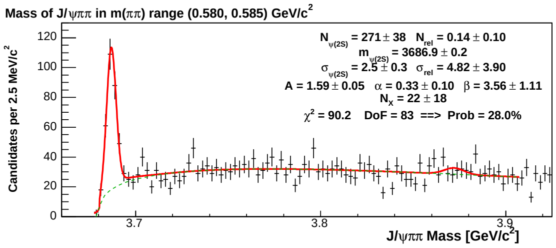

Fit F-27-F: mass fit with the fit range increased to 250 MeV/c^2.

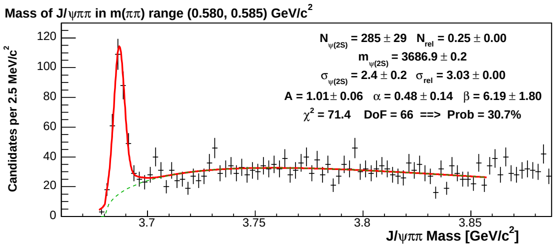

Fit F-27-G: mass fit with fixed relative normalization and relative width.

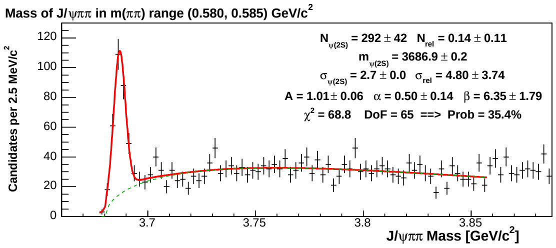

Fit F-27-H: mass fit with $\psi(2S)$ width fixed.

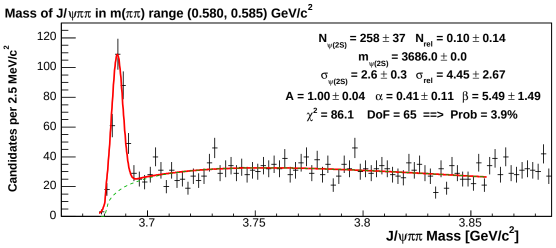

Fit F-27-H1: mass fit with $\psi(2S)$ mass fixed.

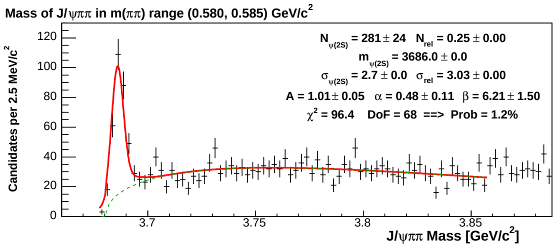

Fit F-27-I: mass fit in the way used for all slices except for last two (N_{rel}, σ_{rel}, $\psi(2S)$ mass and width are fixed).

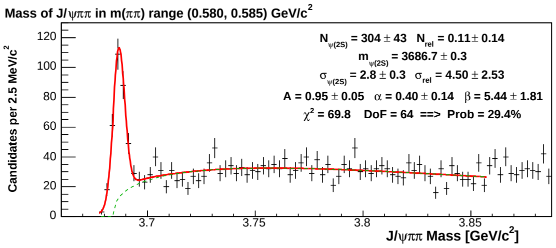

Fit F-27-M: the turn-on is shifted up so that the χ^2 gets increased by 1.

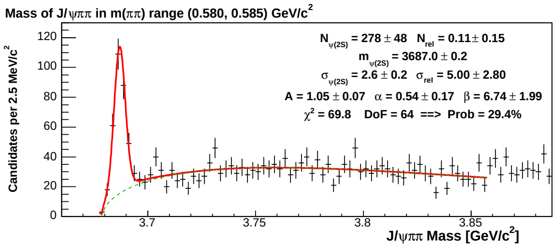

Fit F-27-N: the turn-on is shifted down so that the χ^2 gets increased by 1.

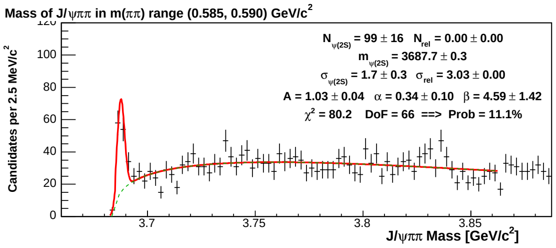

Fit F-28-A: nominal mass fit ($N_{rel} = 0$, mass and width of $\psi(2S)$ are floating).

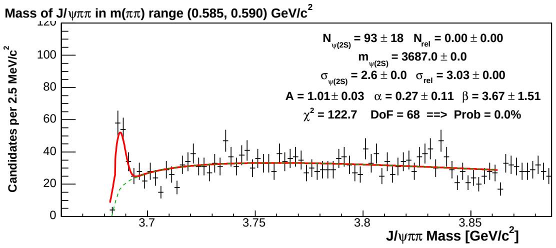

Fit F-28-C: the $\psi(2S)$ width is shifted by one standard deviation up from the nominal value.

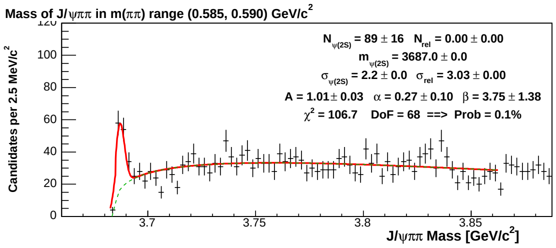

Fit F-28-D: the $\psi(2S)$ width is shifted by one standard deviation down from the nominal value.

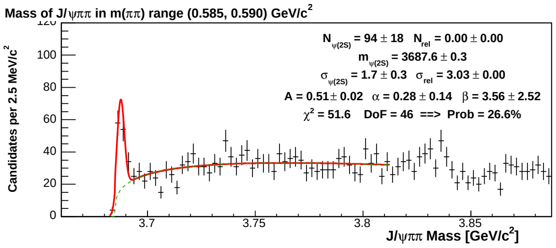

Fit F-28-E: mass fit with the fit range decreased to 150 MeV$/c^2$.

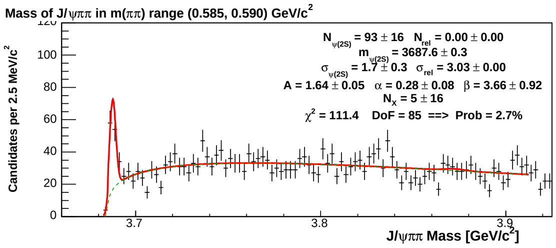

Fit F-28-F: mass fit with the fit range increased to 250 MeV$/c^2$.

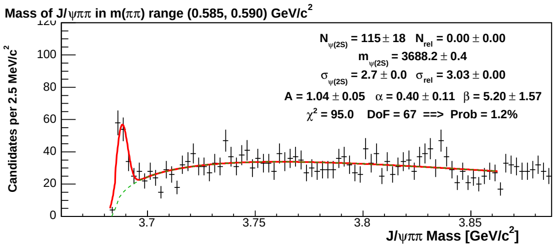

Fit F-28-H: mass fit with $\psi(2S)$ width fixed.

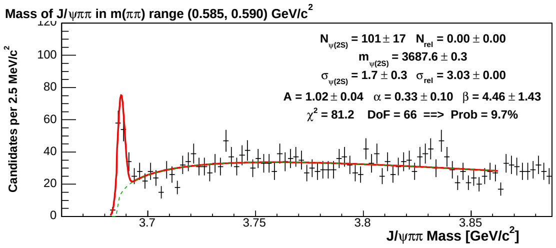

Fit F-28-M: the turn-on is shifted up so that the χ^2 gets increased by 1.

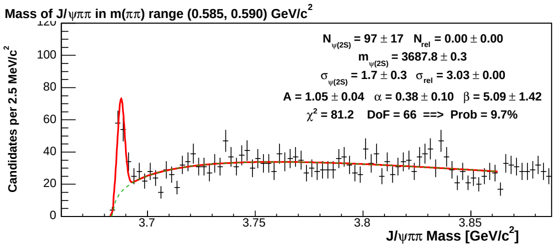

Fit F-28-N: the turn-on is shifted down so that the χ^2 gets increased by 1.

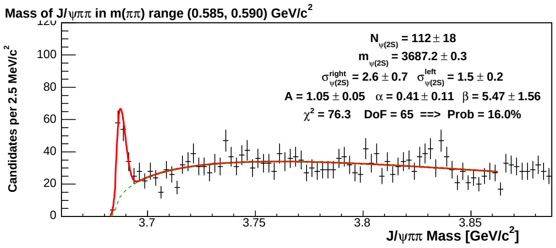

Fit F-28-R: using asymmetric gaussian for the fit.

Appendix G

Efficiency Corrections for Phase Space $m_{\pi\pi}$ Distribution

To estimate the systematic uncertainty due to our imperfect knowledge of the $m_{\pi\pi}$ spectrum for the $X(3872)$, we grossly change our nominal S-wave parametrization of this spectrum to a phase space parametrization, given by Equation 5.1. The appropriate detector efficiency curves and the input p_t spectra for the Monte Carlo generation for this *phase space model* are shown in Figure G-1 for the $\psi(2S)$ and Figure G-2 for the $X(3872)$. We fit them with the same parameterizing function $\exp(a_0 + a_1 p_t + a_2 p_t^2)$ as for the S-wave case. The fitted slope parameter a_1 is different from the S-wave case, but only by 1.4 standard deviations for the $\psi(2S)$. This difference for the $X(3872)$ is much smaller: only 0.3 standard deviations. Of course, these small differences can not be dismissed as statistically insignificant, as the same data is being fit in both cases. We will use these differences to estimate the systematics.

The comparison plots for the η and p_t spectra between the phase space Monte Carlo and the data are displayed in Figures G-3 and G-4. As we can see, the χ^2 match quality is almost the same as for the S-wave parametrization (Figures 4-5 and 4-6).

We use the phase space Monte Carlo result to obtain the inverse detector efficiency correction function $\xi^{PS}(m_{\pi\pi})$, which is different from the nominal S-wave inverse detector efficiency $\xi(m_{\pi\pi})$. The inverse efficiency $\xi^{PS}(m_{\pi\pi})$ is obtained by fitting the ratio of the corresponding $m_{\pi\pi}$ distributions before and after the detector, $\zeta^{PS}(m_{\pi\pi})/\overline{\zeta}^{PS}(m_{\pi\pi})$, as shown in Figure G-5 for both the $\psi(2S)$ and $X(3872)$. The plots in this figure display the $m_{\pi\pi}$ spectra before (triangles) and after (boxes) detector simulation and event selection. The points with error bars give the inverse detector efficiency with the corresponding scale at the right-hand side of the plot. The fitting function $\xi^{PS}(m_{\pi\pi})$ is also shown in each plot. The graphical comparison between $\xi(m_{\pi\pi})$ and $\xi^{PS}(m_{\pi\pi})$ curves for the $\psi(2S)$ and the $X(3872)$ is given in Figure 5-7. From this figure one can see that our detector efficiency corrections are only slightly sensitive to the $m_{\pi\pi}$ shape and that it is not necessary to achieve a better approximation for the $X(3872)$ than the S-wave shape, which we use.

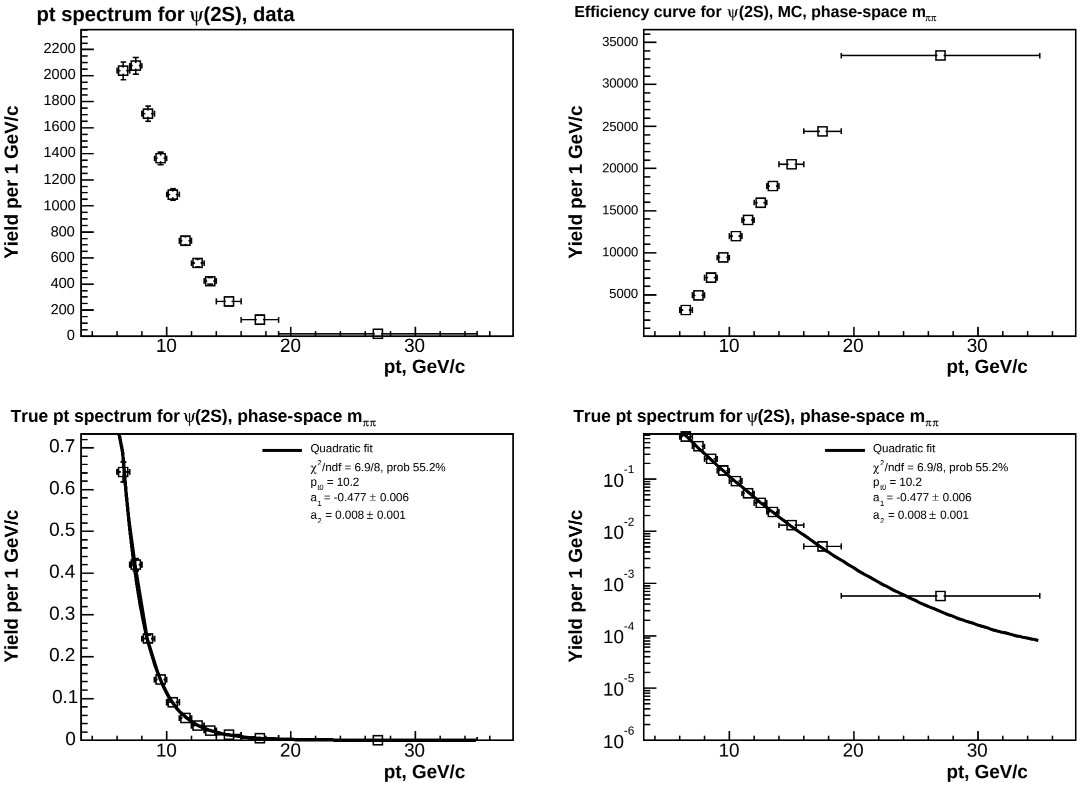

Figure G-1: The p_t distributions of $\psi(2S)$. Upper-left plot: raw data. Upper-right plot: the detector efficiency curve. Two lower plots are the ratio of the data and the efficiency curve in both linear and logarithmic scales. The $m_{\pi\pi}$ parametrization used in the Monte Carlo generation for this Figure is phase space (Equation 5.1).

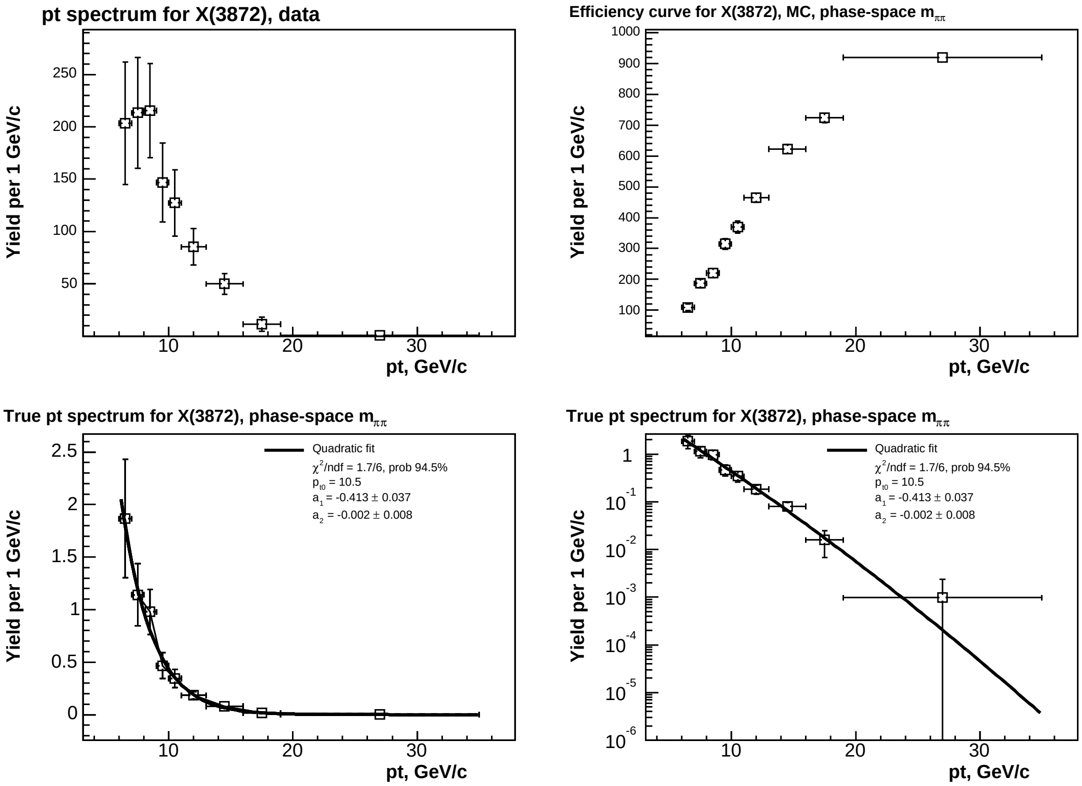

Figure G-2: The p_t distributions of $X(3872)$. Upper-left plot: raw data. Upper-right plot: the detector efficiency curve. Two lower plots are the ratio of the data and the efficiency curve in both linear and logarithmic scales. The $m_{\pi\pi}$ parametrization used in the Monte Carlo generation for this Figure is phase space (Equation 5.1).

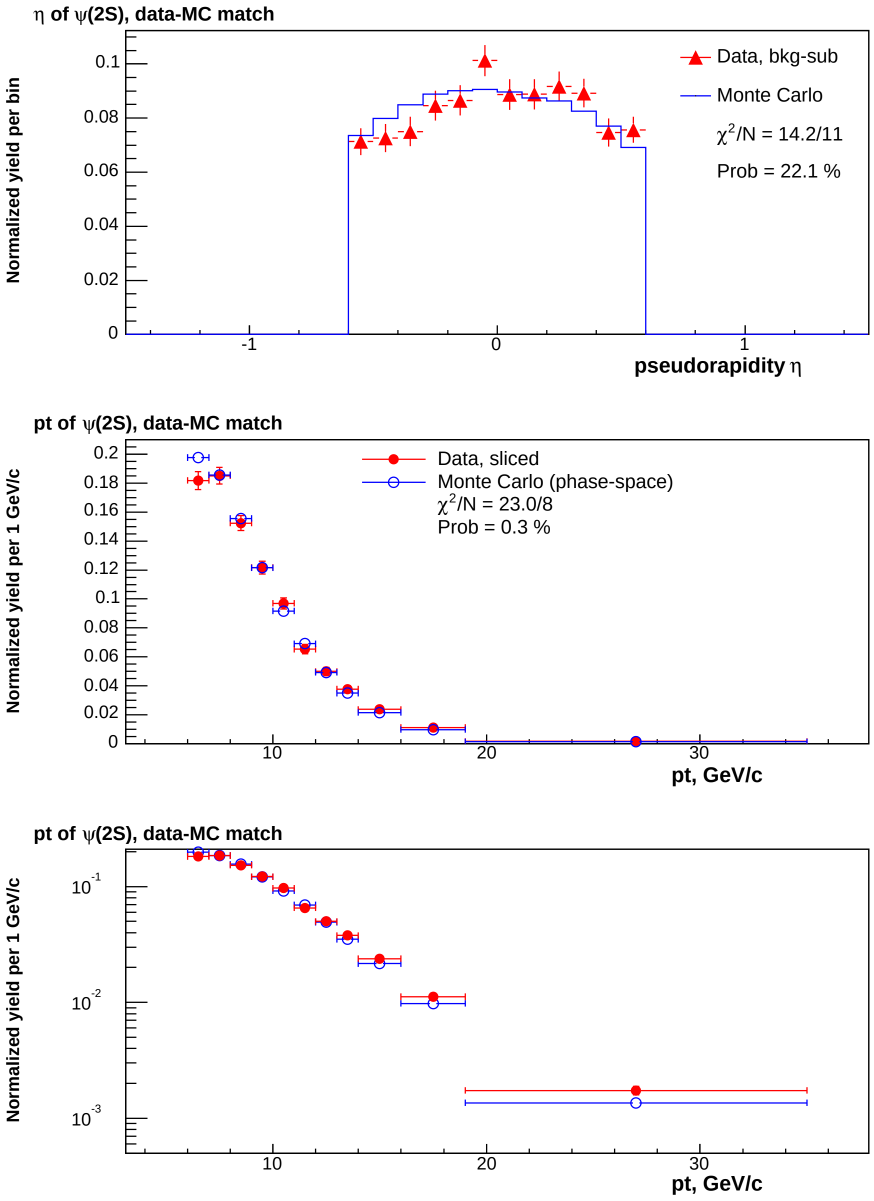

Figure G-3: Top: the comparison between the η distributions of $\psi(2S)$ in raw data and after Monte Carlo simulation, generated with the phase-space $m_{\pi\pi}$ parametrization (Equation 5.1); middle and bottom: the comparison between the p_t distributions in linear and logarithmic scales.

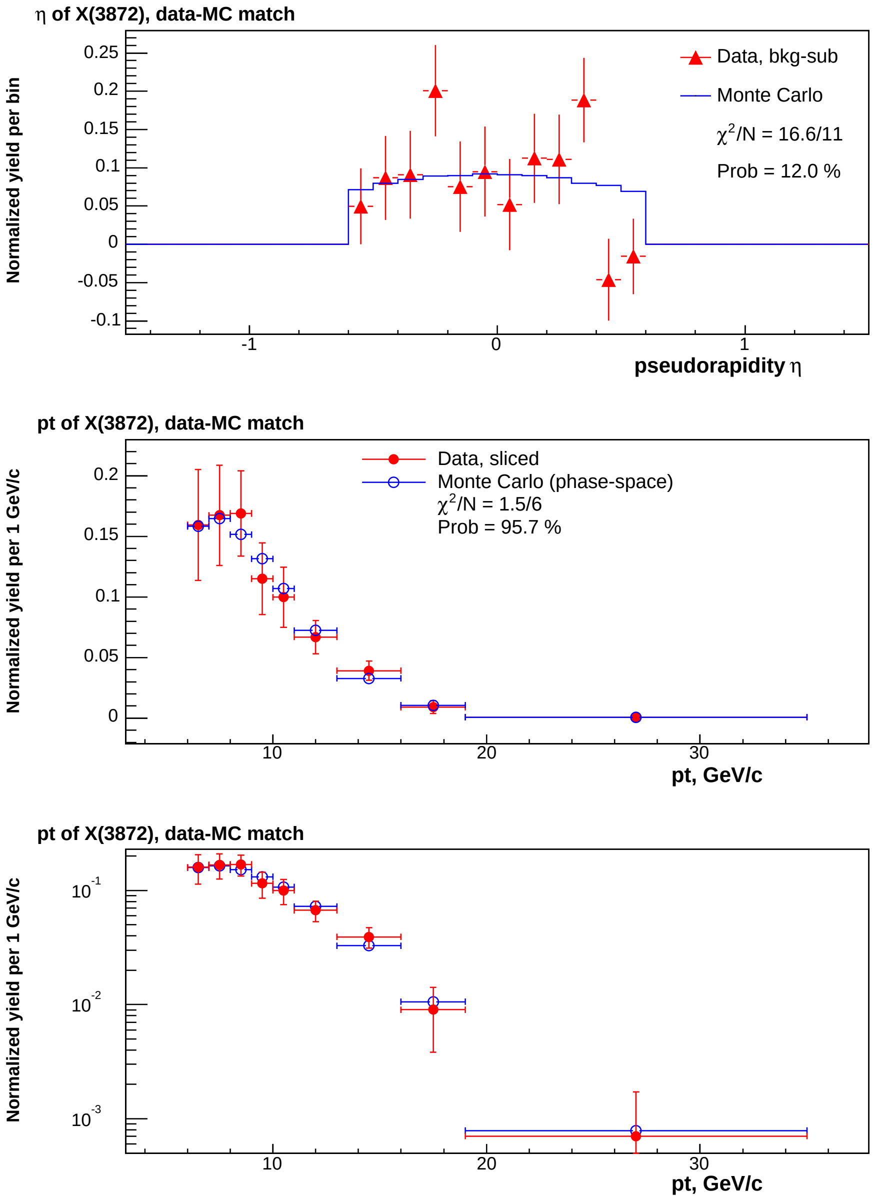

Figure G-4: Top: the comparison between the η distributions of the $X(3872)$ in raw data and Monte Carlo simulation, generated with phase-space $m_{\pi\pi}$ parametrization (Equation 5.1); middle and bottom: the comparison between the p_t distributions in linear and logarithmic scales.

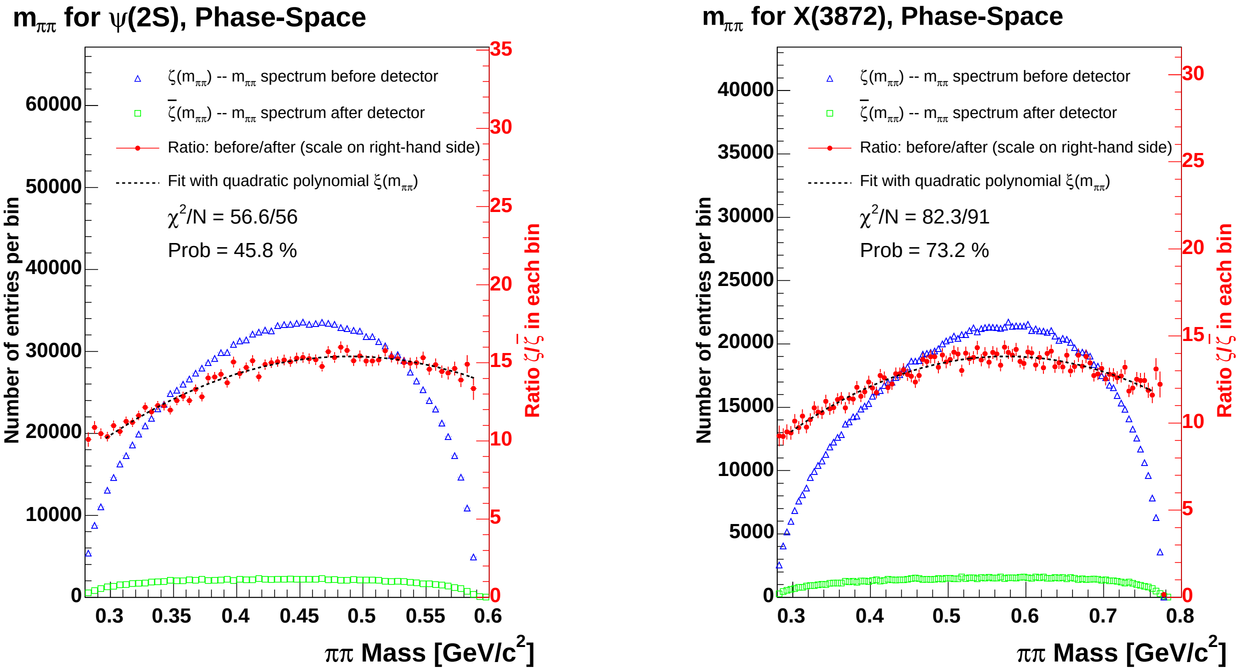

Figure G-5: The ratios (points) of pre-detector (triangles) to post-detector (boxes) $m_{\pi\pi}$ distributions, (*i.e. inverse* efficiency) for the phase space $m_{\pi\pi}$ parametrization for the $\psi(2S)$, left; and for the $X(3872)$, right.